Ecole Normale Supérieure de Cachan

Laboratoire de Photonique Quantique et Moléculaire

THÈSE DE DOCTORAT

Spécialité: Sciences Physiques et Chimiques

par

MARCIN ZIELIŃSKI

pour obtenir le grade de Docteur de L'Ecole Normale Supérieure de Cachan

Le 9 Février 2011

NANOSCALE ENGINEERING OF SEMICONDUCTOR HETEROSTRUCTURES FOR QUADRATIC NONLINEAR OPTICS AND MULTIPHOTON IMAGING

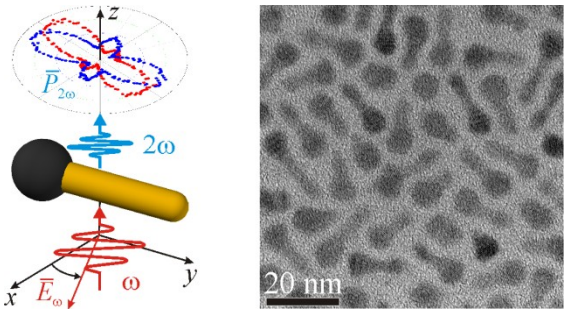

Composition du jury:

M. BENOIT BOULANGER	Président du jury
M. HERVÉ RIGNEAULT	Rapporteur
M. LIBERATO MANNA	Rapporteur
M. DAN ORON	Examinateur
M. DOMINIQUE CHAUVAT	Codirecteur de thèse
M. JOSEPH ZYSS	Directeur de these

Institut d'Alembert (IDA)

NaBi CNRS-Weizmann Institute European Associated Laboratory (LEA)

To Dominique,

who has delivered the light and instilled my passion

Résumé en français

Les phénomènes de diffusion cohérente non-linéaire ont été récemment proposés en alternatives à la fluorescence comme processus de marquage en microscopie multiphotonique. Les matériaux couramment appliqués dans ce contexte buttent toutefois sur une limite inférieure en taille déterminée par le seuil de détection de signaux faibles en optique non-linéaire. Aucun des efforts récents en détection en génération de second-harmonique (GSH), qui est le processus non-linéaire d'ordre le plus bas, n'a permis de descendre à ce jour au-dessous d'une barrière en taille de ~40 nm même en ayant recours aux techniques de détection les plus sensibles telles que le comptage de photons uniques. Les nanoparticules (NPs) restent ainsi dans la famille des nano-diffuseurs de "grande" taille.
Il apparaît toutefois possible de déplacer de façon significative cette limite inférieure vers les plus petites tailles en substituant aux isolants diélectriques ou aux semi-conducteurs à grands gaps des particules quantiques (PQs) à base de semi-conducteurs à gaps directs.

Dans ce travail, un nouveau type de nanosondes hautement non-linéaires a été conçu et développé de façon à franchir cette barrière de taille minimale pour atteindre l'échelle de nanoparticules uniques. Nous considérons ainsi l'excitation résonnante à deux photons de nanoparticules quantiques individuelles à base de CdTe (de la famille des "zinc-blendes") d'un diamètre d'environ 12.5nm, qui fournissent une émission cohérente efficace par GSH jusqu'à hauteur de 10^5 comptages de photons par seconde. Elles présentent de plus l'avantage d'une remarquable sensibilité à l'orientation de leur réseau cristallin octupolaire.

De plus, il a été démontré que les effets de confinement quantique déterminent fortement les caractéristiques de la susceptibilité non-linéaire du second-ordre $\chi^{(2)}$. La caractérisation quantitative du $\chi^{(2)}$ des PQs, en particulier leur dispersion spectrale et leur dépendance en taille est menée par spectroscopie de particules uniques ainsi qu'en moyenne d'ensemble par diffusion Hyper-Rayleigh (HRS). Nous fournissons en particulier la preuve que sous certaines

conditions, le $\chi^{(2)}$ de structures à base de semi-conducteurs en mode de confinement quantique peut très largement dépasser sa valeur en milieu massif. De plus, un nouveau type de PQs hybridant des semi-conducteurs en géométries de type "bâtonnet sur sphère" (BS) a été développé sur la base de composantes cristallines de symétries différentes, afin d'augmenter leur non-linéarité quadratique effective, tout en maintenant leur taille dans un régime proche d'un fort confinement quantique. Le nouveau tenseur hybride complexe $\chi^{(2)}$ est analysé en terme d'interférence des susceptibilités constitutives, en prenant en compte les différentes formes et symétries associées aux composantes octupolaires et dipolaires. Il en résulte pour de telles structures une exaltation significative du $\chi^{(2)}$, qui excède celle des PQs à constituant unique compte tenu du couplage entre matériaux non-linéaires et d'un temps de décohérence plus long, que nous attribuons à un effet de separation de charge photo-induit.

Mots-clés: microscopie multiphotonique, la génération de seconde harmonique, polarimétrie non linéaire, particules quantiques semi-conducteurs, confinement quantique, hétérostructures hybrides.

Abstract

Nonlinear coherent scattering phenomena from single nanoparticles have been recently proposed as alternative processes for fluorescence in multiphoton microscopy staining. Commonly applied nanoscale materials, however, have reached a certain limit in size dependent detection efficiency of weak nonlinear optical signals. None of the recent efforts in detection of second-harmonic generation (SHG), the lowest order nonlinear process, have been able to cross a ~40 nm size barrier for nanoparticles (NPs), thus remaining at the level of "large" nanoscatterers, even when resorting to the most sensitive detection techniques such as single-photon counting technology. As we realize now, this size limitation can be significantly lowered when replacing dielectric insulators or wide gap semiconductors by direct-gap semiconducting quantum dots (QDs).

Herein, a new type of highly nonlinear nanoprobes is engineered in order to surpass above mentioned size barrier at the single nanoparticle scale. We consider two-photon resonant excitation in individual zinc-blende CdTe QDs of about 12.5 nm diameter, which provide efficient coherent SHG radiation, as high as 10^5 Hz, furthermore exhibiting remarkable sensitivity to spatial orientation of their octupolar crystalline lattice. Moreover, quantum confinement effects have been found to strongly contribute to the second-order nonlinear optical susceptibility $\chi^{(2)}$ features. Quantitative characterization of the $\chi^{(2)}$ of QDs by way of their spectral dispersion and size dependence is therefore undertaken by single particle spectroscopy and ensemble Hyper-Rayleigh Scattering (HRS) studies. We prove that under appropriate conditions, $\chi^{(2)}$ of quantum confined semiconducting structures can significantly exceed that of bulk.

Furthermore, a novel type of semiconducting hybrid rod-on-dot (RD) QDs is developed by building up on crystalline moieties of different symmetries, in order to increase their effective

quadratic nonlinearity while maintaining their size close to a strong quantum confinement regime. The new complex hybrid $\chi^{(2)}$ tensor is analyzed by interfering the susceptibilities from each component, considering different shape and point group symmetries associated to octupolar and dipolar crystalline structures. Significant SHG enhancement is consequently observed, exceeding that of mono-compound QDs, due to a coupling between two nonlinear materials and slower decoherence, which we attribute to the induced spatial charge separation upon photoexcitation.

Keywords: multiphoton microscopy, second-harmonic generation, nonlinear polarimetry, semiconducting quantum dots, quantum confinement, hybrid heterostructures.

Contents

Contents 1

Introduction 3

Chapter I | Optical properties of semiconducting quantum confined heterostructures 7

I.1 Shrinking dimensionality of the bulk into the quantum dot scale 8
I.1.1 Quantum Confinement 8
I.1.1.1 Density of states 12
I.1.1.2 Coulomb interactions and confinement regimes 14
I.1.2 Band structure of CdTe 16
I.2 Optical interactions 17
I.2.1 Scattering 19
I.3 Chapter summary 20

Chapter II | Colloidal CdTe-based QD samples: synthesis and characterization 21

II.1 Guidelines for material selections 22
II.2 Characterization of dot-shaped CdTe/CdS core/shell QDs 22
II.2.1 Chemical synthesis of dot-shaped CdTe/CdS core/shell QDs 23
II.2.2 Shape and size distribution of dot-shaped CdTe/CdS QDs 23
II.3 Synthesis and characterization of dot-shaped CdTe QDs 25
II.4 Characterization of rod-on-dot CdTe/CdS heterostructures 27
II.4.1 Chemical synthesis of rod-on-dot CdTe/CdS heterostructures 29
II.4.2 Shape determination and effective size distribution of RD CdTe/CdS heterostructures 30
II.5 The role and importance of the shell in type-II QDs 32
II.6 Sample preparation 33
II.7 Chapter summary 34

Chapter III | Coherent second-harmonic microscopy for detection of single semiconducting QDs 35

III.1 Contrast mechanisms for two-photon nonlinear microscopy 36
III.1.1 Two-photon excited fluorescence 36
III.1.2 Second-harmonic generation 38
III.2 Second-order nonlinearity of CdTe – from bulk to single QD scale 41
III.3 Nonlinear two-photon polarization sensitive microscopy setup 45
III.3.1 Optical and effective spatial resolution in multi-photon microscopy 48

III.4 Time correlated single photon counting in detection of single nanoparticles 51
III.5 Chapter summary 53

Chapter IV | Second-harmonic generation from CdTe QDs: single dot studies 55

IV.1 SHG from single dot-shaped CdTe/CdS core/shell QDs 56
IV.1.1 Spectral dependence of the SHG process from spherical CdTe/CdS core/shell QDs 59
IV.1.2 Contribution of the CdS shell to the overall SHG emission process 62
IV.1.3 Orientation dependent SHG polarization response from spherical CdTe/CdS core/shell QDs 63
IV.1.3.1 Analysis of the SHG polarization dependence 64
IV.1.3.2 SHG polarization response with respect to the CdTe symmetry constraint 68
IV.2 SHG from single rod-on-dot CdTe/CdS heterostructures 70
IV.2.1 Special features of SHG emission from rod-on-dot QD heterostructures 73
IV.2.2 Polarization analysis of the SHG emission of rod-on-dot CdTe/CdS QDs 78
IV.2.2.1 Simulation model for polarization analysis of RD QD heterostructures 80
IV.2.2.2 The role and impact of the CdS rod length into the total SHG intensity 81
IV.2.2.3 Errors in inferring the orientation of the crystalline lattice from SHG polarization analysis 85
IV.3 Accuracy of the polarization analysis from a reduced set of raw data points 86
IV.4 Chapter summary 89

Chapter V | Size dependence of the second-order nonlinearity – single dot and HRS studies 91

V.1 Size dependence of SHG from single CdTe quantum dots 92
V.1.1 Detection threshold of the size dependent SHG signal intensity 93
V.1.2 Estimate of the second-order nonlinear susceptibility 97
V.1.3 Error sources in determining the size dependence of the second-order nonlinear susceptibility 99
V.2 Hyper-Rayleigh Scattering from CdTe QDs 101
V.3 Relations between spectral and size dependence of CdTe $\chi^{(2)}$ features 105
V.4 Chapter summary 107

General conclusions 109

Appendix A: Correction of the raw data for SHG wavelength dependence 113

Appendix B: Model for SHG polarization response of spherical CdTe/CdS QDs 121

Appendix C: Model for SHG polarization response of RD QD heterostructures 133

Appendix D: The list of publications 145

Bibliography 161

Introduction

Recent achievements in fabrication and characterization of inorganic nanoparticles of high optical quality have inspired new areas of research into the fundamental properties and applications of these nanoscale materials. Basically divided into metals, semiconductors and insulators, morphologically and geometrically tailored nanoscale systems are driven in order to selectively combine desirable properties at the sub-wavelength regime towards optical probing. This approach becomes particularly fascinating and challenging when is put on nonlinear optical effects occurring with small nanoparticle assemblies of typical size below 20 nm. At this scale, the electronic properties of such small nanostructures lie at an intermediate distance between those of a single atom and those of bulk materials. In consequence, this scale provides an inspiring avenue onto the molecular regime for physical properties better known at the bulk level, possibly leading to novel and remarkable responses, depending on size, composition and shape of the nanocrystals.

Applied nanoscale nonlinear optics has reached a certain limit in size dependent detection efficiency of weak signals in nonlinear processes, e.g. in our case the lowest-order nonlinear scattering which is known as second-harmonic generation (SHG). Recent efforts in detection of nonlinear scattering from noncentrosymmetric nanocrystals, deriving from the high nonlinearities of their well known bulk counterparts such as $KTiOPO_4$ (Le Xuan et al. [1]) or $BaTiO_3$ (Hsieh et al. [2]), have shown photostable and efficient SHG emission with a high damage threshold for these nanoparticles. None of these efforts, however, has been able to pass a ~40 nm size barrier, thus remaining at the level of large nanoscatterers while resorting to the most sensitive available technologies for SHG detection. As we realize now, this barrier can be overcome when replacing dielectric insulators by direct-gap semiconducting materials.

Shrinking the size while maintaining an efficient coherent scattering process requires a new approach towards nanoengineering of semiconducting nanoscale heterostructures as potential sources of enhanced optical nonlinearities. This approach has been introduced nearly a decade ago by Jacobsohn and Banin [3] and demonstrated at a preliminary level by hyper-Rayleigh scattering (HRS) from a colloidal suspension of II-VI semiconductor CdSe quantum dots (QDs), with sizes varying from 20 to 100 Å. A strongly size dependent, incoherent SHG signal was evidenced and attributed both to the nanocrystal volume and its surface. Nevertheless, the crucial experimental evidence that 10 to 15 nm large QDs can emit the coherent SHG at a detectable level in the case of single nanoparticle studies remained elusive. Therefore, this was the prime objective of this work.

Indeed, for the first time, we have successfully surpassed this single nanoparticle size barrier by considering two-photon resonant SHG in individual QDs, in order to find an alternative emission system for fluorescent nanolabels. In our first work (Zielinski et al. [4]), we shown that highly nonlinear zinc-blende structures like CdTe QDs are ideally suited for this task. Due to their perfectly octupolar crystalline structure, size scaled energy band gap, and above all, high values of nonlinear coefficients, CdTe nanocrystals of about 12.5 nm diameter can efficiently provide very high SHG count rates, as high as 10^5 Hz. Additionally, remarkable sensitivity to orientation of the crystalline lattice was clearly demonstrated. Moreover, quantum confinement effects have been found to strongly contribute to the second-order nonlinear optical susceptibility, suggesting that QD scale materials are not limited by their bulk properties. Hence our attention focused on quantitative characterization of the nonlinear susceptibility of quantum confined QDs by way of their spectral dispersion and size dependence. Using single particle spectroscopy and ensemble HRS methods, we shown that under appropriate conditions, the nonlinear susceptibility of quantum confined structures can significantly exceed that of bulk (Winter et al. [5]), and therefore allow for better understanding and control the nonlinear properties at the individual QD scale.

Further motivations of this work originate from the interest in the engineering of high optical nonlinearities, by the optimal choice of semiconducting materials with adequate electronic properties. Our ambition is to extend their range to any particular application in high resolution microscopy. Current studies carried out by several research groups, designate many possible ways towards such goal, each of them involving electronic band structure engineering, and excitonic or electron–plasmon interactions of hybrid heterostructures of high complexity. Worth mentioning here is, the work presented by group of Psaltis [6], on huge

SHG nanocavity-like enhancement in ~80 nm large $BaTiO_3$ nanoparticles covered by a ~10 nm thick gold shell. In addition, interesting approach of synergistic SHG coupling of gold nanorods into a semiconductor QD cores (Shaviv and Banin [7]) are worth attention. At a more basic level, a novel approach for SHG obtained from purely semiconducting materials can attract a significant interest. As a proof-of-principle experiment, composite rod-on-dot hybrids built from different crystalline symmetry moieties were recently reported (Zielinski et al. [8]), as capable to further improve initially reported results. Their high quadratic nonlinearity was precisely engineered following the blueprint of a pointwise sum of the susceptibilities for each of the components. The nonlinear susceptibility of such hybrid leads to a significant SHG enhancement assigned to slower decoherence and improved spatial charge separation upon excitation, which exceeds that of 'mono-compound' material QDs.

This thesis is organized as follows: Chapter I provides an introduction to the downscaling of semiconductors from bulk to the nanoscale. Quantum confinement effects in nanoparticles of different dimensionality are explained using a simple '*spherical box*' approximation. These fundamental properties are further investigated towards a better understanding of the electronic band structure as well as optical interactions in QDs. Chapter II deals with fabrication and characterization of suitable materials for second-order nonlinear microscopy, this imaging method being then reviewed in Chapter III. Coherent SHG emission from isolated mono-compound CdTe QDs and hybrid rod-on-dot semiconductor heterostructures is investigated in Chapter IV. These studies focus on spectral features of the second-order nonlinear optical susceptibility of both types of materials. Strong orientational dependence of the SHG tensorial features is pointed out, allowing to infer the spatial orientation of each single nanocrystal. Chapter V addresses single nanoparticle spectroscopy and HRS studies of the size dependent nonlinear susceptibility of CdTe QDs. These studies, together with spectral features reported in the preceding chapter, demonstrate the superiority of QDs over the bulk in the context of second-order nonlinear properties. In the last part of the thesis we provide details about the simulation algorithms used in this work. Finally, this work is summarized and final conclusions and future prospects are drawn.

Chapter I | Optical properties of semiconducting quantum confined heterostructures

I.1 Shrinking dimensionality of the bulk into the quantum dot scale 8
I.1.1 Quantum Confinement 8
I.1.1.1 Density of states 12
I.1.1.2 Coulomb interactions and confinement regimes 14
I.1.2 Band structure of CdTe 16
I.2 Optical interactions 17
I.2.1 Scattering 19
I.3 Chapter summary 20

The case of nanoscale semiconductors illustrates the understanding of material properties as a function of size and composition. In this chapter the key features of quantum confined semiconducting structures are briefly introduced, following the literature. Our interest here is to point out the originality of semiconducting nanocrystals (SC NCs) in the context of their optical features. Firstly, we start by explaining the quantum confinement effect, using a simple model, and show how SC properties evolve while crystal dimensionality decreases, starting from the bulk all the way to a single quantum dot. We point out how the NC shape and its material composition translate onto the optical properties, and explain optical excitation mechanisms in relation with absorption and scattering processes. Finally the electronic band structure of bulk CdTe is discussed and compared to that of a single CdTe QDs.

I.1 Shrinking dimensionality of the bulk into the quantum dot scale

The properties of quantum confined SC NCs place these materials between isolated atoms (or small molecules) and a bulk phase of condensed matter.[9] Like in any material, fundamental electrical and optical features of SCs vary when the size is reduced and the electronic energy level spacing exceeds different energies characterizing the structural properties, e.g. the temperature of the surrounding environment (*kT*), the binding energy or the exciton Rydberg energy. Here we show that this size dependence becomes extremely significant when the crystal is shrunk into a quantum confined structure. Semiconductor crystals, where the Fermi level lies between two bands (Figure I-1) exhibit completely different behavior from that of metals or insulators. The band edges dominate the low-energy optical and electrical interactions, so optical excitations across the band gap (BG) depend strongly on cluster size variations (for clusters starting from approximately 10,000 of atoms). This leads also to strong size dependence of electrical carriage transport through the crystalline volume due to the energy variations required for charge appearance or withdrawal on the NC.[10]

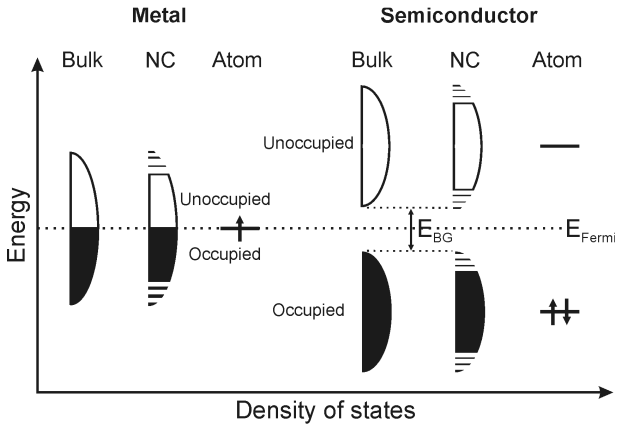

Figure I-1 | Comparison of the changes in the electronic structure accompanying a reduction in size, in metals and semiconductors.

I.1.1 Quantum Confinement

The first attempts in understanding the quantum mechanics of confined SC NCs were considered nearly three decades ago, resulting in a description of diffraction by the charges (electrons and holes) of the periodic lattice potential in the semiconductor NC.[11-13] A key feature of SC materials is that charge diffraction leads to a characteristic band structure,

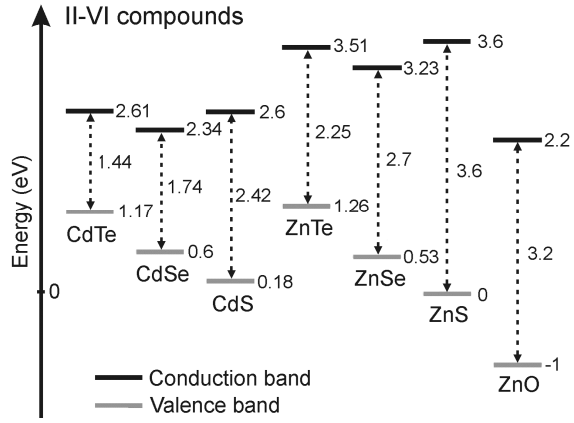

Figure I-2 | Comparison of the energy levels of conduction and valence bands as well as band gaps for different bulk semiconducting materials (II-VI groups SC compounds).[14-15]

where allowed electronic energy states exhibit the form of broad valence and conduction bands (VB and CB, respectively), resulting from a complex set of anisotropic relations between energy and momentum.[14] At the macroscopic scale, the bands are continuous, and the energy band gap (E_{BG}) between them is a fixed parameter, determined by the crystalline material composition (Figure I-2). However, decrease in dimensionality of the SC heterostructure, where at least one of the dimensions ($L_{x(y,z)}$, see Figure I-3) is under quantum confinement regime results in more confined electronic excitations due to the interaction between the nanoparticle (NP) boundaries (with energies between the orbital spacing) and confined electrons. Decrease in the NC size also increases the energy band gap, as confirmed by the blue-shifted luminescence. In direct-gap size confined SC NCs (such as II-VI SCs), absorption of a photon above the BG usually leads to generation of a single, Coulomb attracted electron-hole pair (an exciton, confined by the material boundaries) and its quick relaxation, with simultaneous reemission of a new photon, which has an energy exactly matching the BG. For example, in CdSe QDs the shift of energy gap varies from 1.2 eV up to 3.0 eV (while its bulk BG energy is equal 1.71 eV).[16]

This effect, however, can be controlled also by composition of the material, e.g. different size of the CdSe and CdTe QDs span the visible (VIS) spectral region,[17-21] whereas PbS QDs traverse from VIS to the near infrared (NIR),[22] while materials like ZnSe exhibit efficient luminescence in the ultraviolet (UV).[23]

In the first approximation, quantum confinement can be described using a simple '*spherical box*' model,[11-12,24] where the SC NC is embedded inside an insulating matrix, as illustrated in Figure I-3(d). The exciton resides in the infinite potential well, which leads to a quantized valence and conduction band structures exhibiting ladder-like discrete energy levels for both hole and electron.

In other words, for an ideal SC NC, quantum confinement occurs when the width of the infinite potential approaches the exciton Bohr radius of the material $a_B = h^2\varepsilon / m_r e^2$, where m_r stands for the reduced mass of the exciton, and ε for the dielectric constant of the material. When the width of the infinite potential well is comparable to a_B (exactly like in the case of QDs), the VB and CB split into discrete energy surfaces in **k**-space. In such a case, the Schrödinger equation take the following form:[25]

$$-\frac{\hbar^2}{2}\nabla\frac{1}{m_{e,h}(z)}\nabla\psi_n(\mathbf{k},\mathbf{r})+\tilde{U}(\mathbf{r})\psi_n(\mathbf{k},\mathbf{r})=E_{n,k}\psi_n(\mathbf{k},\mathbf{r}) \tag{I.1}$$

where the infinite potential $\tilde{U}(\mathbf{r})=V(\mathbf{r})+U(z)$ and the effective masses of the hole and electron $m_{e,h}(z)$ depend on the coordinate *z* of the confined direction due to the bandgap mismatch. We assume Bloch function – like eigenstates subsequently summed over **k** to describe bonding between the delocalized molecular orbitals (MOs), to be identical throughout the various material shells:

$$u_{\bar{k},u}(\mathbf{r})=e^{i\bar{k}\cdot\bar{r}}\chi_{\bar{k},u}(\mathbf{r}) \tag{I.2}$$

where $\chi_{k,u}$ is subject to the periodicity of the unit cell (with relatively weak *k* dependence), the $e^{i\bar{k}\cdot\bar{r}}$ factor is a plane wave-like factor with a wavelength $\lambda = 2\pi / k$ longer than that of the unit cell. The Bloch MO in the case of a single $\bar{k}$ is infinitely delocalized.

Following this assumption, the wave function takes the form: $\psi(\mathbf{k},\mathbf{r})=u(\mathbf{k},\mathbf{r})\phi(z)$, where $\phi(z)$ is the '*envelope function*' of the confined state. Combining the Bloch function behavior with the Schrödinger equation, we obtain:

$$-\frac{\hbar^2}{2}\nabla\frac{1}{m_{e,h}(z)}\nabla\phi(z)+U(z)\phi(z)=E_{n,0}\phi(z) \tag{I.3}$$

For infinitely high barriers of the potential barrier, the energy of the *n*-th state confined in a rectangular potential well (2D) of width L_z is:

$$E_{n,0} = n^2 \frac{\pi^2 \hbar^2}{2m_{e,h} L_z^2} \qquad (2D) \tag{I.4}$$

Further reduction of the SC NC dimensionality (illustrated in Figure I-3) by confining in L_x and L_y directions lead to quantum rods (QRs) and QDs. Therefore the quantum energies of the *n*-th confined states inside the infinite potential barrier can be expressed as:

$$E_{n_y,n_z} = \frac{\pi^2 \hbar^2}{2m_{e,h}} \left(\frac{n_y^2}{L_y^2} + \frac{n_z^2}{L_z^2} \right) \qquad (1D) \tag{I.5}$$

$$E_{n_x,n_y,n_z} = \frac{\pi^2 \hbar^2}{2m_{e,h}} \left(\frac{n_x^2}{L_x^2} + \frac{n_y^2}{L_y^2} + \frac{n_z^2}{L_z^2} \right) \qquad (0D) \tag{I.6}$$

These expressions lead to a simple common conclusion: the energy of an extra electron in a tiny semiconducting crystallite structure amounts to the conduction band energy (E_c) plus the quantum localization energy of a '*pseudo electron*' of effective mass m_e (treated as a pseudo particle), which has no direct relationship with the real electron mass, and often displays a smaller value.[12]

The wave function $\psi_n(\mathbf{k},\mathbf{r})$, as a product of an '*envelope function*' and a Bloch function can be generalized to determine confined VB and CB states in the wake of progressive reduction of the dimensionality (where coupling between the bands has to be considered). Generalized forms for the CB wave function $\psi^e_{m_s}(\mathbf{r})$ and VB wave function $\psi^h(\mathbf{r})$ can be written as follows:[25]

$$\psi^e_{m_s}(\mathbf{r}) = \phi^e(z) u^e_{m_s}(x,y) \qquad m_s = \pm\frac{1}{2} \tag{I.7}$$

$$\psi^h(\mathbf{r}) = \sum_{m_j} \phi^h_{m_j}(z) u^h_{m_j}(x,y) \qquad m_j = \pm\frac{3}{2}, \pm\frac{1}{2} \tag{I.8}$$

where m_s is the spin of the electron.

I.1.1.1 Density of states

As illustrated in Figure I-3 the density of states ρ (DOS) critically depends on the NC dimensionality. The DOS expresses directly the number of possible solutions of the Schrödinger equation (I.1) within a given interval eigenstate energy *E* and is seen to depend on the structure confinement:

$$\rho = \frac{m}{\pi^2 \hbar^3} \sqrt{2mE} \qquad (3D) \tag{I.9}$$

$$\rho = \frac{m}{\pi \hbar^2 L_z} \sum_{n_z} \theta\left(E - E_{n_z}\right) \qquad (2D) \tag{I.10}$$

$$\rho = \frac{\sqrt{2m}}{\pi \hbar L_y L_z} \sum_{n_z, n_z} \sqrt{\frac{1}{E - E_{n_y, n_z}}} \qquad (1D) \tag{I.11}$$

$$\rho = \frac{2}{L_x L_y L_z} \sum_{n_z, n_z, n_z} \delta\left(E - E_{n_z, n_z, n_z}\right) \qquad (0D) \tag{I.12}$$

A detailed discussion how the SC NC shape impacts on the optical properties can be found for example in an excellent review by Scholes.[26] Here we explain only how the shape influences the major DOS features, which are directly related to the SC NC optical properties. In our considerations the most important features are that of QRs and QDs. In the case of the QRs, the DOS is strongly peaked and decays as $1/\sqrt{E}$ (Figure I-3(c)). Heavy and light hole sub-bands are mixed, leading to coupling between the energy levels of the VB.[27]

On the contrary, QDs exhibit atypical Dirac $\delta(E)$ function like behavior for 3*D* confined DOS, which allows for accommodation of only two carriers of opposite spins on a single quantized energy level, therefore called "*artificial atoms*". The first approximation model of the parabolic band, however, does not fully reflect the real complexity of the QD DOS, because there are no SCs exhibiting such simple parabolic conduction and valence bands.[11] Therefore, more realistic approaches have to be considered, e.g. the multiband effective mass approximation,[16,28] which takes into account degenerated sub-bands, dispersion of light and heavy hole branches for non-zero *k*, and spin-orbit splitting of the electron sub-bands. The multiband effective mass approximation is more efficient in quantitative description of the

optical properties of SC NCs than the parabolic approximation, and can be used in order to describe the transitions between the quantum size levels (QSLs), and to calculate their energies.[16,28]

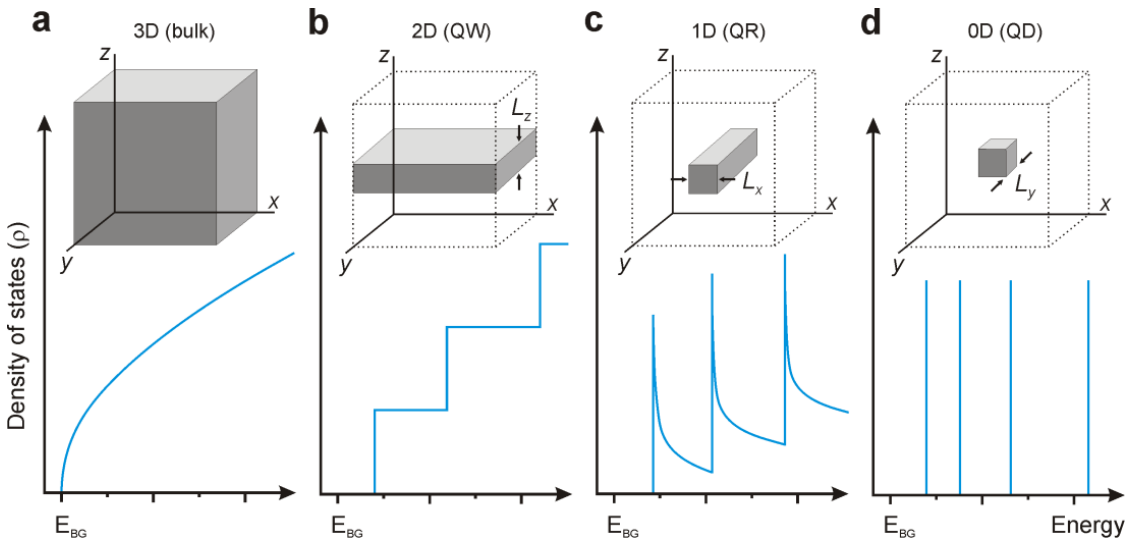

Figure I-3 | Schematic representation of decreasing dimensionality of a SC crystal from bulk (a), quantum well (QW, (b)), and quantum rod (QR, (c)) into the single QD scale (d), as shown with corresponding densities of states (ρ).

For tight-bounded semiconducting NCs, the frequency dependent rate of a spontaneous transition from an excited electron-hole state $|j\rangle$ to the ground state $|0\rangle$ can be determined from Fermi's '*golden rule*' namely:[29]

$$\Gamma_j = \frac{e^2}{3\pi\varepsilon_0 m^2 \hbar c^3} \omega_j \left|\langle o|\mathbf{p}|j\rangle\right|^2 \tag{I.13}$$

where e is the electron charge, ε_0 is the permittivity of vacuum, m is the electron rest mass, ω_j is the frequency of the emitted light, and $\left|\langle o|\mathbf{p}|j\rangle\right|$ is the matrix element of the momentum, related to the dipolar matrix element by $\left|\langle o|\mathbf{p}|j\rangle\right| = i\,m\,\omega_j \left|\langle o|\mathbf{r}|j\rangle\right|$.[30] Note, that this dependency applies to both absorption, and scattering processes. The size dependence of Γ_j is determined by that of the matrix element modulus $\left|\langle o|\mathbf{p}|j\rangle\right|$ and the emission frequency ω_j. Assuming, that the exciton states is located near the band extrema, its wave function be

expressed as a product of the Bloch function $u(\mathbf{r})$ and an '*envelope function*' $\phi(\mathbf{r})$, and the matrix element of the momentum for an allowed transition is given by $\langle u_{CB}|\mathbf{p}|u_{VB}\rangle$.[29-30] Therefore the interband transitions are largely determined by crystalline lattice defined Bloch functions, and the $\langle u_{CB}|\mathbf{p}|u_{VB}\rangle$ term does not depend on the NC size. The decay rate of an ideal two-level exciton is expected to be proportional to the emission frequency, e.g. $\Gamma_j = const \cdot \omega_j$.[31]

I.1.1.2 Coulomb interactions and confinement regimes

In strongly confined structures, positions of the electrons and holes are constrained. Electrostatic screening is less effective, leading to reduction of the effective dielectric constant ε, which results in an increase of the binding energy (E_B). For strong enough confinement, Coulomb interactions can be neglected in the confinement direction. In such conditions the single particle '*envelope function*' $\phi^{e,h}(z_{e,h})$ can be used in order to describe the exciton wave function:

$$\Phi_X(\mathbf{r_e},\mathbf{r_h}) = \phi^e(z_e)\phi^h(z_h)\ \phi(\varrho_e,\varrho_h) \tag{I.14}$$

where the $\phi(\varrho_e,\varrho_h)$ function accounts for the in-plane confined motion of the electron and hole expressed with respect to respect to in-plane coordinates $\varrho_{e,h}$. The in-plane wave function $\phi(\varrho_e,\varrho_h)$ abides to a single-particle Schrödinger equation (with an effective excitonic potential U_X):[25]

$$-\frac{\hbar^2}{2(m_e+m_h)}\nabla^2\,\phi(\varrho_e,\varrho_h)+U_X\,\phi(\varrho_e,\varrho_h)=E_B\,\phi(\varrho_e,\varrho_h) \tag{I.15}$$

where: $m_e + m_h = M_{exciton}$ is the exciton translation mass. The remaining dispersion of the exciton is expressed by its kinetic energy: $E_{kin} = \hbar^2 K^2 / 2M_{exciton}$ (with **K** as the excitation vector). A similar rules holds for the QRs, therefore their shape has no impact on the binding

energy. For both, 1*D* and 0*D* confined structures it is only the strength of the confinement which determines E_B.

The strength of the quantum confinement is related to the Coulomb energy of the electron-hole interaction, which is of the order of $e^2/\varepsilon a$. As the size is downscaled, the quantization energy increases as $1/a^2$, therefore the Coulomb energy, which scales as $1/a$ becomes only a small correction factor.[16,21] On the contrary, for larger SC NCs the Coulomb electron-hole interaction may surpass the quantization energy. These interactions define the quantum confinement regime, which can be characterized by the ratio between the NC radius, *a*, and the Bohr radius a_B of the bulk exciton. From there on, three different quantum confinement regimes can be distinguished:[24,32]

'*Weak confinement regime'*, where $a \gg a_B$, and the binding energy of an exciton, E_{exc}, is larger than the quantization energy of the electrons and holes. In first approximation, the exciton ground state energy is then expressed as:[32]

$$h\omega = E_{BG} - E_{exc} + \frac{h^2\pi^2}{2(m_e + m_h)a^2} \tag{I.16}$$

Under a weak confinement regime, Coulomb interactions between the electron and hole are strong and have to be taken into account.

'*Intermediate confinement regime'*, which occurs in the SCs exhibiting different effective masses of the electron and hole in an intermediate size ratios $a_e > a > a_h$, where $a_{e(h)} = h^2\varepsilon / m_{e(h)}e^2$ are the Bohr radii of electron and hole, respectively. In this regime, the hole moves in the average potential of a much faster electron (about three orders of magnitude), and stays localized in the center of the NC. The region of its motion around the NC center is much smaller than *a*, therefore size dependence of the exciton ground state may be determined as a localized donor.

'*Strong confinement regime'* occurring for small NCs, where $a \ll a_B$. The electron-hole Coulomb interactions are surpassed by the quantization energy of transitions, so the reduction of the transition energies is relatively small. Interband transitions between quantum-size energy levels of the parabolic VB and CB are governed by selection rules, which limit allowed transitions to levels with the same quantum numbers.

I.1.2 Band structure of CdTe

The band structures of typical II-VI group bulk semiconductors have been well researched using, e.g. 'semi-*ab initio*' approach.[33] Figure I-4(a) illustrates band structures for the case of bulk zinc-blende CdTe crystal, where a single Brillouin zone stems from the Bloch wave of the face-centered cubic crystalline periodic structure of the CdTe crystal. The wave vector k crosses the critical points of the crystalline symmetry, which are as follows: L – a center of a hexagonal facet, Γ – center of the Brillouin zone, X – center of a square facet, and K – middle of an edge joining two hexagonal facets. The center point Γ determines the band edges for the parabolic VB and CB in the first approximation model.

Early efforts on measurements and assignments of the size dependent optical spectrum in QDs were constrained by difficulties in preparation of weakly dispersed, high quality colloidal QDs, with well maintained control over the size dispersion. Successful assignment of the lowest quantized energy levels in many SC QDs could be obtained from a single-band effective mass model.[34] Assignment of the higher excited quantized levels remained difficult due to, e.g. valence-band degeneracy in zinc-blende CdTe QDs,[35] where the conduction band is made of *s* orbitals of cadmium and its valence band is composed of *p* orbitals of tellurium. Following the work of Masumoto et al. [36], the orbital angular momentum in CdTe QDs is mixed with spin angular momentum, and the valence band is split into the topmost $J = 3/2$ band and the split-off $J = 1/2$ band. Quantum confined hole envelope function has an additional angular momentum *L*, therefore possible *L* – *J* coupling may lead to a complicated energy level structure for the VB. Nevertheless, CdTe has a less complicated VB than wurtzite CdS and CdSe QDs, and exhibits a larger spin orbit splitting of 0.927 eV and a smaller E_{BG} = 1.44 eV, therefore the split-off band is expected to mix weakly with the topmost VB.

Since advances in colloidal synthesis techniques allows to obtain NCs of a sufficient quality, e.g. CdSe and CdTe QDs, assignments of multiple numbers of states using size-dependent photoluminescence excitation (PLE) spectroscopy at cryogenic temperatures close to 0 K were carried out with some success.[18,36]

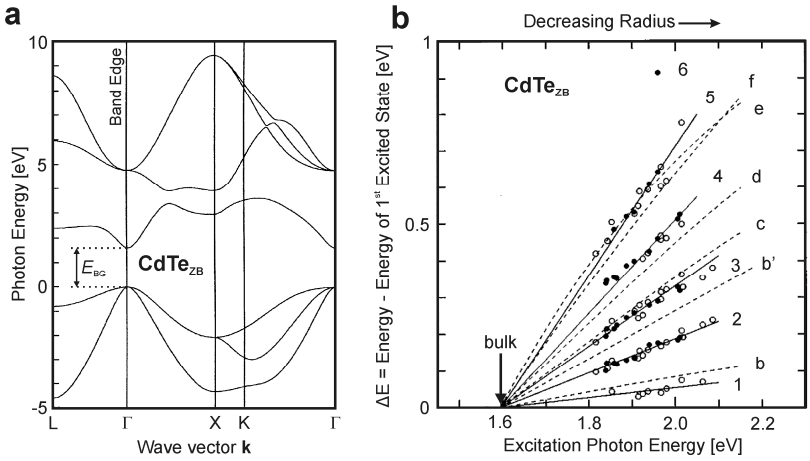

Figure I-4 | a) The band structure of the bulk, zinc-blende like CdTe crystal. Critical points of the Brillouin zone are explained in the text. Adapted from Huang et al.[33] b) Spacing of the excited states of strongly confined CdTe QDs. Dashed lines (labels from *b* to *f*) correspond to the transitions $2SDD_{3/2} \rightarrow 1S_e$, $1PFP_{3/2} \rightarrow 1P_e$, $1PFF_{5/2} \rightarrow 1P_e$, $2PP_{1/2} \rightarrow 1P_e$, $2PFF_{5/2} \rightarrow 1P_e$, and (label *b'*) $3SDD_{3/2} \rightarrow 1S_e$, calculated using the data from Ref. [35], assuming that the lowest burned structure correspond to the transition $1SDD_{3/2} \rightarrow 1S_e$. Straight lines (from 1 to 5) represent experimentally measured data, with the converging point at the lowest exciton energy transition of bulk CdTe, at 1.596 eV. Figure adapted from Ref. [36].

Spacing between the excited states of several samples of strongly confined CdTe QDs is illustrated in Figure I-4(b). The quantized energies of $1SDD_{3/2}$ and $1PFP_{3/2}$ states vary by about 0.1 eV, however the energy separation between these states changes at most by 6.4 meV. On the other hand, the energy separation $1SDD_{3/2}$ and $1PFP_{3/2}$ for ~2 nm large dots changes significantly by 68 meV, due to a strongly varying effective mass of the electron. The absorption spectrum of ~5.1 nm large dots exhibits an energy splitting of about 44 meV, showing strong dependence on the QD sizes, however there was no experimental effort towards large-size CdTe QDs, which reach the region close to the intermediate confinement regime of about 10-12 nm diameter.

I.2 Optical interactions

Both linear and nonlinear optical properties in SC QDs result from the transitions between the electron and hole QSLs. In linear process, as recalled, the absorption of an electron from the VB into the CB can be triggered by the absorption of a photon with energy above the BG. In

general, direct semiconductors transitions involve electrons and holes of equal momentum, for which the spectral distribution of possible transitions is described by the optical DOS:[37]

$$O_{DOS}\left(\hbar\omega\right)=\sum_{e,h}\int\left|M\right|^{2}\delta\left(E_{e}\left(\mathbf{k}\right)-E_{h}\left(\mathbf{k}\right)-\hbar\omega\right)d\mathbf{k} \tag{I.17}$$

The Dirac δ function ensures energy conservation, with summation over a system dimensionality dependent $\mathbf{k}$ vector. The optical matrix element can be calculated for a dipole approximation from the wave functions (I.7) - (I.8), and takes the following form:

$$\left|M\right|=\left\langle\psi_{m_s}^{e}\left|\epsilon\cdot\mathbf{p}\right|\psi^{h}\right\rangle=\sum_{m_j}\left\langle\phi_{m_s}^{e}\left(\mathbf{r}\right)\middle|\phi_{m_j}^{h}\left(\mathbf{r}\right)\right\rangle\cdot\left\langle u_{m_s}^{e}\left|\epsilon\cdot\mathbf{p}\right|u^{h}\right\rangle \tag{I.18}$$

The oscillator strength is directly proportional to the overlap of the '*envelope functions*' of the recombining excitons, which prevents transitions between levels of opposite parity. The second term on the right-hand side of the expression determines the product of the polarization vector ϵ and the momentum operator $\mathbf{p}$ between the Bloch functions (known as the Kane matrix element). It imposes additional selection rules on the polarization of the absorbed/emitted photon in interband transitions, which is determined by the heavy or light character of the hole.

For the first approximation, the absorption spectra (electron-hole interactions) under strong quantum confinement is given by:[11-12,16]

$$\hbar\omega_{\nu}=E_{BG}+E_{\nu}^{h}\left(a\right)+E_{\nu}^{e}\left(a\right)-1.8\frac{e^{2}}{\varepsilon a}=E_{BG}+\frac{\hbar^{2}\pi^{2}}{2(m_{\nu}^{e}+m_{\nu}^{h})a^{2}}-1.8\frac{e^{2}}{\varepsilon a} \tag{I.19}$$

where $E_{\nu}^{h,e}\left(a\right)\sim1/a^{2}$ are the energies of the νth hole and electron QSLs, respectively. The Coulomb interaction can be calculated from first order perturbation theory. Recombination of the exciton may be assisted by the emission of the photon, which possesses an energy $\hbar\omega=hc/\lambda$ and a momentum $k_{\nu}=2\pi/\lambda$ (negligible when compared to that of the exciton), where λ the photon wavelength and c the speed of light. The energy of the lowest transition for a known Bohr radius a_{B}, and effective masses of the electron and hole $m_{e(h)}$, for a parabolic band inside an infinite potential ($\psi_{e}=\psi_{h}$) is given by:

$$\Delta E=\left(\frac{\pi a_{B}}{a}\right)^{2}\mathcal{R} \tag{I.20}$$

where: $\mathcal{R} = h^2 / 2m_r a_B^2$ is the exciton Rydberg energy, dependent on the reduced mass of the exciton.

Radiative relaxation of the exciton exhibits nearly single-exponential character of the emission decay curves. At a given size dependent emission frequency, all the QDs are therefore expected to emit the light at the same rate. The emission decay rates increase with the frequency. Considering the complex structure of CdTe VB, where several hole levels are located close to the band edge, leads to exciton states lying close to the lowest excitation energies. These excitons exhibit much lower probability for spontaneous decay to the ground state, and a high rate of exchange with the lowest energy exciton. The population of the lowest energy exciton is then reduced due to thermal distribution, leading to a lowered rate of the radiative recombination and increased rate for dark excitons.[20,29]

I.2.1 Scattering

Non-resonant excitation, where the energy of exciting photon does not match k = 0 transitions, can leads to generation of an exciton, with an excess kinetic energy:

$$\Delta E_{kin} = \frac{\hbar^2 k^2}{2m_{e,h}} \tag{I.21}$$

Before it recombines such an exciton loses all or part of this kinetic energy, then relaxes towards the band edge. Relaxation of a non-resonant exciton leads to inelastic scattering, where the kinetic energy is not conserved. In zinc-blende CdTe nanocrystals excess energy of the exciton is carried out by longitudinal optical phonons (LO).[38] The energy level structure of CdTe is such that the electrons are completely delocalized in the CB, and holes are localized in the VB, where the level spacing is very small, because an effective mass of the hole is much larger than the effective mass of the electron ($m_h \gg m_e$), the relaxation of the hole leads to its coupling with 1 LO phonon. Decreasing of the energy level spacings in the CB may lead to coupling of the electron with several LO phonons, and decrease for higher energy levels down to 1 – 2 LO phonons.

I.3 Chapter summary

In conclusion, this chapter contains a theoretical introduction to physical properties of semiconductor NPs, and explains how these properties evolve with the decrease of their size, and how they impact on to the optical features of the nanoscale structures. Quantum confinement effects related to the size, material composition, as well as to the shape of SC NC have been discussed. We point out how Coulomb interactions and the binding energy of the QD structure change with increasing quantum confinement, and explained how these interactions are breaking down into different quantum confinement regimes. Understanding these properties allowed for the introduction of the band structure of the CdTe crystal, where the bulk structure has been compared with that of a single CdTe QD. Finally we have described fundamental optical interactions, which occur in QD structures, showing that both linear and nonlinear optical properties of SC crystals result from transitions between the electron and hole quantized energy levels.

Chapter II | Colloidal CdTe-based QD samples: synthesis and characterization

II.1 Guidelines for material selections 22
II.2 Characterization of dot-shaped CdTe/CdS core/shell QDs 22
II.2.1 Chemical synthesis of dot-shaped CdTe/CdS core/shell QDs 23
II.2.2 Shape and size distribution of dot-shaped CdTe/CdS QDs 23
II.3 Synthesis and characterization of dot-shaped CdTe QDs 25
II.4 Characterization of rod-on-dot CdTe/CdS heterostructures 27
II.4.1 Chemical synthesis of rod-on-dot CdTe/CdS heterostructures 29
II.4.2 Shape determination and effective size distribution of RD CdTe/CdS heterostructures 30
II.5 The role and importance of the shell in type-II QDs 32
II.6 Sample preparation 33
II.7 Chapter summary 34

Over the last decade, significant advances in the field of NP synthesis enabled fabrication of increasingly complex heterostructures. Composite materials that simultaneously retain quantum confinement are therefore becoming of interest towards the nonlinear optics, mainly due to the enhancement of their nonlinearity. This lead us to propose SHG active CdTe based semiconducting QDs and QD heterostructures as promising candidates for nanolabels in nonlinear microscopy. The following chapter contains structural characterization of dot-shaped QDs and rod-on-dot QD hybrids, which have been used throughout this work. We describe their morphology, methods for their synthesis, and give details about sample preparation for microscopic measurements at the sub-wavelength single QD scale.

II.1 Guidelines for material selections

The contents of this work deal mainly with an investigation of the second-order nonlinear optical properties of NPs exhibiting enhanced nonlinearity, thus opening the way towards decrease of their size and application to two-photon scanning microscopy (TPSM). These NPs have been obtained from semiconductors rather than from insulating inorganic materials, to as to be in a position to benefit from quantum confinement effects. We have chosen to work mainly with CdTe QDs and CdTe/CdS quasi-type-II QDs for the reasons outlined hereafter. Firstly, CdTe exhibits a relatively strong second-order nonlinearity from a noncentrosymmetric zinc-blende – like crystalline lattice structure.[4-5] The energy band gap of CdTe is 1.44 eV,[14-15] and it can be tuned up to approximately 2.0 eV as a function of QD size. This appears to match the correct range of available frequencies from a Ti-Sapphire femtosecond oscillator. CdTe has the refractive index of about 3.0 at ~1.5eV (295 K), and it is nearly transparent for NIR range.[39] Another important issue is the following: in a strong quantum confinement regime (when QD sizes are about that of the exciton Bohr radius a_B or smaller), the transition dipole moment of these NPs or their two-photon cross-section does not follow the same scaling rules as observed for the bulk, but evidence significant enhancement.[5] This makes SC colloidal QDs promising candidatess for nonlinear optical microscopy.

II.2 Characterization of dot-shaped CdTe/CdS core/shell QDs

Over the last decades, significant advances in the field of semiconductor nanoparticles synthesis enabled fabrication of various core/shell heterostructures.[40-42] During this period well developed methodologies of colloidal quantum dot synthesis were defined and implemented, resulting in a high reproducibility and good optical quality of the NPs, to a level making them compatible with commercial exploitation.

In dot-shaped quasi-type-II CdTe/CdS NCs, CdTe has a zinc-blende structure (with $\bar{4}3m$ point group symmetry). A stereograph showing the symmetry elements of $\bar{4}3m$ group is presented in Figure II-1(a). It consists of three 4-fold inversion axes perpendicular to four $\{1,1,1\}$ cube facets, four 3-fold axes along the main diagonals, and six planes of symmetry along the diagonals of facets. Additionally, a set of 24 equivalent points is presented.[14,43-44] The single crystalline unit cell of a CdTe zinc-blende like structure is shown in Figure II-1(b).

II.2.1 Chemical synthesis of dot-shaped CdTe/CdS core/shell QDs

Synthesis of the CdTe/CdS core/shell NPs dedicated to SHG emission required NC sizes of about 10–15 nm diameter. CdTe/CdS dot-shaped QDs used in this work were prepared in a non-coordinating solvent, following the main lines of the procedure given by Peng and coworkers.[45] A scheme of the synthesis and apparatus is shown in Figure II-2(a,b). The synthesis was carried out under argon atmosphere. In short, 0.1 mM CdO was dissolved in 5 ml of octadecene (ODE) and 0.06 g tetradecyl phosphonic acid and heated-up to 280 °C. At this temperature 0.1 mM Te dissolved in trioctylphosphine (TOP) is injected, leading to the formation of approximately 4 nm diameter quantum dots. These were further grown at 290 °C by additional multiple injections of a 0.1 M cadmium oleate solution in ODE and 0.1 M TOP:Te until the emission peak reached about 760 nm (Figure II-3(c)). Once the cores have reached the desired size, the temperature was decreased in order to thermodynamically terminate their growth. The solution was heated again when TOP:Te injections were replaced by TOP:S to initiate shell growth. Injections of sulfur containing reagent were sufficient to form approximately three monolayers of CdS shell, resulting in the formation of an approximately 1 nm thick CdS layer (Figure II-3(b)). Particles were then dissolved in toluene and precipitated by addition of methanol and centrifugation.

II.2.2 Shape and size distribution of dot-shaped CdTe/CdS QDs

Transmission electron microscopy (TEM) characterization shown that particles are somewhat ellipsoidal, with an effective diameter of 10.9 ±1.8 nm (considering the square root of the product of the short and long axes), and a typical ellipticity of 1.17 ±0.13. A typical TEM image (obtained with a Philips CM120 Super Twin transmission microscope) of several NPs appears in Figure III-3(a). Under the prescribed synthesis conditions, some ripening occurs during CdTe NC growth, leading to some relative broadening of the size distribution. The largest particle observed using TEM had an overall (core + shell) effective diameter of 15 nm, while the smallest observed particles had an effective diameter of about 10 nm.

Alternatively, the size distribution was confirmed using calibrating curves proposed by the group of Peng et al.,[45] where the emission peak position determines the quantum dots size (neglecting the relatively small Stokes shift of about 8 nm between the emission and first

excitonic absorption peaks at these sizes), following the empirical function for CdTe QDs given below:

$$D = \left(9.8127 \cdot 10^{-7}\right) \lambda^3 - \left(1.7147 \cdot 10^{-3}\right) \lambda^2 + 1.0064\,\lambda - 194.84 \qquad \text{(II.1)}$$

where D (nm) is the NC diameter, and λ (nm) is the wavelength of the first excitonic absorption peak of the corresponding sample. The sizing curve obtained with this empirical function is shown in Figure II-4.

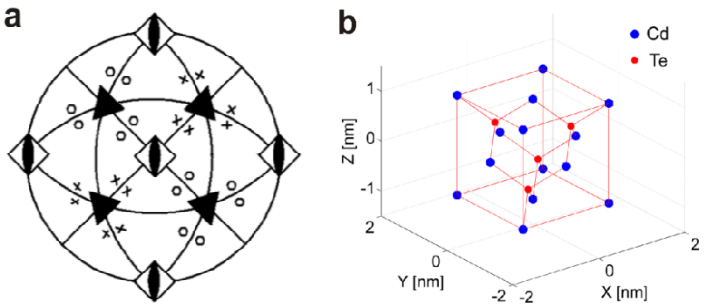

Figure II-1 | a) Stereograph presenting the symmetry elements of $\bar{4}3m$ point group. b) CdTe single crystalline unit cell. The lattice constant is a_0 = 0.6482 nm.

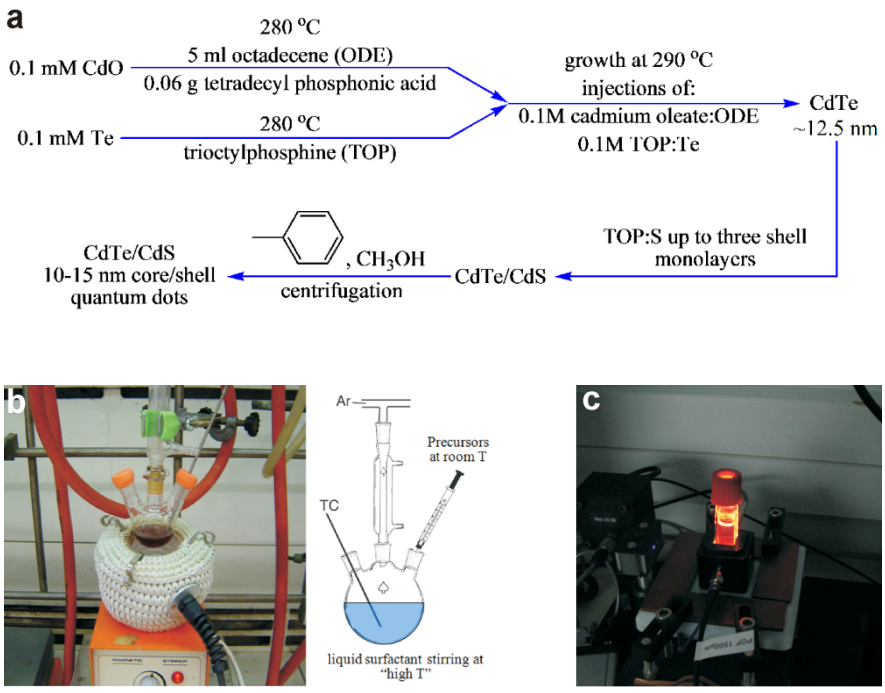

Figure II-2 | a) Synthesis way of CdTe/CdS dot-shaped core/shell QDs. b) Picture and schematic of the synthesis apparatus (Ar – argon flow; TC – temperature control). c) Measurements of the emission / absorbance of diluted QDs colloidal solution, carried out in order to control the NPs size during the synthesis process.

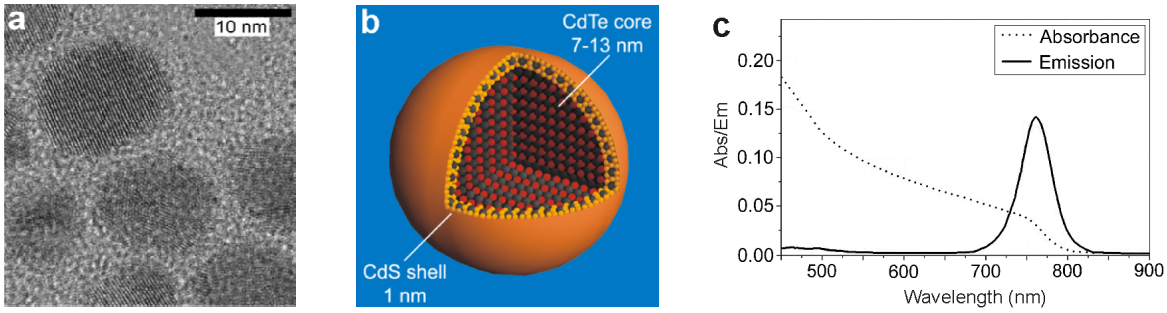

Figure II-3 | a) TEM image of monodispersed CdTe/CdS dot-shaped QDs. b) Schematic cross-section of the single CdTe/CdS core/shell QD. c) Absorption and emission curves of dot-shaped CdTe/CdS QDs, obtained from their colloidal mother solution.

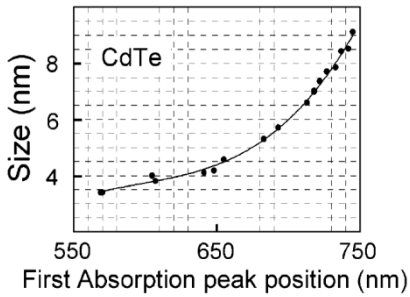

Figure II-4 | Sizing curve for CdTe QDs (Yu et al. [45]).

Absorption/emission traces of the final synthesis product of CdTe/CdS dot-shaped QDs are shown in Figure II-3(c). The emission peak appears at 760 nm, approximately corresponding (following proposed sizing curves) to 10.4 ±2.5 nm diameter NCs.

II.3 Synthesis and characterization of dot-shaped CdTe QDs

Synthesis of CdTe NPs used for size dependence studies of the SHG emission, required preparation of differently sized NCs made from the same material, under the same synthesis conditions. This was obtained by preparing one chemical synthesis, while different sizes of NPs were collected during their growth. In order to investigate the size dependence of SHG at the single NP level we decided to detect SHG signal from CdTe QDs with average diameters of QDs about 7, 9 and 11 nm, as determined from the optical emission spectrum following the approximation (II.1).[45] Note that the size range is partially outside the measured range in Yu

et al. (see Figure II-4), hence the extrapolation is merely a reasonable approximation. The absorption and emission curves corresponding to three different sizes of CdTe NPs are shown in Figure II-5.

For obtaining CdTe QDs with such control over their size distribution, we have used similar synthesis conditions as described in Paragraph IV.2.1. First, cadmium oxide (0.09 mMol) was dissolved in 5 mL of octadecene (ODE) and 55 mg of tetradecyl phosphonic acid and heated up to 270 °C under Argon. Tellurium (0.12 mMol) dissolved in 2 mL of trioctylphosphine (TOP) was quickly injected into the solution, leading to the formation of approximately 3.5 nm dots. Immediately after injection, the temperature was lowered to 250 °C. After the QDs reached a size of ~4 nm diameter over several minutes, the temperature was raised up to 280 °C and the QDs were further grown by alternate injections of cadmium oleate solution in ODE and TOP/Te (concentration of both was 0.1 mM). In order to avoid nucleation of new particles, the Te injections were carried out slowly (at a rate of 1-2 mL per hour) by way of a syringe pump. Injections were performed until the QD diameter reached about ~11.5 nm.

Size determination in case of these three sets of samples (7, 9, 11 nm dots) was a crucial issue towards measurements of the SHG size dependency. Effective size was thus confirmed by the TEM analysis (see Figure II-6(a)). The effective diameter of the largest NPs obtained with TEM analysis was 12.2 ±1.2 nm, as shown on the histogram in Figure II-6(b). The largest CdTe QDs presented in Figure II-6(a) exhibit some inhomogeneities in crystalline structure orientations, as well as variations of their shapes, which is common for “large” QDs.

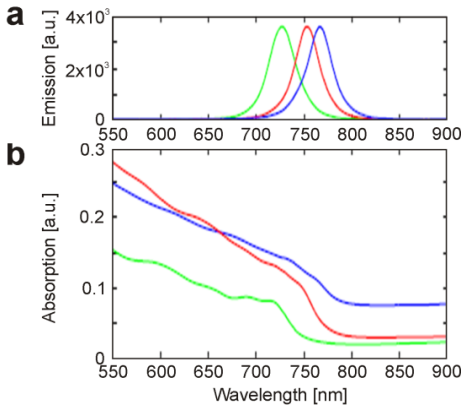

Figure II-5 | a) Emission and b) absorption curves of 7 nm (green), 9 nm (red) and 11 nm (blue) CdTe QDs.

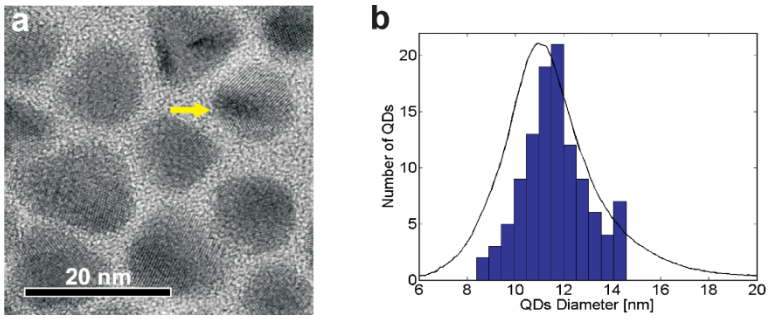

Figure II-6 | a) TEM image of ~11 nm large CdTe QDs. Yellow arrow indicates an example of QD with different crystalline facets orientations. b) Histogram of the size distribution of the largest CdTe QDs based on TEM analysis (with an effective diameter 12.2 ±1.2 nm). The black line delineates a size distribution obtained by using the emission spectrum (using the empirical function (III-1)), with a mean diameter of 11.1 ±2.4 nm. Larger size obtained from the TEM images can be attributed to the occurence of organic materials in the QD solution, which do not affect the emission spectra.

Emission and absorption spectra show of 11 nm diameter QDs sample show a very small Stokes shift. In order to obtain the size distribution from the emission spectrum we had to ignore small differences in the absorption cross-sections of different size QDs, and assume a constant quantum yield (QY) for all sizes. The absorption cross-section, however, would blue-shift the size distribution since it is larger for larger QDs. Taking into account the QY, size distribution should be red-shifted since the larger QDs are known to exhibit more structural defects and surface traps which lowers the QY.[17-18,20,46] Despite these effects, the extracted size distribution is convenient and more reliable than values obtained from TEM analysis, therefore we chose to use these result in subsequent studies. The mean diameter obtained from the emission spectrum is 11.1 ±2.4 nm. Larger size obtained from the TEM images can be attributed to the appearance of organic materials in the QD solution (which does not affect the emission spectra), as well as to spectral diffusion of individual QDs. The emission of single QDs of the same size can be broadened by ~kT, by about 25 eV, resulting in a total inhomogeneous spectral linewidth of about 70 meV.

II.4 Characterization of rod-on-dot CdTe/CdS heterostructures

SHG active rod-on-dot (RD) heterostructures were developed as a proof-of-principle with the intention of obtaining SHG emission from single hybrid SC QDs, where the nonlinearity can be controlled through the relative contribution of the participating QD materials and their

geometrical parameters. As in the case of previous materials, we have used once again CdTe/CdS structure. However, RD QDs exhibit expanded CdS shell into a quantum rod (QR) structure, grown on one facet of the CdTe core. This has a crucial meaning in further studies because SHG is expected to scale as the squared volume of the scatterer size. Another important issue is that RD heterostructures are made of two SC materials: CdTe and CdS, each one featuring different crystalline lattices (zinc blende and wurtzite, respectively), nonlinear susceptibility tensors and spatial geometries. Both components are thus expected to contribute differently to the overall SHG field.

The complexity of RD NCs entails several consequences, arising from the new geometry and resulting physical features of such hybrid NPs. This consequently impacts on the SHG studies described in Chapter IV, e.g. the analysis of the SHG polarization dependency requires a precise definition of the mutual orientation of the CdTe cubic zinc-blende lattice, which belongs to the $\bar{4}3m$ point group symmetry, with respect to the CdS rod structure. In this particular case, synthesis conditions (described in the next paragraph) are defined so as to impose growth of the CdS rod into the hexagonal wurtzite form, with $6mm$ point group symmetry. The stereograph representing the $6mm$ symmetry elements of that group and the elementary crystalline lattice of CdS are shown in Figure II-7(a,b). However to show the overall symmetry of the CdS structure a larger repeat unit has to be presented, containing three single unit cells (Figure II-7(c)). To describe their relative lattice orientation at the interface we used the convention described in the literature.[14,43-44,47] The epitaxial relationships are therefore characterized by the $[01\bar{1}0]$ axis of CdS oriented parallel to the $[11\bar{2}]$ axis of CdTe, and the CdS $[0001]$ axis oriented parallel to the $[111]$ axis of CdTe, which means that the 6-fold axis of symmetry (parallel to $[0001]$) is oriented along the rods growth direction - shown in Figure II-8 and on the magnified TEM image – Figure II-10(b). This orientation comes from the compatibility of the zinc-blende $\pm\{111\}$ and wurtzite $\pm(0001)$ facets at the interface,[47-49] whereas the two materials, CdTe and CdS, namely provide minimized mismatch along this interface of about ~9.8% between two lattices.[50] Thus, the relative rotation angle of the CdS rod around its $[0001]$ axis relative to the CdTe core is frozen.

In order to obtain the relative orientation of CdTe and CdS in the RD crystalline structure, we have chosen an arbitrary system of coordinates, which can be found in Appendix C. These coordinates are further applied towards the analysis of the SHG polarization response.

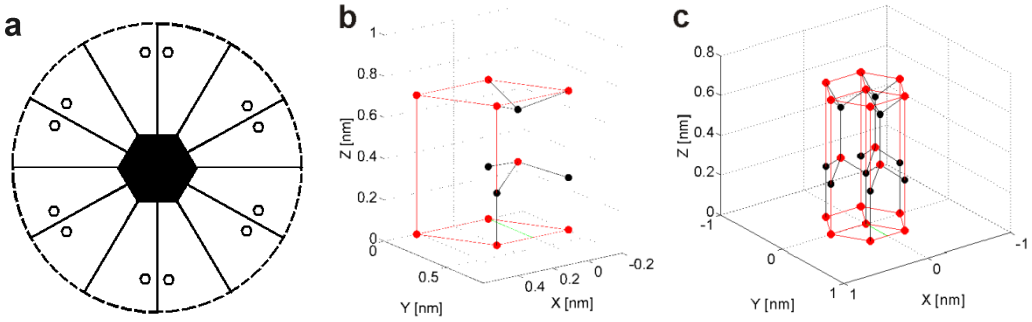

Figure II-7 | a) Stereograph representing the symmetry elements of the 6*mm* point group. b) Single unit cell of the CdS wurtzite - like crystal, based on the convention adopted in Refs. [14,43-44]. c) Part of the CdS crystalline structure, showing the symmetry of a right prism with hexagonal base. Coordinates are in nm. The lattice constants are: $a_0 = 0.4135$ nm and $c_0 = 2\sqrt{6}/3\, a_0 = 0.6752$ nm.

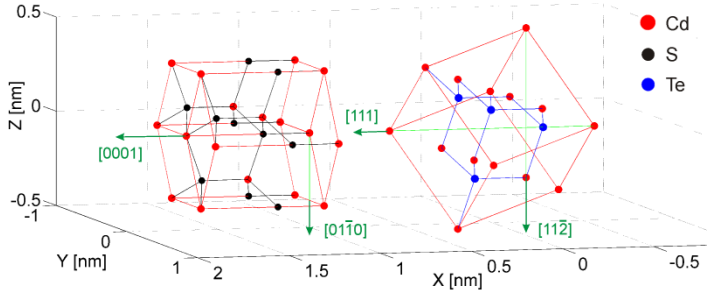

Figure II-8 | Relative orientation of CdTe and CdS crystalline lattices represented by the unit cell of CdTe and a triple unit cells of CdS. The relations between the $[111]$ and $[11\bar{2}]$ crystalline axis of the CdTe and the $[0001]$ and $[01\bar{1}0]$ axis of the CdS are marked by green arrows. Rotations of both lattices are discussed in Appendix C.1 and C.2.

II.4.1 Chemical synthesis of rod-on-dot CdTe/CdS heterostructures

Rod-on-dot NCs were synthesized by the standard colloidal one-pot growth technique. Briefly, spherical CdTe QDs were grown in a non-coordinating solvent using tetradecyl phosphonic acid as a ligand, following modified procedures suggested by Peng et al.[45] CdS QRs growth was performed by multiple injections of cadmium oleate and sulphur solutions at appropriate temperature and injection rates. The final product can be considered to be a degenerated (one-armed) tetrapod.[48,51] In detail, 60 mg tetradecyl phosphonic acid (PCI synthesis) and 13 mg Cadmium Oxide were added to 5 mL octadecene (ODE) and heated up to 260 °C under an Argon atmosphere, until full dissolution of the Cadmium oxide. At this point, 0.013 g of elemental Tellurium in 2ml trioctylphosphine (TOP) was swiftly injected to the flask and the temperature was lowered to 210 °C. After several minutes the temperature

was raised to 250 °C and alternate injections of 0.1M Cadmium oleate in ODE and 0.1 M TOP:Te, separated by 10 minutes. When the size of QDs reached ~6 nm, the TOP:Te was replaced by elemental Sulfur dissolved in a 1:1 mixture of ODE and TOP. Three consecutive injections were performed at increasing temperatures starting from 210 °C and ending at 250 °C. Following this step, emission had shifted from 708 nm to 713 nm. At this stage, a more reactive sulfur precursor was used (0.1M bis(trimethylsilyl)sulfide in ODE). Injections were carried out at temperatures varying from 180 °C to 230 °C. During these injections, emission was slowly red-shifting, finally reaching a value of 720 nm (see Figure II-9). QDs were then precipitated from a toluene solution by addition of methanol, and resolubilized in an anisole solution containing 2% PMMA (Microchem). Unless noted otherwise, all chemicals were obtained from Sigma-Aldrich.

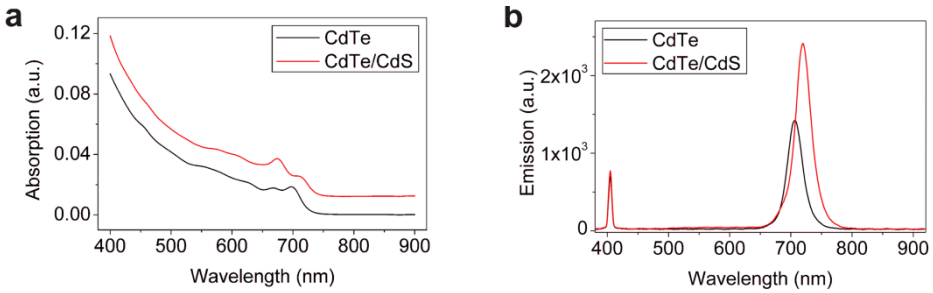

Figure II-9 | Emission (a) and absorption (b) spectra of RD QDs. Black line represents grown CdTe cores, measured just before injecting S:ODE/TOP solution before shell growing process. Red lines represent spectra of the final synthesis product – CdTe/CdS RD QDs.

II.4.2 Shape determination and effective size distribution of RD CdTe/CdS heterostructures

The QD geometrical features were investigated using TEM (see Figure II-10(a,b)) and by atomic force microscopy (AFM) (see Figure II-10(c,d)). Despite appearance of a few dot-shaped QDs, TEM images evidence well dispersed and structurally well determined RD CdTe/CdS heterostructures, mostly with a regular and well determined shape of the CdTe core and a CdS rod attached to it.

Size determination is quite important since SHG is expected to scale as the squared volume of the scatterer, this being especially critical when applied to complex structures composed of at least two different types of materials with a strong necessity for characterization of a morphology and dimensions of these heterostructures towards further SHG studies.

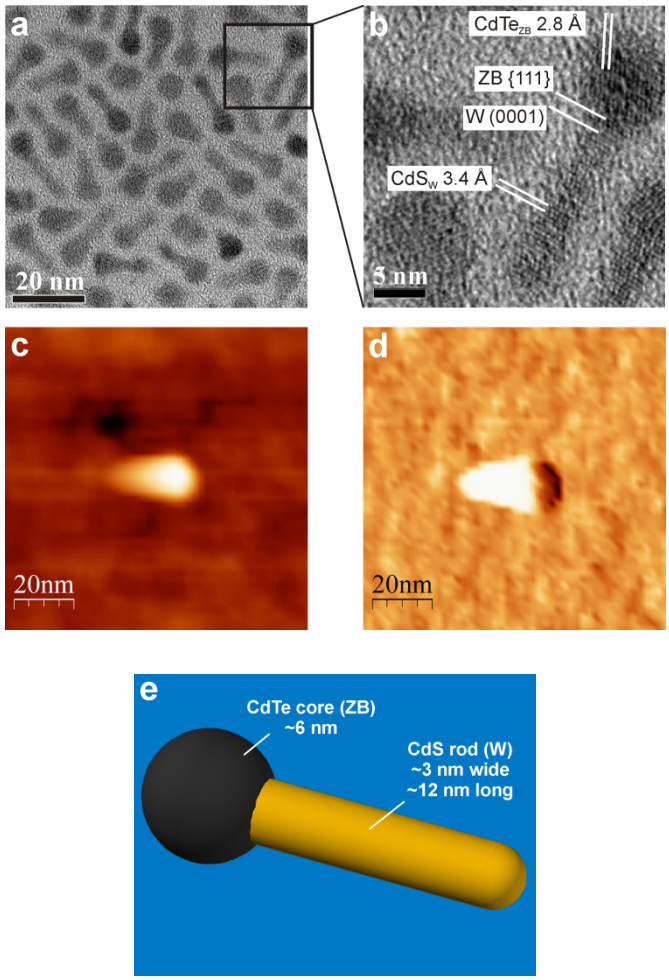

Figure II-10 | a) TEM image showing monodispersion and shape determination of rod-on-dot QDs. b) Magnification of the single RD QD illustrating important structural facets and atomic distances.[52,i] c-d) AFM topographical and phase scans of a single and well isolated RD QD embedded into a ~30 nm thick PMMA host-matrix. e) Cross-section model of the rod-on-dot CdTe/CdS QD.

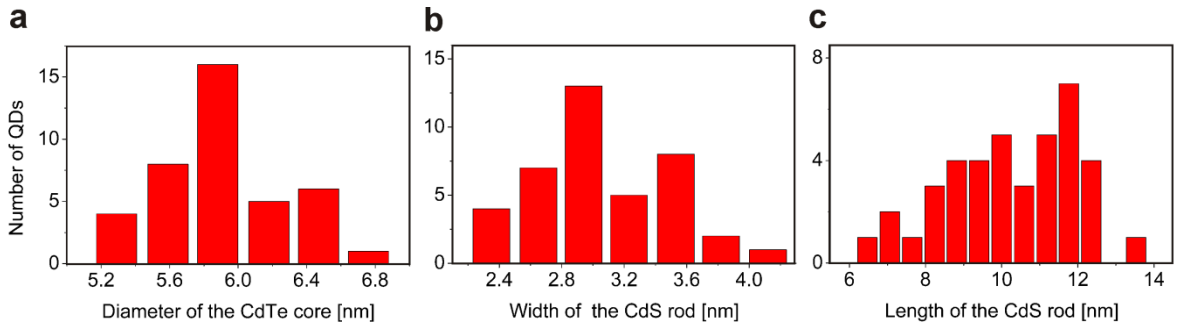

Figure II-11 | a) Determination of the effective diameter of the CdTe core. b) Width dispersion of the CdS rod. c) Length dispersion of the CdS rod.

[i] CdTe nearest-neighbor distance given for 300 K; source: http://www.semiconductors.co.uk

The size of spherical CdTe cores was determined from the absorption spectrum during growth to 5.9 nm, following the (II.1) empirical function.[45] In the case of geometrically complex heterostructures, such as RD NCs, dimensions are best obtained directly from the TEM images. The size distribution of forty isolated RD NCs, directly obtained from the TEM images is shown in the histograms in Figure II-11(a-c). Size dispersion varies in a range between 5.7 – 6.2 nm diameter of the CdTe core (consistent with the optical measurements), and 2.4 – 3.6 nm diameter of the CdS rod. The length of the CdS rod is dispersed in a wider range, from 6.0 -16.0 nm, with a mean value of 11.0 nm.

II.5 The role and importance of the shell in type-II QDs

The optical properties of type-II core/shell QDs under the strong confinement regime are very sensitive to the smallest changes in core or shell dimensions. Compared to organically passivated cores, core/shell QD heterostructures can tolerate harsher processing conditions and environments.[53] In general the shell overcoating in QDs increases the chemical stability by protecting the core from the environment, and passivates the core surface trap sites. Shell deposition can, in principle, enable all surface atoms to be passivated, insulating the core from its environment, both physically and electronically. Appearance of the shell simply buries the semiconductor in the potential energy well, and energetically confines the electron and hole, leading to the charge carriers concentrating in the nanocrystal core, away from the surface. This directly modifies the optical properties of the QD.[10,40,54-55] As a result, surface defects states and trap sites have a reduced impact on the luminescence emission efficiency, allowing to come close to ideal conditions (for an ideal QD - without crystalline defects of the surface), whereby for every photon that creates an exciton, one photon is emitted, reaching a 100% luminescence QY. Shell made of the material with a wider band gap than the core increases the probability of the radiative recombination.

The band offset of type-II colloidal QDs can be controlled by careful choice of the material, e.g. quasi-type-II CdSe/CdS or CdTe/CdS (where the electrons are completely delocalized) core/shell heterostructures, or type-II CdTe dots overcoated with a ZnS shell. Wider band gap of the CdS or ZnS shells (for CdS the band gap is 2.42 eV, ZnS 3.6 eV; whereas for the CdSe and CdTe cores band gaps are 1.74 eV and 1.44 eV, respectively)[14-15] not only electronically insulate the cores, but results in a higher threshold to photo-oxidative

degradation and formation of the surface defects, due to a much lower oxidation potential of S^{2-} than Se^{2-} or Te^{2-} anions.[46] The energy band gaps of most popular SC NCs in colloidal synthesis of QDs are illustrated in Figure I-2.

II.6 Sample preparation

Before preparing the samples, QDs had first to be purified after the synthesis, as well as separated from the chemical compounds left in the growth solution. In each case, QDs were purified by dissolving them in toluene and precipitation from the suspension by adding methanol and centrifuging for approximately 5 min. Such a process was repeated usually several times to obtain a high degree of purification. A well performed purification process had a high impact on further optical properties, and reflected in improved signal photostability under two-photon excitation of NPs.

Sample preparation for microscopy measurements required a few conditions. For single NP studies we had to use a polymer host-matrix to embed QDs inside a thin layer and avoid their motion during surface scans. It was important to use a polymer with a similar refractive index to the one of cover slip glass ($n \approx 1.50$ in the VIS region), to minimize their refractive index mismatch. Poly(methyl methacrylate) (PMMA) with $n \approx 1.49$ (VIS) was found to be a good candidate. After precipitation, QDs were redissolved in toluene or in anisole and mixed with a PMMA-anisole solution (MichroChem 495 MW PMMA 6A, dissolved in anisole with a 2% concentration in mass).

The concentration of the QDs was usually about 2.0 mg of precipitate per 1 mL of the PMMA-solvent solution. This concentration resulted in high enough QDs dispersion on the cover slip glass surface. To avoid aggregation and creation of big multi-crystalline clusters during further processing, QDs solution was sonicated for 1 hour directly before deposition. The substrates – cover slip glasses (#1) were cleaned in isopropanole, treated with the oxygen plasma and heated up on the hot plate (180 °C).

The prepared colloidal solution of QDs was deposited by spin-coating with 3000 rpm, 1000 acc., through 40 s to allow the solvent to evaporate, which resulted in approximately 40 – 50 nm thick polymer layer (measured with the *DEKTAK 3ST* surface profiler). In some cases (rod-on-dot QDs), when the polymer layer had to be thicker, the deposition was carried out at 4000 rpm, resulting in a ~30 nm thick PMMA host-matrix. After spin-coating, all the samples were held at 180 °C for 1 min to allow QDs to be in contact with the glass surface.

II.7 Chapter summary

We have synthesized and characterized the morphology of three different types of CdTe - based QD samples: spherical CdTe QDs, spherical core/shell CdTe/CdS, and rod-on-dot CdTe/CdS QD heterostructures. We have proved a reasonable high degree of control in obtaining these materials with a high reproducibility over their shape and size distributions. Morphological features were characterized with different microscopy (i.e. TEM, AFM) and single-photon spectroscopy techniques, which allowed determining their respective effective size and shape distributions. These have a high importance towards nonlinear optical properties, which evaluate with the change of the NP shape, size and material composition. We have also demonstrated a reasonably high degree of control in obtaining these materials with a high reproducibility over their shape and size distributions.

Chapter III | Coherent second-harmonic microscopy for detection of single semiconducting QDs

III.1 Contrast mechanisms for two-photon nonlinear microscopy 36
III.1.1 Two-photon excited fluorescence 36
III.1.2 Second-harmonic generation 38
III.2 Second-order nonlinearity of CdTe – from bulk to single QD scale 41
III.3 Nonlinear two-photon polarization sensitive microscopy setup 45
III.3.1 Optical and effective spatial resolution in multi-photon microscopy 48
III.4 Time correlated single photon counting in detection of single nanoparticles 51
III.5 Chapter summary 53

In this chapter we briefly introduce the differences between the two-photon excited fluorescence (TPEF) and the second-harmonic generation (SHG) microscopy, putting them in a context of basic underlying processes of different optical properties. Then, we describe a detailed description of the experimental setups and methodologies used for SHG detection from single isolated nanoscatterers, such as quantum dots. Firstly, nonlinear two-photon scanning polarization sensitive microscopy (TPSM) is discussed. We introduce important features of this technique towards further spectral and polarization analysis of the SHG emission from colloidal QDs. Furthermore we discuss a modified version of TPSM experiment based on time correlated single photon counting (TCSPC), which allows for selection of the instantaneously scattered photons arriving subsequent to the laser pulse, excluding the dark counts of the detector. We explain why the TCSPC detection results in an improved signal-to-noise ratio, and allows for the detection of weak SHG signals obtained from small sized QDs.

III.1 Contrast mechanisms for two-photon nonlinear microscopy

Since its first application in nonlinear microcopy at the turn of 70s and 80s, SHG has become a powerful contrast mechanism in nonlinear optical imaging,[56-57] due to the stringent structural conditions in the ability of the specimen to generate second-harmonic of the incident excitation light, which is constrained by the noncentrosymmetry of the medium.[58] Properties of the SHG process are such that it can be applied, e.g. in phase-sensitive interferometric SHG microscopy,[59-60] as a probe of local anisotropies,[61] or to probe surface plasmon enhanced interactions.[62-63] Similar to TPEF microscopy,[64] SHG – based microscopy techniques provide all the benefits of TPEF mechanism, such as superior axial resolution due to the quadratic dependence of SHG on the illumination intensity, entailing reduction of out-off-plane photobleaching and phototoxicity in live cell imaging.[65-67] These two processes, however, result from completely different mechanisms and thus exhibit significantly different properties. Here we aim to outline the main features and differences between them, which are of concern for nonlinear microscopy.

III.1.1 Two-photon excited fluorescence

The theory of two-photon absorption and emission process has been developed by Maria Göppert-Mayer during her doctoral research in Göttingen, under the supervision of Max Born.[68-69] TPEF is a resonant absorption process, which involves four energy levels (Figure III-1(a)). Two photons of about the same energy (usually from the same laser source) with frequencies ω are absorbed via a virtual state (with a life time typically shorter than 1 fs) allowing to excite the electron into a real excited molecular vibronic sub-level of the electronically excited state, with identical spectral positioning to the absorption of a single photon possessing twice the energy. Relaxation via up-converted emission of TPEF back to the S_0 ground state follows non-radiative vibrational relaxation into the S_1 energy level (leading to an energy loss). The emitted TPEF photon has an energy slightly lower than the input energy and corresponds to a photon of wavelength slightly longer than half of the excitation wavelength λ_{exc}. TPEF is a second-order nonlinear process resulting in incoherent emission, with a typical radiative life time of about 10^{-9} s. It does not comply with the

symmetry constraints typical of SHG and may therefore occur for both, centrosymmetric and noncentrosymmetric media or randomly oriented fluorophores.

The efficiency of the TPEF process depends on the probability of two-photon absorption as given by $P_{abs}^{(2p)} \simeq \left|\bar{\mu}_{abs}\bar{E}_{\omega}\right|^4 \simeq \sigma_{TPEF}E_{\omega}^4$, where: $\bar{\mu}_{abs}$ is the absorption transition dipole and $\bar{E}_{\omega}$ is the incident electric field vector. σ_{TPEF} is the two-photon absorption cross-section in Göppert-Mayer units (GM)[ii] which provides a quantitative measure of $P_{abs}^{(2p)}$, and E is the incident electric field. Due to difficulties in the direct measurement of the two-photon cross-section, σ_{TPEF} usually is characterized by the two-photon action cross-section, that is the product of the fluorescence quantum yield ϕ_{TPEF} by the absolute value of the σ_{TPEF}.[70-72] In choosing the optimal wavelength for TPEF measurements, doubling the maximum single-photon excitation wavelength is usually a good approximation, however many fluorophores, e.g. Rhodamine B, exhibit different selection rules for single- and two-photon processes, therefore both the wavelength dependence and the absolute value of $\phi_{TPEF}\sigma_{TPEF}$ are important. When excited with a fs pulsed laser, most common fluorescence dyes have $\phi_{TPEF}\sigma_{TPEF}$ values in the range of 1 – 300 GM,[70-71,73] however using the SC nanolabels, luminescence core/shell CdSe/ZnS QDs, they may approach extremely large values up to 50,000 GM.[74]

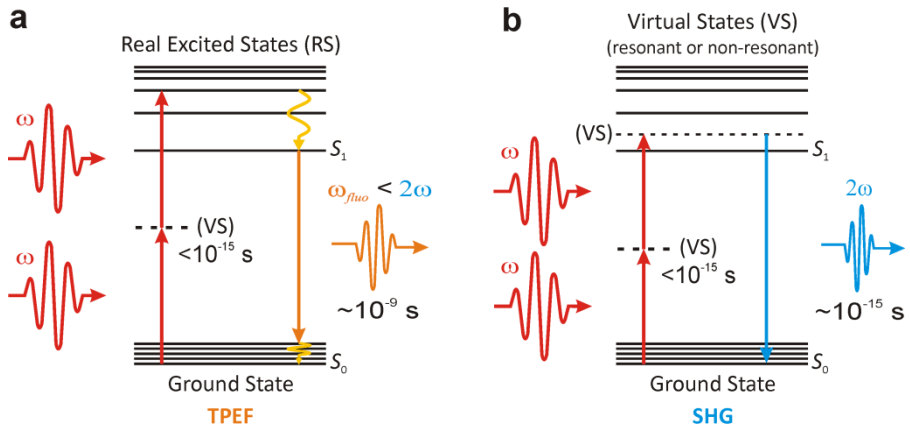

Figure III-1 | Perrin-Jablonski energy diagrams of the TPEF (a) versus SHG process (b). Solid black lines correspond to the real energy levels of ground and excited states. The yellow wavy line corresponds to the vibrational relaxation of the electron (with energy loss leading to a small probability of photobleaching) due to the non-radiative transition into the S_1 energy level of the real excited state (RS), followed by TPEF emission. Dashed lines are un-populated virtual energy levels (VS) with life times shorter than 1 fs.

[ii] 1 GM = 1×10^{-50} cm^4 s $photon^{-1}$

For the two-photon absorption process, the number of TPEF photons detected per unit time and volume can be expressed as:[75]

$$N^{fluo} = N \times K \times \left[\phi_{TPEF} \frac{1}{2} \sigma_{TPEF} I_{\omega}^{2} \right] \quad \text{(III.1)}$$

where: N is the number of fluorescent molecules per unit volume (m^{-3}); $K \propto \left| \hat{\mu}_{abs} \hat{E}_{\omega} \right|^{4} \left| \hat{\mu}_{em} \vec{u}_{I} \right|^{2}$ is the experimental factor which reflects the collection efficiency, the polarization of the incident electric field E_{ω} and its effectiveness in causing two-photon absorption relative to the fluorophore orientation, and the direction of analysis $\vec{u}_{I}$ ($\hat{\mu}_{abs}$, $\hat{\mu}_{em}$, $\hat{E}_{\omega}$ are normalized vectors associated respectively with absorption / emission dipoles and the incident field). The factor $1/2$ reflects the fact that only one photon is emitted, while two photons of the pump beam are absorbed. I_{ω} is a flux of incident photons (photon cm^{-2} s^{-1}), and its power of two is due to the second-order nature of the nonlinear process. For TPEF active nanocrystalline emitters we can roughly assume that number of emitted photons is:

$$N^{fluo} \propto \left| \bar{E}_{\omega} \right|^{4} \propto \sum_{emitters\ i} I_{i}^{fluo} \propto V = a^{3} \quad \text{(III.2)}$$

where: I_{i}^{fluo} is a flux of TPEF photons obtained from i emitters within a volume V of average dimension a.

III.1.2 Second-harmonic generation

SHG is a second-order nonlinear scattering process which has a primarily electronic origin. To be observed SHG requires a high pump energy, therefore it could be discovered only in 1961 by Franken et al.,[76] having had to wait development of the first lasers. The three-level SHG process is illustrated in Figure III-1(b). In general two photons of the same frequency ω 'coalesce' to a virtual state to form a single photon of energy exactly twice that of the incident photons. Depending on the excitation wavelength and material features, SHG can be obtained for resonant or in non-resonant energy conditions. The 2ω second-harmonic photon is generated almost instantaneously (within a few fs), therefore it is coherent. The electronic origin of SHG can be explained by looking at the response of an atomic system to a

propagating incident electric field E^{ω}, which exerts a dynamical Coulomb force on the internal charge distribution of the material, giving rise to additional components in the spectrum of the incoming field. The nonlinear terms contribute to the polarization only when the high-order terms of the Taylor expansion of *E* are non-negligible, which is the case for a focused laser beam. The material response is then specified by means of the polarization *P* (dipole moment per unit volume), which can be explained in a power series of the amplitude E^{ω} of the incident optical electric field:[58]

$$\tilde{P}(t) = \varepsilon_0 \left[\chi^{(1)} \tilde{E}(t) + \chi^{(2)} \tilde{E}^2(t) + \chi^{(3)} \tilde{E}^3(t) + ... \right] \tag{III.3}$$

where: ε_0 is the dielectric constant, $\chi^{(1)}$ is the linear optical susceptibility, and $\chi^{(n=2,3,...)}$ are the *n*-order nonlinear optical susceptibilities (being *n*+1 rank tensors). Second-harmonic generation is determined by the second-order nonlinear optical susceptibility $\chi^{(2)}_{ijk}$ (third-rank tensor), which can be expressed as a cubic matrix as follows:

$$\chi^{(2)}_{ijk} = 2d_{ijk} = 2 \begin{array}{c} i = \\ \\ \\ k = \end{array} \begin{array}{c} 1 \\ \\ \\ 1 \end{array} \left[\begin{pmatrix} d_{111} & d_{112} & d_{113} \\ d_{121} & d_{122} & d_{123} \\ d_{131} & d_{132} & d_{133} \end{pmatrix} \right. \begin{array}{c} 2 \\ \\ \\ 2 \end{array} \begin{pmatrix} d_{211} & d_{212} & d_{213} \\ d_{221} & d_{222} & d_{223} \\ d_{231} & d_{232} & d_{233} \end{pmatrix} \begin{array}{c} 3 \\ \\ \\ 3 \end{array} \left. \begin{pmatrix} d_{311} & d_{312} & d_{313} \\ d_{321} & d_{322} & d_{323} \\ d_{331} & d_{332} & d_{333} \end{pmatrix} \right] \begin{array}{c} j = \\ 1 \\ 2 \\ 3 \end{array} \tag{III.4}$$

where d_{ijk} are the *i,j,k* nonlinear coefficients, reflecting the symmetry and nonlinear optical properties of the material. Due to the basic parity constraint attached to odd rank tensors d_{ijk} coefficients vanish for materials with inversion symmetry, therefore SHG can be obtained only for noncentrosymmetric media. The specimen has to be also relatively transparent at both fundamental illumination wavelength and the generated harmonic.[58,77]

In order to obtain the intensity of the SHG signal from statistically oriented microscopic dipoles with microscopic nonlinearity β, $\vec{P}^{(2)} = \varepsilon_0 \chi^{(2)} : \vec{E}\,\vec{E}$ can be simply related to β via an oriented gas model:[78]

$$\chi^{(2)}_{IJK} = N f_I^{2\omega} f_J^{\omega} f_K^{\omega} \left\langle \beta(\Omega_n) \right\rangle_{IJK} \tag{III.5}$$

where N is the molecular density, $f_i^{\omega} = \left((n_i^{\omega})^2 + 2\right)/3$ is the Lorentz-Lorenz local field correction factor depending on the refractive index *n*, $\langle \beta(\Omega_n) \rangle$ is the statistical tensor of the first hyperpolarizability (dependent on a priori unknown Euler set of angles $\Omega_n = (\theta_n, \phi_n, \psi_n)$). Ω_n can be either a random variable in the case of statistical media (e.g. guest-host polymer), or a well defined unknown quantity for an arbitrary oriented nanocrystal. We take the simplest approximation that SHG is detected along the polarization analysis unit vector $\vec{u}_I$ and is thus proportional to the $\left|\vec{P}^{(2)} \cdot \vec{\mu}_I\right|^2$.). Therefore, the induced second-order nonlinear polarization SHG intensity can be expressed as:[75]

$$I^{SHG} \propto \left|P_I^{(2)}\right|^2 \propto N^2 \left| \sum_{J,K} \langle \beta(\Omega_n) \rangle_{IJK} E_J E_K \right|^2 \qquad \text{(III.6)}$$

Following equation (III.6) we can determine the number of emitted SHG photons N_{SHG} in a similar manner to that in the case of TPEF, using the second-harmonic scattering cross-section:[79]

$$\sigma_{SHG} = \frac{4 n_{2\omega} \hbar \omega^5}{3\pi n_{\omega}^2 \varepsilon_0^3 c^5} |\beta|^2 \qquad \text{(III.7)}$$

where $n_{\omega(2\omega)}$ are the refractive indexes at the pump and SHG frequencies, $\hbar$ is a Dirac constant, ε_0 is a dielectric constant of the material, and *c* is the speed of light. In practice the SHG cross-section is usually much smaller (about four orders of magnitude) than σ_{TPEF} when considered for a single molecule. It may be increased, however, when the molecule is excited near resonance, typically by one to two orders in magnitude, and it scales quadratically with the number of molecules *N* per volume unit (in contrast to linearly scaling for σ_{TPEF}).[79] Note, that the molecules are assumed to be uniaxial, with the hyperpolarizability β tensor dominated by a single component in the molecular frame. Such an orientation together with a tightly clustered distribution of the molecules around the SHG focal center accounts for the dipolar nature of the SHG radiation, which is expected to be equally radiating in the forward and backward directions. In other words all the individual molecules coherently scatter the incident field according to their SHG scattering cross-section, which results in the summation

of scattered harmonic electric fields in the same manner as for a phase-locked antenna system.[79]

The total radiated power P_{SHG} scattered by a single NP can be determined by integrating the SHG intensity over all possible emission angles:[79]

$$P_{SHG} = \frac{1}{2}\Theta_2 N^2 \sigma_{SHG} I_\omega^2 \tag{III.8}$$

where: I_ω is the excitation field at the focal spot (for fs laser source the focused pulsed peak intensity will be defined in Subsection III.3), *N* is the effective number of radiating molecules (which can be assumed as equal to one for a single QD), and $\Theta_2 \approx \left(0.1\,\lambda / w(\lambda)\right)^2$ is a yield parameter accounting for the reduction of the radiated fields when the molecules are spread over the surface at least of order of λ_{exc} as compared to the situation where they would be concentrated at the beam waist and radiate a perfectly in phase ($w(\lambda_{exc})$ is the waist of the focal spot, further defined in Subsection III.3.1). Since a single QD is treated as a single molecule (because its size $\ll \lambda_{exc}$), its radiation is assumed to be in phase, the Θ_2 parameter is being then negligible. Expression (III.8) is further used in order to calculate QD SHG cross-sections, with known values of the incident focused pulsed peak intensity and experimentally measured SHG count rates (where we assume that $N_{SHG} \propto P_{SHG}$).

III.2 Second-order nonlinearity of CdTe – from bulk to single QD scale

The high bulk second-order nonlinearity of cadmium telluride arises from its noncentrosymmetric zinc-blende tetrahedral structure (abiding to $\bar{4}3m$ point group symmetry), and it is associated to a nonlinear electronic polarization mechanism. The form of the *d*-matrix of nonlinear coefficients for regular $\bar{4}3m$ symmetry class of the bulk CdTe crystal, assuming the Kleinman symmetry, reduces to the following form:[58]

$$d_{XYZ} = \begin{bmatrix} 0 & 0 & 0 & d_{14} & 0 & 0 \\ 0 & 0 & 0 & 0 & d_{25} = d_{14} & 0 \\ 0 & 0 & 0 & 0 & 0 & d_{36} = d_{14} \end{bmatrix} \tag{III.9}$$

For $\bar{4}3m$ class crystal structures, such as CdTe there are six nonvanishing tensor elements. Intrinsic permutation symmetries of CdTe crystalline axis further lead to: $d_{xyz} = d_{xzy} = d_{yxz} = d_{yzx} = d_{zxy} = d_{zyx}$. Thus the i component (i = x, y, z) of the second-order nonlinear polarization response can be expressed as:

$$P_i(2\omega) = 2d_{14}\begin{bmatrix} 0 & 0 & 0 & 1 & 0 & 0 \\ 0 & 0 & 0 & 0 & 1 & 0 \\ 0 & 0 & 0 & 0 & 0 & 1 \end{bmatrix}\begin{bmatrix} E_x(\omega)^2 \\ E_y(\omega)^2 \\ E_z(\omega)^2 \\ 2E_y(\omega)E_z(\omega) \\ 2E_x(\omega)E_z(\omega) \\ 2E_x(\omega)E_y(\omega) \end{bmatrix} \quad \text{(III.10)}$$

Downscaling from bulk crystal size to the nanometric scale – when NP becomes much smaller than the excitation wavelength (QDs may be compared here to a single molecule), enables to describe the nonlinear scatterer as a dielectric sphere,[2,58,80-81] thus it can be considered as a Rayleigh scatterer. The electric field inside such a particle $E(\omega)$ induced by linearly polarized electromagnetic wave is uniform and in-phase, so due to the Landau's electrostatic theory of dielectrics it can be taken as:[80,82]

$$E(\omega) = \left[\frac{3\varepsilon_m}{(\varepsilon + 2\varepsilon_m)}\right] E_m(\omega) \quad \text{(III.11)}$$

where $E_m(\omega)$ is the fundamental electric field in the surrounding medium (PMMA host-matrix in the case of our experiment), ε and ε_m are the linear permittivities of the NP and the surrounding medium respectively.

For SHG, which is simply a frequency doubling process, expression (III.3) transforms into:

$$P(2\omega) = 2\varepsilon_0 d_{XYZ} E^2 = \chi^{(2)} \cdot E(\omega)E(\omega) \quad \text{(III.12)}$$

Since the CdTe cubic zinc-blende – like lattice is an example of a perfectly octupolar symmetry,[4] one may expect a multipolar character for the emitted SHG field. These properties are, however, related only to the CdTe material features, which cannot sustain a dipole by virtue of its spatial arrangement (nor any other property of a vectorial nature). When addressing the quantum particles, such as single CdTe QDs with a linearly polarized

fundamental beam, electrons oscillating at the frequency 2ω have a second harmonic nonlinear polarization which is a vector by the very nature of a polarization. This is not in contradiction with the octupolar character of the CdTe material. Therefore, acting on an '*artificial atom*' by linear polarization induces a dipolar polarization of the field.

The $P(2\omega)$ polarization is in-phase and uniform inside the NP, however due to our experimental conditions (where the collection sensitivity of the emitted light can be neglected along the *Z* axis) it implies that only two electric field components along two different crystalline axes of the lattice, such as *X* and *Y* can couple to generate a second-harmonic emission dipole moment along the third crystalline axis, such as *Z*. Thus the nonlinear dipole moment of the CdTe QD can be defined as:

$$p(2\omega) = \left(\frac{4}{3\pi a^3}\right) P_i(2\omega) \qquad \text{(III.13)}$$

and it radiates like a '*nanoantenna*' at the frequency 2ω, where *a* is the radius of the scatterer, and $P_i(2\omega)$ are the elements of the nonlinear polarization (*i* = *X*, *Y*, *Z*). When these considerations are translated into tensorial properties of the second-order nonlinear susceptibility of CdTe we can limit ourselves to coefficients such as $\chi^{(2)}_{X(Y),j,k}$, and in that particular case we discard the $\chi^{(2)}_{Z,j,k}$ coefficients. Thus the nonlinear dipole for the CdTe QD can be reduced to the following form:

$$p_{X,Y}(2\omega) = \varepsilon_0 \sum_{j,k} \chi^{(2)}_{X(Y),j,k} E_j^{(\omega)2} E_k^{(\omega)2} \qquad \text{(III.14)}$$

In case of CdTe QDs, excitation with a linearly polarized optical electric field (or with circular polarization, defined further in Subsection V.1), oriented perpendicularly to the *z* propagation axis of the laboratory frame, allows to generate satisfactory results. We can therefore assume in the following that collection of signal orientating from a $\chi^{(2)}_{Z,j,k}$ component is negligible.[4-5,8]

SHG detection from very small NPs is mainly limited by the nonlinearity of the material. Additionally other constraining factors may appear from a technical point of view, such as due to the numerical aperture of the microscope objective, incident polarization aspects, and quantum efficiency of detectors.[83] Many SHG-active insulating (alternatively wide-gap)

inorganic NPs have been recently reported and studied at the single NP scale, e.g. ZnO,[84-85] $KNbO_3$,[86-87] $Fe(IO_3)_3$,[88] $BaTiO_3$,[2,89] and $KTiOPO_4$.[1,90] Nevertheless, these materials due to their nonlinearity are difficult to detect with standard detection techniques, at least when their size is decreased much below the excitation wavelength (< ~40 nm).

Table (III-I): Second-order nonlinear optical coefficients of selected inorganic and SC crystals.[77]

Material	Symmetry class	λ_ω [nm]	n_ω	$n_{2\omega}$	d [pm V^{-1}]	Additional Ref.
Barium titanate ($BaTiO_3$)	Trigonal 4*mm*	1,064			d_{15} = 17.0 d_{31} = 15.7 d_{33} = 6.8	[91]
Cadmium selenide (CdSe)	Hexagonal 6*mm*	10,600 800	n^o = 2.427 n^e = 2.445	n^o = 2.462 n^e = 2.482	d_{15} = 18.0 d_{33} = 36.0	[92]
Cadmium sulfide (CdS)	Hexagonal 6*mm*	1,064	2.3481 2.3316	2.6494 2.6495	d_{15} = 44.0 d_{31} = 40.2 d_{33} = 77.9	[93-94]
Cadmium telluride (CdTe)	Tetrahedral $\bar{4}3m$	10,600 1,064 1,500	2.69	2.71	d_{14} = 168 d_{14} = 109 d_{14} = 73	[5,94-95]
Cinnabar (HgS)	Trigonal 32	10,600	n^o = 2.594 n^e = 2.845	n^o = 2.628 n^e = 2.888	d_{11} = 50.0	
Gallium arsenide (GaAs)	Tetrahedral $\bar{4}3m$	10,600	3.27	3.30	d_{14} = 368	
Potassium titanyl phosphate-KTP (KTiOPO)	Rhombic *mm*2	880			d_{15} = 3.92 d_{24} = 2.04 d_{31} = 4.74 d_{32} = 2.76 d_{33} = 18.5	
Zinc oxide (ZnO)	Hexagonal 6*mm*	1,064	1.95	2.05	d_{15} = 5.9 d_{33} = 18.0 d_{35} = 5.4	
Zinc selenide (ZnSe)	Tetrahedral $\bar{4}3m$	10,600			d_{36} = 33.0	
α-Zinc sulfide (ZnS)	Hexagonal 6*mm*	1,064			d_{15} = 7.0 d_{33} = 14.0	
Zinc telluride (ZnTe)	Tetrahedral $\bar{4}3m$	10,600	2.69	2.70	d_{14} = 90	

To the best of our knowledge, the minimal observable size so far of nanocrystals made of these materials at the single NP scale is larger than 30 nm. The main difficulty arises from a nonlinear scattering nature of SHG, which is expected to scale with the squared volume of the nanoscatterer ($I_{SHG} \propto V_{scatt}{}^2$). Therefore when we consider real experimental conditions, the number of emitted SHG photons in approximation is proportional to the diameter of the NP (a_{NP}) to the power of sixth:

$$N_{SHG} \propto \left(\chi^{(2)}\right)^2 \left(\frac{\langle P \rangle^2}{f_{rep} \cdot \tau}\right) a_{NP}{}^6 \qquad \text{(III.15)}$$

where P is the power of incident excitation optical electric field, f_{rep} is a repetition rate of the laser pulses (80 MHz for standard *Mai-Tai HP, Spectra-Physics* oscillator), and τ is a laser pulse duration (typically about 100 fs). Expression (III.15) together with the significant background noise level that goes with nonlinear scattering put a strong limitation for SHG detection from very small NPs. On the other hand, the importance of developing small and photostable NCs, applicable to bio-labeling in cellular or tissue imaging, where the size reduction of nanolabels is a prerequisite, as shown in Ref. [74,96-98] have objected our investigations to a noncentrosymmetric materials, exhibiting much higher second-order nonlinearity than the above mentioned inorganic NPs. Nonlinear coefficients of some inorganic materials and most popular SCs are presented in Table (III-I). The comparison of II-VI group SCs against typical wide-gap inorganic nonlinear crystals highlight SC NCs as excellent candidates towards nanocrystal downsizing.

III.3 Nonlinear two-photon polarization sensitive microscopy setup

In principle, the nonlinear TPSM setup used for SHG studies is similar to the one described in Refs. [75,90]. However, it has been significantly improved in terms of the laser source, mechanical stability and quality of the optical components. The idea of the experiment is illustrated on the schematic of the optical setup in Figure III-2. The laser source used for excitation is a commercial *Spectra–Physics Mai–Tai HP* (100 fs pulse duration, 80 MHz repetition rate) mode-locked Ti-Sapphire rod oscillator cavity. In this system the pump laser is a solid state continuous wavelength (CW) *Millennia* diode-pumped laser, with Nd:YVO_4 lasing medium (Na^+ ions doped in a yttrium vanadate crystalline matrix). The 1.064 μm emission is converted to the visible through frequency doubling (SHG) in a 90°, noncritically phase-matched, temperature-tuned lithium triborate (LBO) nonlinear crystal. The CW 532 nm output is used to pump the Ti-Sapphire rod in a four level scheme. The Ti-Sapphire rod (with absorption peak at about 510 nm) is composed of Ti_2O_3 introduced into a melt of Al_2O_3, where the Ti^{3+} ions responsible for a lasing are substituted to a small fraction of the Al^{3+} host. This system provides smooth wavelength tuning in a range from 690 – 1020 nm (wavelength

dependence of the laser output power, as well as characteristics of other optical components can be found in Appendix A).[iii] One of the main advantages of the *Mai–Tai* laser system stems from its user-friendly control panel, and the option for automatized continuous scanning over the whole accessible wavelength range, which has been used in this work in order to study the wavelength dependence of the SHG emission, radiated by single QDs.[4,8]

Other essential components of the experimental setup are an achromatic half-wave plate (λ/2), mounted on a compact motorized rotation stage (*Newport*, PR50) and a polarizing beam splitter (PBS), placed in the detection channel. These components allow for measurements of the incident polarization dependence of the emitted signal for arbitrary orientations of the source NC. In this case, precise rotation of the λ/2 plate turns the incident polarization angle, while the PBS works like an analyzer, which separates the emitted signals (TPEL or SHG) into two different detection channels with different polarization components: vertical P_p in a transmission (*y* or *p*) and horizontal P_s in a reflection mode (*x* or *s*). Signal detection was carried out using two single photon counting – avalanche photodiodes (APDs, *Perkin-Elmer*, Si-based *SPCM-AQR-14*), both with comparable dark counts ratio ($C_{dark\ counts}$) of about 100 Hz (at the room temperature). Without illumination, randomly generated dark counts of the APDs follow a Poisson distribution, where the standard deviation is equal to the square root of the counts mean value $\sigma = (I_{dark\ counts}^{average})^{1/2}$. The real value of the signal count rate can be obtained using the correction factor: $C_f = 1/1-(t_d \cdot C_{output})$, where t_d is a module dead time (~50 ns), and C_{output} is an output count rate. Finally, the actual photon count rate can be calculated using the following expression:[iv]

$$C_{real} = \frac{C_{output} \cdot C_f - C_{dark\ counts}}{QE_{APD}} \qquad \text{(III.16)}$$

where QE_{APD} is the wavelength dependent APD quantum efficiency, which can be found in Appendix A (Figure A-8).

The pump light with known incident polarization and controlled radiation power was directed into the main unit of the setup - an inverted confocal microscope (*Nikon*, Eclipse T2000–U) by a system of adjustable mirrors. Next, it is being reflected by the dichroic mirror

[iii] Source: User's Manual, *Mai-Tai HP, Spectra-Physics.*
[iv] Single Photon Counting Module SPCM-AQR Series datasheet, *Perkin-Elmer*.

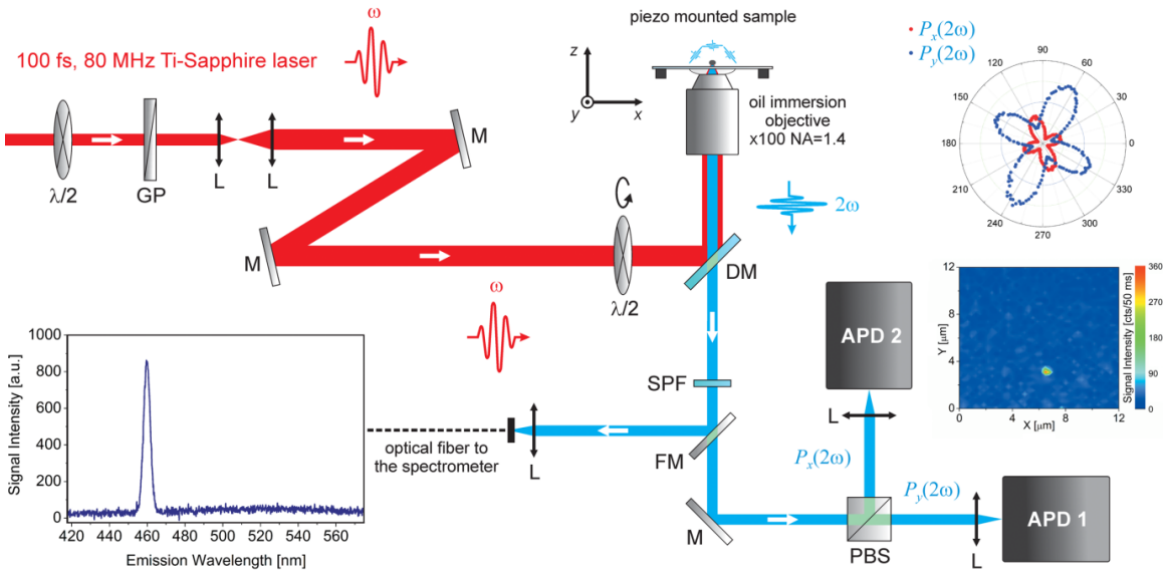

Figure III-2 | Schematic of the two-photon nonlinear scanning microscopy setup: λ/2 – half wave plates, GP – Glan-Taylor prism, L – lenses, M – adjustable silver-protected mirrors, DM – dichroic mirror, SPF – short-pass filter (also additional BG38-39 filters), FM– flip-mounted mirror, PBS – polarizing beam splitter, APD 1-2 – avalanche photodiodes. Circularly oriented arrow corresponds to the motorized rotation stage.

(DM, fixed at 45°, with a cutting wavelength at 730 nm) into the microscope objective. Major parameters of the DM, such as dichroism (γ) and its phase shift (φ_{DM}) were taken into account for further data processing (see Appendix A, Figure A-10).

In detection of SHG from such small objects as single QDs, providing phase-matching conditions is negligible because for all practical purposes we deal with a scattering by a '*point-like dipole*'. Applications of the SHG process in nonlinear microscopy of larger objects, however, demand consideration of high pump electric field intensities in order to obtain efficient enough signals via tight focusing of the incident beam. For tightly focused driving field with an aperture limited angular distribution of half-width α_0, multi-harmonic radiation patterns are confined into twin-lobed or conical geometries (related to a surface and volume generation, respectively), which are quasi phase-matched and highly peaked at the Gouy phase shift dependent off-axis angles ($\pm\alpha_0/\sqrt{2}$ and $\alpha_0/2$ for a surface and volume multi-harmonic generation, respectively).[79,99-100] For both, surface and volume cases multi-harmonic scattering propagation is highly limited in the backward direction. Nevertheless, use

of the microscope objectives with wide enough angular numerical apertures ($NA = n\sin\alpha$) may essentially provide collection of all the scattered harmonic light in the backward direction.

In order to obtain high pulsed peak intensity in a tightly focused excitation volume we used a high numerical aperture oil immersion objective (*Nikon*, Plan Apo IR, ×100, *NA* = 1.4). Its high *NA* value allows for efficient collection of the SHG radiation in the backward direction. The collected signal was spectrally separated from the NIR excitation beam by the DM. Additional spectral filtration (short-pass / band-pass filters) was applied in order to select the SHG emission peak in case of potentially appearing TPEL emission. Emitting NPs were localized by scanning surface of the sample carried out with a *Piezojena x,y,z* positioning piezo stage, with a minimal step of 20 nm. The nature of the emission was confirmed by measuring its spectra, as acquired by *Oriel* Multispec 7740 spectrometer (160 nm narrow slit) equipped with an *Andor Technology* DV420-OE CCD camera.

III.3.1 Optical and effective spatial resolution in multi-photon microscopy

The minimal optical resolution of the focused laser beam determines the minimal achievable diameter of the focal spot, which in practice corresponds to the Airy-disk distribution function (Figure III-3(a)). Considering the Rayleigh criterion, imaging of two incoherent point sources (sum of two known, identical, overlapping component functions) is confined by the diffraction limit.[101-102] Two incoherent point sources are considered distinguishable when the center of the Airy intensity pattern generated by one point source falls exactly on the first zero of the Airy pattern generated by the second. For the VIS region the Rayleigh distance δ is about 250 nm. Theoretically the minimum resolvable distance is characterized by Abbe's diffraction limit: $d = \lambda / 2n\sin\alpha$.[103] In incoherent two-photon microscopy, where the excitation probability is proportional to the square of the fundamental incident intensity, the effective spot size is sharpened by a factor of $\sqrt{2}$ (assuming the Gaussian distribution of the intensity profile), thus the Rayleigh criterion for two-photon excitation (TPE) can be expressed as:[102]

$$\delta = 0.61\frac{\lambda}{NA} \qquad \text{(III.17)}$$

The intensity distribution in the image of two equally bright incoherent point sources separated by the δ distance is illustrated in Figure III-3(b). The central dip is found to fall by a Δ ratio of about 27% below both peak intensities.

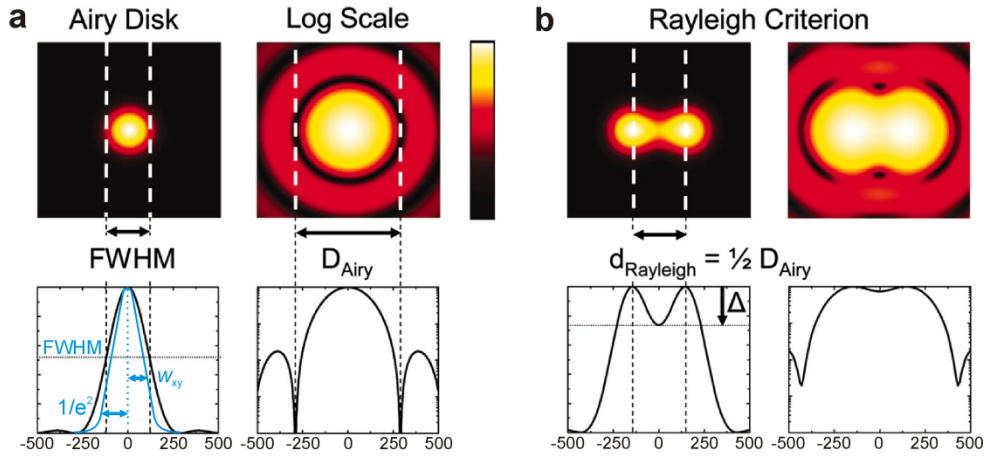

Figure III-3 | Images of incoherent point-like sources in the optical microscope: a) Airy Disk intensity distribution and its profile (left), in logarithm scale (right). The blue profile shows a Gaussian function related to the IPSF^2. Profiles were normalized for λ = 690 nm, *NA*=1.45. Defined distances are: $D_{Airy} = 2\delta = 1.22\lambda / NA$, FWHM = $0.29D_{Airy}$, and $\delta = 0.5D_{Airy}$. b) Intensity profiles (left) and their logarithm scale (right) corresponding to incoherent two point sources distanced by δ. Adapted from Michalet et al. [104].

For coherent point sources, the diffraction limit requires consideration of both the intensity and phase distributions associated with the object. A profile along one of the lateral axis of the image intensity can be expressed in normalized image coordinates as:[102]

$$I(x) = \left| 2\frac{J_1\left[\pi(x-0.61)\right]}{\pi(x-0.61)} + e^{j\phi}\, 2\frac{J_1\left[\pi(x+0.61)\right]}{\pi(x+0.61)} \right|^2 \qquad \text{(III.18)}$$

where *J* is a mutual intensity, that is a measure of the spatial coherence of the light at the two coherent point sources, and ϕ is the relative phase between these two sources. Basically, depending on ϕ, we can distinguish three situations which are illustrated in Figure III-4. In the first situation ($\phi = 0$) both coherent point sources are totally in phase (this is applied further for SHG imaging of single and isolated QDs). Second case ($\phi = \pi/2$ rad) illustrates the case where both sources are in a quadrature (with identical intensity profile to that of incoherent sources). The last situation ($\phi = \pi$ rad) shows the two sources in phase opposition.[102]

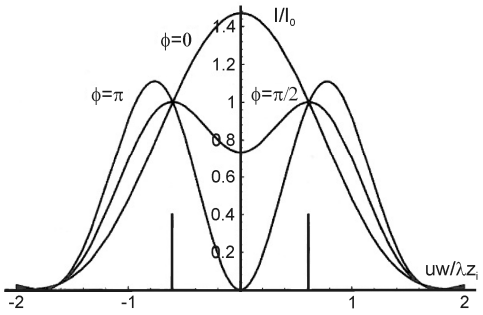

Figure III-4 | Phase dependent image intensities for two equally bright coherent point sources (marked by the two vertical lines), separated by the Rayleigh resolution distance δ. Figure adapted from Ref. [102].

The two-photon focal volume produced by a converging excitation field can be determined by the illumination point spread function (IPSF), which maps the intensity distribution everywhere in space near the focus point. The IPSF can be equally regarded as the probability distribution of the pump photons in the focal plane, thus a smaller extent of the IPSF provides a better localization of the photons and a better resolution. The focal waists can be determined for the lateral *x y* and axial *z* directions as follows (assuming $NA > 0.7$):[72]

$$w_{xy} = \frac{0.325\lambda}{\sqrt{2}NA^{0.91}}; \quad w_z = \frac{0.532\lambda}{\sqrt{2}}\left(\frac{1}{n-\sqrt{n^2-NA^2}}\right) \tag{III.19}$$

In order to define the real optical resolution in multi-photon microscopy we need IPSF^2, which can fit the lateral and axial intensity-squared profiles to a Gaussian function, estimating the diffraction-limited lateral and axial $1/e^2$ radii of the IPSF^2 (blue profile in Figure III-3(a)). Conversion to a more common measure of the optical resolution, such as the full width of the curve shape taken at half height of the maximum (FWHM) can be obtained from $1/e^2$ by multiplication by $2\sqrt{\ln 2}$ (or inversely by $\sqrt{2}$). Note, however, that in order to achieve the diffraction limited focus point, the laser beam must be collimated at least into the full diameter of the objective lens back aperture.[72]

TPE volume can be found by approximating the IPSF^2 to a three-dimensional Gaussian volume, based on averaging the TPE potential over all space. Integration of a three-dimensional Gaussian yields:

$$V_{TPE} = \pi^{3/2} w_{xy}^2 w_z \tag{III.20}$$

Expression (III.20) provides a reasonably good estimation for the center of the IPSF[2], however regions far from the focus point are not taken into account, therefore the integrated Gaussian volume yields about 68% of that which can be obtained from the full vectorial approach. Using this estimation, we characterized the effective TPE volume for our experimental conditions (NA = 1.4, n_{PMMA} = 1.5) to range from about 0.21 μm^3 ($\lambda_{exc} = 800$ nm) up to 0.41 μm^3 ($\lambda_{exc} = 1.0\,\mu$m).

III.4 Time correlated single photon counting in detection of single nanoparticles

Since the number of the SHG photons (at least in the nonresonant case) is proportional to the squared volume of the scatterer, it is extremely difficult to detect low amounts of SHG photons radiated by very small scatterers such as, e.g. strongly confined CdTe QDs. The impediments in detection arise from the technical properties of standard detector devices such as APDs or PMTs, due to the significant signal noise (dark counts), which can basically overwhelm the real SHG signal. The TCSPC gated detection technique allows to exclude the dark counts of the detector, thereby allowing to detect low signal intensities obtained from small NPs. This opens the way towards spectroscopy studies of the size dependent SHG emission from small and strongly confined single CdTe QDs, which are a major part of this thesis (Chapter V).[5] Schematic of the optical experimental setup adapted for the TCSPC detection method is illustrated in Figure III-5. Its concept is similar to that of the TPSM experiment (Figure III-2). It contains basically similar laser source: a mode-locked *Tsunami, Spectra-Physics* Ti-Sapphire 130 fs oscillator, emitting at 800 nm with 80 MHz pulse repetition rate. Before reaching the inverted confocal microscope (*Zeiss, Axiovert 200*), the laser pulse is split into two optical paths: one is focused on the trigger diode (reference beam), while the other one is used as the excitation beam. In order to minimize the incident polarization dependency, we introduce a circularly polarized excitation beam by using an achromatic quarter-wave plate ($\lambda/4$) oriented by 45° with respect to the $\lambda/2$ plate. The incident light is tightly focused on the piezo-mounted sample by a high numerical aperture oil immersion objective (×63, NA = 1.4). The signal is further collected in the same backward geometry as in previously described TPSM setup, and then spectrally separated from the reflected pump beam by the first dichroic mirror (DM1). The detection channel contains a second dichroic (or dielectric mirror, DM2), which spectrally separates the SHG signal from

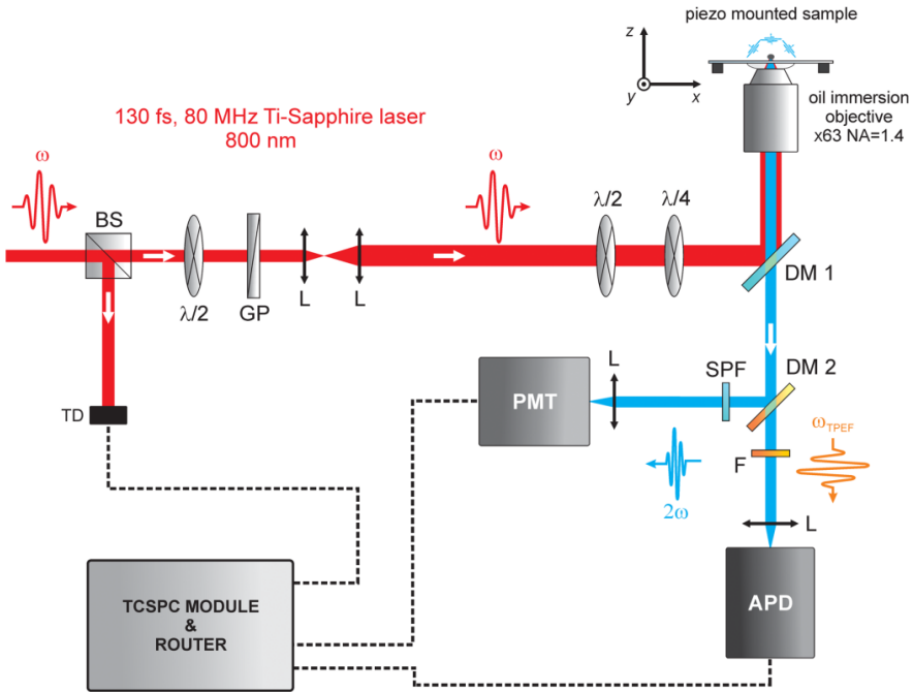

Figure III-5 | Schematic of the optical setup for time correlated single photon counting measurements: BS – beam splitter, λ/2 – half wave plate, GP – Glan prism, L – lenses, λ/4 – quarter wave plate, DM – dichroic mirrors, SPF – short-pass filter, F– fluorescence filter, PMT – single photon-counting photomultiplier tube, APD – avalanche photodiode.

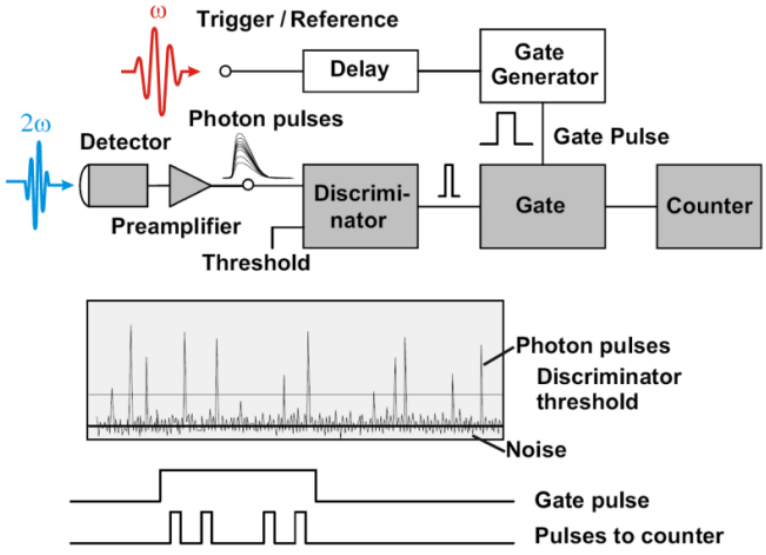

Figure III-6 | Schematic of gated TCSPC single channel system, illustrating the idea for measurements of instantaneously scattered photons, arriving subsequent to the reference laser pulse. Adapted from Ref. [105].

the TPEF emission. Both signals are collimated and injected into a multimode optical fibers (50/120 μm, optimized for the VIS spectral range) connected to ultra-low noise detectors (exhibiting the dark count rates < 20 Hz) PMT (*Picoquant*) and APD (*id100-MMF50, idQuantique*), for SHG and TPEF, respectively. The PMT is used in the SHG detection channel thanks to its higher quantum efficiency in the near UV range (with the *Tsunami* laser we generate SH photons at 400 nm). The APD detected TPEF signal allows for more efficient localization of small luminescent QDs, which may eventually exhibit very low SHG quantum yields. Both detectors are connected to the double-channel TCSPC module (*PH300, Pico Harp* with 4 ps channel width) and then to the four-channel router (*PHR800, Pico Harp*). Reference laser pulses are detected by the trigger diode (*TDA200, Pico Harp*), connected to the same TCSPC system.

The principle of gated photon counting measurements is illustrated in Figure III-6. The measurement is based on the logic gate between the discriminator and the counter, which provides counting of the single-photon pulses within narrow time intervals. In a first step a discriminator separates the single-photon pulses (signal) from the background noise of the detector, which is below the discriminator threshold. The discriminator output pulses are sent through a logic gate, and only pulses within the gate pulse are counted. The gate pulses are basically triggered externally by the same laser source as the excitation beam, and detected by the trigger diode.[105] Combination of time-tagged TCSPC module with slow scanning microscopy setup works best in single-molecule spectroscopy, e.g. for fluorescence life-time imaging.[106] Nevertheless it can be successfully applied for detection of the SHG or TPEL photons emitted by a single and small NPs. Detection of the SHG signals from a single QD immersed in a polymer host-matrix, however, does not fully discard the background noise, which is due to the coherent SHG scattering of the incident light at the interface between a glass cover slip and a polymer film (e.g. PMMA), although its quantitative occurrence of about 10 - 20 Hz is much lower than the dark counts of a standard APD detector.

III.5 Chapter summary

Two different contrast mechanisms such, i.e. SHG and TPEF, commonly used in the two-photon microscopy has been reviewed and compared. Properties of both processes were discussed in order to highlight their differences, and point out the importance for development

and application of SHG-active nanoprobes, e.g. CdTe QDs, which can give all the features derived from coherent SHG process, alternatively to common fluorescent markers used in bioimaging.

By considering a Rayleigh nanoscatterer model, we compared the physical aspects of the SHG process in CdTe from the bulk, down to the single QD scale. The second-order optical nonlinearity of CdTe was additionally compared with common nonlinear insulators and wide gap semiconducting crystals.

The second part of the chapter contains detailed descriptions of the optical setups used in the experimental part of the thesis. We introduced the diffraction limited TPSM technique used for coherent SHG detection from single QDs (which to our best knowledge are the smallest detectable single SHG-active nanoparticles), and for wavelength dependence of scattered SHG radiation.[4,8] Furthermore combination of TPSM with the time-tagged TCSPC detection setup was proposed for single QD spectroscopy and size dependent measurements of the second-order nonlinear susceptibility.[5]

Chapter IV | Second-harmonic generation from CdTe QDs: single dot studies

IV.1 SHG from single dot-shaped CdTe/CdS core/shell QDs 56
IV.1.1 Spectral dependence of the SHG process from spherical CdTe/CdS core/shell QDs 59
IV.1.2 Contribution of the CdS shell to the overall SHG emission process 62
IV.1.3 Orientation dependent SHG polarization response from spherical CdTe/CdS core/shell QDs 63
IV.1.3.1 Analysis of the SHG polarization dependence 64
IV.1.3.2 SHG polarization response with respect to the CdTe symmetry constraint 68
IV.2 SHG from single rod-on-dot CdTe/CdS heterostructures 70
IV.2.1 Special features of SHG emission from rod-on-dot QD heterostructures 73
IV.2.2 Polarization analysis of the SHG emission of rod-on-dot CdTe/CdS QDs 78
IV.2.2.1 Simulation model for polarization analysis of RD QD heterostructures 80
IV.2.2.2 The role and impact of the CdS rod length into the total SHG intensity 81
IV.2.2.3 Errors in inferring the orientation of the crystalline lattice from SHG polarization analysis 85
IV.3 Accuracy of the polarization analysis from a reduced set of raw data points 86
IV.4 Chapter summary 89

In this chapter the SHG emission obtained in the case of individual, well isolated CdTe/CdS SC QDs is discussed. We focus on the second-order nonlinearity of the CdTe material, and comparing its response for the bulk and nanometric scale. We further analyze the spectral response and photostability of observed SHG signals at different conditions of the two-photon excitation. Optimization of the experiment allows to study the spectral dependence of the SHG emission, which is found to be directly connected to effects arising from the quantum confinement in CdTe QDs. Due to the vectorial properties of observed SHG emission, reflecting in a strong optical polarization sensitivity to the properties of CdTe zinc-blende structure, we are able to probe and infer the spatial orientation of crystalline unit cell of individual QDs. Finally we show that the second-order nonlinear response of hybrid CdTe/CdS heterostructures can be engineered based on optimization of material, size and geometrical features.

IV.1 SHG from single dot-shaped CdTe/CdS core/shell QDs

The choice of CdTe bulk nonlinearity was made to obtain a SHG response which does not strongly depend on the NP shape. Reported values of CdTe nonlinear coefficients range from 64 pm V^{-1} to 200 pm V^{-1} (depending on the size and excitation wavelength),[5,77,94-95] i.e. about one order of magnitude larger than KTP (see Table IV-I). With high values of the nonlinear coefficients and a noncentrosymmetric tetrahedral crystalline lattice, we expect to be able to downscale the size of SHG active spherical CdTe - based QDs down to about 10 - 15 nm, while maintaining the signal intensity at the level of at least 1×10^3 cts s^{-1}. Such a size range is also commensurate with the 7.3 nm exciton Bohr radius of CdTe, which marks the onset of size - dependent effects due to quantum confinement.

The nonlinear optical response was measured with the TPSM setup illustrated in Figure III-2. Examples of diffraction limited spots corresponding to the SHG emission, from two single dot-shaped CdTe/CdS core/shell QDs (a, b) are shown in Figure IV-1. Scanning conditions were determined by setting the signal acquisition time to 50 ms, and the piezo-scanner step to 80 nm per image pixel. Both SHG scans appear somehow ellipsoidal, showing wider cross-sections in vertical directions with a FWHM function of about 350 nm, and a FWHM of about 236 nm for cross-sections in the horizontal direction. Thus the diagonal cross-sections FWHM can be taken as 295 ±56 nm, which is consistent with the diffraction limited experimental system. This anisotropy may be related to vector effects, due to the elliptical excitation region with the ellipse stretched along the direction of the linear polarization. In Figure IV-2 we show smoothed SHG scans with their three-dimensional profiles corresponding to the two SHG spots (a-b), shown in Figure IV-1. The presented SHG emission scans were obtained at an excitation wavelength of λ_{exc} = 980 nm from 100 fs pulsed laser light, and with the incident power of P_{exc} = 0.7 mW (measured at the front of the microscope), which leads to a focused pulsed peak intensity of about 18.2 GW cm^{-2} at the focal point. The SHG emission was spectrally filtered from eventual contamination by TPEF emission, using a high transmission band-pass filter (480 ±20 nm) and a high quality short-pass filter (transmission ~95%, cut-off at 561 nm). These conditions were enough to obtain a SHG count rate of about 7.5×10^4 cts s^{-1}, which after correction by the APDs detection efficiency (40% for 490 nm at ambient temperature) yields a signal of about 1.05×10^5 cts s^{-1}, what is the real SHG photon flux. The observed background appears mainly due to the APDs

dark counts at the level of about 950 cts s^{-1}, leading to a signal-to-noise ratio of about 80, thus providing a high enough contrast. Detection of such a high signal, almost two orders of magnitude higher than the usual limit for bio-imaging, highlights spherical CdTe/CdS core/shell QDs as a promising material for bio-labeling.

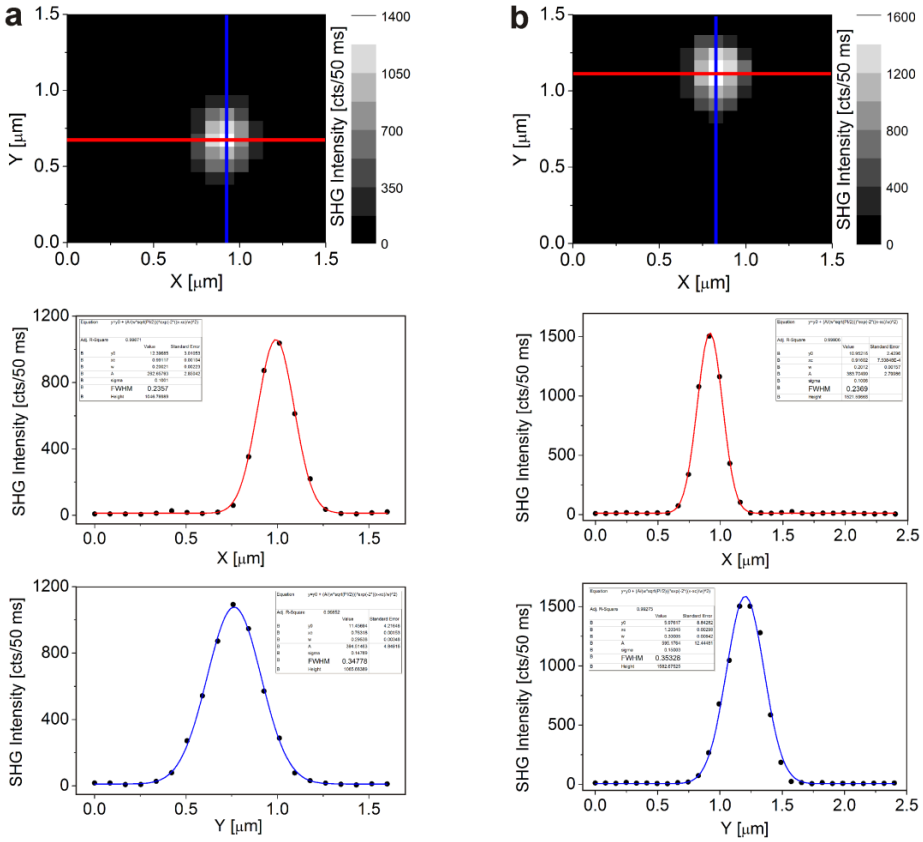

Figure IV-1 | (a-b) Scans of SHG spots obtained from two different single CdTe/CdS core/shell QDs. Corresponding cross-sections (organized in columns, where red is a horizontal and blue is a vertical direction) were fitted using Gauss distribution function, and show average FWHM value about 295 ±56 nm.

An important issue of any tested CdTe – based QDs is that the character of the emission has a strong impact on its photostability of the signal. In general our observations show that signals obtained from QDs emitting SHG with a high QY for this efficient process exhibit a higher degree of photo-stability, even at high intensities of the pump light, i.e. ~80 GW cm^{-2} of the focused pulse peak intensity (see Figure IV-3(a-c)).[4] In the context of bio-labeling, SHG observed from CdTe/CdS QDs under strong excitation intensities shown reduced photobleaching, which is a main limitation for many organic fluorophores,[72,107] and fully eliminates the problem of emission intermittency such as '*blinking*' which is commonly observed for luminescent QDs.[108-111]

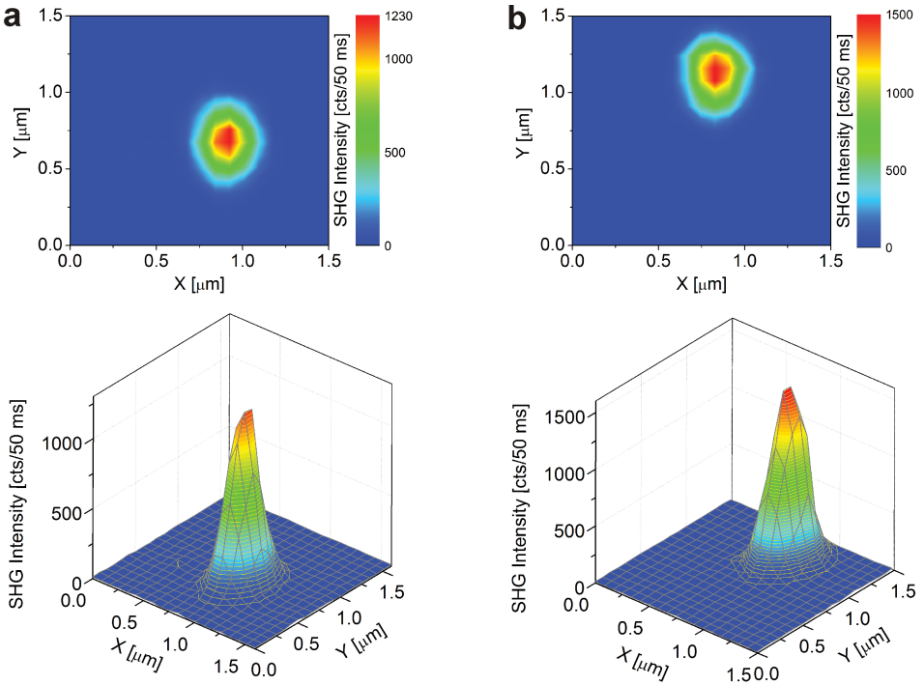

Figure IV-2 | (a-b) Smoothed scans (with large increment) of the SHG Gauss-like signal distribution, obtained from two different single CdTe/CdS core/shell QDs – presented in Figure IV-1. Corresponding three-dimensional profiles show signal-to-noise ratio of about 70.

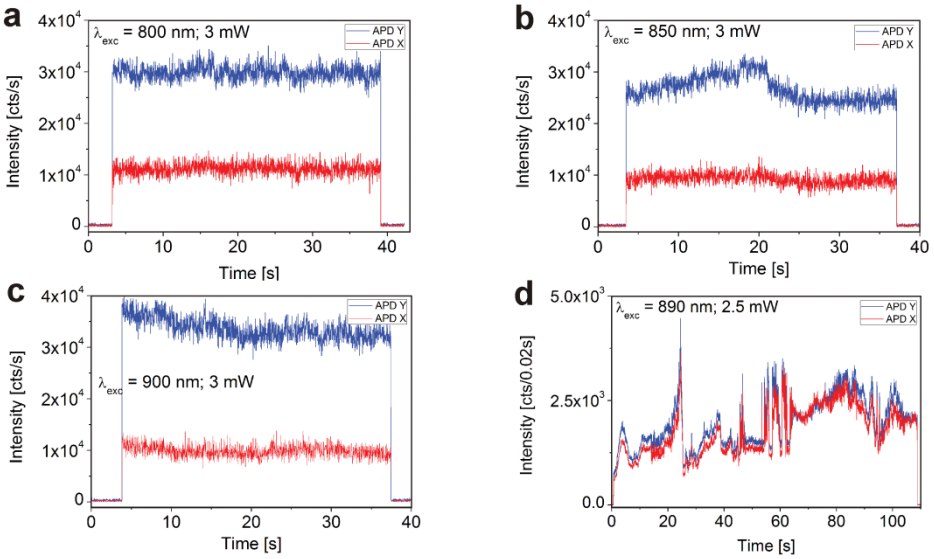

Figure IV-3 | Photostability of the SHG emission, obtained from a single CdTe/CdS core/shell QD exhibiting very low luminescence QY at the different excitation wavelengths: a) 800 nm, b) 850nm, c) 900 nm. d) Example of strong signal fluctuation, observed from a single CdTe/CdS QD with a high luminescence yield.

Beside SHG, undesirable two-photon excited luminescence (TPEL) can appear as competing nonlinear process. Figure IV-4(b) exemplifies some QDs (obtained with the pulsed peak intensity of about 135 GW cm^{-2}, and without spectral separation of the SHG emission peak) which, when excited at frequencies far from the one-photon resonance (which appears at 760 nm – see Figure II-3(c)) exhibit TPEL emission with a maximum at about 520 nm, with a decisive influence on the photostability of the NP. Studies of many CdTe/CdS core/shell QDs have shown that even small amounts of luminescence photons observed simultaneously with SHG emission, can dramatically reduce the intensities of both processes, which is a reversed correlation to that which has been observed for a pure and highly photostable SHG signal. We believe that the reduced stability of QDs exhibiting stronger band-edge luminescence is due to induced excited state absorption at the excitation frequency. In QDs exhibiting low luminescence QY the excited state population completely decays non-radiatively within the ~12 ns time interval between excitation pulses, eliminating such possible effect. Longer exposure of QDs exhibiting high luminescence QY under strong intensities results in strong signal fluctuations finally leading QDs to structural damage, and a strong decrease of the emission intensity (Figure IV-3(d)), and sometimes to its complete disappearance.

IV.1.1 Spectral dependence of the SHG process from spherical CdTe/CdS core/shell QDs

To analyze the spectral dependence of the SHG process, we considered a single spherical CdTe/CdS core/shell QD, emitting a relatively intense and photostable SHG signal. The spectral response of the SHG emission was first obtained using an *Oriel Multispec* 77400 spectrometer (160 nm narrow slit), equipped with an *Andor Technology* DV420-OE CCD camera. For each spectrum the collected SHG emission was obtained from a single QD (Figure IV-4(a)), in presence of a short-pass filter cutting eventual TPEL emission. The excitation wavelength was tuned in a range between 850 nm and 1.0 μm while keeping the incident power at the level of 2.0 mW (measured at the front of the microscope), leading to a mean pulsed peak intensity of about 54.5 GW cm^{-2}. Spectra were recorded with doubled acquisition time of 10s, including background correction to avoid the appearance of any noise bursts. In this particular case, the SHG QY was not high, however SHG peaks at half the

incident wavelength are clearly visible, showing a maximal SHG intensity for the excitation region around 970 nm. This wavelength was further confirmed to be optimal in order to obtain the highest possible SHG intensity, and therefore favorable towards further studies of these QDs.

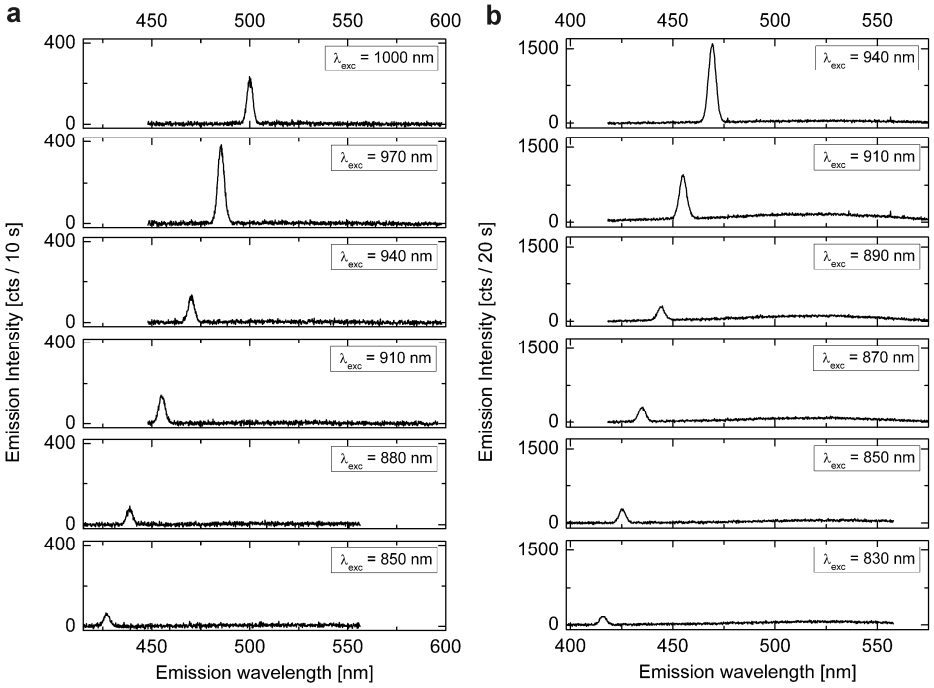

Figure IV-4 | a) Set of SHG emission spectra obtained from a single spherical CdTe/CdS QD, showing drift of the SHG peak (FWHM ~3.8 nm) when the excitation wavelength is tuned from 850 nm to 1.0 μm. Intensities of the SHG peaks were not corrected by transmission factors. b) SHG emission spectra with appearance of TPEL, tuned from 830 – 940 nm.

Reliable results for wavelength dependence of SHG emission could be obtained only with a high degree of emission photostability, thus we have chosen to study QDs with a high SHG QY, allowing exciting them at a low incident power. Each dot was firstly investigated using the spectrometer to confirm the absence of TPEL emission. However spectral separation of the SHG peak from an eventual TPEL was ensured setting a good quality short-pass filter in the detection channel during the next experimental step. The wavelength dependence of the second-harmonic (SH) emission has been investigated by tuning the excitation wavelength (using an automatic laser scan with a step of 1 nm per 1 s, controlled by the *Mai-Tai* control software) and measuring the intensity of the SHG peak observed from CdTe/CdS QDs using two APD detectors (with an acquisition time of 1s). Our femtosecond laser is tunable from

700 nm up to 1020 nm, however our Silicon-based APDs are strongly limited with their quantum efficiency adapted to the green region, thus limiting detection of the SHG signal to wavelengths higher than 400 nm. The SHG emission reflects an effective nonlinear coefficient $\left(\chi_{eff}^{(2)}\right)^2$ corresponding to the squared second-order nonlinear susceptibility. Therefore we were able to obtain reasonable dependence of the effective $\chi^{(2)}$ from 820 nm up to 1000 nm (or from 410 to 500 nm at the doubled frequency), as shown in Figure IV-5(a,b),[4] which provides most relevant data for evaluating the SHG efficiency.[112] Obtained raw data was corrected for the Ti-Sapphire laser characteristic – taking into account the incident power dependence on the emission wavelength, transmission and reflection of the optical components of the two-photon microscope setup, as well as the detection efficiency of the Silicon APDs. Detailed description of the data processing can be found in Appendix A.

Experimental results show that the SHG signal from four different single QDs exhibit almost the same spectral dependence, implying that the results are reasonably reproducible for QDs of similar size. A maximum of the SHG efficiency appears at 970 nm. The one-photon absorption gap of our NPs has been measured and corresponds to 760 nm (see Figure II-3), in agreement with CdTe NPs with sizes from 10 to 15 nm. Therefore the excitation wavelengths we use are far both from one-photon and two-photon resonances near the band gap which would occur for incident photons respectively at 760 and 1520 nm. Our excitation spectral range actually corresponds to deep resonance two-photon excitation with high-excited transitions, in conditions similar to the probe beam used in Ref. [112]. Low-lying excited levels of CdTe have been discussed in the literature; however it is difficult to assign energy levels for such a deep resonant excitation. Therefore we can only propose a tentative explanation for the excitation spectra shown in Figure IV-5(a,b). The shape of the SHG efficiency about 970 nm may be interpreted as a tradeoff between two competing mechanisms: in a Fermi golden rule picture, the density of states for the two-photon transition is higher for higher energies of the excitation light, which should lead to an increase in the two-photon absorption cross-section. However, exciting a state farther above the band edge implies more rapid decoherence, which leads to the reduction of the SHG QY (and preferential branching to two-photon excited fluorescence). Moreover, at least another secondary maximum can be singled-out in this excitation spectrum at about 910 nm. This corresponds to an energy step of about 0.15 eV between the peaks.

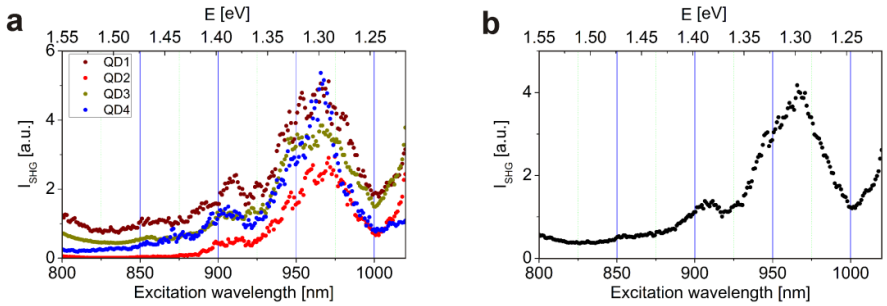

Figure IV-5 | a) Excitation wavelength dependence of the SHG intensity, measured for four different and well isolated dot-shaped CdTe/CdS QDs with an average size of about 12.5 nm. b) Averaged excitation wavelength dependence of the SHG intensity over four different spherical QDs. All the curves are given in arbitrary units, and were normalized after their corrections (see Appendix A).

From one-photon spectroscopy of similar-sized CdSe NCs,[18] it can be seen that when exciting via one-photon transitions up to 1.0 eV above the band gap (as is the case here for 970 nm excitation of QDs with a band gap of 760 nm), the inter-level spacing is of the order of 0.1 eV, roughly corresponding to the observed energy difference in the SHG excitation spectrum. Despite the symmetry difference between one-photon and two-photon transitions, this may suggest that the peaks can be associated with the discrete energy level diagram of the NPs. Our experimental setup does not permit to access the excitation spectrum below 810 nm or above 1020 nm, but it would certainly be interesting to study SHG response when reaching one-photon resonance at 760 nm, as well as two-photon resonance, which is expected at 1520 nm. Although the 970 nm excitation wavelength may not correspond to the highest second-order nonlinear efficiency it nevertheless leads, to an easily detectable as well as photostable emission for the commonly used wavelength range of the Ti-Sapphire oscilator.[4]

IV.1.2 Contribution of the CdS shell to the overall SHG emission process

Dot-shaped CdTe/CdS core shell QDs are built from two noncentrosymmetric materials, both exhibiting nonlinearity (see Table IV-I), thus from this point of view the CdS shell can generate SH emission and also contribute to the total SHG field. Using the simple rules of SHG emission by nanoscatterers (briefly described in Paragraph IV.1), we can estimate the 'classical' role of the shell by considering the nonlinearities of the corresponding bulk materials and the square dependence of the volume of the emitter. For bulk CdS crystal reported values can be as high as 78 pm V^{-1} at 1.064 μm for d_{33} nonlinear coefficient,[77] while

averaged value for the bulk CdTe is estimated to be about 140 pm V^{-1}.[77,94] With the CdTe core diameter of about 12 nm, and thickness of the CdS shell of ~1 nm, the squeezed volume ratio of CdTe over CdS is of about 13.6. The contribution from the shell is expected to be below 10% of the total observed SHG signal.[4] Thus in further processing of the SHG response from dot-shaped CdTe/CdS QDs we only take into account only a role of the CdTe core. This assumption is very important to further discussed SHG polarization analysis, and it was found to be in a good agreement between experimentally obtained SHG polarization response and the theoretical model.[4] We note however, that this estimation is very dependent on the actual ratio of the core-shell radius and of the nonlinear coefficients. Clearly a thicker CdS shell would play a major role both on the amplitude and the shape of the SHG signals, since CdTe and CdS belong to different symmetry classes. Finally it has to be pointed out that the epitaxial growth of CdS QDs may lead to two different symmetries of the CdS structure, resulting in a zinc-blende,[113] or wurtzite crystalline lattices.[114] In the case of our QDs, since CdS shells are grown on the zinc-blende CdTe core, it is possible that it also grows in accordance with a zinc-blende structure, as it is composed of three monolayers. Therefore, in any case, a not well characterized shell structure with possible presence of structural defects, is neglected due to its unknown symmetry and related unknown nonlinearity as well as its weaker volume ratio.

IV.1.3 Orientation dependent SHG polarization response from spherical CdTe/CdS core/shell QDs

One issue in imaging with markers is to separate the signal coming from the nanolabel and the background emission originating from the studied sample. Second-harmonic generation is generally a weaker signal as compared to one or two-photon fluorescence, but it exhibits striking features in contrast with fluorescence signals from an emission dipole (see Sections III.1.1 and III.1.2). One of these distinctive features is coherence, which is being increasingly investigated, [115] and allows to separate the signal coming from the NP, from those obtained from the background scattering. Another one is the symmetry and optical polarization sensitivity of the SHG response, which recently has been explored also at the single NP level.[1,4,75,116-118] From this second point of view, CdTe is a peculiar material since it exhibits a tetragonal $\bar{4}3m$ symmetry, which has been seldom used for other non-centrosymmetric NPs,

and which is generally not encountered in SHG-active biological macromolecules. This leads to an uncommon SHG polarization response of four-clover leafs like pattern, which arises due to the octupolar crystalline lattice of a zinc-blende CdTe QDs. This feature could be used as a signature of the NC presence even for a weak SHG intensities due to a small size of the QD,[4] additionally allowing for the distinction between nanoscatterer and the biological specimen.

IV.1.3.1 Analysis of the SHG polarization dependence

Analysis of the optical polarization of the radiated SHG field, divided into *x* and *y* components can be achieved by rotating the angle of the incident electromagnetic field $\bar{E}^{\omega}$ at the fundamental frequency ω. The applied model neglects depolarization and propagation effects associated with the dielectric material.[82] Therefore, the SHG response can be accounted for by the second-order polarization $P_i^{2\omega}$ oscillating at the frequency 2ω:[77]

$$P_i^{(2)}(2\omega) = \varepsilon_0 \sum_{j,k} \chi_{ijk}^{(2)}(-2\omega;\omega,\omega)\, E_j(\omega)\, E_k(\omega) \qquad \text{(III.21)}$$

where ε_0 is the vacuum permittivity, and $E_{j(k)}(\omega)$ is the amplitude of the $j(k)$ component of the excitation field at excitation frequency ω; *i*, *j* and *k* are the components of the second-order nonlinear optical susceptibility tensor $\chi_{ijk}^{(2)}$, associated with the Cartesian *x*, *y* and *z* axes of the laboratory frame. $P_i^{(2)}(2\omega)$ is obtained by rotating the second-order nonlinear susceptibility tensor $\chi^{(2)}$ of the CdTe structure in the (*X*, *Y*, *Z*) crystalline axes conventionally attached to $\bar{4}3m$ symmetry,[77] by the Euler set of angles $\Omega = (\phi, \theta, \psi)$ describing the NC orientation leading to a new (*X'*, *Y'*, *Z'*) crystalline frame, located inside the fixed (*x*, *y*, *z*) laboratory frame (see Figure IV-6).

In theory when the (*X*, *Y*, *Z*) frame of the $\bar{4}3m$ zinc-blende crystalline lattice of CdTe has exactly the same orientation as the (*x*, *y*, *z*) laboratory frame: $\Omega = (\theta = 0°, \phi = 0°, \psi = 0°)$ – no SHG signal can be observed, due to the fact that the incident optical electric field is probing a symmetrically oriented structure, illustrated on the top-view in Figure IV-7(d). Note that even

a small inclination in the lattice position appears as noncentrosymmetric to the incident field probing its structure, and leads to the appearance of the SHG signal (Figure IV-7(b)).

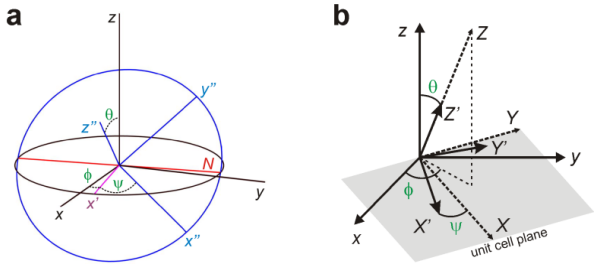

Figure IV-6 | a) Definition of the Euler set of angles $\Omega = (\phi, \theta, \psi)$, with respect to the fixed laboratory axis frame (*x*, *y*, *z*), where *N* is the line of nodes (perpendicular to both *z* and *z"* axis). b) Determination of position of the crystalline unit cell frame (*X'*, *Y'*, *Z'*) by the Euler angles in the fixed laboratory frame (*x*, *y*, *z*). The (*X*, *Y*, *Z*) axes relate to the starting position.

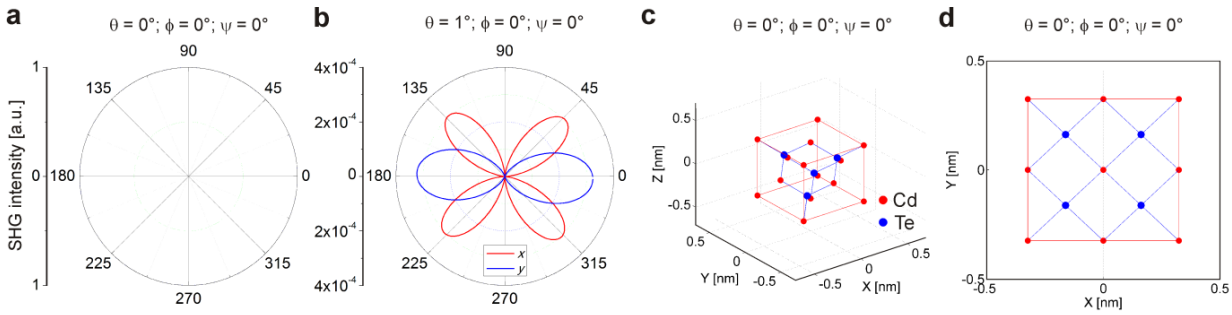

Figure IV-7 | Simulation results of the incident polarization dependent response of the SHG when the CdTe crystalline lattice orientation corresponds to the Euler set of angles at: (a) $\Omega = (\theta = 0°, \phi = 0°, \psi = 0°)$, and (b) $\Omega = (\theta = 1°, \phi = 0°, \psi = 0°)$, for which the crystalline lattice is minimally inclined. Note that the observed SHG signal pattern has very low intensity. c) Three-dimensional view on the CdTe crystalline single unit cell with crystal axis oriented according the laboratory axis frame $\Omega = (\theta = 0°, \phi = 0°, \psi = 0°)$, d) shows its top-view, corresponding to the orientation probed by the incident beam along the *z* laboratory axis.

In order to carry out the SHG polarization analysis of the spherical CdTe QDs we use the (*z*-*y*-*z*) Euler angles convention (for which the rotation matrix can be found in Appendix B.2). The $\bar{4}3m$ symmetry of the NC implies that only two electric field components along two different crystalline axes of the crystal structure, e.g. *X*, *Y*, couple to generate a SHG emission dipole along the third crystalline axis, i.e. *Z*. This feature translates in a polarization analysis of the SHG emission. The obtained response along *x* and *y* polarization analysis axes (see Figure IV-8) is significantly different from that with two leaves displayed by most known nonlinear NCs. Its four-fold clover leaf pattern (see Figure IV-8(a)) is a signature of the

perfectly octupolar character of the CdTe crystalline lattice. The latter, having non-zero diagonal elements in the second-order susceptibility tensor, exhibit a dipolar emission pattern corresponding very often to two lobes for one analysis orientation.

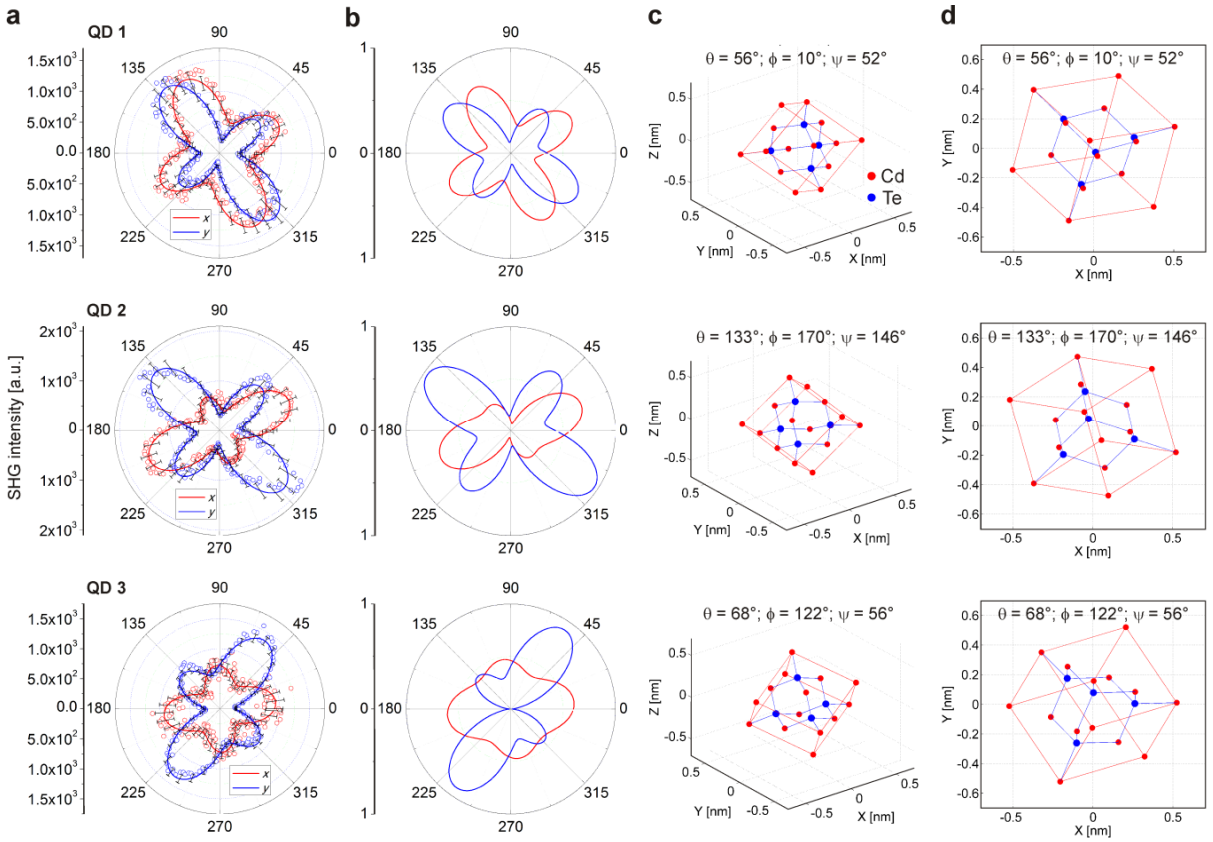

Figure IV-8 | Polarization analysis of the SHG obtained from three different QDs (1-3). a) Experimental results (scattered points) with inserted smoothing function (SF given with continuous lines) curves. b) Simulation results of the experimental polarization response, determining the orientation of the CdTe crystalline lattice (intensities are normalized to 1). c) Three-dimensional orientation of the CdTe single unit cell crystalline lattice, extracted from the simulation results. d) Top-view on the CdTe crystalline single unit cell presented on c) – this view corresponds to the direction probed by the incoming incident beam.

Simulations of experimentally obtained SHG signals (Figure IV-8(a)) by applying equation (III.21), allowed us to extract orientation dependent Euler set of angles Ω of CdTe QDs within ±5° error when comparing positions of the maxima. In practice, obtaining the fit of the experimental data is carried out using numerical calculations, following several steps of the simulation algorithm. In short, a simulation contains several steps, where the most important are:

1. smoothing the raw data traces using a general form of the SF function, which is directly related to the second-order nonlinear tensor, in order to obtain symmetrical positions of maxima and remove signal noise;
2. the obtained SF function is used as new input data and fitted by a similar function, which is directly related to the $\chi^{(2)}$ second-order nonlinear susceptibility of CdTe structure;
3. orientation of the CdTe crystalline lattice is obtained by multiplying the $\chi^{(2)}_{CdTe}$ tensor by the Euler set of angles $\Omega=(\phi,\theta,\psi)$, where the correct position is found during the scan over the full possible space of Ω, using criteria discussed in Appendix B. These criteria decide about a matching degree between both, experimental and calculated SHG polarization patterns.

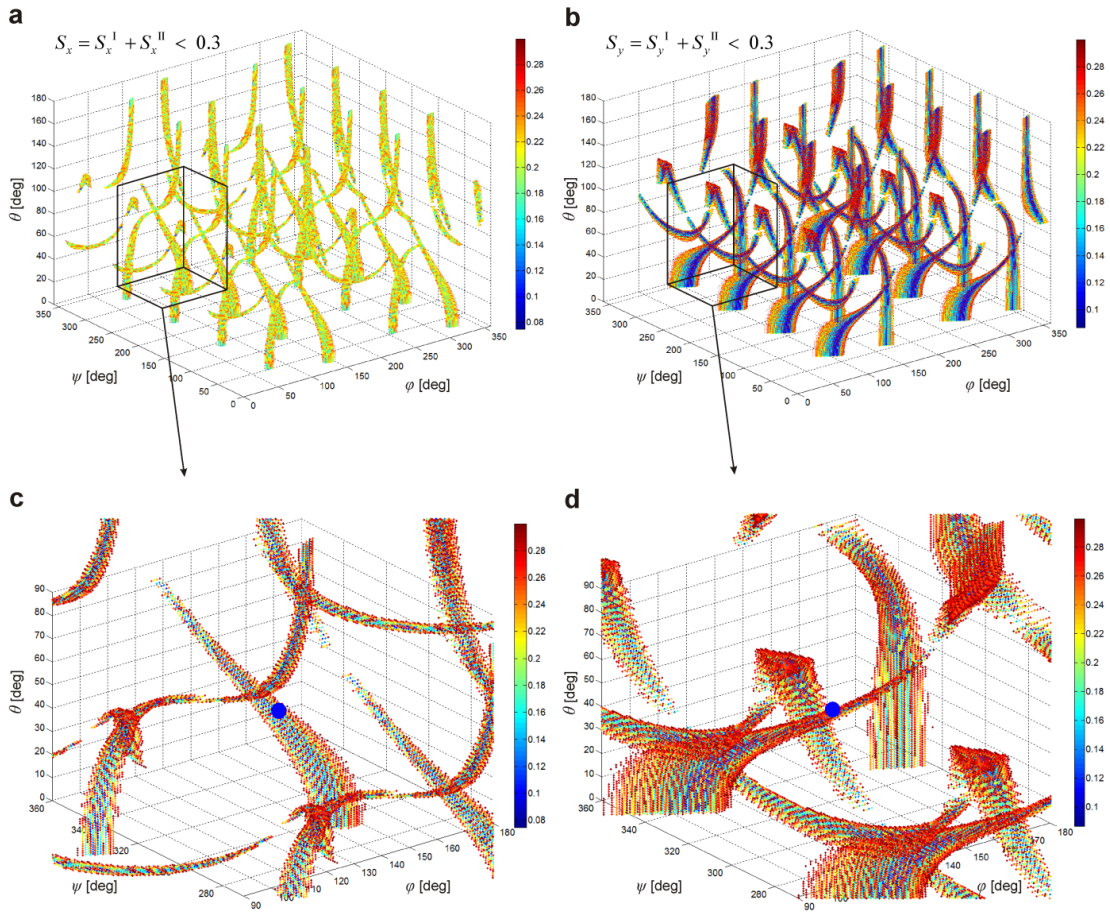

Figure IV-9 | Projections of all possible Ω angles, determined by the simulation program using the criteria of $S_{x(y)} < 0.3$, which correspond to the fit of QD1 experimental data (illustrated in Figure IV-8(a)) for both: *x* and *y* polarization components ((a) and (b), respectively). Optimized fits are obtained for smallest possible values of $S_{x(y)}$ (see the blue markers on (c-d)). The full range scans show eight repeated units of different combinations of Ω angles, for which comparable polarization responses can be obtained. Lower graphs (c-d) relate to marked single units areas of both polarization components.

IV.1.3.2 SHG polarization response with respect to the CdTe symmetry constraint

The results illustrated in Figure IV-8 prove, that the SHG polarization response is very sensitive to any variations in orientation of the crystalline lattice, thus opening the way to three-dimensional tracking of SHG-active NCs. However, due to the zinc-blende symmetry of the CdTe lattice, simulation analysis of its SHG polarization response may result in several different and not distinguishable orientations of the QD. In Figure IV-9 we show how the simulation program is scanning over the $\Omega=(\phi,\theta,\psi)$ space, in order to optimize the result (which is a fit of the QD1 response, illustrated in Figure IV-8) to define scan criteria. In this particular case we use $S_{x(y)}=S_{x(y)}{}^{\mathrm{I}}+S_{x(y)}{}^{\mathrm{II}}>0.3$ criterion which significantly minimizes the error in matching calculation with the experiment (Appendix B.1.4). These lead to eight repeated units for corresponding optimal results. Further narrowing the criterion by introducing a more strict function $S_x+S_y+S_{xy}$ results in six similar polarization responses obtained in comparable Ω range as in Figure IV-9, further summarized in Table (IV-I). These three pairs of different crystal orientations (shown in Figure IV-10) reflect intrinsic symmetries with respect to the *X'* crystalline axis, obtained after rotation by the ϕ angle. Due to these symmetry properties, obtaining the three-dimensional orientation of the crystalline lattice needs an additional technique, which is defocused imaging.[1,90,119] This technique provides an information about the orientation of the emitting dipole in the (*x*, *y*) plane, and determines its deviation angle from the *z* axis of the laboratory frame, as illustrated in Figure IV-10(c). Here we did not measure the defocused imaging response experimentally; however, in order to prove the symmetry constraint of the polarization response, we have investigated this analytically for the three pairs of different sets of Ω angles, which basically result in the same polar graphs. Calculated defocused imaging patterns of the SHG emitting dipoles are illustrated in Figure IV-10(c). The results obtained for each pair of polar graphs exhibit mirror-reflected like distribution of the SHG emission patterns, with symmetrical positions of their maxima. These lead to the conclusion, that for the same ϕ angle, the two θ angles are symmetric with respect to 90° (which is in agreement with the equivalence between θ and $180°-\theta$). A similar symmetry effect is observed for the ψ angle of each pair of polar graphs with respect to the 45° (related to the equivalence between ψ and $90°-\psi$).

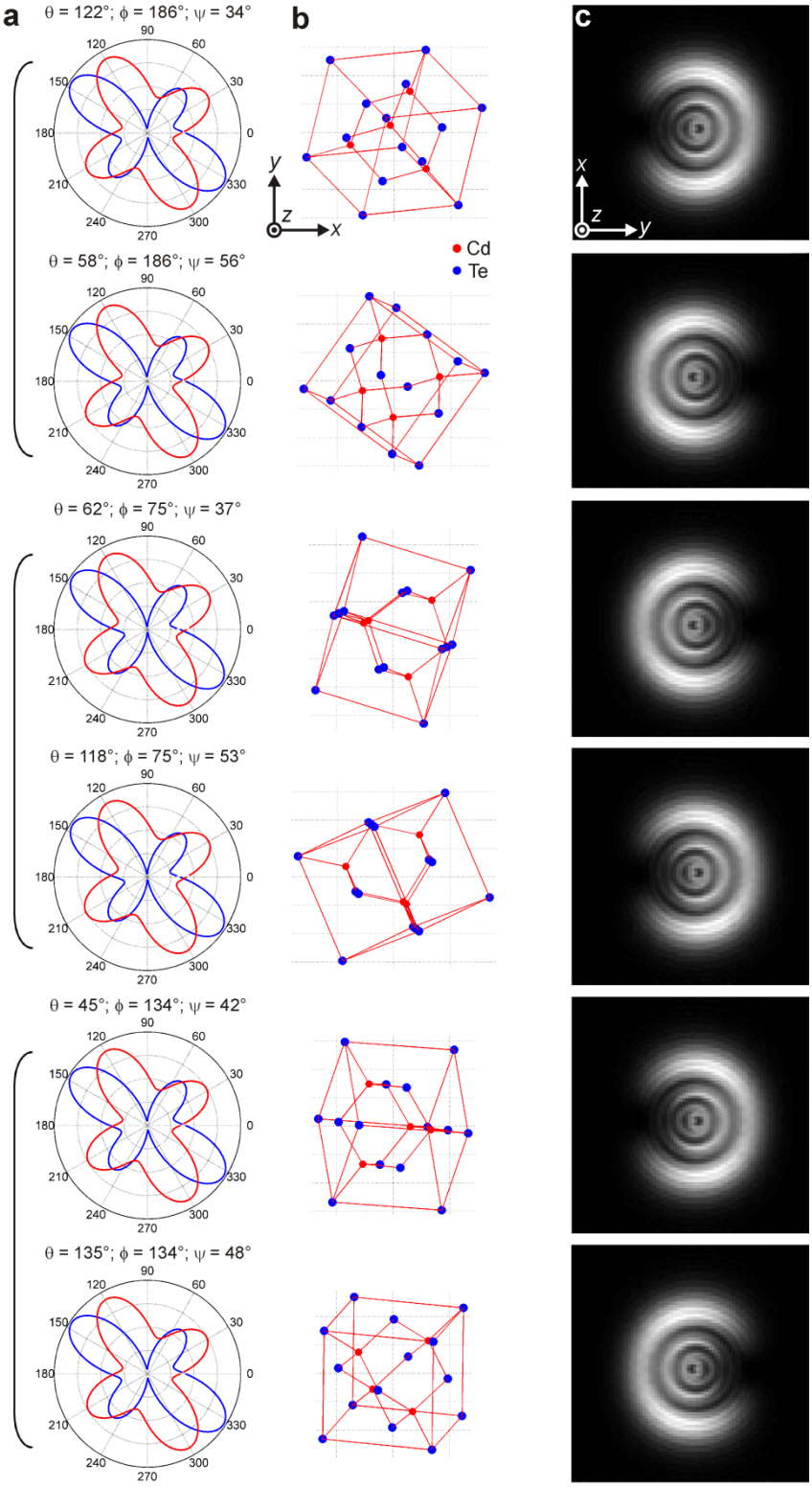

Figure IV-10 | a) Three pairs of simulation results (fits corresponding to QD1, shown in Figure IV-8), with the same values of ϕ angle for each pair. b) Corresponding orientations of the CdTe crystalline lattice, and c) calculated defocused images of the emitting dipoles. All figures are referred to the laboratory frame.

Table (IV-I): Six polarization response fits obtained for $S_x + S_y + S_{xy}$ simulation criteria, corresponding to QD1 experimental data.

Fit	$\Omega = (\phi, \theta, \psi)$	$S_x + S_y + S_{xy}$
a	186, 122, 34	0.7040
b	186, 58, 56	0.7040
c	75, 62, 37	0.7103
d	75, 118, 53	0.7103
e	134, 45, 42	0.7145
f	134, 135, 48	0.7145

These results appear as a limitation in orientational tracking of single NCs, due to the number of possible crystalline orientations resulting in the same SHG polarization response. These can be obviously narrowed down by defocused imaging, with the inconvenience of longer acquisition times. On the other hand, a possible solution may be found in limiting the freedom of motion of the NC itself, by attaching additional specimen to its surface, e.g. rod-like crystal with a heterojunction between both structures, as in the case of rod-on-dot (RD) CdTe/CdS QD heterostructures,[8] or biological specimen, e.g. complex protein molecule.

IV.2 SHG from single rod-on-dot CdTe/CdS heterostructures

The previous subsection dealt with SHG emission from single dot-shaped CdTe/CdS core-shell QDs using the TPSM technique. The strong second-order nonlinearity of the CdTe core with a large nonlinear coefficient d_{14} up to 200 pm V^{-1},[5] due to its non-centrosymmetric, tetrahedral zinc-blende crystalline lattice,[77,94-95] allowed for downsizing QDs to a 10-15 nm diameter, while maintaining a strong SH emission, in the range of 7.5×10^4 cts s^{-1} from a single spherical QD. This was achieved with standard 100 fs pulses of near infrared (NIR) laser light at 80 MHz repetition rate. The observed SH emission is polarization-sensitive, tunable and satisfactorily photostable out of the one-photon resonance.[4] However, since these spherical CdTe/CdS core-shell QDs are composed of a 7-13 nm diameter CdTe core over-coated by a three monolayer's thick CdS shell (approximately 1 nm thick), the observed SH emission results mainly from the scattering process inside the volume of the octupolar – like CdTe crystalline lattice. The contribution of CdS shell to the different SHG field (when considered with classical additive rules for second harmonic generation from nanoscatterers) is then assumed to account for less than 10%, and can be neglected when simulating the total SHG

field. Besides, it was also unclear if such a thin layer of CdS, grown on the zinc blende-like CdTe core is well formed, and deprived of crystalline defects, which could possibly influence the bulk wurtzite nonlinearity. Therefore, the total SH emission was considered to originate only from the CdTe core, resulting in a good agreement between the experimental SHG polarization analysis and the theoretical model (see Subsection IV.1.2).[4]

The high potential of SC heterostructures in the field of efficient nanoscale light sources stems from the sensitivity of their optical properties, at both linear and nonlinear levels to modifications of their size, shape and material composition, providing the possibility to control and engineer. This flexibility results from quantum confinement, which strongly determines the density of states and hence the QDs optical properties.[10,24] Significant advances in the field of nanoparticle synthesis has enabled fabrication of increasingly complex NPs, such as various core/shell heterostructures,[40-42,49] anisotropically shaped or branched NPs containing different semiconducting materials,[48,120-123] metal oxide – semiconducting quantum rods,[52] and semiconductor-metal nanocrystal heterostructures.[7,124] State-of-the-art techniques in the development of complex nanoscale objects provide the possibility to engineer the nonlinear properties of these structures. These properties would reflect the combination of tensorial optical responses from different assembled hybrid heterostructure components according to the precise structural engineering guidelines:

$$\chi^{(2)}_{hybrid} = \chi^{(2)}_{sym1} + \chi^{(2)}_{sym2} + \chi^{(2)}_{sym3} + ... \qquad \text{(III.22)}$$

where $\chi^{(2)}_{hybrid}$ is a third rank tensor of the second-order nonlinear susceptibility of the whole hybrid heterostructure, composed of susceptibilities corresponding to different constituent parts and the related materials with specific symmetries $\chi^{(2)}_{sym1(2,3,...)}$. This approach is of interest for matching the nonlinear nanometric size sources, e.g. their linear and nonlinear electromagnetic radiation, to any particular application in high resolution optical microscopy. This leads to explore semiconductor-semiconductor hybrid nanostructures in order to tailor their optical nonlinearities.[8]

In this subsection we report on nonlinear scattering from single hybrid SC QDs where the nonlinear emission is controlled through the choice of QD materials and their geometrical parameters. As a proof-of-principle concept validating experiment we consider RD quantum confined heterostructures made of two SC materials: CdTe and CdS, each having a different crystalline structure (zinc blende corresponding to the $\bar{4}3m$ point group symmetry for CdTe,

and wurtzite with its 6*mm* point group symmetry for CdS), nonlinear susceptibility tensors and spatial geometry (quantum dot and quantum rod, respectively) leading to:

$$\chi_{RD}^{(2)} = \chi_{\bar{4}3m}^{(2)} + \chi_{6mm}^{(2)} \tag{III.23}$$

Detailed description of the morphology of these RD QDs (Chapter III, Subsection III.4) shows obvious geometrical differences compared to previously described dot-shaped CdTe/CdS QDs. Thus, the complexity of the RD NCs leads to several implications on their nonlinear properties, arising from the innovative geometry of such hybrid NPs. The consequences on SHG studies described further, e.g. analysis of the SHG polarization dependency, require knowledge on mutual orientation of the CdTe core with respect to the CdS rod structure.

A diluted sample containing isolated CdTe/CdS RD QDs was studied with the same TPSM setup, which has been used before for SHG emitting spherical CdTe/CdS QDs studies. Examples of *epi*-detected diffraction limited and well-contrasted SHG spots (FWHM ~290 nm), obtained by scanning the sample containing isolated RD NCs are shown in Figure IV-11. Because of their geometrical features (described in details in Paragraph 3.4.2, or in the Ref. [8]) and low thickness of the PMMA host-matrix (~30 nm), RD NCs were expected to lie on the surface of the sample. Thus localization of the single emitters exhibiting dipolar-like emission pattern required scanning the sample with different angles for the incident polarization. To skip this inconvenience, the excitation beam was first circularly polarized in order to minimize the dependence of the SHG intensity on random RD QD orientations. This allowed for efficient localization of all the emitters within the range of the scan. Further studies of single isolated RD QDs required more precise angular characterization of the NC dipole orientation by performing polarization analysis. Figure IV-11(a, b) shows differences in a SHG intensity for the same dot, obtained with the circular incident polarization, in contrast with linear polarization oriented along the dipole – extracted from the polarization analysis (Figure IV-12(c)), and resulting with an approximately 30% higher SHG emission intensity. Both scans were obtained at 890 nm, with the incident excitation power P_{exc} = 3.0 mW, leading to a focused pulse peak intensity of about 94.4 GW cm^{-2}.

IV.2.1 Special features of SHG emission from rod-on-dot QD heterostructures

Figure IV-12(d) shows SHG emission signal traces observed with/without spectral filtering of an eventual TPEL contribution. Very small fluctuations observed when the whole spectral range is collected, indicate simultaneous emission of SHG together with a very low amount of TPEL photons, which can be neglected in as much as it does not reduce the SHG intensity. This opens very an interesting perspective on the emission photostability, especially when RD QDs are compared with dot-shaped QDs described before, highlighting the importance of the CdS shell and its good quality, as well as quantum confinement effects. Our findings show that signals obtained from purely SHG emitting RD NCs (Figure IV-13(a)) show a high degree of photostability over a long exposure time, even when doubling the intensity of the excitation in comparison with signals obtained with P_{exc} = 3.0 mW of incident excitation light (at λ_{exc} = 890 nm). We observe here again, an inverse correlation between the intensity of TPEL from these QDs and their photostability. Hence, a high TPEL yield, photostability of the SHG emission is strongly reduced, as shown in Figure IV-13(b). Reduced photostability of some RD QDs exhibiting stronger band-edge luminescence is probably due to induced excited state absorption at the excitation frequency. Due to the CdS monolayer which transforms into a QR on one facet, geometrically well defined RD QDs exhibit improved performance for charge separation, preventing their short times scale radiative recombination, and allowing for longer coherence times of the electron–hole exciton pairs.

Examples of the emission spectra illustrated in Figure IV-14, recorded at different excitation frequencies between 850 – 950 nm, show about 3.8 nm narrow (FWHM) line-width peaks of SHG, and exhibit high signal-to-background ratio. The second-order character of the SH emission is confirmed by the quadratic dependency on the incident power of the excitation laser light, measured in a power range from 1.0 – 7.0 mW until the SH emission starts to fluctuate strongly due to photo-induced damages of the crystalline structure (Figure IV-15).

In order to obtain a high SHG signal intensity from photostable RD NCs (where the TPEL yield is close to zero) it is not necessary to use such a high excitation power. For 3.0 mW of λ_{exc} = 890 nm (when polarization of the incident optical electric field is oriented along the dipole moment of a single RD QD) we observed a signal intensity of about 7×10^4 cts s^{-1} (shown in Figure IV-13(a)), as strong as the typical luminescence level from bright QDs, de-

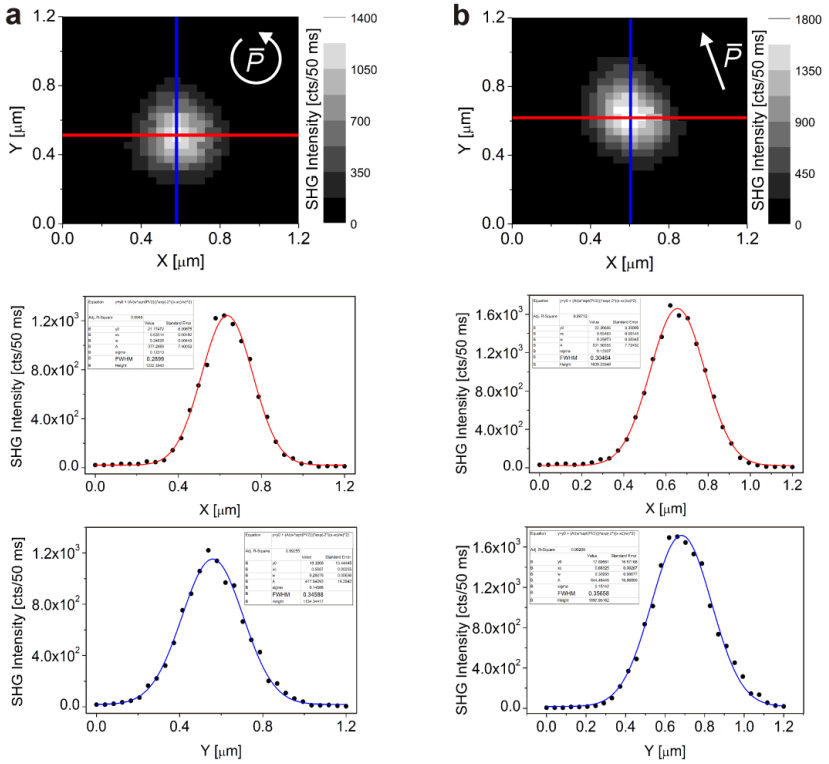

Figure IV-11 | Scans of SHG spots obtained for the same single rod-on-dot CdTe/CdS heterostructure with: a) circular incident polarization, and b) linear incident polarization oriented along the emission dipole (characterized on the polarization plot – Figure IV-12(d)). Corresponding cross-sections (organized in columns, where red is a horizontal and blue is a vertical direction) were fitted using a gaussian function, and show average FWHM value about 290 nm, close to the diffraction limit.

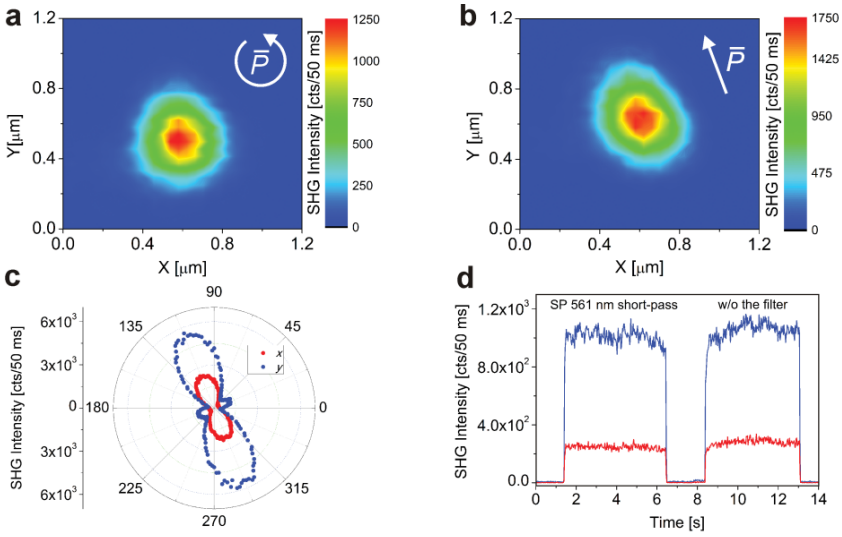

Figure IV-12 | Smoothed scans of the SHG Gaussian-like signal distribution, obtained from the same single rod-on-dot CdTe/CdS heterostructure (also presented in Figure IV-9) with: a) circular incident polarization, and b) linear polarization oriented along the dipolar emission pattern. c) Polarization analysis showing dipolar-like SHG emission pattern, oriented at +110 °. d) SHG signal traces (red and blue correspond to *x* and *y* polarization components, respectively) showing differences in the intensities and photostability when low amount of TPEL photons is collected, or spectrally removed (by a high transmission > 96% short-pass filter cutting at 561 nm).

spite the relatively low quantum efficiency of the APDs in the blue range: ~28% at 445 nm (at ambient temperature). Taking into account the transmission of the collection optics as well as the detection efficiencies, this corresponds to the SHG cross-section of the order of 50 GM. Correction by the APDs efficiency would give a corresponding SHG photons count rate of ~9×10^4 cts s^{-1}, illustrating the real photon flux at the detectors. This surprisingly high value of the count rate was obtained from ~ 18 nm long RD NC hybrid (CdTe core 6 nm diameter and 12 nm long / 3 nm wide CdS rod), having a volume of about 113 nm^3 for the CdTe core and 85 nm^3 for the CdS rod, so that the total volume of about 198 nm^3 is nearly six times smaller than that of spherical CdTe/CdS core/shell QDs (~1150 nm^3 for 13 nm diameter QDs).[4,8] It is however important to mention, that excitation at λ_{exc} = 890 nm for this particular RD NC does not involve the highest possible SHG cross-section. Therefore, investigation over the SHG wavelength dependency (blue trace in Figure IV-16) for particular RD NC evidences the high potential for this type of material as efficient nonlinear light sources.

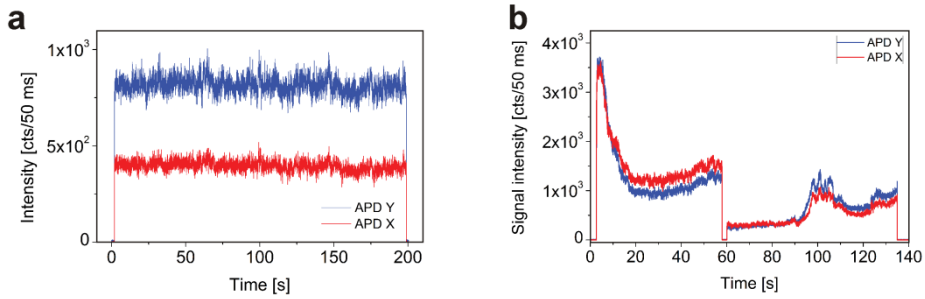

Figure IV-13 | a) Signal intensity trace observed for purely SHG emitting RD QD with a high degree of photostability. Observed signal have been obtained with λ_{exc} = 890 nm (3.0 mW). b) Decay of the SHG signal intensity trace (including 20 nm narrow TPEL background) and its fluctuations, observed from a RD QD exhibiting strong TPEL yield. The SHG has been obtained with λ_{exc} = 890 nm and an incident power of 2.0 mW. Spectral separation of the SHG signal from the TPEL was obtained by a 445 ±10 nm band-pass filter.

Measured in conditions guaranteeing a high level of photostability (without phase-matching requirements), and corrected following the same procedure as described in Appendix A, the presented curve provides comprehensive information about spectral regions for optimized two-photon cross-section within the excitation range (currently limited by the setup capabilities). Excitation at λ_{exc} = 925 nm instead of λ_{exc} = 890 nm would then result with a nearly 50% higher count rate, then reaching 1.1×10^5 cts s^{-1}. SHG obtained with that excitation frequency could be also detected with higher accuracy by Silicon-based APDs, due to their improved detection efficiency at green.

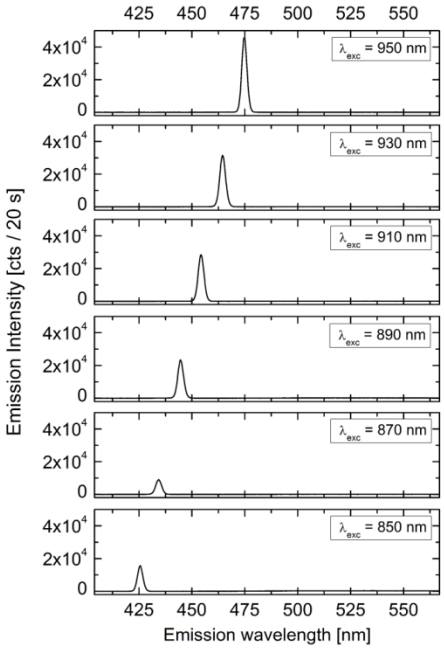

Figure IV-14 | Set of SHG emission spectra obtained from a single rod-on-dot CdTe/CdS heterostructure showing drift of the SHG peak (FWHM ~3.8 nm) when the excitation wavelength is tuned from 850 nm to 950 nm. Intensities of the SHG peaks were not corrected by the transmission factors.

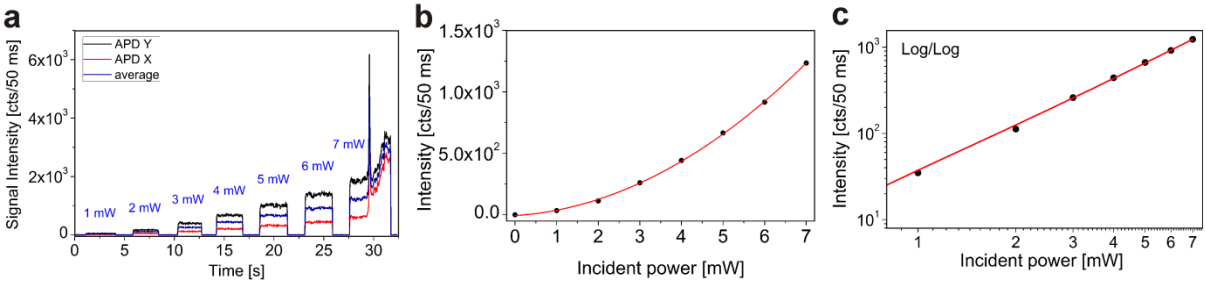

Figure IV-15 | a) Signal traces recorded for different incident power from 1-7 mW at 890 nm excitation wavelength (black and red traces correspond to *x* and *y* polarization channels respectively, while the blue trace show their averaged values). Strong emission fluctuations appearing at 7 mW are clearly visible. b) Quadratic dependence of the SHG emission intensity on the incident excitation power – data points were extracted from the averaged signal traces (a) by the linear approximation of their 'flat' parts. c) Quadratic dependence of the SHG emission intensity in logarithmic scale.

The SHG emission intensity (Figure IV-16) reflects an effective nonlinear coefficient $(\chi^{(2)}_{RD})^2_{eff}$, which corresponds to the squared second-order nonlinear susceptibility for the entire heterostructure. As can be expected from a system with a discrete energy level spectrum, it exhibits multiple peaks. The real meaning of peaks appearing on the excitation spectra has been briefly discussed in Paragraph IV.2.1 in the case of spherical core/shell CdTe/CdS dots (placed here for comparison, see open-black trace). As in the previous case, an optimal

excitation wavelength appears at about 925 nm (blue scattered signal trace), corresponding to 1.34 eV. It is, nevertheless, significantly blue-shifted by 45 nm (~0.06 eV) with respect to the peak position for larger spherical CdTe/CdS QDs (open black signal trace), with a maximum at 970 nm (1.28 eV), as could be expected due to the stronger carrier confinement.

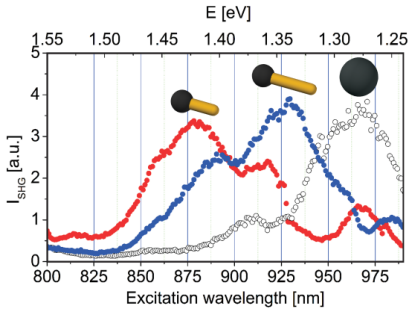

Figure IV-16 | Excitation spectra showing wavelength dependence of the SHG intensity observed from two different size for RD QDs (red and blue traces), using linearly polarized excitation light along their dipoles. The open-black trace represents averaged signal obtained from four different spherical core/shell CdTe/CdS QDs, placed here for comparison.

Despite the fact that the slope of the blue excitation spectrum in Figure IV-16 corresponds to the averaged curve, obtained for spherical QDs, the red scattered dots trace, however, shows slightly different features. It is difficult to analyze and consider this result with respect to what has been discussed above without statistical studies. It is nevertheless expected to reflect the stronger quantum confinement effect from a slightly decreased QD size. The obtained curve has three clearly distinguishable maxima at 858, 880 and 918 nm, and two other maxima with low SHG cross-sections at about 818 and 968 nm. At first sight the highest SHG cross-section peak at 880 nm appears as the maximum, which completely changes spectral dependence of this response. However, if we consider it as directly corresponding to previously discussed highest peaks at 925 and 970 nm (for the RD and for the spherical QDs, respectively), then it may result from a smaller RD NC. Thus RD QDs structural inhomogeneity, especially variations in the CdTe core diameter and CdS rod length reflecting in different CdTe/CdS volume ratio (see Figure II-11), can efficiently tune the spectral features thus allowing to optimize the SHG emission intensity. Tunable and high SHG cross-section peaks are then available even from smaller RD QD heterostructures, leading to signal count rates of the order of ~9.8×10^4 cts s^{-1}, when excited at the optimal frequency of 880 nm, using the same excitation power as for much larger QDs.

Understanding why, for smaller RD QDs the observable signal is still strong despite a reduced volume is a crucial issue, entailing two possible origins for that effect. For larger SC NPs - like intermediate confined ~12 nm diameter CdTe QDs, the level spacing is tighter, so when excited close to the resonance they exhibit more rapid decoherence via longitudinal optical (LO) phonons, which may lower the SHG QY. Shrinking the size is expected to reduce decoherence, because intraband level spacings are larger for smaller QDs, thus decoherence by exciton-phonon coupling should be slowed down. A second possible origin can arise from the charge separation in the quasi–type–II RD hybrid structure, such as RD CdTe NPs. Reduced decoherence is most probably due to the separation between the hole localized inside the CdTe core and the electron delocalized in the heterostructure. Such an effect has been reported for enhanced spin coherence times in CdSe/CdTe type-II rod-like heterostructures by the group of Scholes, where charge separation has reduced the relaxation rate by one order of magnitude.[125]

IV.2.2 Polarization analysis of the SHG emission of rod-on-dot CdTe/CdS QDs

One of the distinct and foremost advantages arising from the SHG process of nanoscale scatterers is undoubtedly its high sensitivity to the polarization of the incident optical electromagnetic field $\bar{E}^{\omega}$. This enables to probe the spatial orientation of the scatterer with respect to the laboratory frame. Such experiments have been successfully conducted with both single-material inorganic and organic NCs, where the SHG response originates from a regular crystalline lattice (where it is relatively easy to analyze the experimental polarization response from a theoretical point of view).[1-2,4,88,116]

Nevertheless, the morphological complexity of the RD QD heterostructures, leads to several implications arising from the new geometry and physical features of such newly engineered hybrid NPs. Indeed, analysis of the SHG polarization dependency requires taking into consideration a precise definition of the mutual geometrical relations between the CdTe core and the CdS rod, which have been described in detail in Subsection III.4.

Decomposition of the *x* and *y* components of the optical polarization response of the emitted SHG field is achieved as a function of the rotation angle of the incident electromagnetic field $\bar{E}^{\omega}$ at the fundamental frequency ω, using the same method already

exposed for dot-shaped CdTe QDs. The RD NC response can thus be specified by a single $\bar{P}^{2\omega}$ dipole oscillating at the 2ω frequency, as described by the equation (III.21). $P_i^{2\omega}(2\omega)$ is obtained by the rotation of the second-order optical susceptibility tensor $\chi_{RD}^{(2)}$ of the overall RD NC structure from the (X, Y, Z) crystalline axes defined by the Euler set of angles $\Omega = (\alpha, \beta, \gamma)$ into the laboratory frame using the (*z*-*y*-x) convention (described in Appendix C.2). In the simplest approximation, $\chi_{RD}^{(2)}$ results from the rotation of two tensors:

$$\chi_{CdTe}^{(2)} = 2\begin{bmatrix} 0 & 0 & 0 & d_{14} & 0 & 0 \\ 0 & 0 & 0 & 0 & d_{14} & 0 \\ 0 & 0 & 0 & 0 & 0 & d_{14} \end{bmatrix} \quad \text{(III.24)}$$

$$\chi_{CdS}^{(2)} = 2\begin{bmatrix} 0 & 0 & 0 & 0 & d_{15} & 0 \\ 0 & 0 & 0 & d_{15} & 0 & 0 \\ d_{31} & d_{31} & d_{33} & 0 & 0 & 0 \end{bmatrix} \quad \text{(III.25)}$$

assigned to the $\bar{4}3m$ and $6mm$ symmetry point groups respectively, where we assume d_{14} = 64.0 pm V^{-1} (see Subsection V.2.2), d_{15} = 44.0 pm V^{-1}, d_{31} = 40.2 pm V^{-1}, d_{33} = 77.9 pm V^{-1}.[5,77]

Inspection of the experimental data obtained for three differently oriented RD NCs (Figure IV-17(a)) evidences very high sensitivity of the polarization response with respect to the orientation of the $\chi_{RD}^{(2)}$ tensor, determined by the spatial position of the hybrid heterostructure lattice. The excellent agreement between the fits (Figure IV-17(b)) and the raw data is a most reliable indication of the single dot origin of the harmonic signal, ruling out the occurrence of complex crystalline multiple NC clusters or aggregates, thus opening possibilities for precise determination of the corresponding spatial orientation of both CdTe core and CdS rod crystalline structures. In order to obtain their orientations we have taken into account the mutual relations between both lattices, using the model subsequently leading to expression (III.26). Generated three-dimensional projections (Figure IV-17(c,d)) of hybrid RD NC lattices corresponding to the orientations of experimentally scanned RD NCs, seen from the top view of the *x*, *y* laboratory frame, display the mutual positions of the CdTe and CdS lattices. It is clear that the orientation of the dipole is determined by the $[0001]$ axis of CdS oriented along the rod axis. In each case, the out-of-plane deviation (described by the angle β

between the CdS $[0001]$ axis and the $\{x, y\}$ plane) is lower than 45°, which to some extent was forced by the spin coating conditions resulting in ~30 nm thick PMMA host-matrix, where the RD NCs were expected to lie on the surface. However, our model (described in Subsection IV.3.2.1) can also consider the less frequent case of NPs with nearly vertically oriented rods.

IV.2.2.1 Simulation model for polarization analysis of RD QD heterostructures

In order to obtain a direct expression of the second-harmonic polarization response from a hybrid RD NC consisting of two different materials, we use a linear combination of components of the CdTe and CdS second-order susceptibility tensors, weighing their respective contribution by a fractional volume factor: $\chi^{(2)}_{RD} \propto \chi^{(2)}_{CdTe} + V_{CdS} \cdot V_{CdTe}{}^{-1} \chi^{(2)}_{CdS}$.

The volumes of the spherical CdTe core and of the cylindrical CdS rod are evaluated by considering the shape of each part from TEM-based histograms of the size distribution (see Figure II-11) with the diameter of the CdTe core D_{CdTe} = 6.0 nm and the diameter of the CdS rod D_{CdS} = 3.0 nm. The length of the rod is treated as a variable, and its impact on the total SHG response is analyzed below. The contribution of SH fields generated from both materials to the total SHG field emitted by a single RD scatterer: $E^{SHG}_{scatt} \propto \frac{\partial^2}{\partial t^2} P^{(2)}_{SHG}$ requires consideration of coupling and eventual occurrence of the interference effects (either constructive or destructive as presented in Figure IV-18 by means of '+' and '–' symbols respectively) occurring between SHG fields from both sources. Thus the SHG intensity $I^{SHG}_{total} \propto \left| E^{SHG}_{scatt} \right|^2$, resulting from a linear combination of the second-harmonic fields can be obtained from the following expression:

$$\left(I^{SHG}_{total}\right)_i = \left(I^{SHG}_{CdTe} + I^{SHG}_{CdS} + I^{SHG}_{Interference}\right)_i \propto$$
$$\propto \sum_{jklm} \left[\chi^{(2)CdTe}_{ijk} \chi^{(2)CdTe*}_{ilm} + v^2 \chi^{(2)CdS}_{ijk} \chi^{(2)CdS*}_{ilm} + v\left(\chi^{(2)CdTe}_{ijk} \chi^{(2)CdS*}_{ilm} + c.c. \right) \right] E^{\omega}_j E^{\omega}_k E^{\omega*}_l E^{\omega*}_m \quad \text{(III.26)}$$

where $v = V_{CdS} \cdot V_{CdTe}{}^{-1} = 3 D_{CdS}{}^2 L_{CdS} \left(2 D_{CdTe}{}^3\right)^{-1}$ is the volume ratio between CdS and CdTe, of the order of unity for the RD QD heterostructures reported here.

This pointwise additive model, when applied separately to both *x* and *y* polarization components, allows for quantitative analysis of the SHG intensity components described by equation (III.26) accounting for the total SHG intensity emitted by the whole hybrid crystalline structure. Figure IV-18 shows an example of such decomposition, conducted for different fits of experimentally obtained results. A fit takes into account three Euler angles: $\Omega = (\alpha, \beta, \gamma)$ (determined by the *z*-*y*-*x* convention), and the relative volume via the length of the rod as a free parameter. Other parameters (diameter of the CdTe core and width of the CdS rod) are set at the values obtained from TEM images in a simple mean value model (Figure II-11). Constructive or destructive interference terms, pointed-out in Figure IV-18 by '+' and '–' symbols, respectively are given with the absolute values for the clarity, thus the real shape of these curves being illustrated in Figure IV-19. Detailed description of the simulation algorithm for SHG polarization response from the RD heterostructures is provided in Appendix C.

IV.2.2.2 The role and impact of the CdS rod length into the total SHG intensity

Detailed studies of the CdS rod length dependence provides clear evidence of the significant contribution of this feature to the overall SHG response. The polarization response of the SHG emission from the CdTe core shows a characteristic fourfold cloverleaf pattern,[126-127] as expected from its octupolar $\bar{4}3m$ symmetry (see Paragraph IV.2.3).[4,128] Growth of the CdS rod changes this response progressively into a dominantly dipolar-like pattern. Extension of the rod leads to a progressive loss of additional maxima for each *x* and *y* component. This is imposed by the dipolar $6mm$ symmetry of the hexagonal form of CdS crystal.

The pointwise additive model has been used to visualize the evolution of the total SHG field upon lengthening of the CdS rod for three RD NCs (QD 1-3). Each dot was examined for five cases (see Figure IV-20): CdTe core with 6 nm diameter, RD NCs with different lengths of the CdS rod: 4, 8, 11-13 (corresponding to the experimental data), up to 20 nm, where the SHG emission pattern appears to be fully aligned along the CdS rod $[0001]$ axis, and without any sizable contribution of the CdTe core to the overall SHG response. It is clear that the appearance of even a short CdS rod, e.g. 4 nm long, changes the SHG pattern in a drastic manner as compared to the fourfold cloverleaf response obtained for the CdTe core.

In intermediary manner, the CdS rod significantly reduces the relative CdTe contribution, leading to approximately equal contributions of both materials when the rod reaches a length of ~8 nm (corresponding to $V_{CdS} \approx 57$ nm^3 versus $V_{CdTe} \approx 113$ nm^3), while longer 11 – 13 nm rods ($V_{CdS} \approx 78$ - 92 nm^3) privilege the dipolar character of the SHG polarization response and prevail over the octupolar core contribution. An overgrown 20 nm long rod completely transforms the SHG field into a quasi dipolar-like. Taking into account two facts, primarily that the number of emitted SHG photons is proportional to the squared volume of the emitter and, secondly, the higher *zzz* nonlinearity of CdTe over that of CdS, it appears that the interference term can have an equally strong constructive or destructive contribution (see Figure IV-18 and Figure IV-19). Based on our model (equation (III.26)) the interference term follows linearly the growth of the CdS quantum rod.

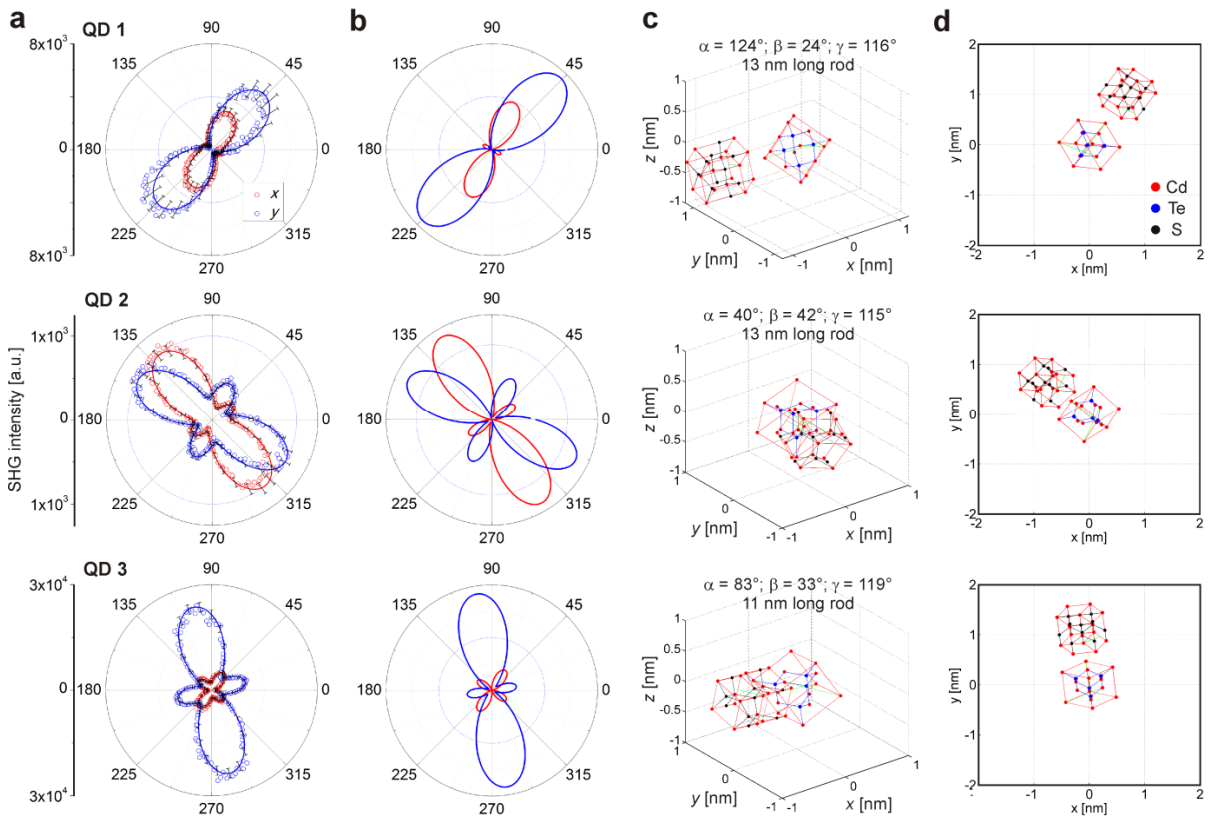

Figure IV-17 | a) Experimentally obtained polarization analysis of the SH emission observed for three RD NCs (QD1-3). Open scattered points represent the raw data, while line traces show smoothed functions (SF). b) Calculated fits of the experimental data smoothed traces. c) 3D projections of the RD crystalline lattice orientations, characterized by the Euler set of angles (in the *z*-*y*-*z* convention) with respect to the laboratory frame (*x*, *y*, *z*). d) Mirror-reflected (with respect to experimental setup configuration) top view of the 3D projections of RD QD crystalline lattices (perpendicularly to the probing incident optical electromagnetic field).

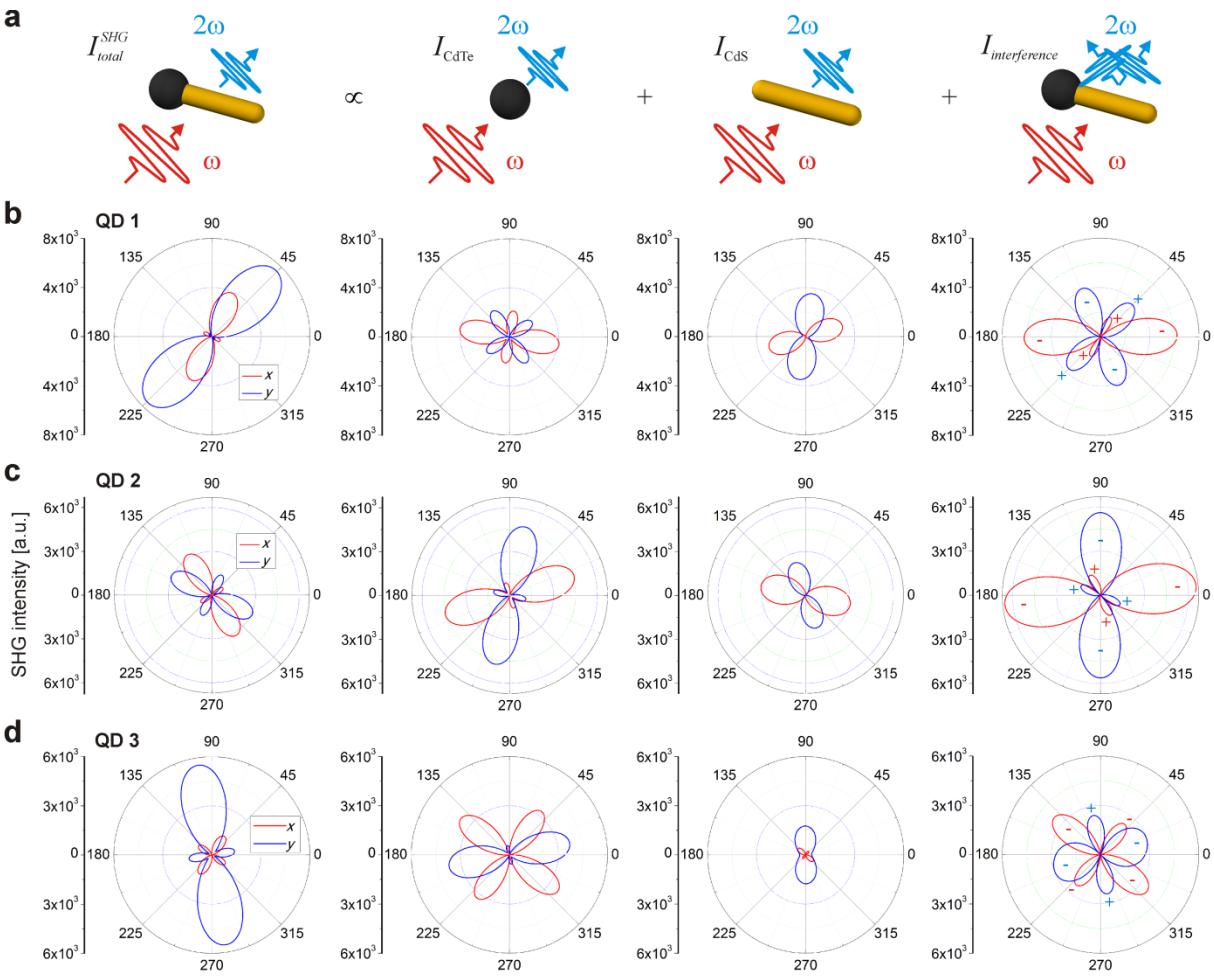

Figure IV-18 | Graphical illustration (a) and analytical analysis of the polarization response of decomposed total SHG intensity I_{scatt}^{SHG}, calculated for three differently oriented single RD NCs (b-d). Polarization plots showing contributions of the CdTe core, CdS rod and of the interference (positive and negative) term to I_{total}^{SHG} (fits of experimentally obtained results shown in Figure IV-17).

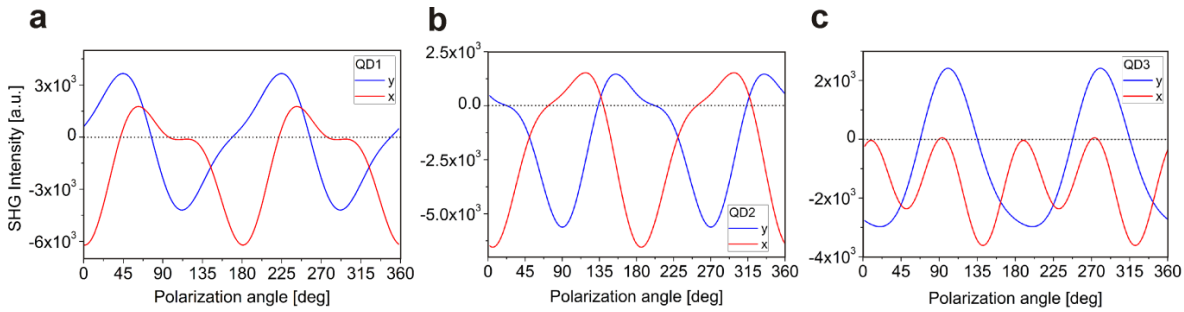

Figure IV-19 | Interference terms between two SHG electric fields: E_{CdTe}^{SHG} and E_{CdS}^{SHG} contributing to the total SHG field E_{scatt}^{SHG}, calculated for three (a-c) different RD NCs (QD1-3 respectively), maintaining a real negative values. Each plot corresponds to polar graphs showing absolute values of the interference terms, shown in the last column of Figure IV-18.

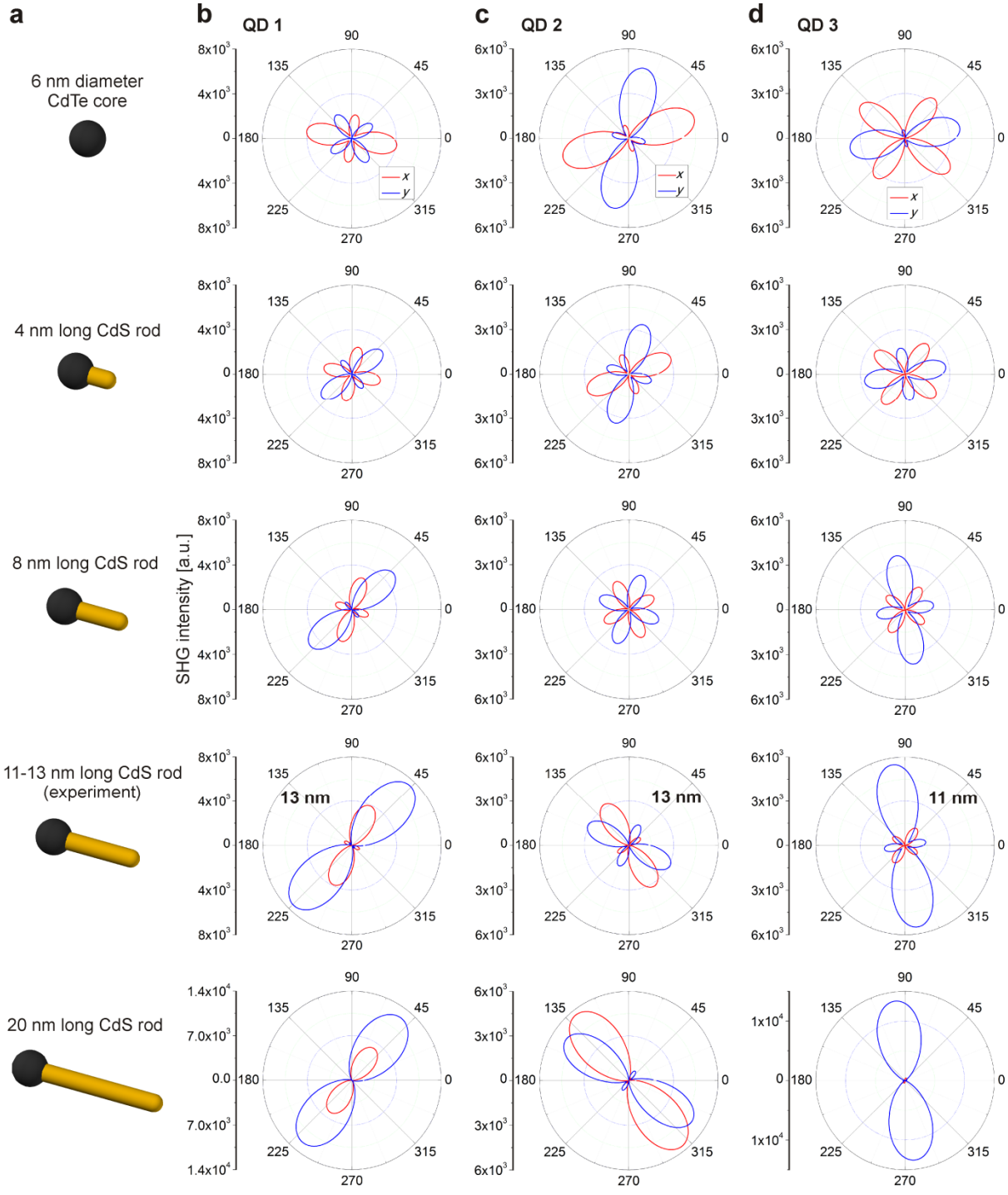

Figure IV-20 | a) Rod-on-dot NC cross-sections illustrating the growth of the CdS quantum rod in a range from 4 – 20 nm on a 6 nm diameter CdTe core. Columns b - d) represent calculated polarization responses of the SHG polarization patterns, obtained for three different RD NCs (with spatial orientation characterized in Figure IV-17), while growth of their rods is progressing. The fourth row corresponds to the experimentally obtained data.

IV.2.2.3 Errors in inferring the orientation of the crystalline lattice from SHG polarization analysis

Any quantitative discussion of the experiment-based simulation results requires a careful inspection of possible error sources. The first significant source undoubtedly comes from optical components inside the experimental setup, especially the dichroism and ellipticity dysfunctions from the dichroic mirror (γ_{DM} (890 nm) = 0.035; ϕ_{DM} (890 nm) = 2.8 rad) which effect the overall shape of the $P_i^{(2)}(2\omega)$ response, and have been indeed corrected.

Another source of error is associated with the signal noise or even with a small decrease of the signal intensity during the measurements (it is clearly visible, e.g. in case of QD1 in Figure IV-17), which deteriorates the simulation and distorts its result. To decrease this type of error and improve the simulation results we have used the raw data smoothing function - SF (defined in Appendix B), which leads to the same intensities for perfectly symmetrical maxima, and become a new set of input data for the simulation program. The SF error is characterized by the relative difference ratios in %, between the raw and smoothed *x* and *y* intensity maxima.

On the one hand applying the SF leads to the appearance of relatively small errors with respect to the raw data – in the worst case (QD1), it can be estimated at ±10.7% for the *x*, and +14.8%, -12.4% for the *y* component, while for much more regular raw data traces, e.g. QD2, QD3 it appears two times smaller. However, use of the SF significantly decreases the error of simulated fits – both in terms of maxima location and relative maxima intensities, providing well-fitted polarization response. Matching the raw data (or SF for higher efficiency) with the simulation fit - since it cannot be considered quantitatively - is determined from absolute differences, firstly in the maxima location (in °) on polar plots, and then in the relative maxima intensities of *x* and *y* components between SF and fit traces ($\Delta I(\%) = \left|\Delta I_{SF}(\%) - \Delta I_{fit}(\%)\right|$). Overall shapes of both polarization responses are additionally characterized by the relative shape difference S_{xy} (defined in Appendix B). The best fit was obtained for SF of QD1, showing its maximal displacements at about 0.7° (*x*) and 0.8° (*y*), with ΔI ~2.2% and the relative shape difference S_{xy} = 0.28. A relatively small error was obtained for SF of QD2, with higher maxima displacements of about 7.3° (*x*) and 3.14° (*y*), and lower maxima displacement by 2.7° (*x*) and 0.7° (*y*), while ΔI was estimated to be of the order of ~1.7% and ~4.1% for lower and higher maxima respectively (with a shape

difference S_{xy} = 0.14). The highest errors occurred for QD3, showing its higher maxima displaced by 4.6 ° (x) and 3.2° (y), and lower maxima displaced by 0.1° (x) and 4.9° (y) (ΔI ~28.3% for lower and ~0.7% for higher maxima; S_{xy} = 1.12).

A final significant source of error stems from the estimation of the length of the CdS rod used for the simulation process. Best fits (Figure IV-17(b), and the fourth row of Figure IV-20) were obtained for rods ranging from 11 – 13 nm, as expected. Simulation of QD2 data with rods varying in the range of 13 ±1 nm leads to ±1.5° of maxima displacements and about 4.0% higher ΔI. Minimization of that error allows for precise determination of the rod length, with an accuracy of ±0.5 nm.

The error on the out-of-plane orientation of crystalline lattices is estimated to vary within ±5° to ±10° range, which remains acceptable considering that it can be applied with capable accuracy even for RD NCs oriented close to the vertical direction.

IV.3 Accuracy of the polarization analysis from a reduced set of raw data points

Efficient and tunable coherent SHG emission, together with the small size of CdTe – based QD heterostructures studied here open a wide field of applications in bio imaging. Since the SHG response obtained from nanocrystalline materials is highly sensitive to their spatial orientation and morphology, which has been proved for both, spherical and rod-on-dot QD heterostructures,[4,8] a possible application would be three dimensional single NP tracking inside a cellular system. Such an experiment, however, requires fast collection of an efficient enough SHG signal, since the nanolabel is expected to be rotating as a result of its interactions with the cellular environment. Our samples exhibit high SHG signal-to-noise ratio, however, so far all the polarization measurements were performed with a small and therefore time consuming increment of 2° for the incident polarization angle (taking 180 s for a full turn), resulting in high precision for the experiment. Therefore, it is important to determine an optimal increment value, in order to shorten the measurement and acquire a polarization response with intense enough SHG signal level to allow for its processing.

As a proof-of-principle, we consider raw data with a more complicated polarization response of RD NC, including a noise level and unsymmetrical positions of the maxima. At first sight it may look simpler than typical response of the spherical dots (compare Figure

IV-8 and Figure IV-17), however, it is much more demanding for simulation processing due to the larger number of variables and nonlinear interaction terms between two different materials, such as CdTe and CdS. In our studies we determine orientation of the crystalline lattice by polarization analysis, where the experimental raw data is firstly smoothed using an analytical SF function, basing on the form of the SHG polarization response (described in Appendix B), corresponding directly to the SHG phenomenon. In order to eliminate the usually significant experimental noise, the corresponding maxima positions of the SF are determined by a nonlinear least square method, which leads to highly accurate fitting in further processing. Here we analyze how the decrease in number of exploited raw data points (which leads to shortening the probing time of the crystalline orientation) impacts on the shape of calculated SF and its error level, using the same integration time (1 s) for each raw data point. An example of such analysis for a few different increments is shown in Figure IV-21. The values of error dependence in the maxima positions of the SF for: 4°, 6°, 8°, 10°, 12°, 20°, 30°, 60° increments were determined with respect to the SF calculated for experimental results obtained with an increment of 2° (first row of Figure IV-21). Final results are displayed in Figure IV-22 and summarized in Table (IV-II).

Dependence of the maxima deviation error for each polarization component on the increment value, was estimated as a square root of the sum of squared errors values for both *x* and *y* components. Generated results (Figure IV-22) indicate an exponential character. The error value corresponding to the last point (60° increment) was estimated taking into consideration that all maxima have split into two (as shown in Figure IV-21). We have thus averaged the error value by dividing by a factor of two.

Our analysis reflects the accuracy and reliability of the applied SF in order to decrease number of raw data points and shorten the measurement time. We found that the optimal value for the increment can be set at 24°, which leads to 15 s for collecting of the raw data and results in a reasonable error of approximately 2.5°.

Table (IV-II): Maxima deviation error dependence on the increment and measurement time for the whole turn.

Increment [°]	2	4	6	8	10	12	20	30	60
Error [°]	-	0.21	0.52	0.15	0.90	0.54	2.73	3.59	24.27
Number of points (equals time [s])	180	85	60	45	36	30	18	12	6

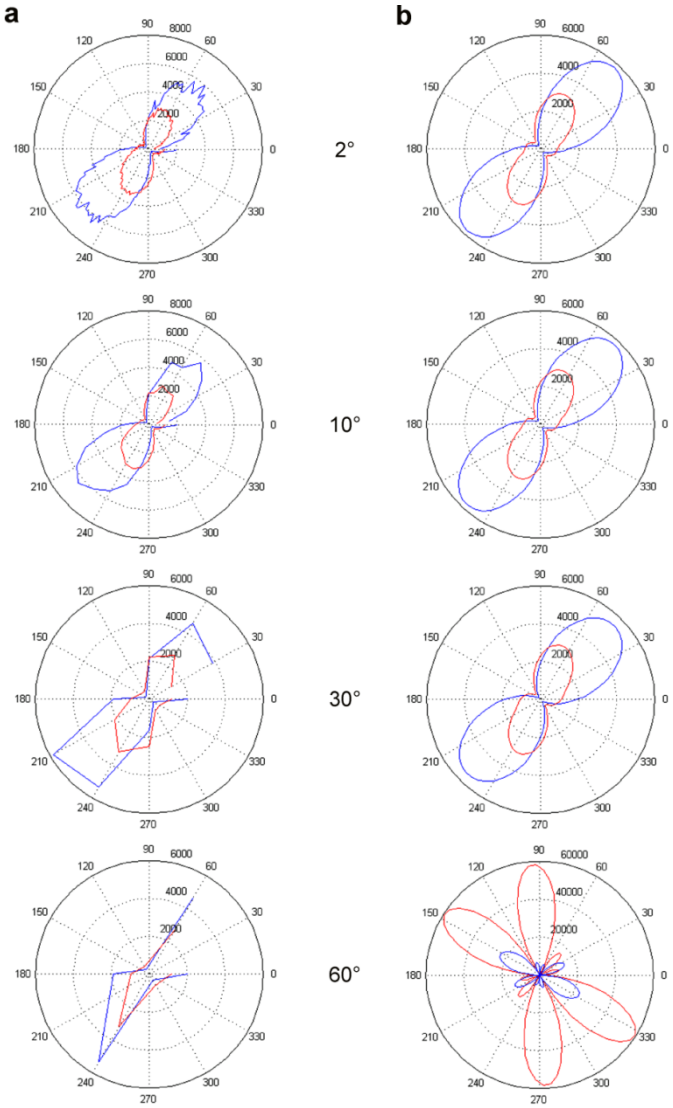

Figure IV-21 | Experimental results of polarization analysis (a), and corresponding SF curves of *x* and *y* components (b), determined by different increments in collecting the raw data: 2°, 10°, 30° and 60°, resulting with: 180, 36, 12, 6 experimental points for the whole turn, respectively.

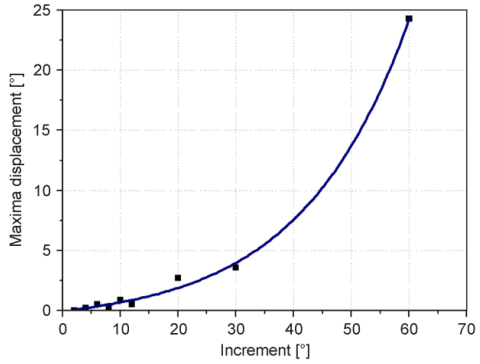

Figure IV-22 | Dependence of maxima deviation error on the increment value. Blue line is an exponential fit obtained for both *x* and *y* polarization components.

These studies, however, did not consider the possibility of a shorter integration time. With a high SHG signal intensity, which can be guaranteed in the case of currently studied RD QDs, the integration time could be shortened by at least by factor of 3, while the error would not vary significantly. Additionally excitation with optimized SHG cross-section with respect to the NP size, and higher value for the power of the incident beam (the analyzed polarization response has been obtained for 3.0 mW at λ_{exc} = 890 nm, which can be still increased at no expense to the signal photostability)[8] should result in a more intense SHG emission, thus allowing for even shorter integration times. Finally, using our algorithm towards three dimensional single NP tracking close to 'real time' data acquisition appears within realistic reach. The only limitation factor is therefore, accurate enough localization of the NP during its motion out of the focal volume.

IV.4 Chapter summary

Concluding our studies on the spherical CdTe/CdS core/shell QDs with ~12.5 nm diameter, it is important to highlight, that choosing these SC NPs allowed for detection of an efficient SHG signal of the order of ~7.5×10^4 cts s^{-1}. Such a small NPs have been detected for a first time with a standard APD detectors, what designate them as competitive nonlinear nanolabels, an alternative to fluorescent labeling.[4] Within the standard 800 to 1000 nm spectral range of the femtosecond Ti-Sapphire laser excitation, these QDs show a sizable SHG response with highest SHG cross-section at about 970 nm. However, an extended spectral analysis towards one-photon and two-photon resonances at the conduction band edge would reveal higher SHG cross-section peaks, providing also comprehensive information about the role of the DOS in the nonlinear optical processes, such as coherent SHG. We have shown that the unique features of SHG emission, such as coherence of the emitted field or strong polarization sensitivity may be exploited to increase the signal-to-background ratio or the recognition of these NPs.[4] Simultaneous measurements of TPEL emission and blinking properties would, moreover, allow us to probe the NP environment, building-up on a well-controlled orientation of the nanoparticle crystalline structure. SHG-analysis alone can also be used for orientational imaging, e.g. three-dimensional single NP tracking.

In the second part of the chapter we have shown, that tailored QD heterostructures may lead to even higher effective SHG cross-sections, tunable with the quantum size confinement

effect. In this approach we have pointed out guidelines towards the engineering of second-order nonlinearity of semiconducting hybrid rod-on-dot CdTe/CdS heterostructures at the single NP scale, which provide photostable SHG emission at comparable level like that observed for the spherical dots. These RD hybrid NPs exhibit extremely strong and stable emission although their volume is reduced by at least a factor of four (up to six) from the dot-shaped CdTe/CdS QDs. Moreover, it emphasizes the structural relationship between the CdTe core and CdS rod and contributions of their respective $\chi^{(2)}$ tensors to the overall SHG field, leading towards a hybrid nonlinear optical susceptibility, which exceeds that of mono-compound QDs. The proposed pointwise additive model allows for comprehensive simulation of the polarization response, evidencing quantitative contributions into the total SH emission from both the CdTe core and the CdS rod, as well as from an additional interference term. The high degree of agreement reached between simulation and experimentally observed results cannot be considered as circumstantial but as evidence for the single crystalline nature of the investigated QD samples. It enables precise determination of the spatial orientation of the crystalline structures. It also shows that the hybrid system can be adequately decomposed into a sum of its constituents in the case of semiconductor-semiconductor hybrids. This simple result had to be demonstrated and is even surprising since it does not hold for metal-semiconductor hybrid particles.[7] Still, coupling of the two semiconductor parts may affect the relative magnitude of the $\chi^{(2)}$ coefficient. Simulation analysis show that the SHG response strongly depends on the CdS rod length and transforms from the four-leaf clover shape characteristic of the octupolar zinc-blende symmetry of the CdTe core, into a typically dipolar response oriented along the CdS rod and imposed by the main polar axis of its hexagonal symmetry point group. The conceptual and practical possibility to fine tune at will the balance between dipolar and octupolar contributions by adequate stoichiometry based engineering, while maintaining control over this delicate multipolar balance at the nanoscale, and minimizing the size of RD NCs, paves the way towards very efficient and precise orientation monitoring for original bio-imaging applications.

Chapter V | Size dependence of the second-order nonlinearity – single dot and HRS studies

V.1 Size dependence of SHG from single CdTe quantum dots 92
V.1.1 Detection threshold of the size dependent SHG signal intensity 93
V.1.2 Estimate of the second-order nonlinear susceptibility 97
V.1.3 Error sources in determining the size dependence of the second-order nonlinear susceptibility 99
V.2 Hyper-Rayleigh Scattering from CdTe QDs 101
V.3 Relations between spectral and size dependence of CdTe $\chi^{(2)}$ features 105
V.4 Chapter summary 107

In the following chapter the size dependence of the magnitude of the second-order nonlinear susceptibility $\chi^{(2)}$ of CdTe QDs, as well as its dispersion features are investigated. Applied experimental methods are the single particle spectroscopy and hyper-Rayleigh scattering (HRS). In these studies we try to address the question as to how quantum confinement effects can modify the nonlinear optical susceptibility of SC QDs. We show that under adequate conditions, the $\chi^{(2)}$ tensor magnitude can significantly surpass that from the corresponding bulk value. These studies prove, most importantly, that careful choice of the material and of the excitation frequencies can result in kilo-counts per second rates for the emission of SHG photons, obtained even from very small appropriately chosen QDs.

V.1 Size dependence of SHG from single CdTe quantum dots

In the previous chapter it was already stated that SHG obtained under nonresonant conditions, as a coherent scattering process, scales as the squared volume of the nanoscatterer.[82] In case of nonlinear properties of nanoscale SC materials, size dependence becomes particularly interesting due to quantum confinement effects and its influence over the energy level spacing. However, until now effects of quantum confinement on coherent nonlinear processes, such as SHG in QDs have not been widely investigated.[3-4,8] Therefore, characterization of the SHG size dependence is particularly important if QDs are to be used as markers in SHG microscopy.[4]

Chemical synthesis and morphological characterization of CdTe spherical QDs used in the following studies have been already described in Subsection III.3. We have selected three different samples of such QDs with average diameters of approximately 7 nm, 9 nm, and 11 nm (as determined from the optical emission spectrum, Figure II-5 following the empirical function (II.1).

The second-order nonlinear polarization response is determined by the third-rank nonlinear susceptibility tensor of CdTe, where the only nonzero and equal elements are d_{14}, d_{25} and d_{36}, as given by equation (III.10). For the statistical studies of SHG obtained from single QDs we have chosen to work under conditions whereby the SHG efficiency is nearly independent of the relative orientation of randomly deposited QDs. In order to obtain such conditions, all studied QDs were excited by a circularly polarized incident excitation beam. The fundamental electric field is expressed in the laboratory frame as:

$$E_{lab} = \frac{1}{\sqrt{2}} E \begin{bmatrix} 1 \\ i \\ 0 \end{bmatrix} \tag{V.1}$$

Rotating it in respect to the crystalline lattice frame leads to:

$$E_{crystal} = \frac{E}{\sqrt{2}} \begin{bmatrix} \cos\phi & \sin\phi & 0 \\ -\sin\phi & \cos\phi & 0 \\ 0 & 0 & 1 \end{bmatrix} \begin{bmatrix} \cos\phi & 0 & \sin\phi \\ 0 & 1 & 0 \\ -\sin\phi & 0 & \cos\phi \end{bmatrix} \begin{bmatrix} 1 \\ i \\ 0 \end{bmatrix} = \frac{E}{\sqrt{2}} \begin{bmatrix} \cos\theta\cos\phi + i\sin\phi \\ -\cos\theta\sin\phi + i\cos\phi \\ -\sin\theta \end{bmatrix} \tag{V.2}$$

where θ is the angle of the *z*-axis in the crystalline lattice frame relative to the *z*-axis of the laboratory frame and ϕ is the angle measuring rotations about the *z*-axis of the crystal. Rotations about the *z*-axis of the laboratory frame need to be considered due to use of the circularly polarized excitation beam. Combining equations (III.10) and (V.2) for the CdTe zinc blende crystalline lattice we obtain:

$$P_i^{(2)}(2\omega) = 2d_{14}E^2 \begin{bmatrix} \cos\theta\sin\theta\sin\phi - i\sin\theta\cos\phi \\ -\cos\theta\sin\theta\cos\phi - i\sin\theta\sin\phi \\ -\cos^2\theta\cos\phi\sin\phi + i\cos\theta\cos^2\phi - i\cos\theta\sin^2\phi - \sin\phi\cos\phi \end{bmatrix} \quad \text{(V.3)}$$

Therefore the SHG signal intensity is expressed as:

$$\begin{aligned} \left|P(2\omega)\right|^2 = {} & 4\left|E\right|^4 {d_{14}}^2 \frac{1}{128}[150 - 6\cos(4\phi) + 4\cos(4\phi - 2\theta) - \cos(4\phi - 4\theta) \\ & -8\cos(2\theta) - 14\cos(4\theta) - \cos(4\phi + 4\theta) + 4\cos(4\phi + 2\theta)] \end{aligned} \quad \text{(V.4)}$$

This expression is weakly varying in terms of theta and phi values (up to approximately ±25%).

V.1.1 Detection threshold of the size dependent SHG signal intensity

SHG size dependent statistical measurements were performed using the optical setup equipped with low noise single photon counting detectors and the TCSPC module (Figure III-5). This is crucial for the detection of a low amount of SHG photons from small (~7 nm diameter) QDs, allowing to select only the instantaneously scattered photons concomitant with the pulse, excluding dark counts of the detector (the ~20 dark counts per second of the detector are minimized here to about ~0.03 counts per pixel, which is negligible). An example of the SHG scan obtained with this technique is presented in Figure V-1. The observed background arises from coherent scattering on the PMMA–glass cover slip interface, which

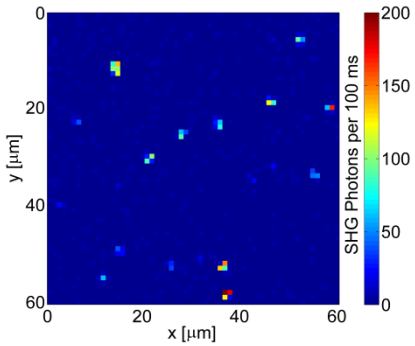

Figure V-1 | Surface scan of 10 by 10 µm area of spin-coated QDs sample, recorded with 60 per 60 pixel resolution and 100 ms integration time. Bright spots of pixels correspond to the SHG emission from single CdTe QDs.

arrives into the detector with the pulse. Typical measured coherent background levels range from 1 to 2 counts per 100 ms (10 – 20 Hz), which were subtracted from the analyzed peak intensities of the SHG signals corresponding to QDs.

Preliminary results have evidenced the importance of choosing the correct threshold value for identifying peaks, which correspond to SHG emission from QDs. This appears especially important in the case of the smallest QDs with a mean diameter of ~7 nm, which have low SHG yield. Some of the possible SHG peaks featuring the lowest count rates turned out to be simply a background noise, due to the overlap between the SHG distribution and the shot noise distribution. The choice of the threshold is a tradeoff between reduction of the background noise pixels and the desire to retain the maximum number of data points, resulting from actual QDs SHG emission. We assume that the background is spatially homogenous and that it follows a discrete Poissonian distribution, the standard deviation (σ) of the background signal is then its square root. The correct standard deviation σ was determined comparing the results obtained for the larger QDs sample (~11 nm). Using thresholds of 3σ, 4σ, 5σ, 6σ and 7σ above the background, the numbers of detected QDs (and corresponding mean SHG count rates in the brackets) were: 827 (250 Hz), 615 (320 Hz), 393 (420 Hz), 350 (500 Hz) and 327 (530 Hz), respectively. From the shot noise distribution, however, we expect that >230 of these peaks in the 3σ and >40 under the 4σ threshold to result from noise. The mean count rates for 6σ and 7σ thresholds are nearly the same within a few percent due to the eliminated noise pixels. However, raising the threshold to these values leads to significant reduction also the number of real data points, therefore we chose a 5σ threshold as a most reasonable value, keeping in mind that some noise peaks are included in

the analysis, whereas symmetrically some real data points have been lost. Exceptionally for the smallest size QDs, we used a lower 4σ threshold, since in this case 5σ eliminates the majority of real data points.

Recorded background counts with 4σ threshold subtracted peak intensities for each QD size are plotted on the histograms shown below (Figure V-2). All three samples exhibit a large number of QDs with SHG signal intensities between 0 and 100 Hz. These low count rate levels can be explained by the appearance of structural defects of QDs (e.g. see the yellow arrow in Figure II-6), which may drastically reduce the SHG yield, and also by background scattering of some of these signal peaks. Using the 4σ threshold, the mean SHG count rates for each 7, 9, 11 nm QDs size are 97, 234, and 320 Hz. For samples containing 7 and 9 nm diameter QDs these values are higher than they should appear as when going from a 3σ to a 4σ threshold, more than 5% of the data points are lost. Average values of SHG count rates from 7 and 9 nm QDs at the 3σ threshold are 70 and 114 Hz, however these results have to be considered as approximated ones, due to the inclusion of shot noise peaks, as well as discarding many real data peaks below the threshold level. For the clarity all measured count rate results are contained in Table (V-I).

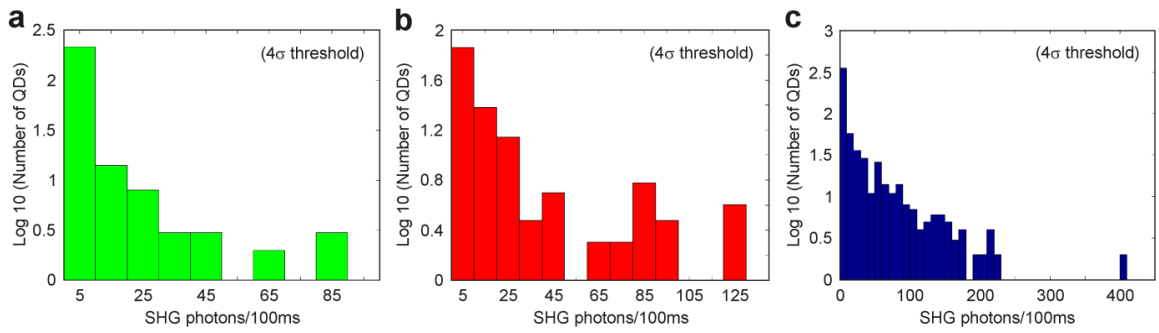

Figure V-2 | Histograms of SHG signal count rates per 100 ms integration time, obtained using 4σ threshold for: a) 7 nm, b) 9 nm, c) 11 nm large CdTe QDs (semi-log10 scaled). Measured numbers of QDs for each sample are 250, 136 and 615, respectively.

TCSPC technique have been used also to test the SHG signal count rates from the spherical CdTe/CdS core/shell ~12.5 nm diameter QDs,[4] characterized in Subsections II.2 and IV.1. Measurements were performed for 3σ and 4σ thresholds, and shown 91 and 102 Hz, respectively, which is comparable to what has been observed for 7 and 9 nm diameter CdTe

Table (V-I): SHG count rates dependence on the QD sizes and standard deviation thresholds ($\sigma = \left(I_{background}^{SHG} \right)^{1/2}$).

QDs mean diameter [nm]	SHG count rate [Hz] with respect to the standard deviation threshold of:				
	3σ	4σ	5σ	6σ	7σ
7	70	97			
9	114	234			
11	250	320	420	500	530
12.5*	91	102			

* corresponding to spherical CdTe/CdS core shell QDs, studied in Ref. [4]

QDs. This is reasonable, since the mean diameter of the CdTe core is about 10.5 nm (excluding the CdS shell, which has been assumed not to contribute to the total SHG field).

The size distribution of 11 nm CdTe dots, determined in Section III.3 translates into the volume squared distribution of the sample. In Figure V-3 we show the predicted histogram for the 5σ threshold using the volume squared and dipole orientation distribution, corrected by the SHG detection efficiency for each dipole angle (following the correction described below), and plotted along the corresponding histogram. The mean value for the SHG count rate at the 5σ threshold of 420 Hz corresponds to a mean QDs size about 12.3 nm (marked as a dashed vertical line in Figure V-3). QDs exhibiting a count rates higher than 1000 Hz are in the tail of

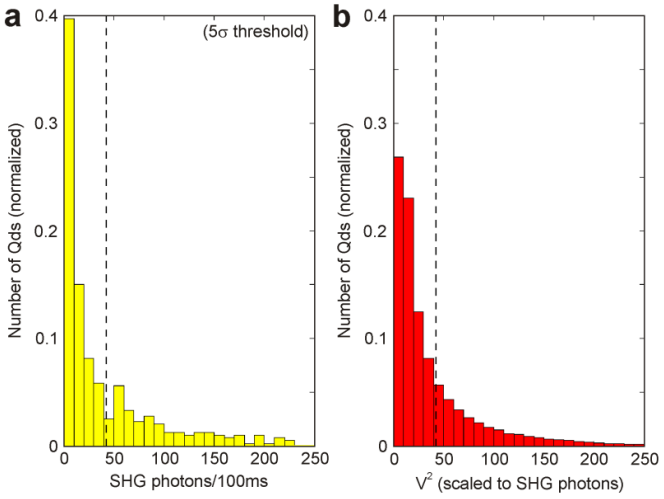

Figure V-3 | Normalized histogram of the SHG count rate of the 11 nm QDs using the 5σ threshold (a), and the squared volume distribution of the same sample (b). Dashed vertical lines correspond to averaged values. The *x* axis of (b) was scaled by fixing the mean value of the squared distribution to the corresponding averaged value of the SHG count rate (420 Hz). Following this, the mean diameter of the QDs corresponding to such a count rate is 12.3 nm.

distribution, and correspond to large volumes. This dependence points out the difficulty in detecting second-order nonlinear scattering from QDs, since under conditions used here (800 nm of the excitation wavelength), reasonably high count rates (suitable for standard APD detection) are obtained only from CdTe QDs with diameters larger than 14 nm.

V.1.2 Estimate of the second-order nonlinear susceptibility

In order to obtain the absolute value of the second-order nonlinear optical susceptibility $\chi^{(2)}_{CdTe}$ of the investigated CdTe QDs, we had first to calculate the electric excitation field and the second-order nonlinear polarization. Without the possibility of determining the crystalline axis for each single dot, we integrate in these statistical studies the nonlinear polarization response (V.4) over all possible crystal orientations, leading to:

$$\left\langle \left| P(2\omega) \right|^2 \right\rangle \simeq 4 \left| E \right|^4 d_{14}{}^2 \times 1.2 = 4.8 \left| E \right|^4 d_{14}{}^2 \tag{V.5}$$

The angle dependent $\left\langle \left| P(2\omega) \right|^2 \right\rangle$ values vary by up to ~25% and the effect of the fixed detection angle and corresponding alignment-dependent SHG detection efficiency was numerically found to be small. The nonlinear CdTe coefficients ($d_{14} = d_{25} = d_{36}$) can then be determined by the integrated nonlinear polarization response which expresses as:

$$d_{14} = \frac{\left(\left\langle \left| P(2\omega) \right|^2 \right\rangle \right)^{1/2}}{2.2 \left| E \right|^2} \tag{V.6}$$

The electric excitation field can be extracted from the power density of the excitation beam. In Gaussian units, the power density *I* is given by:

$$I = \left(\frac{n_0 c}{2\pi} \right) \left| E \right|^2 \tag{V.7}$$

where $n_0 = (\varepsilon_0)^{1/2}$ is the refractive index of the surrounding medium (PMMA polymer), *c* is the speed of light, and *E* is the electric field.

To obtain the real value of the electric field inside the NP sphere, we take into account its reduction inside the QD due to the higher dielectric constant of CdTe as compared with that of the surrounding PMMA polymer, as from equation (III.11). Accordingly, *E* should be multiplied by a $3\varepsilon_m/(\varepsilon+2\varepsilon_m)$ factor,[82] where ε is the dielectric constant of the scattering nanosphere (CdTe QD), leading to:

$$|E|^2 = \left(\frac{3\varepsilon_m}{\varepsilon+2\varepsilon_m}\right)^2 \frac{2\pi I}{n_0 c} \tag{V.8}$$

The ielectric constant ε of CdTe at 1.5 eV (800 nm) is ~9.0,[39,129] and that of PMMA is $\varepsilon_m \sim 2.25$.[130]

The power density is estimated using the laser power measured at the front of the microscope. In order to obtain the actual value reaching the sample it has to be corrected by the reflectance of the dichroic mirror and transmission of the microscope objective at 800 nm. The power reaching the sample (~2.3 mW) is then divided by the illumination field size, obtained from the diffraction limited spot size. We have observed some uncertainties in determining the illumination area. The waist of the diffraction limited spot was found by multiplying the measured FWHM of the SHG spot size from 50 individual QDs (~208 nm) by $\sqrt{2}$ since SHG is a second-order process. Thus, the mean FWHM is found to be 295 ±37 nm, leading to an error of 25% on the area. From this diameter the illumination field size is found to be 7.45×10^4 nm^2.

To calculate the second-order nonlinear polarization $P(2\omega)$, we need the power (*p*) of the emitted SHG signal since:

$$p = 2\ddot{D}^2/3c^3 \tag{V.9}$$

where $D = PV$ is the dipole moment and $\ddot{D} = \omega^2 PV$ where *V* is the volume of the scatterer. By taking into account the collection efficiency and losses through the optical components of the setup, the number of SHG photons emitted per 100 ms (integration time of the measurement) can be related to the number of measured SHG photons N^{SHG}. In order to obtain its real value the raw data had to be corrected following a similar procedure to the one described in Appendix A, taking into account the transmission of the optical components inside the excitation and detection channels: reflectance (at 800 nm) and transmission (at 400 nm) of the

dichroic mirror, microscope objective parameters, as well as quantum efficiency of the detectors (single-photon counting *Picoquant* PMT, and *idQuantique* APD). The collection efficiency was calculated by determining the angular distribution of the SHG dipoles and the percentage of signal collected for each dipole orientation by the microscope objective based on its *NA*.

The energy per laser pulse is the number of SHG photons emitted per 100 ms (integration time) divided by the 80 MHz pulse repetition rate and multiplied by the energy of a single SHG photon. Than by dividing the energy per pulse by the ~130 fs pulse duration we get the power of the emitted SHG signal.

Obtained for a 11 nm QD sample, the 420 Hz SHG count rate (using 5σ threshold) leads to a d_{14} value of 1.5×10^{-7} cm statvolt^{-1}, what corresponds to 64 pm V^{-1} (using the convention that, in MKS units system $P = \varepsilon_0 dE^2$).[v] This value has been assumed in the model for polarization analysis of RD QD heterostructures described in the previous chapter.

V.1.3 Error sources in determining the size dependence of the second-order nonlinear susceptibility

In our single dot studies, three main sources of error have been identified (all of them are summarized in Table (V-II)). The first one comes from difficulties in determining the properties of the background coherence. Since we do not know its polarization, it is difficult to remove it from the measurement. Therefore we have assumed it is incoherent and subtracted it from the measured count rate, which may have led to an overestimation of the SHG counts. The threshold 5σ used to distinguish QDs from the background counts also introduces error in the SHG count rate, since as a tradeoff threshold means that still some of the included pixels are noise, while using a higher threshold leads to the removal of real data points. An error of ±20% is estimated for the SHG count rate, which is the difference in the mean count rates obtained when using the 4σ and 6σ standard deviations.

The second significant source of errors arises from the average QD volume. Since values of the nonlinear coefficients *d* scale with the assumed volume of the scatterer, even relatively

[v] The conversion factor from statvolt cm^{-1} to pm V^{-1} is $4\pi / (3\times10^{-8})$

small errors in determining the QD diameter may be significant. We estimate the error in the determination of the QD volumes as ±15%, by taking the difference between the mean volumes as shown in Figure II-6. We note that our analysis assumes that $\chi^{(2)}$ can be regarded as dependent only on the NC volume within the size range of our samples. This is not entirely fulfilled but is a reasonable approximation for the relatively narrow experimental size distribution.

The third significant source of error arises from uncertainties in determining the illumination area. The measured FWHM of the spot size of the SHG signal from 50 individual QDs has been found to be 295 ± 37 nm, leading to an error of 25% on the area.

Other small sources of error include errors in the signal collection efficiency (< 10%), the detector quantum efficiency at 400 nm (< 10%), the pulse duration at the sample (~10%), and losses through the optical components (~10%). We also neglect dielectric effects on the dipole emission pattern due to the asymmetry in refractive index between the glass substrate and air. Taking into account that tensor $\chi^{(2)}$ follows a square root dependence on the SHG count rate, losses due to the optical components inside the detection channel, and the detector quantum efficiency, a linear dependence on all other quantities, and that the errors are uncorrelated and can be added in quadrature, the $\chi^{(2)}$ of CdTe QDs using 800 nm excitation lies within the range 43-85 pm V^{-1}.[5]

Table (V-II): Summary of the error sources in $\chi^{(2)}$ studies for a single dot case.

Source of Error	Percentage Error
Mean SHG intensity	20%
Mean QD volume	30%
Area of illumination	+50%, -0%
Signal collection efficiency	< 10%
Detector Quantum efficiency	< 10%
Optical components	~10%

V.2 Hyper-Rayleigh Scattering from CdTe QDs

The Hyper-Rayleigh Scattering (HRS) experiment was performed to confirm results obtained from single dot studies, discussed in the previous paragraph. Measurements were carried out for four CdTe QD samples of 5, 7, 9, and 11 nm diameters, each one at several concentrations. QDs were firstly separated from their ligands by centrifugation and then dissolved in toluene. The concentration of each solution was characterized using the Beer-Lambert law:

$$A = \epsilon CL \tag{V.10}$$

where A is the absorbance of the first exciton peak in the absorption spectrum, ϵ is the extinction coefficient per mole, C is the molar concentration of the solution, and L is the length of the optical beam path used for recording the spectrum.

The experiment was performed by focusing the linearly polarized output beam of a *Spectra-Physics Tsunami* Ti-Sapphire laser (λ_{exc} = 800 nm, 130 fs, 80 MHz; the same as used before for single dot studies) onto a quartz cuvette containing the QD solution and collecting the scattered signal at 90° with respect to the direction of the NIR excitation laser beam (see Figure V-4). The signal was collected by a low - *NA* objective, then passed through a monochromator and detected by PM tube. Figure V-5(a) shows the HRS signal intensity (after correction for the self-absorption of the SH frequency on the detection path) as a function of QDs concentration. A measurement was taken for pure toluene, providing the *y*-intercept value on the graphs.

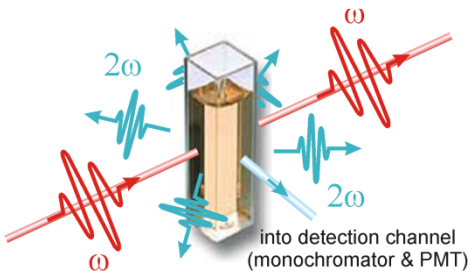

Figure V-4 | Schematic of the hyper-Rayleigh scattering experiment.

Our analysis of the HRS signal followed that of conventional HRS experiments.[3,131] A value of the first hyperpolarizability β_{CdTe} per unit cell of CdTe relative to the hyperpolarizability of the solvent β_s (toluene in our case) can be extracted from the linear dependence of the HRS signal on the sample concentration, as given by following expression:

$$I(2\omega) = G\left(N_s \left\langle \beta_{HRS}^2 \right\rangle_s + N_{CdTe} \left\langle \beta_{HRS}^2 \right\rangle_{CdTe}\right) I(\omega)^2 \tag{V.11}$$

where G is a geometrical factor including the local fields factors, N_s and N_{CdTe} are the number concentrations of the solvent and solute QDs, and $\left\langle \beta_{HRS}^2 \right\rangle$ is the orientational average form of the quadratic β tensor components. The common intercept of the HRS signal intensity plots, presented in Figure V-5 as a function of the QDs concentration, is therefore $b = GN_s \left\langle \beta_{HRS}^2 \right\rangle_s I(\omega)^2$ and the slope of each fit is $a = G\left\langle \beta_{HRS}^2 \right\rangle_{CdTe} I(\omega)^2$, giving:

$$\frac{\sqrt{\left\langle \beta_{HRS}^2 \right\rangle_{CdTe}}}{\sqrt{\left\langle \beta_{HRS}^2 \right\rangle_s}} = \sqrt{\frac{aN_s}{b}} \tag{V.12}$$

The number n of unit cells in a QD of volume V is:

$$n = V \frac{d_{CdTe}}{M_{CdTe}} N_A \tag{V.13}$$

where d_{CdTe} and M_{CdTe} are the density and the molecular weight of CdTe, respectively, and $N_A = 6.02\times10^{23}$ mol^{-1} is Avogadro's number. The slopes of the linear fits to the data for 5, 7, 9, and 11 nm diameter QD samples are 7×10^9, 7×10^{10}, 4×10^{11}, and 1×10^{12} counts M^{-1}, respectively. Dividing equation (V.12) by n results in $\bar{\beta}_{CdTe}$ defined from $\sqrt{\left\langle \beta_{HRS}^2 \right\rangle_{CdTe}}$ per unit cell in units of β_s defined as $\sqrt{\left\langle \beta_{HRS}^2 \right\rangle_s}$. For CdTe we used the values of d_{QD} = 5.86 g cm^{-3} and M_{QD} = 240 g mol^{-1}. The concentration of toluene was obtained by dividing its density (0.866 g mL^{-1}) by its molecular weight (92.14 g mol^{-1}), giving N_s = 9.4 mol L^{-1}.

Using these inputs, the size dependent values of $\bar{\beta}_{CdTe} / \beta_s$ were 8.8, 10.1, 11.3, and 9.8, corresponding respectively to to 5 nm, 7 nm, 9 nm, and 11 nm QD sizes, as plotted in Figure V-5(b), and summarized in Table (V-III). An average value of $\bar{\beta}_{CdTe} / \beta_s$ = 10.0 is marked by the dashed line in Figure V-5(b). Obtaining the value for single tensor elements which can be then compared with known elements of the $\chi_{CdTe}^{(2)}$ tensor is important, since CdTe and toluene have different symmetries.

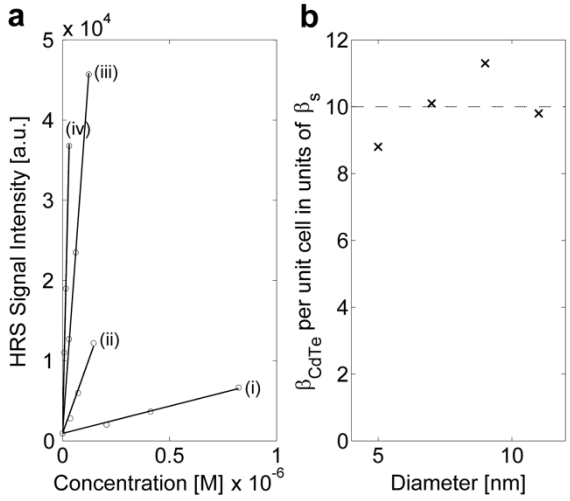

Figure V-5 | a) Dependence of the signal intensity on QD concentration in the HRS experiment performed for: (i) 5 nm, (ii) 7 nm, (iii) 9 nm, (iv) 11 nm CdTe QDs. The solid lines are linear fits of the experimental data (the signal obtained from toluene) is separated). b) Orientational mean hyperpolarizability per unit cell, in units of β_s, for each QD sizes. The dashed line represents averaged value over all QD sizes.

CdTe belongs to zinc blende crystalline symmetry (with three $d_{14} = d_{25} = d_{36}$ non-zero tensor elements), while for toluene we assume that the only contributing element is β_{zzz} (corresponding to the d_{33} matrix element). In order to find the total SHG signal intensity for both CdTe and toluene we follow the method described in Section V.2 taking into account a linearly polarized fundamental field, and assuming that the only collected SHG signal is that one propagating at 90° through a low - *NA* objective. After summing over all angles we found that in order to satisfy the ratio of total signal intensities $\overline{\beta}_{CdTe} / \beta_s = 10.0$ corresponding to the dashed line in Figure V-5(b), the nonzero coefficients of CdTe have to be 5.5 times higher than the effective β of toluene.

The nonlinear susceptibility d_{il} for the bulk material can be expressed in terms of the first-order hyperpolarizability β_{ijk}:[132]

$$d_{il} = \frac{N\ f(\omega) f^2(\omega)}{2\varepsilon_0} \beta_{ijk} \tag{V.14}$$

where N is the number density and $f(\omega)$ is the local field factor of the material at the incident frequency ω, and ε_0 is a vacuum permittivity. In our experiment the local field factor must include the reduced screening in the composite solution of QDs dissolved in

toluene as compared to the screening in a bulk semiconductor material, a corrected local field factor being then:[82]

$$f(\omega) = f_s(\omega)\frac{2\varepsilon_s + \varepsilon_{CdTe}}{3\varepsilon_s} \tag{V.15}$$

where $f_s(\omega) = \left(n_s(\omega)^2 + 2\right)/3$ is the Lorentz-Lorenz local field factor of toluene,[133] dependent on the refractive index *n*, $\varepsilon_s \approx n_s^2(\omega) \approx n_s^2(2\omega)$ = 2.25 is the dielectric constant of toluene, and $\varepsilon_{CdTe} \approx n_{CdTe}^2(\omega) \approx n_{CdTe}^2(2\omega)$ = 9.0 is the dielectric constant of bulk CdTe.[39,129]

The experimental value of β of toluene at 800 nm was found in the Ref. [134] to be ~0.23× 10^{-30} esu. We take into account the factor of 5.5 of β_{zxy} relative to the hyperpolarizability of toluene, which leads to a CdTe nonlinear coefficient d_{36} = 88 pm V^{-1},[135, vi] which is in a relatively good agreement with the single QD studies,[5] despite a relatively large experimental error. The result of d_{36} = 88 pm V^{-1} is expected to be subject to an error larger than 25%, arising from that in determining the solution concentrations from the optical densities (~20%), the uncertainty in the hyperpolarizability value of toluene (5%), and the standard deviation of $\overline{\beta}_{CdTe}/\beta_s$ obtained from four different QD samples (10%). Another source of error comes from the assumption of the bulk value for the dielectric constant of CdTe, for which the size dependence is expected to be small,[136] which can nevertheless overestimate the *d* value. A last source of error is the polarity of the solvent, which may lead to an error for the local field factor in expression (V.14), however it is assumed to be small for toluene,[137] and thus negligible in our analysis.

Table (V-III): Obtained $\overline{\beta}_{CdTe}/\beta_s$ values in respect to the QD diameters, and SHG intensity versus QD concentrations linear fit slope values.

QD diameter [nm]	$\overline{\beta}_{CdTe}/\beta_s$	$a = G\left\langle\beta_{HRS}^2\right\rangle_{CdTe} I(\omega)^2$ [counts M^{-1}]*
5	8.8	7×10^{9}
7	10.1	7×10^{10}
9	11.3	4×10^{11}
11	9.8	1×10^{12}

* where *G* is a geometrical factor including the local field factors

[vi] Using the conversion factor of: 1 $C^3 m^3 J^{-2}$ = 2.7×10^{20} esu^{-1}

V.3 Relations between spectral and size dependence of CdTe $\chi^{(2)}$ features

Both, single dot spectroscopy and HRS investigations of the $\chi^{(2)}$ size dependence of CdTe QDs,[5] have confirmed our earlier observations, reported before for single QD spectral dependence measurements (Subsection IV.3.1 - Figure IV-5).[4] These two different approaches to the problem are, in a sense, complementary with respect to each other. Information gained from the spectral dependence experiment (Sections IV.1.1 and IV.2.1), where the excitation frequency varies while the size of the QD is kept constant, determines how far into two photon resonance the efficient SHG process occurs. Results shown in this chapter for single dot studies and HRS experiments show a reversed situation whereby, the distance from the band edge of the two-photon resonance excitation is varied by changing the size and therefore the QDs band gap (BG), while the excitation frequency is set at a constant value of 800 nm. Combining these two approaches, the wavelength dependent dispersion curve of $\chi^{(2)}$ and numerically obtained values opens the possibility for comparing the nonlinear susceptibility of QDs to that of bulk CdTe, as illustrated in Figure V-6.

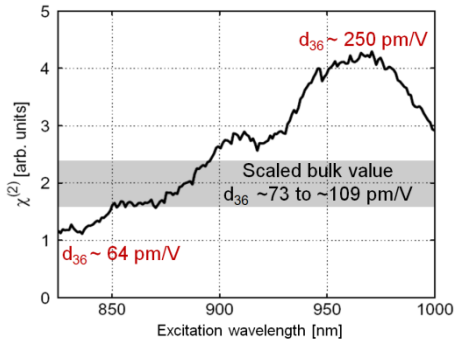

Figure V-6 | Wavelength dependence of the $\chi^{(2)}$ dispersion curve, measured for spherical CdTe QDs (marked with the black line). The grey area is related to the variation of bulk d_{36} coefficient, scaled at a similar ratio of the excitation energies between 12 nm CdTe QDs (E_{BG} ~760 nm, excited at 970 nm), and bulk CdTe (E_{BG} ~840 nm, excited at 1.06 μm).[4-5,94]

The obtained result of d_{36}(800 nm) = 64 ±21 pm V^{-1} is close to the bulk values of 73 pm V^{-1} (at 1.5 μm) – 109 pm V^{-1} (at 1.06 μm), reported in the literature.[94] Changing the excitation wavelength from 800 nm to resonance with an optimized SHG cross-section at ~970 nm (as shown in Figure IV-5) would lead to four times increase at least for the value of $\chi^{(2)}$, resulting in $d_{36} \geq$ 250 pm V^{-1}. When comparing the 11-12 nm diameter large CdTe QDs

($E_{BG} \simeq 1.63$ eV) illuminated at 970 nm laser light, with the bulk CdTe crystal ($E_{BG} \simeq 1.47$ eV) at 1.06 μm, the excitation conditions in terms of the relative excitation energy relative to the band gap appear to be similar. Therefore due to the quantum confinement effects, $\chi^{(2)}$ of the single QD can significantly exceed its bulk value, showing completely different behavior when compared to the expected monotonous-like $\chi^{(2)}$ dispersion of the bulk crystal.[77,94]

Complementary to our spectroscopic single–dot results HRS studies, comparing to the first hyperpolarizability measurements of the most known CdSe QDs,[3] allow for drawing similar conclusions as in the case of single–dot experiments. Converting the values given for $\overline{\beta}_{CdSe} / \beta_s$ by Jacobson et al. [3] to the form of d_{33} coefficient using the same procedure as have been used in our CdTe studies (using a CdSe density of 5.91 g cm^{-1}, M = 191 g mol^{-1}, and $n(\omega) = 2.7$), gives d_{33}(800 nm) = 40 pm V^{-1} (for 9 nm diameter QDs), which is close to the reported bulk value of 36 pm V^{-1}.[92] Comparing the higher hyperpolarizability of CdTe with reported by Jacobson et al. results for CdSe, we expect it to follow the trend for bulk nonlinearities of CdTe and CdSe crystals.

The HRS experiment conducted for smaller 2.4 nm diameter CdSe QDs reports d_{33} nonlinear coefficient of 160 pm V^{-1},[3] which is much larger than the one obtained for 9 nm diameter QDs and reported for the bulk CdSe. This has pointed out a possibility for the increase of the nonlinear susceptibility by quantum confinement effect, observed while the QDs size has been decreased. As the separation between the band gap and excitation energies shrinks, i.e. as the QD size becomes larger, the resonance enhancement should increase due to the higher density of states further from the band edge, whereas the opposite effect is seen.[3] Therefore, the reported results are attributed to surface SHG, which becomes more significant as the NP volume decreases.

Summarizing our results on the spectral dependence and size dependence experiment of the relative $\chi^{(2)}$, we suggest that resonant effects are important. Both experiments show that E_{SHG} farther above the band gap leads to a lower $\chi^{(2)}$ than E_{SHG} closer to the band gap, exhibiting a non-monotonous increase as a function of the E_{SHG} / E_{BG} ratio. Fourfold increase in d_{36} observed for a ~12.5 nm diameter CdTe QDs (Figure IV-5) occures when the E_{SHG} goes from $1.9\,E_{BG}$ to $1.5\,E_{BG}$,[4-5] while for d_{33} of CdSe NPs, the observed increase is more than a factor of two as E_{SHG} changes from $1.6\,E_{BG}$ to $1.2\,E_{BG}$.[3] Our spectral dependence experiment

has minimized the importance of surface SHG (highlighted by Jacobson et al.), showing nonlinear $\chi^{(2)}$ dispersion curves obtained for constant QD surface, while the incident excitation frequency was tuned. The main contribution to the observed effects can then be assigned to quantum confinement effects. Exciting QDs above the band edge into deep two-photon resonant conditions, leads to more rapid decoherence due to increased DOS in spectral regions where the energy levels are more closely spaced. Thus optimization of the SHG cross-section is the interplay between resonant enhancement and fast decoherence, which determines the level of signal intensity at different relative excitation energies (as illustrated in Figure IV-5).[4-5]

V.4 Chapter summary

Concluding our studies on the second order nonlinear susceptibility of CdTe QDs, we have directly measured the nonlinear coefficient *d* of single isolated SC nanoscatterer. Supplementary HRS measurements provide an independent confirmation of our single dot studies and follow the same trend as previously reported HRS experiment on similar SC CdSe NPs.[3] We have determined the *d* nonlinear coefficient of ~11.5 diameter CdTe QDs excited at 800 nm to reach 64 pm V^{-1}, which is not far from the bulk value of 73-109 pm V^{-1}. The importance of resonant enhancement and optimized decoherence is highlighted and shown to play an important role in the SHG emission obtained from QDs under two-photon resonant conditions, leading therefore to an optimized SHG QY. Under proper excitation conditions, the nonlinear susceptibility of SC QDs may considerably surpass the value of the corresponding bulk material, what shows an important role of the quantum confinement effect in nonlinear optics.[5]

General conclusions

This thesis concerns the development of new types of SHG-active probes, which are quantum confined semiconductor nanocrystals, in order to break through the barrier of the smallest detectable size, met for previously researched nanoparticles (>40 nm for insulators or wide gap semiconductors, with SHG count rates of at least 1×10^3 cts s^{-1}) towards two-photon nonlinear microscopy.[1-2,84-88,138]

The main questions at the starting point of this work were: is the efficiency of nanoscale scatterers really limited by the material bulk properties? If so, how can we deal with such limitation to as to signal, and significantly shrink the size of nanoprobes? As are shown in this work, the most important factors towards the achievement of positive results are a proper choice of materials, well developed chemical synthesis and characterization methods of the samples, and most importantly, optimized conditions for nonlinear optical measurements.

The selected materials are quasi-type-II QDs, based on the CdTe core and CdS overcoating shell, eventually evolved into quantum rod, which belong to the II-VI group of direct gap semiconducting crystals. This choice was made for several reasons (discussed in detail in Chapters I & II). Firstly, CdTe exhibits relatively strong second-order nonlinearity, characteristic of a noncentrosymmetric zinc-blende structure, what is a prerequisite to even-order terms (corresponding to odd rank tensor) nonlinear scattering processes, as the lowest order one being SHG.[58,77,94] The energy band gap of CdTe QDs can be tuned in a range from 1.44 eV up to about 2.0 eV as a function of QD size,[15] and corresponds to the tunable range of frequencies of a Ti-Sapphire fs oscillator. Finally the most important reason, as we realize now, under a strong / intermediate quantum confinement regime is the dipole moment of CdTe QDs and the related two-photon cross-section, which exhibits remarkable enhancement when compared to that of bulk.[5]

In the first report [4], it was shown that efficient and photostable SHG radiation of the order of ~7.5 $\times 10^4$ cts s^{-1} (nearly 75 times above assumed the lowest detectable value) could be obtained for an individual isolated ~12.5 nm diameter core/shell CdTe/CdS QD under reasonable intensities of the fundamental light. Detailed studies presented within the first part of Chapter IV, shown the assets from the coherent SHG-active QD nanoprobes. Moreover, in contrast to fluorescent QD labels,[110-111,139] SHG active CdTe QDs do not exhibit any emission intermittency such as '*blinking*', nor bleaching. Since SHG is a frequency conversion process achievable in non-resonant conditions, its narrow emission peak can be tuned following that of the fundamental light far from the TPEL range, allowing to filter out the latter. Therefore, it may be also easily separated from the auto-fluorescence emission of the biological specimens.

Two-photon resonance conditions, however, can increase TPEL emission, which may then lead to decay of both TPEF and SHG signals. The same contradiction between quantum yield of the TPEL emission and photostability of the SHG signal was observed for different types of samples.[4-5,8] It was shown that higher TPEL QY may lead to strong fluctuations of the emitted light and finally destroy the dot, while QDs emitting pure SHG signals exhibit remarkable photostability, and endure extremely high pulsed peak intensities up to ~150 GW cm^{-2}. The effect of reduced stability can be attributed to induced excited state absorption at the excitation frequency of QDs exhibiting stronger band-edge luminescence, while for low luminescence QY the excited state population completely decays nonradiatively within the ~12 ns time interval between excitation pulses. Additional studies are necessary for better understanding of these issues.

Within the standard 800 to 1020 nm spectral tenability range of the fs Ti-Sapphire laser excitation, spherical CdTe/CdS QDs display their highest SHG cross-section around 970 nm.[4] An extended spectral analysis towards one- and two-photon resonances at the CB edge is expected to reveal even higher SHG cross-section peaks. Such studies would lead to obtaining comprehensive information about the role of DOS in nonlinear optical processes, such as coherent SHG. Therefore, two-photon excitation of the CdTe QDs within a range from 760 nm to 1.52 μm (using an optical parametric oscillator (OPO), and a frequency doubler) retains as an open question and is planned as a continuation to this work.

The new approach for purely semiconducting hybrid QD heterostructures, discussed in the second part of Chapter IV, shows that further engineering of the structural and morphological features at the single nanoparticle level may lead to much higher optical nonlinearities,

exceeding that of single-material QDs. The RD QD hybrids built from 6 nm diameter CdTe core, and attached to ~12 nm long / 3 nm wide CdS rod, exhibit comparable SHG signals to that observed from ~12.5 nm diameter spherical CdTe QDs. At the optimal excitation range of 925 nm, where the SHG cross-section reaches a maximum, the obtainable signal count rate resulting from coupling the two materials may reach about 1.1×10^5 cts s^{-1}, although the overall volume is reduced by at least a factor of four (up to six) from that of spherical QDs.[8] Taking into account the transmission of the collection optics as well as the detection efficiencies, this corresponds to a SHG cross-section of the order of 50 GM, as obtained from a standard size RD QD (with a volume of about 200 nm^3). This result is remarkable, since reported SHG cross-section value for 100 nm diameter $BaTiO_3$ (what gives 5.23×10^5 nm^3) is equal ~1000 GM.[6] Obviously, the volume ratio of 1:2600 does not scales with the 1:20 ratio between SHG cross-sections of BaTiO3 and RD QD hybrids. Moreover, the formation of such structures has further contributed to their photostability. This progress has been attributed to the smaller size of the RD QDs, which leads to slower decoherence process. Basically, larger intraband level spacings of small QDs slow down the exciton – LO phonon coupling, which reflects in more intense and stable SHG radiation.

SHG emission from both types of QDs was analyzed in terms of their incident polarization. The experimental results relate to the crystalline symmetries of the studied nanoparticles. The perfectly octupolar lattice of CdTe QDs features the characteristic four-leaf clover polarization pattern, which is also a proof of monocrystallity.[4] The same experiment carried out for RD QDs provides substantially different results, evidencing the expected dipolar like polarization response. Analysis of these data, however, due to the complex structure of these hybrid NPs required implementation of a new algorithm. A pointwise tensorial additive model allowed for comprehensive simulation, showing quantitative contributions of the CdTe core and the CdS rod, as well as that of an additional interference term into radiated SHG, which depends in a linear manner on the CdS rod length.[8] For both spherical and hybrid structures, a high degree of agreement between simulation and experimental observations was reached, allowing to determine the spatial orientation of the probed crystalline structures. It has also been shown that the hybrid system can be adequately decomposed into a sum of its constituents in the case of purely semiconducting hybrids.[8] This simple result is all the more interesting and surprising as it does not hold for metal-semiconductor hybrid particles.[7] These vectorial-like properties of the SHG radiation pave the way towards very efficient and precise

orientation monitoring in original bio-imaging applications, e.g. three dimensional tracking of single nanoparticles.

Considering the size and spectral dependence of the second-order nonlinear susceptibility of CdTe QDs, as discussed in Chapter V, allowed to reach its absolute values at different conditions. Using single nanoparticle spectroscopy studies and complementary HRS experiments, it was shown that at 800 nm of the excitation frequency, the nonlinear coefficient d_{14} of ~11.5 nm diameter CdTe QDs is found to equal 64 pm V^{-1}.[5] Following the spectral analysis, which was carried out in Ref. [8], these may lead to a value of 250 pm V^{-1}, largely exceeding the bulk value ranging from 73 pm V^{-1} (at 1.5 μm) to 109 pm V^{-1} (at 1.06 μm).[77,94] This study illustrates the importance of quantum confinement, and point out its remarkable impact on the resonant enhancement of the SHG nonlinear scattering process.

As a final remark, this work supports the case future applications of semiconducting QD heterostructures as new probes for two-photon polarization sensitive nonlinear microscopy. The careful choice of material properties such as quantum confined CdTe QDs was justified, allowing to significantly decrease the nanoparticle size much below the earlier ~40 nm barrier. The second-order nonlinear susceptibility features in two-photon resonance conditions are maintained and follow quantum confinement selection rules. Moreover, such previously unexplored results and adapted simulation algorithms based on quadratic tensorial properties discussed within this thesis, path the way towards advanced applications at the sub-wavelength regime for optical probing.

Appendix A: Correction of the raw data for SHG wavelength dependence

The excitation spectra of SHG emission have been performed using two APDs in two different polarization planes: *X* and *Y*, with an acquisition time of 1 s. Each data series was measured with a constant change of the excitation wavelength with a step 1 nm, in the range 820 – 1000 nm, performed automatically with the Ti:Sapphire laser (*Mai-Tai HP, Spectra-Physics*) control software. For SHG signal below 410 nm we were limited in the detection range by the Silicon APDs, exhibiting quantum efficiency close to zero at 400 nm (at the room temperature). We have also to take into account the wavelength dependence of the transmission / reflection of all optical components, in the excitation / detection channels.

Mirrors, with power variations less than 1%, high quality short-pass filter (*Semrock* SP01-561RS), and lenses with more than 99% of the transmission, were not taken into consideration. First beam-splitter (BS) was used only to check the emission spectra with the spectrometer, and removed for excitation spectral measurement performed with avalanche photodiodes.

A.1 Correction for the excitation channel

Conversion of the excitation power measured at the input of the microscope to the mean value reaching the sample $\left\langle P^{IR} \right\rangle_{sample}$ can be obtained from following dependence:

$$\left\langle P^{IR} \right\rangle_{sample} = R_{DM}^{IR} \cdot T_{Obj.}^{IR} \cdot P_{measured}^{IR} \tag{A.1}$$

where: R_{DM}^{IR} is the reflectivity of the dichroic mirror for IR light; $T_{Obj.}^{IR}$ is the transmission of the objective; $P_{measured}^{IR}$ is the power measured at the front of the microscope.

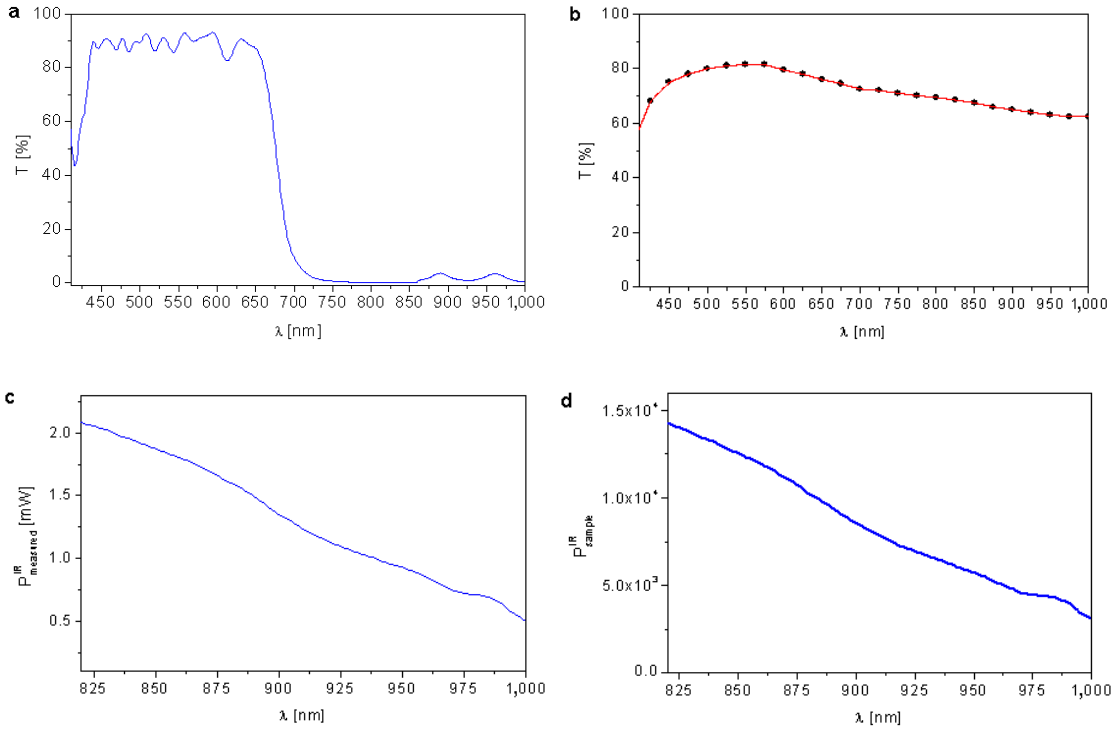

Figure A-1 | a) Wavelength dependence of the dichroic mirror transmission, measured for VIS and NIR spectral regions. b) Wavelength dependence of the *Nikon* AP IR oil immersion (×100, N.A. 1.4) objective transmission. c) Incident laser power, measured at the front of the microscope. d) Characteristic of the incident laser power, which reaches the sample, after corrections by the reflectivity of the dichroic mirror and transmission of the *Nikon* AP IR objective.

Corrected wavelength dependency of the incident laser power (shown in Figure A-1(d)) is the characteristic corresponding to the optical electric field reaching the sample.

A.2 Correction for the detection channel

Transformations of detected SHG photon counts raw data traces (see Figure A-2) into the corrected emission wavelength dependency is discussed below. All the corrections were made step by step, taking into account the transmission of each optical component on the detection path and the detection efficiency of Si-based avalanche photodiodes (*Perkin-Elmer*) in the spectral range of 410-500 nm, what corresponds to emitted SHG signal.

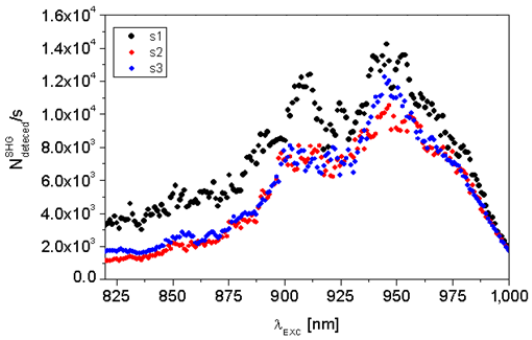

Figure A-2 | The SHG count rate raw data, measured for three different spherical CdTe/CdS core/shell QDs.

Transmission correction of the raw data was calculated using following expression:

$$(N^{SHG}_{photons} / s)_{sample} = \frac{(N^{SHG}_{photons} / s)_{\det}}{T^{VIS}_{Obj.} \cdot T^{VIS}_{DM} \cdot T^{VIS}_{BG39} \cdot T^{VIS}_{BG38} \cdot T^{VIS}_{PBS} \cdot D^{VIS}_{APD's}} \quad (A.2)$$

where: $(N^{SHG}_{photons} / s)_{\det}$ - is the raw number of detected SHG photons per second; $T^{VIS}_{Obj.}$ - is the transmission of the objective at 410 - 500 nm; T^{VIS}_{DM} - transmission of the dichroic mirror; T^{VIS}_{BG39} - transmission of BG39 filter; T^{VIS}_{BG38} - transmission of BG38 filter; T^{VIS}_{PBS} - transmission of polarization beam splitter; $D^{VIS}_{APD's}$ - detection efficiency of silicon avalanche photodiodes.

a) Correction for the transmission of *Nikon* ×100 AP IR objective (detection of SHG photons in backward direction):

b)

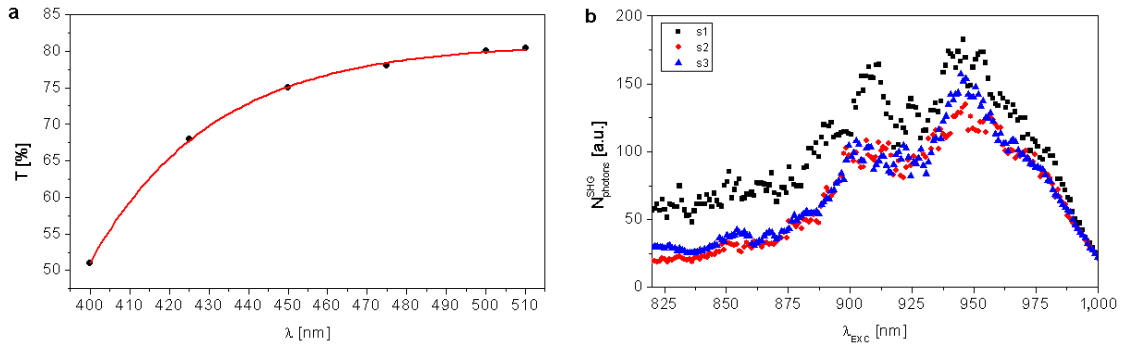

Figure A-3 | a) *Nikon* AP IR microscope objective transmission, measured for the spectral range of emitted SHG signal. b) Corrected SHG signal.

c) Correction for the dichroic mirror transmission:

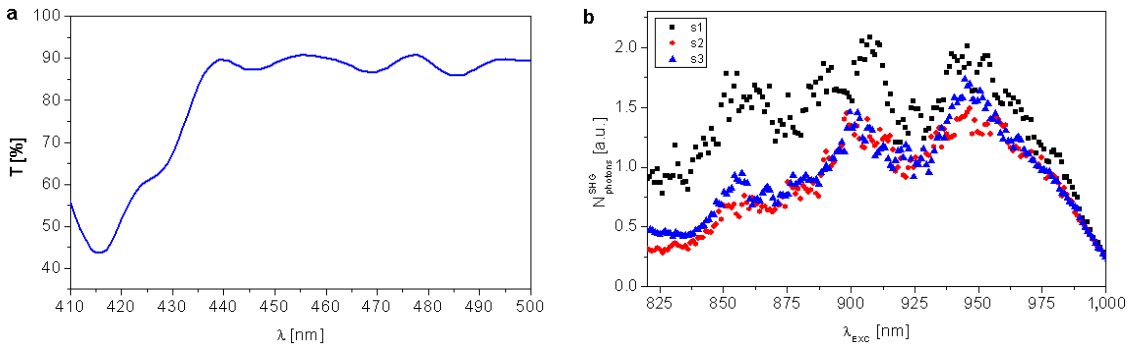

Figure A-4 | a) Transmission of the dichroic mirror, measured at the spectral range of 400 - 510 nm. b) Corrected SHG signal.

d) Correction by the BG39 filter transmission:

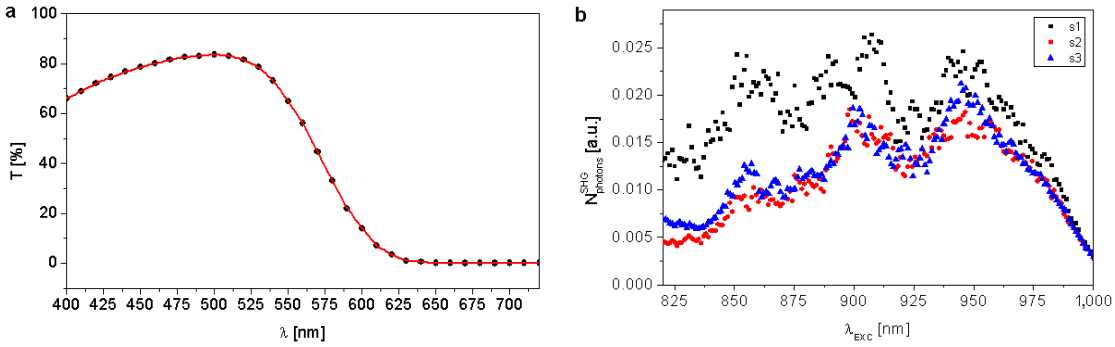

Figure A-5 | a) BG39 filter transmission. b) Corrected SHG signal.

e) Correction for BG38 filter transmission:

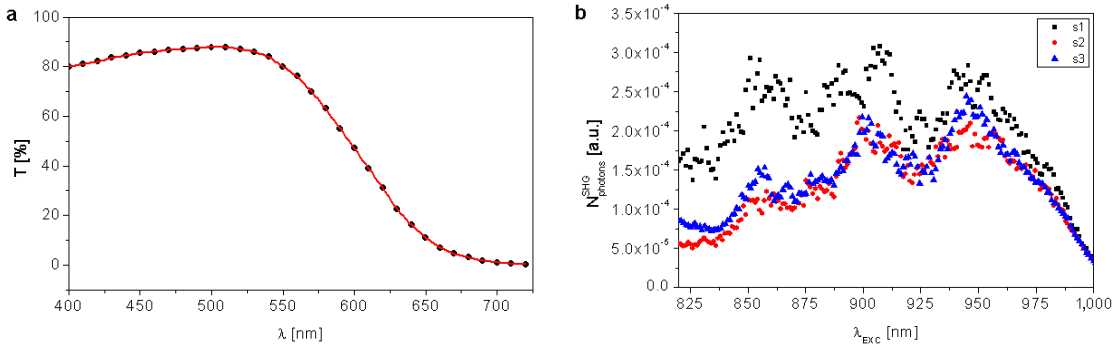

Figure A-6 | a) BG38 filter transmission. b) Corrected SHG signal.

f) Correction given by the polarization beam-splitter:

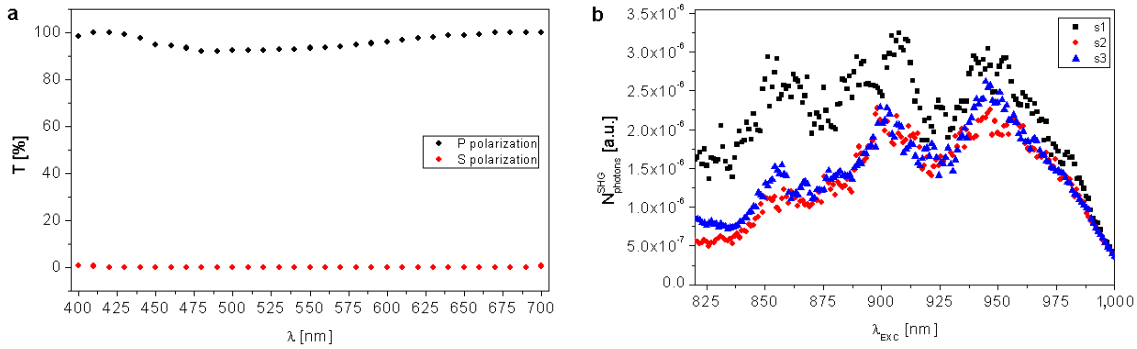

Figure A-7 | a) Transmission of the polarizing beam splitter. b) Corrected SHG signal.

g) Correction for the *Perkin-Elmer* avalanche photodiodes detection efficiency (22 °C):

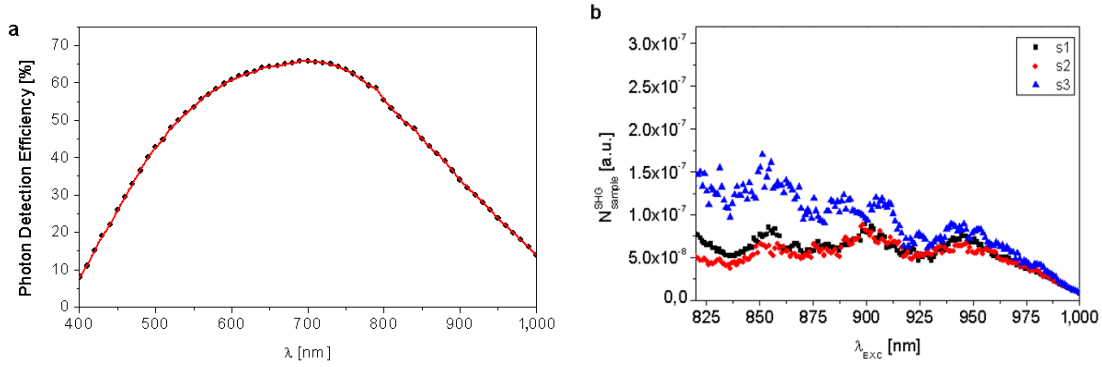

Figure A-8 | a) Detection efficiency of the avalanche photodiodes. b) Corrected SHG signal.

The SHG count rates, shown in Figure A-8(b) relate to the real number of SHG photons detected in *epi*–direction, and correspond to the corrected incident electric field power dependency (Figure A-1(d)) which is probing the sample.

A.3 Extraction of the $\chi^{(2)}(\lambda)$ wavelength dependence

Following equations have been used to extract the second order nonlinear susceptibility tensor $\chi^{(2)}(\lambda)$:

$$\left(\frac{N_{photons}^{SHG}}{s}\right)_{sample} \propto \left(I^{SHG}\right)_{sample} \cdot f_{rep} \cdot \tau \tag{A.3}$$

where: $\left(I^{SHG}\right)_{sample}$ is the peak intensity of second harmonic generation, emitted by the sample; f_{rep} is the pulse repetition rate (80 MHz), τ is the pulse time duration (100 fs).

$$\left(I^{SHG}\right)_{sample} \propto \left(\chi^{(2)}(\lambda)\right)^2 \cdot \left(I^{IR}\right)_{sample}^2 \tag{A.4}$$

where: $\left(I^{IR}\right)_{sample}$ - is the pulsed peak intensity of the excitation IR light.

$$\left(I^{IR}\right)_{sample} = \frac{\left\langle P^{IR}\right\rangle_{sample}}{f_{rep} \cdot \tau} \cdot \frac{1}{S(\lambda)} \propto \frac{\left\langle P^{IR}\right\rangle_{sample}}{f_{rep} \cdot \tau} \cdot \frac{1}{\lambda^2} \tag{A.5}$$

where: $S(\lambda) \approx \pi \cdot w^2$ is the surface of the focal point of the objective at the diffraction limit, and *w* is the waist of the focus point. At the diffraction limit the lateral (*x,y*) waist profile $w(\lambda) \propto \lambda$ (defined in Subsection III.3).

Taking into account equations (A-III), (A-IV4) and (A-V), we finally get:

$$\left(\frac{N_{photons}^{SHG}}{s}\right)_{sample} \propto \left(\chi^{(2)}(\lambda)\right)^2 \cdot \frac{\left\langle P^{IR}\right\rangle_{sample}}{\lambda^4} \cdot \frac{1}{f_{rep} \cdot \tau} \tag{A.6}$$

which finally gives the second order nonlinear susceptibility $\chi^{(2)}(\lambda)$ described by the following equation:

$$\left(\chi^{(2)}(\lambda)\right)^2 \propto \frac{\left(N_{photons}^{SHG} / s\right)_{sample} \cdot \lambda^4}{\left\langle P^{IR}\right\rangle_{sample}^2} \tag{A.7}$$

or:

$$\chi^{(2)}(\lambda) \propto \frac{\sqrt{\left(N_{photons}^{SHG} / s\right)_{sample}} \cdot \lambda^2}{\left\langle P^{IR}\right\rangle_{sample}} \tag{A.8}$$

The results of wavelength dependence of the second order nonlinear susceptibility $\left(\chi^{(2)}(\lambda)\right)^2$ and $\chi^{(2)}(\lambda)$, extracted from the SHG emission spectra of studied CdTe(CdS) core(shell) NPs are shown in Figure A-9.

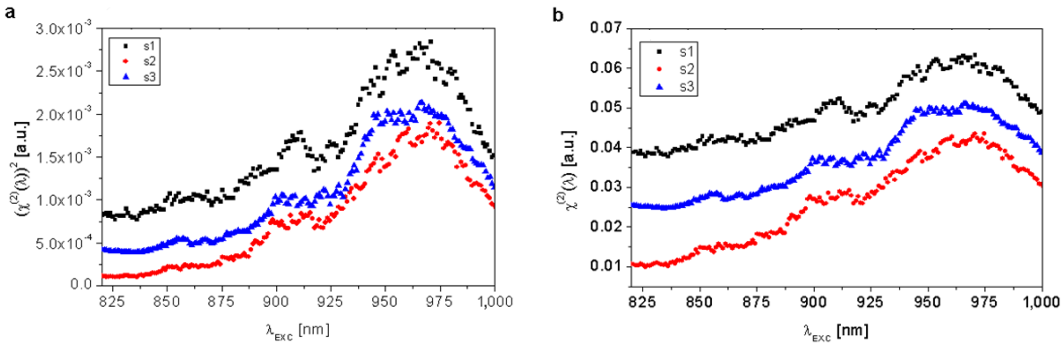

Figure A-9 | Wavelength dependence of the second-order nonlinear susceptibility squared $\left(\chi^{(2)}(\lambda)\right)^2$ (a), and the second-order nonlinear susceptibility $\chi^{(2)}(\lambda)$ (b), obtained from three different CdTe/CdS core/shell QDs. All these almost superimposed curves have been intentionally shifted for clarity.

Dichroic mirror (DM) reflectivity ratio between *p* and *s* incident polarizations (*x* and *y* components, respectively) are related to a dichroism (γ) and a phase shift (φ_{DM}) as follows:

$$\frac{r_p}{r_s} = \frac{r_x}{r_y} = \frac{1}{1-\gamma}\exp\left(-j\varphi_{DM}\right) \tag{A.9}$$

In each case wavelength dependence of the $\chi^{(2)}(\lambda)$ was measured with fixed incident polarization angle, therefore we avoid the correction by γ and φ_{DM} (shown in Figure A-10).

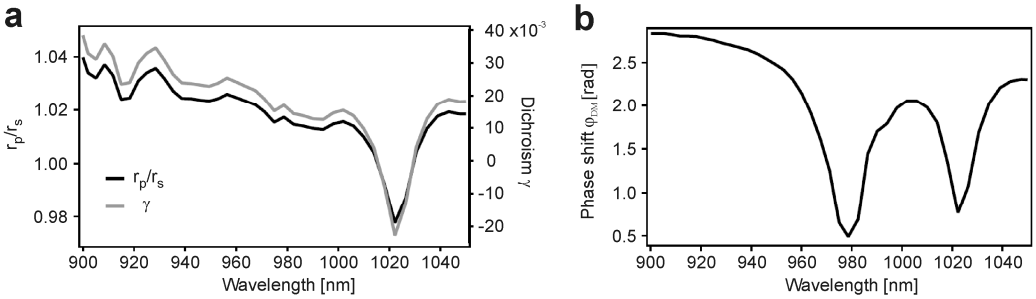

Figure A-10 | Characteristic of the dichroic mirror, measured for its position at 45° in respect to the incident beam: a) *p*/*s* incident polarization reflectivity ratio and the dichroism γ; b) phase shift φ_{DM} (V. Le Floc'h, PhD thesis).[75]

Appendix B: Model for SHG polarization response of spherical CdTe/CdS QDs

B.1 Determining the crystalline lattice orientation of spherical CdTe QDs

In order to determine the Euler set of angles Ω resulting with the SHG polarization components *x* and *y*, which correspond to calculated SF (being a form of the experimental results) we scan over the whole possible sets of Ω angles (23,328,000 possibilities for the increment of 1°).

B.1.1 General form of the SHG polarization response (smoothing function, SF), related to the second-order nonlinear tensor properties

In order to minimize error coming from the noise in the polarization dependence of SHG signal intensity (i.e. non-symmetric positions of the maxima and intensity variations), we have applied SF function, which is directly related to the SHG features understood in general, and can be applied for any type of the crystalline symmetry.

We consider a nonlinear NC, for which the second-order susceptibility tensor is allowed to take any form that can be generally expressed as:[58]

$$d_{ijk} = \begin{array}{c} i = \\ k = \end{array} \begin{array}{c} 1 \\ 1\quad 2\quad 3 \end{array} \begin{array}{c} \qquad\qquad 2 \qquad\qquad\qquad 3 \qquad\qquad\qquad j = \\ \end{array} \left[\begin{pmatrix} d_{111} & d_{112} & d_{113} \\ d_{121} & d_{122} & d_{123} \\ d_{131} & d_{132} & d_{133} \end{pmatrix} \begin{pmatrix} d_{211} & d_{212} & d_{213} \\ d_{221} & d_{222} & d_{223} \\ d_{231} & d_{232} & d_{233} \end{pmatrix} \begin{pmatrix} d_{311} & d_{312} & d_{313} \\ d_{321} & d_{322} & d_{323} \\ d_{331} & d_{332} & d_{333} \end{pmatrix} \right] \begin{array}{c} 1 \\ 2 \\ 3 \end{array} = \frac{1}{2}\chi_{ijk}^{(2)} \qquad \text{(B.1)}$$

Applied optical electric field of a linearly polarized excitation beam is expressed as:

$$E(\alpha) = \begin{pmatrix} E_x(\alpha) \\ E_y(\alpha) \\ E_z(\alpha) \end{pmatrix} = \frac{1}{\sqrt{1+(1-\gamma)^2}} \begin{pmatrix} \cos\alpha \\ (1-\gamma)e^{\varphi_{DM} i} \sin\alpha \\ 0 \end{pmatrix} \qquad \text{(B.2)}$$

where: γ is a dichroism and φ_{DM} is a phase shift - wavelength dependent properties of the dichroic mirror, between *x* and *y* polarization components of the emitted SHG signal (shown in Figure A-10); α is the angle of the linear incident polarization determined in the (x, y) plane.

The i-component of second-order nonlinear polarization is equal to:

$$P_i^{(2)} = 2\sum_j \sum_k d_{ijk} E_j E_k \qquad \text{(B.3)}$$

We assume that *z* polarization component is equal zero, and take into consideration the *x* and *y* polarization components, which can be written in a following form:

$$\begin{aligned} P_x &= 2\left(d_{111}E_xE_x + d_{112}E_xE_y + d_{121}E_yE_x + d_{122}E_yE_y\right) \\ P_y &= 2\left(d_{211}E_xE_x + d_{212}E_xE_y + d_{221}E_yE_x + d_{222}E_yE_y\right) \end{aligned} \qquad \text{(B.4)}$$

In practice the intensity of SHG signal, which is detected by APDs during polarization measurements, is related to:

$$\begin{aligned} I_x &= \kappa \cdot P_x \cdot (P_x)^* \\ I_y &= \kappa \cdot 0.99 \cdot P_y \cdot (P_y)^* \end{aligned} \qquad \text{(B.5)}$$

where: factor 0.99 comes from the transmission coefficients of the polarizing beam splitter, placed at the front of both APDs, κ is a proportionality factor for simplicity set to the unity, without changing on the results.

Derivations of the full form SF's for both: *x* and *y* SHG polarization components are shown below:

$$P_x = 2d_{111}E_xE_x + 2\left(d_{112}+d_{121}\right)E_xE_y + 2d_{122}E_yE_y = \frac{2}{1+(1-\gamma)^2}\cdot \\ \cdot\left(d_{111}\cos^2\alpha + \left(d_{112}+d_{121}\right)(1-\gamma)e^{\varphi_{DM}i}\sin\alpha\cos\alpha + d_{122}(1-\gamma)^2 e^{2\varphi_{DM}i}\sin^2\alpha\right) \tag{B.6}$$

$$\left(P_x\right)^* = \frac{2}{1+(1-\gamma)^2}\left(d_{111}\cos^2\alpha + \left(d_{112}+d_{121}\right)(1-\gamma)e^{-\varphi_{DM}i}\sin\alpha\cos\alpha + \right. \\ \left. + d_{122}(1-\gamma)^2 e^{-2\varphi_{DM}i}\sin^2\alpha\right) \tag{B.7}$$

Thus we can obtain expressions for the angle polarization dependent intensities:

$$I_x = \frac{4}{\left[1+(1-\gamma)^2\right]^2}[{d_{111}}^2\cos^4\alpha + 2\left(d_{112}+d_{121}\right)d_{111}(1-\gamma)\cos\varphi_{DM}\sin\alpha\cos^3\alpha + \\ + \left[\left(d_{112}+d_{121}\right)^2 + 2d_{122}d_{111}\cos 2\varphi_{DM}\right](1-\gamma)^2\sin^2\alpha\cos^2\alpha + \\ + 2\left(d_{112}+d_{121}\right)d_{122}(1-\gamma)^3\cos\varphi_{DM}\sin^3\alpha\cos\alpha + {d_{122}}^2(1-\gamma)^4\sin^4\alpha] = \\ = (\mathrm{x}_0 + \mathrm{x}_1\cdot\tan\alpha + \mathrm{x}_2\cdot\tan^2\alpha + \mathrm{x}_3\cdot\tan^3\alpha + \mathrm{x}_4\cdot\tan^4\alpha)\cos^4\alpha = SF_x \tag{B.8}$$

Which relates to the *x* polarization component on polarization graphs, where:

$$\mathrm{x}_0 = \frac{4}{\left[1+(1-\gamma)^2\right]^2}\cdot {d_{111}}^2 \tag{B.9}$$

$$\mathrm{x}_1 = \frac{4\cdot(1-\gamma)\cos\varphi_{MD}}{\left[1+(1-\gamma)^2\right]^2}\cdot 2\left(d_{112}+d_{121}\right)d_{111} \tag{B.10}$$

$$\mathrm{x}_2 = \frac{4\cdot(1-\gamma)^2}{\left[1+(1-\gamma)^2\right]^2}\cdot\left[\left(d_{112}+d_{121}\right)^2 + 2d_{122}d_{111}\cos 2\varphi_{DM}\right] \tag{B.11}$$

$$\mathrm{x}_3 = \frac{4\cdot(1-\gamma)^3\cos\varphi_{MD}}{\left[1+(1-\gamma)^2\right]^2}\cdot 2\left(d_{112}+d_{121}\right)d_{122} \tag{B.12}$$

$$\mathrm{x}_4 = \frac{4\cdot(1-\gamma)^4}{\left[1+(1-\gamma)^2\right]^2}\cdot {d_{122}}^2 \tag{B.13}$$

SF for the intensity of the *y* SHG polarization component is obtained in a similar way and given by ($\kappa = 1$):

$$\begin{aligned} I_y = \kappa \cdot 0.99 \cdot \frac{4}{\left[1+(1-\gamma)^2\right]^2} [& {d_{211}}^2 \cos^4\alpha + 2d_{211}\left(d_{212}+d_{221}\right)(1-\gamma)\cos\varphi_{DM}\sin\alpha\cos^3\alpha + \\ & + \left[\left(d_{212}+d_{221}\right)^2 + 2\cos 2\varphi_{DM} d_{211} d_{222}\right](1-\gamma)^2\sin^2\alpha\cos^2\alpha + \\ & + 2\left(d_{212}+d_{221}\right)d_{222}(1-\gamma)^3\cos\varphi_{DM}\sin^3\alpha\cos\alpha + {d_{222}}^2(1-\gamma)^4\sin^4\alpha] = \\ & = \kappa \cdot 0.99\left(\mathrm{y}_0 + \mathrm{y}_1\cdot\tan\alpha + \mathrm{y}_2\cdot\tan^2\alpha + \mathrm{y}_3\cdot\tan^3\alpha + \mathrm{y}_4\cdot\tan^4\alpha\right)\cos^4\alpha = SF_y \end{aligned} \tag{B.14}$$

Which relates to the *y* polarization component on polarization graphs, where:

$$\mathrm{y}_0 = 0.99 \cdot \frac{4}{\left[1+(1-\gamma)^2\right]^2} \cdot {d_{211}}^2 \tag{B.15}$$

$$\mathrm{y}_1 = 0.99 \cdot \frac{4\cdot(1-\gamma)\cos\varphi_{MD}}{\left[1+(1-\gamma)^2\right]^2} \cdot 2d_{211}\left(d_{212}+d_{221}\right) \tag{B.16}$$

$$\mathrm{y}_2 = 0.99 \cdot \frac{4\cdot(1-\gamma)^2}{\left[1+(1-\gamma)^2\right]^2}\left[\left(d_{212}+d_{221}\right)^2 + 2d_{211}d_{222}\cos 2\varphi_{DM}\right] \tag{B.17}$$

$$\mathrm{y}_3 = 0.99 \cdot \frac{4\cdot(1-\gamma)^3\cos\varphi_{MD}}{\left[1+(1-\gamma)^2\right]^2} \cdot 2\left(d_{212}+d_{221}\right)d_{222} \tag{B.18}$$

$$\mathrm{y}_4 = 0.99 \cdot \frac{4\cdot(1-\gamma)^4}{\left[1+(1-\gamma)^2\right]^2} \cdot {d_{222}}^2 \tag{B.19}$$

Note that we use only sets of: d_{111}, d_{112}, d_{121}, d_{122}, and d_{211}, d_{212}, d_{221}, d_{222} tensor components in order to determine *x* and *y* coefficients.

These $x(y)_0$, …, $x(y)_4$, coefficients are unknown, and can be determined from the experimental data, by solving over-determined system of equations $B\vec{x} = \vec{I}_x$ and $B\vec{y} = \vec{I}_y$ using the least square method, where :

$$B=\begin{pmatrix}\cos^4(2^\circ)\\ \cos^4(4^\circ)\\ \vdots\\ \cos^4(360^\circ)\end{pmatrix}\begin{pmatrix}1 & \tan(2^\circ) & \tan^2(2^\circ) & \tan^3(2^\circ) & \tan^4(2^\circ)\\ 1 & \tan(4^\circ) & \tan^2(4^\circ) & \tan^3(4^\circ) & \tan^4(4^\circ)\\ \vdots & \vdots & \vdots & \vdots & \vdots\\ 1 & \tan(360^\circ) & \tan^2(360^\circ) & \tan^3(360^\circ) & \tan^4(360^\circ)\end{pmatrix} \tag{B.20}$$

is the coefficient matrix (written for 2° increment, used for collection of the raw data in experiment), and $\vec{I}_{x(y)}(\alpha)=\begin{pmatrix}I_{x(y)}(2^\circ)\\ I_{x(y)}(4^\circ)\\ \vdots\\ I_{x(y)}(360^\circ)\end{pmatrix}$ are the experimentally obtained values of SHG intensities. The least square method is based on transformation of over-determined system of equations into square system by multiplying both sides of equation on the left, by a transposed coefficient matrix: $\left(B^{\mathrm{T}}B\right)\vec{\mathrm{x}}(\vec{\mathrm{y}})=B^{\mathrm{T}}\vec{I}_{x(y)}$, therefore missing *i* coefficients (*i* = 0, …,4) of the SF function can be found as: $\vec{\mathrm{x}}(\vec{\mathrm{y}})_i=\left(B^{\mathrm{T}}B\right)^{-1}B^{\mathrm{T}}\vec{I}_{x(y)}$.

B.1.2 Positions of the maxima

Positions of the SF maxima are determined by calculation of the roots of first-order SF derivative (and by analysis of the sign of its second-order derivative, which in fact has the same form), here shown for I_x:

$$\begin{aligned}\frac{dI_x}{d\alpha}&=\mathrm{x}_0(-4\cos^3\alpha\sin\alpha)+\mathrm{x}_1(\cos^4\alpha-3\cos^2\alpha\sin^2\alpha)+\\&+\mathrm{x}_2(2\cos^3\alpha\sin\alpha-2\cos\alpha\sin^3\alpha)+\\&+\mathrm{x}_3(3\cos^2\alpha\sin^2\alpha-\sin^4\alpha)+\mathrm{x}_4(4\cos\alpha\sin^3\alpha)=\\&=\mathrm{x}_1\cos^4\alpha+(2\mathrm{x}_2-4\mathrm{x}_0)\cos^3\alpha\sin\alpha+(3\mathrm{x}_3-3\mathrm{x}_1)\cos^2\alpha\sin^2\alpha+\\&+(4\mathrm{x}_4-2\mathrm{x}_2)\cos\alpha\sin^3\alpha-\mathrm{x}_3\sin^4\alpha=\\&=(\mathrm{x}_1+(2\mathrm{x}_2-4\mathrm{x}_0)\tan\alpha+(3\mathrm{x}_3-3\mathrm{x}_1)\tan^2\alpha+(4\mathrm{x}_4-2\mathrm{x}_2)\tan^3\alpha-\mathrm{x}_3\tan^4\alpha)\cos^4\alpha=\\&=(\mathrm{x'}_0+\mathrm{x'}_1\tan\alpha+\mathrm{x'}_2\tan^2\alpha+\mathrm{x'}_3\tan^3\alpha+\mathrm{x'}_4\tan^4\alpha)\cos^4\alpha\end{aligned} \tag{B.21}$$

where: $\mathrm{x'}_0=\mathrm{x}_1;\quad \mathrm{x'}_1=2\mathrm{x}_2-4\mathrm{x}_0;\quad \mathrm{x'}_2=3\mathrm{x}_3-3\mathrm{x}_1;\quad \mathrm{x'}_3=4\mathrm{x}_4-2\mathrm{x}_2;\quad \mathrm{x'}_4=-\mathrm{x}_3$, or for all *n*-order SF derivatives:

$$\frac{d^n I_x}{d\alpha^n} = (\mathrm{x}_0^{(n)} + \mathrm{x}_1^{(n)}\tan\alpha + \mathrm{x}_2^{(n)}\tan^2\alpha + \mathrm{x}_3^{(n)}\tan^3\alpha + \mathrm{x}_4^{(n)}\tan^4\alpha)\cos^4\alpha \tag{B.22}$$

where the set of coefficients are related to the one-order lower derivatives:

$$\begin{aligned}
\mathrm{x}_0^{(n)} &= \mathrm{x}_1^{(n-1)} \\
\mathrm{x}_1^{(n)} &= 2\mathrm{x}_2^{(n-1)} - 4\mathrm{x}_0^{(n-1)} \\
\mathrm{x}_2^{(n)} &= 3\mathrm{x}_3^{(n-1)} - 3\mathrm{x}_1^{(n-1)} \\
\mathrm{x}_3^{(n)} &= 4\mathrm{x}_4^{(n-1)} - 2\mathrm{x}_2^{(n-1)} \\
\mathrm{x}_4^{(n)} &= -\mathrm{x}_3^{(n-1)}
\end{aligned} \tag{B.23}$$

The roots of SF derivatives are equivalent to roots of fourth-degree polynomial:

$$\mathrm{x'}_0 + \mathrm{x'}_1 t + \mathrm{x'}_2 t^2 + \mathrm{x'}_3 t^3 + \mathrm{x'}_4 t^4 = 0, \quad t = \tan\alpha \tag{B.24}$$

and the positions of the maxima are equal to $\alpha = arc\tan(t)$, if only the imaginary part of the roots *t* are equal to zero and the values of second-order derivative in *t* are negative.

For $\alpha = \frac{2k+1}{2}\pi, \quad k = 0, 1, 2, \ldots$, above mentioned conditions are not true, however this relates only to a case of perfectly localized maxima at 90° (or -90°).

B.1.3 Direct simulation of the CdTe SHG response

Simulation process has three steps:

a) Rotation of the second-order susceptibility tensor of the NC over three Euler angles Ω:

$$d_{xyz} = \Omega(\varphi, \theta, \psi) \cdot d_{XYZ} \tag{B.25}$$

where, as shown in the Section III.2, the *d*-matrix of CdTe has a form of:

$$d_{XYZ} = \begin{bmatrix} 0 & 0 & 0 & d_{14} & 0 & 0 \\ 0 & 0 & 0 & 0 & d_{25} = d_{14} & 0 \\ 0 & 0 & 0 & 0 & 0 & d_{36} = d_{14} \end{bmatrix} \tag{B.26}$$

For convenience of further simulation we assume $d_{14} = 1$;

b) Applying the linearly polarized incident optical electric field:

$$P_i^{(2)} = 2\sum_{j,k} d_{ijk} E_j E_k \tag{B.27}$$

c) Calculation of the SHG intensities for both: *x* and *y* components, in order to fit with the experimental measurements:

$$I_i = P_i \cdot (P_i)^* \tag{B.28}$$

Following equation (B.26) we can express the *d*-matrix as:

$$d_{XYZ} = d_{14}\left[\begin{pmatrix}0&0&0\\0&0&1\\0&1&0\end{pmatrix}\begin{pmatrix}0&0&1\\0&0&0\\1&0&0\end{pmatrix}\begin{pmatrix}0&1&0\\1&0&0\\0&0&0\end{pmatrix}\right] \tag{B.29}$$

In order to determine the spatial orientation of the spherical CdTe QDs we use the (*z*-*y*-*z*) convention for the Euler set of angles, for which the rotation matrix is expressed as:

$$\Omega(\phi,\theta,\psi) = \begin{bmatrix}\cos\phi\cos\theta\cos\psi - \sin\phi\sin\psi & -\cos\phi\cos\theta\sin\psi - \sin\phi\cos\psi & \cos\phi\sin\theta\\ \sin\phi\cos\theta\cos\psi + \cos\phi\sin\psi & -\sin\phi\cos\theta\sin\psi + \cos\phi\cos\psi & \sin\phi\sin\theta\\ -\sin\theta\cos\psi & \sin\theta\sin\psi & \cos\theta\end{bmatrix} \tag{B.30}$$

Details of the (*z*-*y*-*z*) convention are given below in Appendix B.2.

Following the expressions (B.25) and (B.30) we obtain:

$$d_{xyz} = \Omega(\phi,\theta,\psi)\cdot d_{XYZ} = \left[\begin{pmatrix}\mathrm{P}&\mathrm{A}&\mathrm{B}\\\mathrm{A}&\mathrm{C}&\mathrm{D}\\\mathrm{B}&\mathrm{D}&\mathrm{E}\end{pmatrix}\begin{pmatrix}\mathrm{A}&\mathrm{C}&\mathrm{D}\\\mathrm{C}&\mathrm{Q}&\mathrm{F}\\\mathrm{D}&\mathrm{F}&\mathrm{G}\end{pmatrix}\begin{pmatrix}\mathrm{B}&\mathrm{D}&\mathrm{E}\\\mathrm{D}&\mathrm{F}&\mathrm{G}\\\mathrm{E}&\mathrm{G}&\mathrm{R}\end{pmatrix}\right] \tag{B.31}$$

where:

$\mathrm{P} = 6(def - ac)(-dec - af)bd$
$\mathrm{Q} = 6(aef + dc)(-aec + df)ab$
$\mathrm{R} = 6(-bf)bce$

$$A = 2(def - ac)(-dec - af)ab + 2(def - ac)(-aec + df)bd + 2(aef + dc)(-dec - af)bd$$
$$B = 2(def - ac)(-dec - af)e + 2(def - ac)bdbc + 2(-dec - af)(-bf)bd$$
$$C = 2(def - ac)(-aec + df)ab + 2(aef + dc)(-dec - af)ab + 2(aef + dc)(-aec + df)bd$$
$$E = 2(def - ac)bce + 2(-dec - af)(-bf)e + 2bd(-bf)bc$$
$$F = 2(aef + dc)(-aec + df)e + 2(aef + dc)abbc + 2(-aec + df)(-bf)ab$$
$$G = 2(-aec + df)(-bf)e + 2(-bf)abbc + 2(aef + dc)bce$$

$$D = (def - ac)abbc + (def - ac)(-aec + df)e + (-dec - af)(-bf)ab + \\ + (aef + dc)(-dec - af)e + (-aec + df)(-bf)bd + (aef + dc)bcbd$$

$$\text{and: } a = \sin\phi \quad d = \cos\phi \quad b = \sin\theta \quad e = \cos\theta \quad c = \sin\psi \quad f = \cos\psi$$

Applying expressions from (B.8) to (B.19), we obtain the coefficients of desired fit function for SHG polarization response of the CdTe NC, spatially characterized by set of Euler angles Ω:

$$x_0 = \frac{4}{\left[1 + (1-\gamma)^2\right]^2} \cdot P^2 \tag{B.32}$$

$$x_1 = \frac{16 \cdot (1-\gamma)\cos\varphi_{MD}}{\left[1 + (1-\gamma)^2\right]^2} \cdot A \cdot P \tag{B.33}$$

$$x_2 = \frac{8 \cdot (1-\gamma)^2}{\left[1 + (1-\gamma)^2\right]^2} \cdot \left[2A^2 + C \cdot P \cdot \cos\left(2\varphi_{MD}\right)\right] \tag{B.34}$$

$$x_3 = \frac{16 \cdot (1-\gamma)^3 \cos\varphi_{MD}}{\left[1 + (1-\gamma)^2\right]^2} \cdot A \cdot C \tag{B.35}$$

$$x_4 = \frac{4 \cdot (1-\gamma)^4}{\left[1 + (1-\gamma)^2\right]^2} \cdot C^2 \tag{B.36}$$

$$y_0 = 0.99 \cdot \frac{4}{\left[1 + (1-\gamma)^2\right]^2} \cdot A^2 \tag{B.37}$$

$$y_1 = 0.99 \cdot \frac{16 \cdot (1-\gamma)\cos\varphi_{MD}}{\left[1+(1-\gamma)^2\right]^2} \cdot A \cdot C \tag{B.38}$$

$$y_2 = 0.99 \cdot \frac{8 \cdot (1-\gamma)^2}{\left[1+(1-\gamma)^2\right]^2}\left[2 \cdot C^2 + A \cdot Q \cdot \cos\left(2\varphi_{MD}\right)\right] \tag{B.39}$$

$$y_3 = 0.99 \cdot \frac{16 \cdot (1-\gamma)^3 \cos\varphi_{MD}}{\left[1+(1-\gamma)^2\right]^2} \cdot Q \cdot C \tag{B.40}$$

$$y_4 = 0.99 \cdot \frac{4 \cdot (1-\gamma)^4}{\left[1+(1-\gamma)^2\right]^2} \cdot Q^2 \tag{B.41}$$

Numerical values of introduced dichroic mirror parameters can be found in Figure B-10, and for λ_{exc} = 970 nm (optimal excitation wavelength for spherical dots, used for polarization analysis), we estimate γ = 0.035 and φ_{DM} =1.05 rad. Therefore we obtain:

$$\begin{aligned} x_0 &= 1.0725 \cdot P^2 \\ x_1 &= 2.0597 \cdot A \cdot P \\ x_2 &= 3.9948 \cdot A^2 + 1.0084 \cdot C \cdot P \\ x_3 &= 1.9182 \cdot A \cdot C \\ x_4 &= 0.9301 \cdot C^2 \end{aligned}$$

, and

$$\begin{aligned} y_0 &= 0.99 \cdot 1.0725 \cdot A^2 \\ y_1 &= 0.99 \cdot 2.0597 \cdot A \cdot C \\ y_2 &= 0.99 \cdot (3.9948 \cdot C^2 + 1.0084 \cdot A \cdot Q) \\ y_3 &= 0.99 \cdot 1.9182 \cdot Q \cdot C \\ y_4 &= 0.99 \cdot 0.9301 \cdot Q^2 \end{aligned}$$

B.1.4 Polar graph matching criteria

The difference between calculated and experimental angular positions α_1, and α_2 of the maxima for *x* and *y* polarization components are used to define expressions for different shapes S^{I}:

$$S_x^{\mathrm{I}} = \left(|\alpha_{1\max,x,calc} - \alpha_{1\max,x,\exp}| + |\alpha_{2\max,x,calc} - \alpha_{2\max,x,\exp}| \right) / 45 \tag{B.42}$$

$$S_y^{\mathrm{I}} = \left(|\alpha_{1\max,y,calc} - \alpha_{1\max,y,\exp}| + |\alpha_{2\max,y,calc} - \alpha_{2\max,y,\exp}| \right) / 45 \tag{B.43}$$

where α and 45 factors are in degrees. We have also taken into account the difference in these maxima intensities. Corresponding formulas for different shapes S^{II} are the following:

$$S_x^{II} = \left(\left| 1 - \frac{r_{x,calc}}{r_{x,\exp}} \right| + \left| 1 - \frac{r_{x,\exp}}{r_{x,calc}} \right| \right) \tag{B.44}$$

where: $r_{x,\exp} = \frac{I_{x,\exp}(\alpha_{1\max,x,\exp})}{I_{x,\exp}(\alpha_{1\max,x,\exp}+90)}$, $r_{x,calc} = \frac{I_{x,calc}(\alpha_{1\max,x,calc})}{I_{x,calc}(\alpha_{1\max,x,calc}+90)}$, and:

$$S_y^{II} = \left(\left| 1 - \frac{r_{y,calc}}{r_{y,\exp}} \right| + \left| 1 - \frac{r_{y,\exp}}{r_{y,calc}} \right| \right) \tag{B.45}$$

where: $r_{y,\exp} = \frac{I_{y,\exp}(\alpha_{1\max,y,\exp})}{I_{y,\exp}(\alpha_{1\max,y,\exp}+90)}$, $r_{y,calc} = \frac{I_{y,calc}(\alpha_{1\max,y,calc})}{I_{y,calc}(\alpha_{1\max,y,calc}+90)}$.

Note that the second angle $\alpha_{1\max}$ appear in the denominator of (B.44) and (B.45) is not the position of second maximum $\alpha_{2\max}$, but the position of first maximum shifted by 90º.

Functions from (B.42) to (B.45) are taken into account separately for *x* and *y* polarization components, to create overall differential shapes: $S_{x(y)} = S_{x(y)}^{I} + S_{x(y)}^{II}$.

To further enhance the fitting process we also minimize the following relative shape different function S_{xy}', which takes into account both *x* and *y* components together:

$$S_{xy}' = \left(\left| 1 - \frac{r_{1,xy,calc}}{r_{1,xy,\exp}} \right| + \left| 1 - \frac{r_{1,xy,\exp}}{r_{1,xy,calc}} \right| \right) + \left(\left| 1 - \frac{r_{2,xy,calc}}{r_{2,xy,\exp}} \right| + \left| 1 - \frac{r_{2,xy,\exp}}{r_{2,xy,calc}} \right| \right) \tag{B.46}$$

where: $r_{1,xy,\exp} = \frac{I_{x,\exp}(\alpha_{1\max,x,\exp})}{I_{y,\exp}(\alpha_{1\max,x,\exp})}$, $r_{1,xy,calc} = \frac{I_{x,calc}(\alpha_{1\max,x,calc})}{I_{y,calc}(\alpha_{1\max,x,calc})}$, and $r_{2,xy,\exp} = \frac{I_{x,\exp}(\alpha_{2\max,x,\exp})}{I_{y,\exp}(\alpha_{2\max,x,\exp})}$,

$r_{2,xy,calc} = \frac{I_{x,calc}(\alpha_{2\max,x,calc})}{I_{y,calc}(\alpha_{2\max,x,calc})}$.

Functions (B.42) - (B.46) significantly improve simulation accuracy, providing results, which are in a good agreement with experimentally obtained data. In order to obtain the best fit, simulation program is looking for the smallest possible value of given criteria, which are defined by these functions.

B.2 Euler angles in (z-y-z) convention - rotation of the CdTe QD lattice

The starting point for rotation in (*z*-*y*-*z*) convention is illustrated in Figure IV-7(c). There are three steps in order to obtain final position of the crystalline frame (*X*, *Y*, *Z*), defined by $\Omega=(\phi,\theta,\psi)$ set of angles in respect to the laboratory frame (*x*, *y*, *z*):

1. Rotation about the *z* axis by ψ angle (counterclockwise, from *x* to *y*);
2. Rotation about the *y* axis by θ angle (counterclockwise, from *z* to *x*);
3. Rotation about the *z* axis by ϕ angle (counterclockwise from *x* to *y*).

The rotation matrix takes a form of:

$$M^{xyz}=M_3^{xyz}M_2^{xyz}M_1^{xyz}=\begin{bmatrix}\cos\phi & -\sin\phi & 0\\ \sin\phi & \cos\phi & 0\\ 0 & 0 & 1\end{bmatrix}\begin{bmatrix}\cos\theta & 0 & \sin\theta\\ 0 & 1 & 0\\ -\sin\theta & 0 & \cos\theta\end{bmatrix}\begin{bmatrix}\cos\psi & -\sin\psi & 0\\ \sin\psi & \cos\psi & 0\\ 0 & 0 & 1\end{bmatrix} \quad \text{(B.47)}$$

What leads to the following form:

$$M^{xyz}=\begin{bmatrix}\cos\phi\cos\theta\cos\psi-\sin\phi\sin\psi & -\cos\phi\cos\theta\sin\psi-\sin\phi\cos\psi & \cos\phi\sin\theta\\ \sin\phi\cos\theta\cos\psi+\cos\phi\sin\psi & -\sin\phi\cos\theta\sin\psi+\cos\phi\cos\psi & \sin\phi\sin\theta\\ -\sin\theta\cos\psi & \sin\theta\sin\psi & \cos\theta\end{bmatrix} \quad \text{(B.48)}$$

This is equal to the rotation steps of the crystalline frame (*X*, *Y*, *Z*), defined by $\Omega=(\phi,\theta,\psi)$ set of angles, as shown in Figure IV-6:

1. Rotation about the *Z* axis by ϕ angle (counterclockwise, from *X* to *Y*);
2. Rotation about the new *Y* axis by θ angle (counterclockwise, from *Z* to new *X*);
3. Rotation about the new *Z* axis by ψ angle (counterclockwise from new *X* to new *Y*).

Appendix C: Model for SHG polarization response of RD QD heterostructures

C.1 Determining the crystalline lattice orientation of RD CdTe/CdS QD heterostructures

Simulation program for RD CdTe/CdS hybrids is based on the same idea like the one described for spherical dots, however, due to the complexity of the whole structure, and different nonlinear properties of CdTe and CdS materials it has to include new effects, such as interference occurring between two SHG fields, as well as morphological features of the overall structure. Relative orientation of the CdTe and CdS lattices is shown in Figure II-8, here we give the rotation matrices for CdS and CdTe crystalline lattices.

1. Rotation matrix of the CdTe crystalline unit cell:

A) First rotation of the $[111]$ axis into the (x, y) plane, in order to orient it at 45° in respect to both x and y axis of the laboratory frame. The angle between $[111]$ of the CdTe cube and the (x, y) plane is equal to $\alpha = \arcsin\left(\frac{1}{\sqrt{3}}\right) = \arccos\left(\frac{\sqrt{2}}{\sqrt{3}}\right) = \operatorname{arctg}\left(\frac{1}{\sqrt{2}}\right)$, and the rotation axis is oriented along the $[1\bar{1}0]$ direction, for which the unit vector is:

$$\hat{u} = \begin{pmatrix} \hat{u}_x \\ \hat{u}_y \\ \hat{u}_z \end{pmatrix} = \begin{pmatrix} \frac{1}{\sqrt{2}} \\ \frac{-1}{\sqrt{2}} \\ 0 \end{pmatrix} \tag{C.1}$$

According to the Rodrigues rotation formula, the rotation matrix is equal to:

$$R_{\mathrm{CdTe,I}} = \hat{u}\hat{u}^{\mathrm{T}} + (I - \hat{u}\hat{u}^{\mathrm{T}})\cos\alpha + [\hat{u}]_{\times}\sin\alpha \tag{C.2}$$

where: $[\hat{u}]_{\times}\mathrm{v} = \hat{u}\times\mathrm{v}$, $\hat{u}\hat{u}^{\mathrm{T}} = \begin{pmatrix} \frac{1}{\sqrt{2}} \\ \frac{-1}{\sqrt{2}} \\ 0 \end{pmatrix}\begin{pmatrix} \frac{1}{\sqrt{2}} & \frac{-1}{\sqrt{2}} & 0 \end{pmatrix} = \begin{pmatrix} \frac{1}{2} & -\frac{1}{2} & 0 \\ -\frac{1}{2} & \frac{1}{2} & 0 \\ 0 & 0 & 0 \end{pmatrix}$, $I - \hat{u}\hat{u}^{\mathrm{T}} = \begin{pmatrix} \frac{1}{2} & \frac{1}{2} & 0 \\ \frac{1}{2} & \frac{1}{2} & 0 \\ 0 & 0 & 1 \end{pmatrix}$,

$\sin(-\alpha) = -\frac{1}{\sqrt{3}}$, and $\cos(-\alpha) = \cos\alpha = \frac{\sqrt{2}}{\sqrt{3}} = \frac{2}{\sqrt{6}}$ (where ‘minus‘ come from the clockwise direction of rotation), therefore:

$$(I - \hat{u}\hat{u}^{\mathrm{T}})\cos\alpha = \begin{pmatrix} \frac{1}{\sqrt{6}} & \frac{1}{\sqrt{6}} & 0 \\ \frac{1}{\sqrt{6}} & \frac{1}{\sqrt{6}} & 0 \\ 0 & 0 & \frac{2}{\sqrt{6}} \end{pmatrix} \tag{C.3}$$

$$[\hat{u}]_{\times} = \begin{pmatrix} 0 & -\hat{u}_z & \hat{u}_y \\ \hat{u}_z & 0 & -\hat{u}_x \\ -\hat{u}_y & \hat{u}_x & 0 \end{pmatrix} = \begin{pmatrix} 0 & 0 & \frac{-1}{\sqrt{2}} \\ 0 & 0 & \frac{-1}{\sqrt{2}} \\ \frac{1}{\sqrt{2}} & \frac{1}{\sqrt{2}} & 0 \end{pmatrix} \tag{C.4}$$

$$[\hat{u}]_{\times}\sin\alpha=\begin{pmatrix}0 & 0 & \frac{1}{\sqrt{6}}\\ 0 & 0 & \frac{1}{\sqrt{6}}\\ -\frac{1}{\sqrt{6}} & -\frac{1}{\sqrt{6}} & 0\end{pmatrix} \tag{C.5}$$

$$R_{\mathrm{CdTe,I}}=\begin{pmatrix}\frac{1}{2}+\frac{1}{\sqrt{6}} & -\frac{1}{2}+\frac{1}{\sqrt{6}} & \frac{1}{\sqrt{6}}\\ -\frac{1}{2}+\frac{1}{\sqrt{6}} & \frac{1}{2}+\frac{1}{\sqrt{6}} & \frac{1}{\sqrt{6}}\\ -\frac{1}{\sqrt{6}} & -\frac{1}{\sqrt{6}} & \frac{2}{\sqrt{6}}\end{pmatrix} \tag{C.6}$$

B) Rotation of the new $[111]$ axis around *z* axis by 45° in order to orient it along *x* axis.

$$R_{\mathrm{CdTe,II}}=\begin{pmatrix}\cos\alpha & -\sin\alpha & 0\\ \sin\alpha & \cos\alpha & 0\\ 0 & 0 & 1\end{pmatrix} \tag{C.7}$$

where $\alpha=-45^{\circ}$ (clockwise rotation)

$$R_{\mathrm{CdTe,II}}=\begin{pmatrix}\frac{\sqrt{2}}{2} & \frac{\sqrt{2}}{2} & 0\\ \frac{-\sqrt{2}}{2} & \frac{\sqrt{2}}{2} & 0\\ 0 & 0 & 1\end{pmatrix} \tag{C.8}$$

Thus the overall rotation matrix is:

$$R_{\mathrm{CdTe,II+I}}=\begin{pmatrix}\frac{\sqrt{2}}{2} & \frac{\sqrt{2}}{2} & 0\\ \frac{-\sqrt{2}}{2} & \frac{\sqrt{2}}{2} & 0\\ 0 & 0 & 1\end{pmatrix}\begin{pmatrix}\frac{1}{2}+\frac{1}{\sqrt{6}} & -\frac{1}{2}+\frac{1}{\sqrt{6}} & \frac{1}{\sqrt{6}}\\ -\frac{1}{2}+\frac{1}{\sqrt{6}} & \frac{1}{2}+\frac{1}{\sqrt{6}} & \frac{1}{\sqrt{6}}\\ -\frac{1}{\sqrt{6}} & -\frac{1}{\sqrt{6}} & \frac{2}{\sqrt{6}}\end{pmatrix}=\begin{pmatrix}\frac{1}{\sqrt{3}} & \frac{1}{\sqrt{3}} & \frac{1}{\sqrt{3}}\\ -\frac{1}{\sqrt{2}} & \frac{1}{\sqrt{2}} & 0\\ -\frac{1}{\sqrt{6}} & -\frac{1}{\sqrt{6}} & \frac{2}{\sqrt{6}}\end{pmatrix} \tag{C.9}$$

In order to add correctly oriented CdS crystalline lattice, we determine a current orientation of the $[1\,1\,\bar{2}]$ CdTe axis, which is parallel to the *z* axis:

$$\begin{pmatrix} \frac{1}{\sqrt{3}} & \frac{1}{\sqrt{3}} & \frac{1}{\sqrt{3}} \\ -\frac{1}{\sqrt{2}} & \frac{1}{\sqrt{2}} & 0 \\ -\frac{1}{\sqrt{6}} & -\frac{1}{\sqrt{6}} & \frac{2}{\sqrt{6}} \end{pmatrix} \begin{pmatrix} 1 \\ 1 \\ -2 \end{pmatrix} = \begin{pmatrix} 0 \\ 0 \\ -\sqrt{6} \end{pmatrix} \tag{C.10}$$

2. Rotation matrix of the CdS crystalline unit cell:

We assume the $[01\bar{1}0]$ axis to be set along *y* direction, and the $[0001]$ axis along *z* direction

A) Counterclockwise rotation of the $[0001]$ axis from *z* to *x* around *y*, where α = 90°, so $\cos\alpha = 0$, and $\sin\alpha = 1$:

$$R_{\mathrm{CdS,I}} = \begin{pmatrix} \cos\alpha & 0 & \sin\alpha \\ 0 & 1 & 0 \\ -\sin\alpha & 0 & \cos\alpha \end{pmatrix} = \begin{pmatrix} 0 & 0 & 1 \\ 0 & 1 & 0 \\ -1 & 0 & 0 \end{pmatrix} \tag{C.11}$$

B) Rotation of the new $[01\bar{1}0]$ axis to *z*. We assume $[01\bar{1}0] \equiv [010]$, where direction of the $[01\bar{1}0]$ axis is along *y* axis, and then it is rotated from *y* to *z* (around *x*), where α = -90° (clockwise rotation), so $\cos\alpha = 0$, and $\sin\alpha = -1$:

$$R_{\mathrm{CdS,II}} = \begin{pmatrix} 1 & 0 & 0 \\ 0 & \cos\alpha & -\sin\alpha \\ 0 & \sin\alpha & \cos\alpha \end{pmatrix} = \begin{pmatrix} 1 & 0 & 0 \\ 0 & 0 & 1 \\ 0 & -1 & 0 \end{pmatrix} \tag{C.12}$$

Thus the overall rotation of CdS matrix is:

$$R_{\mathrm{CdS}} = R_{\mathrm{CdS,II}} R_{\mathrm{CdS,I}} = \begin{pmatrix} 1 & 0 & 0 \\ 0 & 0 & 1 \\ 0 & -1 & 0 \end{pmatrix} \begin{pmatrix} 0 & 0 & 1 \\ 0 & 1 & 0 \\ -1 & 0 & 0 \end{pmatrix} = \begin{pmatrix} 0 & 0 & 1 \\ -1 & 0 & 0 \\ 0 & -1 & 0 \end{pmatrix} \tag{C.13}$$

Defined orientations of both: CdTe and CdS crystalline lattices in respect to each other are illustrated in Figure II-8.

C.2 Euler angles in (z-y-x) convention - rotation of the CdTe/CdS hybrid structure

To determine spatial position of the rod-on-dot heterostructures we use (*z*-*y*-*z*) Euler angles convention. A starting point for the rotation, as well as relative position of the CdTe core and the CdS rod are illustrated in Figure II-8, where [111] axis of CdTe and [0001] axis of CdS are parallel to the *y* axis of the laboratory frame. There are three steps in order to obtain final position of the crystalline frame (*X*, *Y*, *Z*), defined by $\Omega = (\alpha, \beta, \gamma)$ set of angles in respect to the laboratory frame (*x*, *y*, *z*):

1. Rotation of the hybrid crystalline lattice around the *Z* axis by the angle α (counterclockwise, from *X* to *Y*).
2. Rotation of the hybrid crystalline lattice around the new *Y* axis by the angle β (counterclockwise, from *Z* to a new *X*). β determines the out of (*x*,*y*) plane angle.
3. Rotation of the structure around the new *X* axis by γ (counterclockwise, from a new *Y* to a new *Z*).

These three steps are associated with the laboratory frame (*x*, *y*, *z*) as follows:

1. Rotation of the hybrid crystalline frame around the *x* axis by the angle γ (counterclockwise, from *y* to *z*).
2. Rotation of the hybrid crystalline frame around the *y* axis by the angle β (counterclockwise, from *z* to *x*).
3. Rotation of the hybrid crystalline frame around the *z* axis by the angle α (counterclockwise, from *x* to *y*).

The rotation matrix is determined by hybrid structure matrix multiplication:

$$M^{xyz} = M_3^{xyz} M_2^{xyz} M_1^{xyz} = \begin{bmatrix} \cos\alpha & -\sin\alpha & 0 \\ \sin\alpha & \cos\alpha & 0 \\ 0 & 0 & 1 \end{bmatrix} \begin{bmatrix} \cos\beta & 0 & \sin\beta \\ 0 & 1 & 0 \\ -\sin\beta & 0 & \cos\beta \end{bmatrix} \begin{bmatrix} 1 & 0 & 0 \\ 0 & \cos\gamma & -\sin\gamma \\ 0 & \sin\gamma & \cos\gamma \end{bmatrix} = \quad \text{(C.14)}$$

$$= \begin{bmatrix} \cos\alpha\cos\beta & \cos\alpha\sin\beta\sin\gamma - \sin\alpha\cos\gamma & \cos\alpha\sin\beta\cos\gamma + \sin\alpha\sin\gamma \\ \sin\alpha\cos\beta & \sin\alpha\sin\beta\sin\gamma + \cos\alpha\cos\gamma & \sin\alpha\sin\beta\cos\gamma - \cos\alpha\sin\gamma \\ -\sin\beta & \cos\beta\sin\gamma & \cos\beta\cos\gamma \end{bmatrix}$$

C.3 Direct simulation of the SHG response for RD CdTe/CdS heterostructures – linear combination of the $\chi^{(2)}_{RD}$ hybrid tensor components

The simulation algorithm of the RD QDs SHG polarization response is similar to the one used for a spherical CdTe dots. Direct simulation, however, needs to take into account the morphological properties of the RD QDs structure, which relates to a direct combination of two $\chi^{(2)}_{CdTe(CdS)}$ tensors with their contributions proportional to the volume of each material: $\chi^{(2)}_{RD} \propto \chi^{(2)}_{CdTe} + V_{CdS} \cdot {V_{CdTe}}^{-1} \chi^{(2)}_{CdS}$, as described in Section IV.2.2.1. Volumes were determined following the TEM analysis (Figure II-10), with only one variable which is a CdS rod length, and the volume ratio is $v = V_{CdS} / V_{CdTe} = 3D^2_{CdS} L_{CdS} / 2D^3_{CdTe}$. Sets of: d_{111}, d_{112}, d_{121}, d_{122}, and d_{211}, d_{212}, d_{221}, d_{222} tensor components (for *x* and *y* components of the polarization response), used in equation (B.4) relate here into the whole RD QD structure as follows: $d_{111} = \mathrm{P} + v\mathrm{S}$, $d_{112} = d_{121} = \mathrm{A} + v\mathrm{H}$, $d_{122} = \mathrm{C} + v\mathrm{T}$, $d_{211} = \mathrm{A} + v\mathrm{V}$, $d_{212} = d_{221} = \mathrm{C} + v\mathrm{K}$, and $d_{222} = \mathrm{Q} + v\mathrm{W}$. For simplicity we use:

$$\mathrm{P} = \mathrm{P}_0 {a_{11}}^3 + 3\mathrm{C}_0 a_{11}({a_{12}}^2 + {a_{13}}^2) + \mathrm{F}_0 a_{13}(3{a_{12}}^2 - {a_{13}}^2)$$
$$\mathrm{Q} = \mathrm{P}_0 {a_{21}}^3 + 3\mathrm{C}_0 a_{21}({a_{22}}^2 + {a_{23}}^2) + \mathrm{F}_0 a_{23}(3{a_{22}}^2 - {a_{23}}^2)$$
$$\mathrm{A} = \mathrm{P}_0 {a_{11}}^2 a_{21} + \mathrm{C}_0(2a_{11}a_{12}a_{22} + 2a_{11}a_{13}a_{23} + {a_{12}}^2 a_{21} + {a_{13}}^2 a_{21}) +$$
$$+ \mathrm{F}_0({a_{12}}^2 a_{23} + 2a_{12}a_{13}a_{22} - {a_{13}}^2 a_{23})$$
$$\mathrm{C} = \mathrm{P}_0 a_{11}{a_{21}}^2 + \mathrm{C}_0(2a_{13}a_{21}a_{23} + 2a_{12}a_{21}a_{22} + a_{11}{a_{22}}^2 + a_{11}{a_{23}}^2) +$$
$$+ \mathrm{F}_0(a_{13}{a_{22}}^2 + 2a_{12}a_{22}a_{23} - a_{13}{a_{23}}^2)$$
$$\mathrm{S} = d_{33}{a_{11}}^3 + d_{31}a_{11}({a_{12}}^2 + {a_{13}}^2) + 2d_{15}a_{11}({a_{12}}^2 + {a_{13}}^2)$$
$$\mathrm{T} = d_{33}a_{11}{a_{21}}^2 + d_{31}a_{11}({a_{22}}^2 + {a_{23}}^2) + 2d_{15}a_{21}(a_{12}a_{22} + a_{13}a_{23})$$

$$\mathrm{V} = d_{33}{a_{11}}^2 a_{21} + d_{31}a_{21}({a_{12}}^2 + {a_{13}}^2) + 2d_{15}a_{11}(a_{12}a_{22} + a_{13}a_{23})$$
$$\mathrm{W} = d_{33}{a_{21}}^3 + d_{31}a_{21}({a_{22}}^2 + {a_{23}}^2) + 2d_{15}a_{21}({a_{22}}^2 + {a_{23}}^2)$$
$$\mathrm{H} = d_{33}{a_{11}}^2 a_{21} + d_{31}a_{11}(a_{12}a_{22} + a_{13}a_{23}) + d_{15}(a_{12}a_{11}a_{22} + a_{13}a_{11}a_{23} + {a_{13}}^2 a_{21} + {a_{12}}^2 a_{21})$$
$$\mathrm{K} = d_{33}a_{11}{a_{21}}^2 + d_{31}a_{21}(a_{12}a_{22} + a_{13}a_{23}) + d_{15}(a_{13}a_{21}a_{23} + a_{12}a_{21}a_{22} + a_{11}{a_{23}}^2 + a_{11}{a_{22}}^2)$$

where: $\begin{bmatrix} a_{11} & a_{12} & a_{13} \\ a_{21} & a_{22} & a_{23} \\ a_{31} & a_{32} & a_{33} \end{bmatrix} = \begin{bmatrix} de & dbc-af & dbf+ac \\ ae & abc+df & abf-dc \\ -b & ec & ef \end{bmatrix}$, $a=\sin\alpha, b=\sin\beta, c=\sin\gamma, d=\cos\alpha,$

$e=\cos\beta,$ and $f=\cos\gamma$. Parameters P_0, C_0, F_0, as well as S_0, T_0, K_0 are new nonzero components of the CdTe and CdS *d* matrixes, respectively. For CdTe we rotate tensor: (B.29) by the rotation matrix (C.9), what gives:

$$d_{XYZ'}^{CdTe} = \left[\begin{pmatrix} P_0 & 0 & 0 \\ 0 & C_0 & 0 \\ 0 & 0 & C_0 \end{pmatrix} \begin{pmatrix} 0 & C_0 & 0 \\ C_0 & 0 & F_0 \\ 0 & F_0 & 0 \end{pmatrix} \begin{pmatrix} 0 & 0 & C_0 \\ 0 & F_0 & 0 \\ C_0 & 0 & -F_0 \end{pmatrix} \right] \tag{C.15}$$

and for d_{14} = 64 pm V^{-1} (Winter et al. [5]) results with: P_0 = 73.9, C_0 = -36.95, and F_0 = -52.26 pm V^{-1}.

In case of the CdS rod we rotate following tensor:

$$d_{XYZ}^{CdS} = \left[\begin{pmatrix} 0 & 0 & d_{15} \\ 0 & 0 & 0 \\ d_{15} & 0 & 0 \end{pmatrix} \begin{pmatrix} 0 & 0 & 0 \\ 0 & 0 & d_{15} \\ 0 & d_{15} & 0 \end{pmatrix} \begin{pmatrix} d_{31} & 0 & 0 \\ 0 & d_{31} & 0 \\ 0 & 0 & d_{33} \end{pmatrix} \right] \tag{C.16}$$

by the rotation matrix (C.13), described in Section C.1, what leads to:

$$d_{XYZ'}^{CdS} = \left[\begin{pmatrix} S_0 & 0 & 0 \\ 0 & T_0 & 0 \\ 0 & 0 & T_0 \end{pmatrix} \begin{pmatrix} 0 & K_0 & 0 \\ K_0 & 0 & 0 \\ 0 & 0 & 0 \end{pmatrix} \begin{pmatrix} 0 & 0 & K_0 \\ 0 & 0 & 0 \\ K_0 & 0 & 0 \end{pmatrix} \right] \tag{C.17}$$

The result of this rotation are: $K_0 = d_{15}$ = 44.0 pm V^{-1}, $T_0 = d_{31}$ = 40.2 pm V^{-1}, and $S_0 = d_{33}$ = 77.9 pm V^{-1}, where the nonlinear coefficient values were found in the literature.[77]

C.3.1 Linear combination of the SHG radiated fields

The total radiated SHG field is a combination of nonlinear field terms determined by contributions of CdTe core and CdS rod, as well as interference occurring between (see equation (III.26), Section IV.2.2.1). In order to calculate polarization components of the

$\left|E_{CdTe}\right|^2$ term we use similar way as shown in Section B.1.3, therefore we express the *x* component as:

$$\kappa\left|E_{x,\mathrm{CdTe}}\right|^2 = I_{x,\mathrm{CdTe}} = \\ = (\mathrm{x}_{0,\mathrm{CdTe}} + \mathrm{x}_{1,\mathrm{CdTe}}\tan\alpha + \mathrm{x}_{2,\mathrm{CdTe}}\tan^2\alpha + \mathrm{x}_{3,\mathrm{CdTe}}\tan^3\alpha + \mathrm{x}_{4,\mathrm{CdTe}}\tan^4\alpha)\cos^4\alpha \tag{C.18}$$

where:

$$\mathrm{x}_{0,\mathrm{CdTe}} = \frac{4}{\left[1+(1-\gamma)^2\right]^2}\cdot \mathrm{P}^2 \tag{C.19}$$

$$\mathrm{x}_{1,\mathrm{CdTe}} = \frac{4\cdot(1-\gamma)\cos\varphi_{MD}}{\left[1+(1-\gamma)^2\right]^2}\cdot 4\mathrm{AP} \tag{C.20}$$

$$\mathrm{x}_{2,\mathrm{CdTe}} = \frac{4\cdot(1-\gamma)^2}{\left[1+(1-\gamma)^2\right]^2}\cdot\left[4\mathrm{A}^2 + 2\mathrm{CP}\cos 2\varphi_{DM}\right] \tag{C.21}$$

$$\mathrm{x}_{3,\mathrm{CdTe}} = \frac{4\cdot(1-\gamma)^3\cos\varphi_{MD}}{\left[1+(1-\gamma)^2\right]^2}\cdot 4\mathrm{AC} \tag{C.22}$$

$$\mathrm{x}_{4,\mathrm{CdTe}} = \frac{4\cdot(1-\gamma)^4}{\left[1+(1-\gamma)^2\right]^2}\cdot \mathrm{C}^2 \tag{C.23}$$

Similarly for *y* polarization components we get:

$$\kappa\left|E_{y,\mathrm{CdTe}}\right|^2 = I_{y,\mathrm{CdTe}} = \\ = (\mathrm{y}_{0,\mathrm{CdTe}} + \mathrm{y}_{1,\mathrm{CdTe}}\tan\alpha + \mathrm{y}_{2,\mathrm{CdTe}}\tan^2\alpha + \mathrm{y}_{3,\mathrm{CdTe}}\tan^3\alpha + \mathrm{y}_{4,\mathrm{CdTe}}\tan^4\alpha)\cos^4\alpha \tag{C.24}$$

where:

$$\mathrm{y}_{0,\mathrm{CdTe}} = 0.99\cdot\frac{4}{\left[1+(1-\gamma)^2\right]^2}\cdot \mathrm{A}^2 \tag{C.25}$$

$$\mathrm{y}_{1,\mathrm{CdTe}} = 0.99\cdot\frac{4\cdot(1-\gamma)\cos\varphi_{MD}}{\left[1+(1-\gamma)^2\right]^2}\cdot 4\mathrm{AC} \tag{C.26}$$

$$y_{2,CdTe} = 0.99 \cdot \frac{4 \cdot (1-\gamma)^2}{\left[1+(1-\gamma)^2\right]^2}\left[4C^2 + 2AQ\cos 2\varphi_{DM}\right] \tag{C.27}$$

$$y_{3,CdTe} = 0.99 \cdot \frac{4 \cdot (1-\gamma)^3 \cos\varphi_{MD}}{\left[1+(1-\gamma)^2\right]^2} \cdot 4CQ \tag{C.28}$$

$$y_{4,CdTe} = 0.99 \cdot \frac{4 \cdot (1-\gamma)^4}{\left[1+(1-\gamma)^2\right]^2} \cdot Q^2 \tag{C.29}$$

In similar manner we obtain *x* and *y* components of the $|E_{CdS}|^2$ SHG field term:

$$\kappa\left|E_{x,CdS}\right|^2 = \frac{1}{v^2} I_{x,CdS} = \\ = (x_{0,CdS} + x_{1,CdS}\tan\alpha + x_{2,CdS}\tan^2\alpha + x_{3,CdS}\tan^3\alpha + x_{4,CdS}\tan^4\alpha)\cos^4\alpha \tag{C.30}$$

where:

$$x_{0,CdS} = \frac{4}{\left[1+(1-\gamma)^2\right]^2} \cdot S^2 \tag{C.31}$$

$$x_{1,CdS} = \frac{4 \cdot (1-\gamma)\cos\varphi_{MD}}{\left[1+(1-\gamma)^2\right]^2} \cdot 4SH \tag{C.32}$$

$$x_{2,CdS} = \frac{4 \cdot (1-\gamma)^2}{\left[1+(1-\gamma)^2\right]^2} \cdot \left[4H^2 + 2ST\cos 2\varphi_{DM}\right] \tag{C.33}$$

$$x_{3,CdS} = \frac{4 \cdot (1-\gamma)^3 \cos\varphi_{MD}}{\left[1+(1-\gamma)^2\right]^2} \cdot 4TH \tag{C.34}$$

$$x_{4,CdS} = \frac{4 \cdot (1-\gamma)^4}{\left[1+(1-\gamma)^2\right]^2} \cdot T^2 \tag{C.35}$$

$$\kappa\left|E_{y,CdS}\right|^2 = \frac{1}{v^2} I_{y,CdS} = \\ = (y_{0,CdS} + y_{1,CdS}\tan\alpha + y_{2,CdS}\tan^2\alpha + y_{3,CdS}\tan^3\alpha + y_{4,CdS}\tan^4\alpha)\cos^4\alpha \tag{C.36}$$

where:

$$y_{0,CdS} = 0.99 \cdot \frac{4}{\left[1+(1-\gamma)^2\right]^2} \cdot V^2 \tag{C.37}$$

$$y_{1,CdS} = 0.99 \cdot \frac{4 \cdot (1-\gamma)\cos\varphi_{MD}}{\left[1+(1-\gamma)^2\right]^2} \cdot 4KV \tag{C.38}$$

$$y_{2,CdS} = 0.99 \cdot \frac{4 \cdot (1-\gamma)^2}{\left[1+(1-\gamma)^2\right]^2}\left[4K^2 + 2VW\cos 2\varphi_{DM}\right] \tag{C.39}$$

$$y_{3,CdS} = 0.99 \cdot \frac{4 \cdot (1-\gamma)^3\cos\varphi_{MD}}{\left[1+(1-\gamma)^2\right]^2} \cdot 4KW \tag{C.40}$$

$$y_{4,CdS} = 0.99 \cdot \frac{4 \cdot (1-\gamma)^4}{\left[1+(1-\gamma)^2\right]^2} \cdot W^2 \tag{C.41}$$

In order to calculate *x* and *y* components of the interference term $\left|E^{SHG}_{Interference}\right|$ we use following equations:

$$\kappa\left(E_{x,CdTe}E^*_{x,CdS} + E^*_{x,CdTe}E_{x,CdS}\right) = \frac{1}{\nu}I_{x,interf} = P_{x,CdTe}\left(P_{x,CdS}\right)^* + \left(P_{x,CdTe}\right)^* P_{x,CdS} = \\ = (x_{0,interf} + x_{1,interf} \cdot \tan\alpha + x_{2,interf} \cdot \tan^2\alpha + x_{3,interf} \cdot \tan^3\alpha + x_{4,interf} \cdot \tan^4\alpha)\cos^4\alpha \tag{C.42}$$

where:

$$x_{0,interf} = \frac{4}{\left[1+(1-\gamma)^2\right]^2} \cdot 2PS \tag{C.43}$$

$$x_{1,interf} = \frac{8 \cdot (1-\gamma)\cos\varphi_{MD}}{\left[1+(1-\gamma)^2\right]^2} \cdot 2(PH + AS) \tag{C.44}$$

$$x_{2,interf} = \frac{4 \cdot (1-\gamma)^2}{\left[1+(1-\gamma)^2\right]^2} \cdot \left[8AH + 2(PT + CS)\cos 2\varphi_{DM}\right] \tag{C.45}$$

$$x_{3,interf} = \frac{8 \cdot (1-\gamma)^3\cos\varphi_{MD}}{\left[1+(1-\gamma)^2\right]^2} \cdot 2(AT + CH) \tag{C.46}$$

$$x_{4,\text{interf}} = \frac{4\cdot(1-\gamma)^4}{\left[1+(1-\gamma)^2\right]^2}\cdot 2CT \tag{C.47}$$

and:

$$\kappa\left(E_{y,CdTe}E^*_{y,CdS}+E^*_{y,CdTe}E_{y,CdS}\right)=\frac{1}{v}I_{y,\text{interf}}=P_{y,CdTe}\left(P_{y,CdS}\right)^*+\left(P_{y,CdTe}\right)^*P_{y,CdS}= \\ =(y_{0,\text{interf}}+y_{1,\text{interf}}\cdot\tan\alpha+y_{2,\text{interf}}\cdot\tan^2\alpha+y_{3,\text{interf}}\cdot\tan^3\alpha+y_{4,\text{interf}}\cdot\tan^4\alpha)\cos^4\alpha \tag{C.48}$$

where:

$$y_{0,\text{interf}} = \frac{4}{\left[1+(1-\gamma)^2\right]^2}\cdot 2AV \tag{C.49}$$

$$y_{1,\text{interf}} = \frac{8\cdot(1-\gamma)\cos\varphi_{MD}}{\left[1+(1-\gamma)^2\right]^2}\cdot 2(AK+CV) \tag{C.50}$$

$$y_{2,\text{interf}} = \frac{4\cdot(1-\gamma)^2}{\left[1+(1-\gamma)^2\right]^2}\cdot\left[8CK+2(AW+QV)\cos 2\varphi_{DM}\right] \tag{C.51}$$

$$y_{3,\text{interf}} = \frac{8\cdot(1-\gamma)^3\cos\varphi_{MD}}{\left[1+(1-\gamma)^2\right]^2}\cdot 2(CW+QK) \tag{C.52}$$

$$y_{4,\text{interf}} = \frac{4\cdot(1-\gamma)^4}{\left[1+(1-\gamma)^2\right]^2}\cdot 2QW \tag{C.53}$$

The total radiated SHG field obtained from a single RD QD heterostructure is according to equation (III.26) a sum of above SHG field terms. Contribution of each term is determined by a volume proportionality factor between each of the SC material. Experimental data is fitted for given dimensionalities of each part of the RD hybrid structure by rotation over the whole space of the Euler set of angles. We use the same matching criteria as described in Appendix B.1.4 in order to obtain the best polar graph fit function.

Appendix D: The list of publications

The list of publications discussed within this thesis:

1. Zielinski, M., Oron, D., Chauvat, D., Zyss, J. Second-harmonic generation from a single core-shell quantum dot. *Small*, **5,** (24), 2835-2840 (2009).
2. Winter, S., Zielinski, M., Chauvat, D., Zyss, J., Oron, D. The Second Order Nonlinear Susceptibility of Quantum Confined Semiconductors – a Single Dot Study. *The Journal of Physical Chemistry C, accepted.*
3. Zielinski, M., Winter, S., Kolkowski, R., Nogues, C., Oron, D., Zyss, J., Chauvat, D. Nanoengineering the second order susceptibility in semiconductor quantum dot heterostructures. *Optics Express, accepted*.

The list of my publications not discussed within this manuscript:

1. Mojzisova, H., Olesiak, J., Zielinski, M., Matczyszyn, K., Chauvat, D., Zyss, J. Polarization sensitive two-photon microscopy study of the organization of liquid crystalline DNA, *Biophysical Journal*, **97,** 2348-2357 (2009). (*attached*)
2. Olesiak, J., Matczyszyn, K., Mojzisova, H., Zielinski, M., Chauvat, D., Zyss, J. Liquid crystalline phases in DNA and dye-doped DNA solutions analysed by polarized linear and nonlinear microscopy and differential scanning calorimetry. *Materials Science – Poland*, **27,** (3), 813-823 (2009).
3. Slablab, A., Le Xuan, L., Zielinski, M., Jacques, V., Chauvat, D., Roch, J.-F. Efficient second-harmonic generation from a single gold dimer. *In submission.* (*attached*)
4. Olesiak, J., Mojzisova, H., Chauvat, D., Zielinski, M., Matczyszyn, K., Tauc, P., Zyss, J. Liquid crystall phases of DNA: evaluation of DNA organisation by two-photon fluorescence microscopy and polarization analysis. *Biopolymers, accepted.*

2348 Biophysical Journal Volume 97 October 2009 2348–2357

Polarization-Sensitive Two-Photon Microscopy Study of the Organization of Liquid-Crystalline DNA

Halina Mojzisova,[†‡*] Joanna Olesiak,[§] Marcin Zielinski,[†] Katarzyna Matczyszyn,[§] Dominique Chauvat,[†] and Joseph Zyss[†]

[†]Laboratoire de Photonique Quantique et Moléculaire, and [‡]Laboratoire de Biotechnologies et de Pharmacologie Appliquée, Institut d'Alembert, Ecole Normale Supérieure de Cachan, Cachan, France; and [§]Group of Physics and Chemistry of Molecular Materials, Institute of Physical and Theoretical Chemistry, Wroclaw University of Technology, Wroclaw, Poland

ABSTRACT Highly concentrated DNA solutions exhibit self-ordering properties such as the generation of liquid-crystalline phases. Such organized domains may play an important role in the global chromatin topology but can also be used as a simple model for the study of more complex 3D DNA structures. In this work, using polarized two-photon fluorescence microscopy, we report on the orientation of DNA molecules in liquid-crystalline phases. For this purpose, we analyze the signal emitted by fluorophores that are noncovalently bound to DNA strands. In nonlinear processes, excitation occurs exclusively in the focal volume, which offers advantages such as the reduction of photobleaching of out-of-focus molecules and intrinsic 3D sectioning capability. Propidium iodide and Hoechst, two fluorophores with different DNA binding modes, have been considered. Polarimetric measurements show that the dyes follow the alignment with respect to the DNA strands and allow the determination of the angles between the emission dipoles and the longitudinal axis of the DNA double strand. These results provide a useful starting point toward the application of two-photon polarimetry techniques to determine the local orientation of condensed DNA in physiological conditions.

INTRODUCTION

In living systems, DNA molecules are tightly packed in micrometric cell compartments. The condensation factor is very high, and DNA local concentration may reach values up to several hundreds of mg/mL (1,2). In such conditions, to decrease the entropy, the intermolecular volume is diminished by setting up a supramolecular order (3). The creation of organized structures such as liquid-crystalline domains was indeed observed in concentrated DNA (4), in both nucleosome particles and plasmid solutions, and in dinoflagellate chromosomes (5,6). These self-ordering properties are of considerable interest, because they might be related to the complex 3D chromatin topology known to influence the transcription and regulation processes in the cell nucleus (7).

The analysis of DNA liquid-crystalline domains represents the first step toward the investigation of DNA condensed states and the DNA topology in vivo. The creation of specific DNA liquid-crystalline phases gives rise to structures presenting long-term order in at least one direction. It occurs at specific temperature and concentration conditions. In simplified in vitro systems, these conditions can be achieved by increasing DNA concentration to a sufficient level. Depending on the characteristics of DNA molecules, the values of critical concentrations for the transition between the isotropic and anisotropic phases are also governed by temperature, ionic strength of the solution, and number and nature of DNA basepairs (1,8,9).

The organization of liquid-crystalline domains is mainly studied by polarized light microscopy, differential scanning calorimetry, nuclear magnetic resonance, and x-ray or electron microscopy techniques (1,8,10). These methods have brought a wealth of information about DNA liquid-crystalline phases, but they are difficult to apply to three-dimensional investigations of micrometer-thick samples in a nondestructive manner. Conversely, laser scanning microscopy techniques, such as confocal or multiphoton microscopy, are known to be well adapted to this type of study (11,12). In the latter case, the infrared pulsed excitation occurs efficiently only in the focal volume, whereas the sample or the laser beam is translated in three directions to allow a ''point-by-point'' 3D scanning. Moreover this local excitation permits minimization of the photobleaching of out-of-focus molecules. The potential of this technique can be enhanced by polarimetric analysis of two-photon processes, as was shown recently in the investigation of nonlinear properties of isolated nanoparticles (13–16).

In this work, we propose to investigate the ordering of DNA by means of polarization-sensitive two-photon microscopy. By analyzing the fluorescence emitted by fluorophores associated to DNA, we show that it is possible to extract the binding angles between the emission dipoles of these molecules and the longitudinal axis of the DNA double strands at the scale of the focal volume. We choose to work with well known DNA markers, i.e., an intercalator—propidium iodide (PI)—and Hoechst dye, which binds to the AT-rich regions in the minor groove of the DNA double helix (17,18). Comparing two dyes with different orientations relative to the DNA axis allows us to evidence the ability of

Submitted January 29, 2009, and accepted for publication July 8, 2009.

*Correspondence: halinam@gmail.com

Editor: Jonathan B. Chaires.

© 2009 by the Biophysical Society

0006-3495/09/10/2348/10 $2.00

doi: 10.1016/j.bpj.2009.07.053

polarimetric analysis to distinguish between two binding modes. In the first step, we evaluate to which extent these dyes follow the DNA organization. In the next step, by adjusting the simulated theoretical data to the experimental curves, we extract the binding angles. Once the binding parameters are established, it becomes possible to infer the DNA ordering properties in liquid-crystalline phases in micrometric domains with high lateral and axial resolution.

MATERIALS AND METHODS

Theory

The two-photon excited volume associated to a highly focused infrared beam is of the order of a micrometer cube. Therefore a lot of dye molecules bound to DNA are excited and detected within the acquisition time. To simulate this ensemble of molecules, a simplified model was used (Fig. 1).

For each fluorophore, the emission dipole $\vec{\mu}_{em}$ forms a random azimuthal angle ψ with respect to the main molecular axis of the DNA double strand. When averaging this orientation by rotating $\vec{\mu}_{em}$ by 360° around the DNA molecule, the ensemble of dipoles is uniformly spread over a "cone" of opening angle ψ. Variations of ψ following small deviations of the DNA strand are taken into account by thickening this cone by an angular variable $\Delta\psi$.

Theoretical calculations are based on the model developed by Le Floc'h and co-workers (13,19). The macroscopic xy coordinates correspond to the plane of the sample, whereas the z axis is along the optical axis of the microscope, perpendicular to the sample. Rotation of the sample around the z axis in the macroscopic xy plane is parameterized by the angle ϕ.

For each molecule, the measured fluorescence intensity, I_{TPFE}, is proportional to the probability of two-photon excitation, P_{abs}, combined with the emission of the fluorescence photon along the direction of the detection, P_{em}

$$I_{TPFE} \propto P_{abs}\, P_{em} \propto |\vec{\mu}_{abs} \times \vec{E}|^4\, |\vec{\mu}_{em} \times \vec{u}_l|^2, \qquad (1)$$

where $\vec{\mu}_{abs}$ and $\vec{\mu}_{em}$ correspond to the absorption and emission dipoles, respectively, $\vec{u}_l$ is the detection polarization, and $\vec{E}$ is the incident field at optical frequency ω. To capture the large number of molecules within the excited volume, this expression has to be integrated over a conical orientation distribution of $\vec{\mu}_{abs}(\Omega)$ and $\vec{\mu}_{em}(\Omega)$, where Ω is the solid angle, leading to

$$I_I^{TPFE}(\alpha) \propto \int |\vec{\mu}_{abs}(\Omega) \times \vec{E}(\alpha)|^4\, |\vec{\mu}_{em}(\Omega) \times \vec{u}_l|^2 d\Omega. \qquad (2)$$

The polarization of $\vec{E}(\alpha)$ at the focal point is obtained through reflection of the incident laser beam on a dichroic mirror (DM) and can be varied. Therefore it is modeled as

$$\vec{E}(\alpha,\delta,\varepsilon,t) = \frac{E}{\left(1+(1-\delta)^2\right)^{1/2}} \begin{bmatrix} \cos\alpha\cos(\omega t) \\ (1-\delta)\sin\alpha\cos(\omega t+\varepsilon) \\ 0 \end{bmatrix}, \qquad (3)$$

where E is the amplitude of the incident field, with α defining the incident polarization angle in the xy reference frame, as illustrated in Fig. 2 *b*. δ and ε are two parameters that account for variation of the electric field by polarization mixing and depolarization effects caused by the setup, mainly due to dichroism and birefringence properties of the DM. δ represents the ratio of the reflectivity, r_p/r_s, of the DM for p (r_p) and s (r_s) components, and ε is the ellipticity induced by the reflection on the DM. This deformation of the initially linear polarization is schematized by the dotted ellipse in Fig. 2 *b*. The fluorescence intensities of the s (I_x) and p (I_y) polarization components are maximal for the direction of the incident electric field corresponding to $\vec{\mu}_{abs}$, assumed here to be parallel to $\vec{\mu}_{em}$. As an example, we took $\vec{\mu}_{em}$ at 45° from the x axis in Fig. 2 *c*.

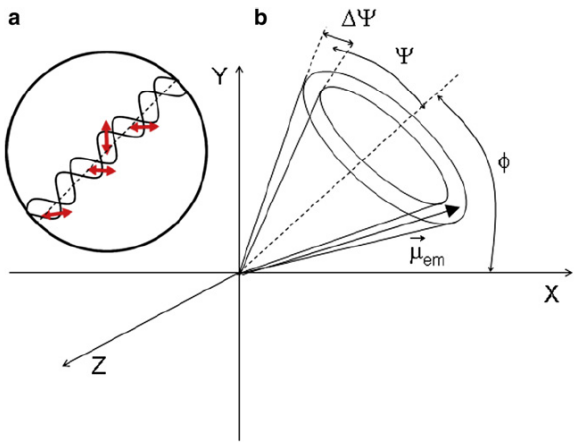

FIGURE 1 (*a*) Simplified model of the binding of an ensemble of molecules to the DNA double strand. (*b*) The emission dipoles, $\vec{\mu}_{em}$, of the dyes follow a conical distribution of a half-angle Ψ with its axis along the DNA molecule. The cone has a variable thickness $\Delta\Psi$. The rotation of the DNA strand in the macroscopic framework xy is accounted for by angle ϕ.

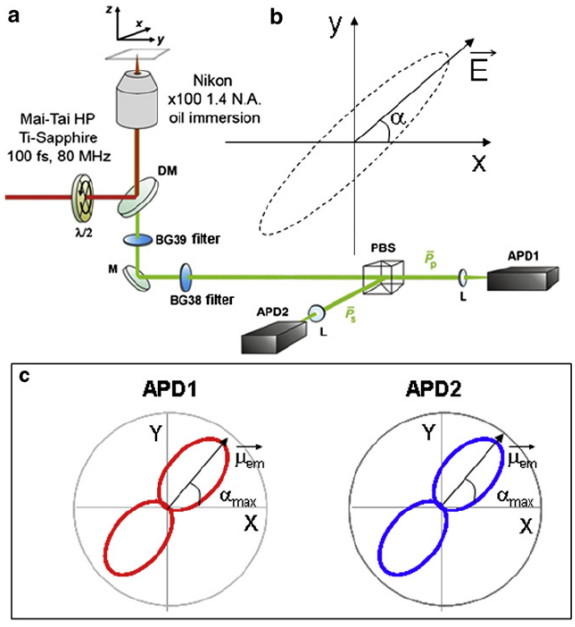

FIGURE 2 (*a*) Scheme of the experimental setup. *DM*, dichroic mirror; *M*, mirror; *PBS*, polarizing beam splitter; *APD*, avalanche photodiode; *L*, lens; *BG39* and *BG38*, filters; $\lambda/2$, half-wave plate. (*b*) For the polarimetry measurement, the incident polarization is rotated by α = 0–360°. In the example presented, α =45°. (*c*) In an anisotropic material, the x and y polarization components of the two-photon fluorescence intensity are measured by two avalanche photodiodes, APD1 and APD2, respectively. α_{max} occurs in the direction parallel to the orientation of the emitting dipoles $\vec{\mu}_{em}$. In the illustrated example, α_{max} = 45°.

The aim of our approach is twofold: 1), with a given orientation of DNA strands, to verify that the angle dependence of the two-photon fluorescence emitted by the dyes fixed to DNA follows our model and subsequent pattern (Figs. 1 and 2) and to determine the binding parameters Ψ and $\Delta\Psi$ for PI and Hoechst; and 2), based on this calibration step, to analyze a priori unknown orientations of DNA strands in various liquid-crystalline domains.

DNA preparation

Salmon DNA was purchased from Sigma-Aldrich (St. Louis, MO). The melting temperature is ~87.5°C. Electrophoresis on agarose gels has revealed a heterogeneous length distribution varying between 260 basepairs (bp) and 6000 bp. The main length of DNA strands is ~2000 bp. The DNA was solubilized in distilled and deionized sterile water for at least 5 h. PI and Hoechst 33342 were purchased from Molecular Probes (Eugene, OR) and the stock solutions were prepared in pure water.

Two kinds of sample were prepared: closed cells and drying droplets. In closed cells, the labeled DNA was solubilized at a concentration of 60 mg/mL. The final concentrations of PI and Hoechst were 0.30 mM and 0.16 mM, respectively, which corresponds to 1 PI molecule/320 bp and 1 Hoechst molecule/600 bp. A 50-μL sample of DNA-dye solution was deposited on a coverslip and covered by another coverslip. The spacer was made from a thin parafilm frame. The samples dried for several hours at room temperature.

For the drying droplet preparation, the DNA concentration was 5 mg/mL. The final dye concentrations were 0.81 mM and 0.67 mM for PI and Hoechst, respectively, which corresponds to 1 PI molecule/10 bp and 1 Hoechst molecule/12 bp. 15 μL of each DNA-dye solution was deposited atop a cleaned coverslip.

In all samples, the presence of liquid-crystalline domains was monitored by polarized light microscopy (PLM), e.g., observation of DNA in white light through crossed polarizers sandwiching the sample.

Two-photon fluorescence microscopy

The scheme of the experimental setup is shown in Fig. 2 *a*. Two-photon microscopy was performed on a Nikon TE 2000-0 ECLIPSE inverted microscope. The excitation is provided by a mode-locked Ti:Sapphire laser (Mai-Tai HP, Spectra Physics, Mountain View, CA) delivering 100-fs pulses with 80-MHz repetition rate. The fundamental wavelength can be tuned from 690 to 1020 nm. The beam is focused on the sample by a high-numerical-aperture Nikon Plan Apo (100×/1.4 NA) oil immersion objective. The lateral and axial spatial resolutions are of the order of 350 and 800 nm, respectively. The signal is collected in epiconfiguration. After passing through the dichroic mirror, the $x(y)$ polarization component that coincides with the $s(p)$ incident polarization on the dichroic mirror is reflected (transmitted) by a polarizing beam-splitter, and the intensity I_x (I_y) is detected separately by an avalanche photodiode (SPCM-AQR-14-FC, Perkin Elmer, Wellesley, MA) working in photon-counting regime. The polarization analysis is performed by recording I_x and I_y simultaneously while rotating the polarization of the incident light from 0° to 360° with a rotating half-wave plate ($\lambda/2$).

One important parameter of the DM is its birefringence, which leads to an ellipticity of the reflected field, accounted for by ε in Eq. 3. Moreover, the multilayer coating on the DM induces a large spectral variation of this ellipticity.

The ellipsometry measurements were performed by an ellipsometer (GESP5, Sopra, Paris, France) illuminated by a white lamp in a configuration where the incidence beam impinges at 45° to the DM surface, as in the microscope.

RESULTS

Polarized light microscopy

As described previously (4,20), DNA in aqueous solution forms multiple lyotropic liquid-crystalline phases (LLC) that can be distinguished at a preliminary level by PLM. Similarly, DNA doped with dye molecules exhibits LLC behavior (21). LLC phases can be observed either in closed LC cells or in drying droplets. These two methods of sample preparation yield different structures at room temperature.

As shown in Fig. 3, *a* and *b*, the closed LC cells filled with solutions of DNA-PI and DNA-Hoechst present PLM images with birefringent phases where DNA strands are aligned in one direction. However, they do not form higher-order structures characteristic of cholesteric and columnar phases. These observations are in agreement with published data concerning the concentration dependence of the creation of anisotropic DNA phases (8).

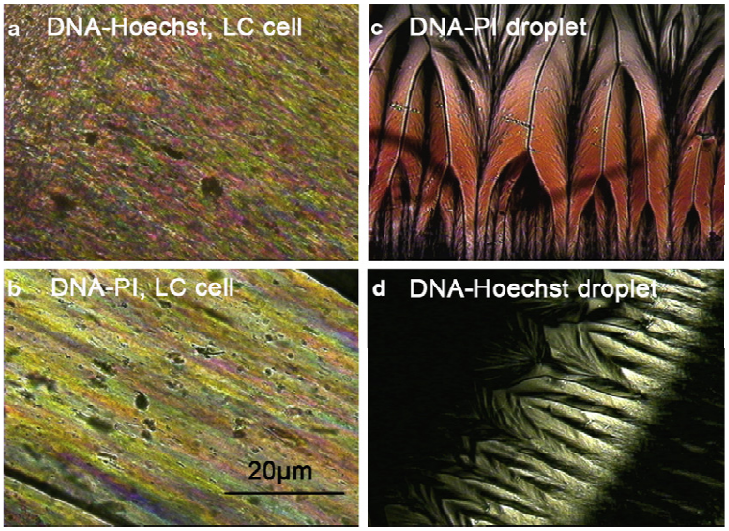

FIGURE 3 PLM images of samples (*a*) LC cell with DNA, $c_{DNA} = 60$ mg/ml, and PI, $c_{PI} = 0.3$ mM. (*b*) Droplets of DNA, $c_{DNA} = 5$ mg/ml, and PI, $c_{PI} = 0.806$ mM. (*c*) LC cell with DNAxs, $c_{DNA} = 60$ mg/ml, and Hoechst, $c_H = 0.16$ mM. (*d*) Droplets of DNA, $c_{DNA} = 5$ mg/ml, and Hoechst, $c_H = 0.67$ mM.

PLM images of DNA-PI and DNA-Hoechst solutions with $c_{DNA} = 5$ mg/mL deposited as droplets are shown in Fig. 3, *c* and *d*. Similar characteristic zig-zag patterns were reported previously by Smalyukh et al. (22) near the rim of the droplet. They correspond to a columnar hexagonal phase with undulations induced by linear defects. In the drying process, DNA chains are deposited along the contact line. Simultaneously, they undulate due to radial stress and form striped domains that are perpendicular to the droplet boundary. Depending on the size of the droplet and the presence of local impurities on the surface of the glass, and probably on the length heterogeneity of DNA strands, different domains are formed. The width of these domains is in the range 5–30 μm for DNA-PI and 4–15 μm for DNA-Hoechst. If the domain thickness is sufficiently high, they become colorful in PLM. DNA strands within one domain are parallel, but they are bent at the border between two domains and form a specific angle with respect to the chains in the adjacent domain. The precise parameters of this structure were evaluated using two-photon microscopy.

Two-photon microscopy

Fig. 4 shows two-photon fluorescence intensity images obtained by scanning the sample together with the corresponding polarization analysis in polar coordinates, which depicts fluorescence intensities I_x and I_y as a function of the incident polarization angle, α. The two-photon fluorescence is emitted by DNA-bound PI and Hoechst. Excitation wavelengths are 920 nm and 810 nm for PI and Hoechst, respectively, and the corresponding maximum average intensities of the incident light are 1 mW and 0.5 mW. These excitation conditions were found experimentally to be the best trade-off between the photostability of the dyes and a sufficient signal/noise ratio. Under such conditions, the intrinsic fluorescence signal of pure DNA is within the noise level, thus below the detection threshold.

In the first step of evaluating the two-photon polarimetry method, we consider an isotropic DNA-PI solution. The fluorescence intensity scan of the DNA-PI solution obtained before the droplet has dried on the glass plate is shown in Fig. 4 *a*. The fluorescence scan is homogeneous. The polar graph (Fig. 4 *b*) shows a characteristic cross pattern for *x* and *y* polarization components, corresponding to random orientation of emitting dipoles. One might have expected a circle-shaped polarization response for each polarization component, in agreement with isotropically oriented dipoles. However, the preferred excitation of the dyes oriented along the polarization axis of the incident light and the detection along *x* and *y* polarization axes lead to a photoselection, well known in fluorescence polarization anisotropy experiments. Indeed, when the incident polarization is rotated by 360° in the *xy* plane and the fluorophore distribution is isotropic, the higher fluorescence intensities along *x* and *y* reflect only the separation of the emitted light by a polarizing beam-splitter along the *x* and *y* components.

In contrast, Fig. 4, *c* and *e*, displays the scanned images of liquid-crystalline domains, where PI- and Hoechst-labeled DNA double strands are aligned along the *y* direction ($\phi = 90°$). The angles of maximum fluorescence intensity in the polar graphs detected along *x* and *y* polarization axes (I_x and I_y) are aligned along the same direction, which clearly indicates the orientation of the emitters. According to these data, it can be roughly estimated that PI (Fig. 4 *d*) is oriented in a direction perpendicular to the DNA double strands ($\Psi \sim 90°$), whereas Hoechst (Fig. 4 *f*) is rather parallel to the DNA molecule ($\Psi \sim 0°$). It should be noted that the orientation of the samples corresponds to the neutral axis

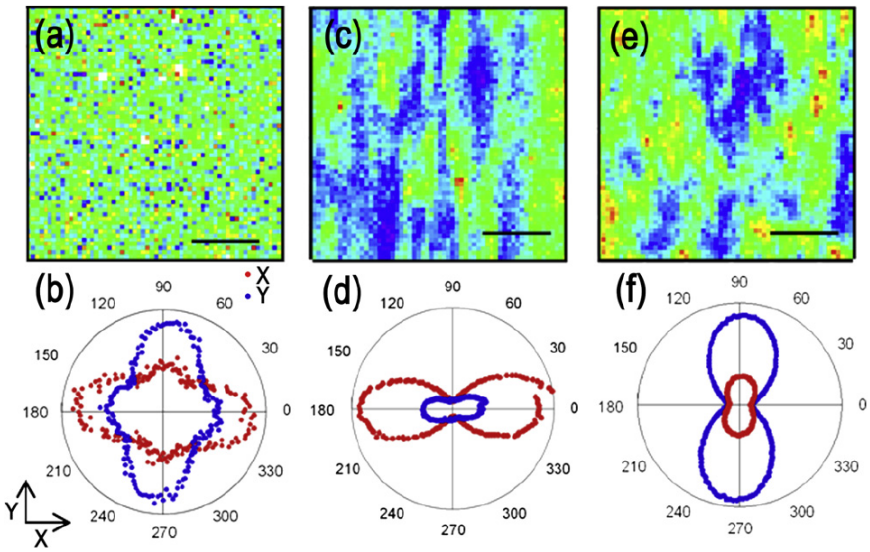

FIGURE 4 Nonlinear imaging and polarimetry measurements of isotropic and ordered DNA samples (60 mg/ml) labeled by PI and Hoechst. (*a* and *b*) Two-photon fluorescence intensity raster scan (*a*) and polar graph (*b*) representing *x* and *y* polarization components of DNA labeled by PI in isotropic solution. (*c* and *d*) Two-photon fluorescence intensity raster scan (*c*) and polar graph (*d*) of DNA labeled by PI in the liquid-crystalline phase. The orientation of DNA strands is $\phi = 90°$. (*e* and *f*) Two-photon fluorescence intensity raster scan (*e*) and polar graph (*f*) of DNA labeled by Hoechst liquid-crystalline phase. The orientation of DNA strands is $\phi = 90°$.

of the DM, and thus is not affected by possible depolarizing effects of the reflection.

To refine the analysis of the orientation of dye molecules bound to DNA, and to verify the conical distribution model for dye binding (Ψ and $\Delta\Psi$), the samples were rotated in the xy plane to an arbitrary angle, ϕ. In these conditions, the polarization of the incident linearly polarized light at the entrance to the microscope is modified by the DM before reaching the sample (23). A more detailed analysis of these effects is presented in Appendix 1.

Fig. 5 represents the polar graphs of PI- and Hoechst-emitted two-photon fluorescence intensity at different sample orientations, ϕ. The direction of the lobes changes upon rotation of the DNA strands in the xy framework, which confirms that the orientation of the dyes is related to the direction of the DNA strands. The comparison between the experimental and theoretical graphs provides the binding angle Ψ. Considering that the emission dipoles of both fluorophores are within the plane of the molecule, the adjusted values are $\Psi = 80°$ ($\Delta\Psi = 10°$) and $\Psi = 20°$ ($\Delta\Psi = 10°$) for PI and Hoechst, respectively. This is compatible with the intercalation for PI and minor groove binding for Hoechst. The Ψ value is in agreement with the binding parameters of PI determined by electrofluorescence spectroscopy (17,18). The binding angle of Hoechst is smaller than that determined by molecular modeling and electrofluorescence spectroscopy, ~35–40° (17,18), which may be due to the bias related to the existence of an angle between the absorption and emission dipoles. However, our data confirm the results of a fluorescence anisotropy study of Hoechst binding to DNA films, where the angle between the emission dipole and the DNA axis was found to be 170° (24).

The main advantage of nonlinear excitation is that it makes possible local analysis of the DNA orientation at a specific point on the sample. As shown in Fig. 3, *c* and *d*, the liquid-crystalline phases formed upon a drying process contain domains with different DNA orientations. Fig. 6 shows a two-photon fluorescence scan of a frontier region between two different domains. Since the polarization of the incident light is horizontal, the intensity of the emitted fluorescence gives a first insight into the PI orientation. The lower zone (*A*) of Fig. 6 *a* is much brighter than the upper zone (*B*), which indicates that PI molecules are aligned close to the horizontal direction in zone A and more vertically in zone B. In Fig. 6 *b*, the two-photon fluorescence intensity in the lower and upper zones (*C* and *D*) is almost identical,

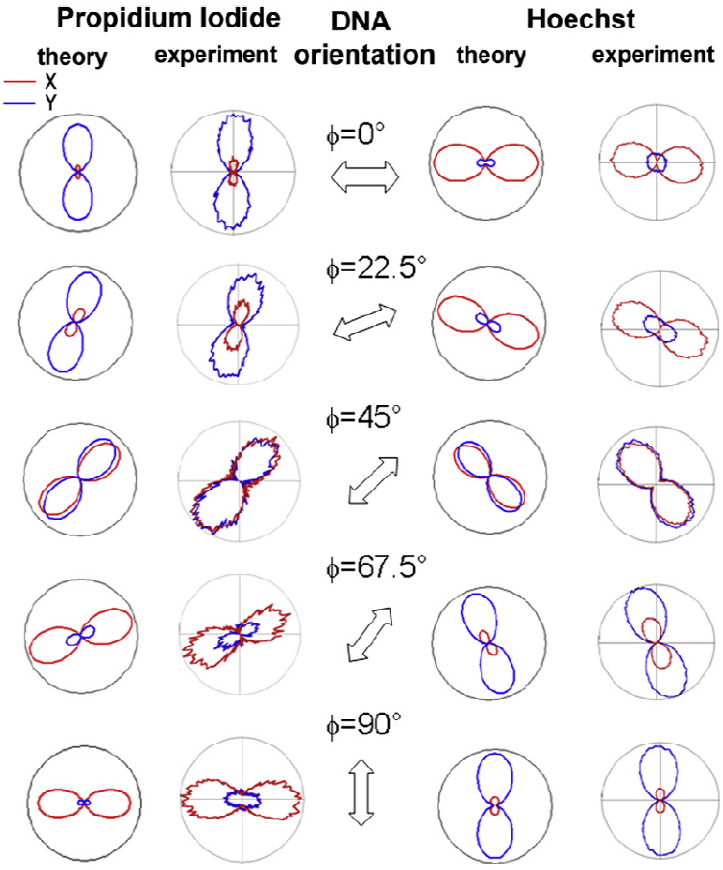

FIGURE 5 Polarimetric analysis of two-photon fluorescence of DNA-bound PI (λ_{exc} = 920 nm, P = 1 mW) and Hoechst (λ_{exc} = 810 nm, P = 0.1 mW). The double arrows represent the orientation of DNA strands (ϕ). For each dye, the polar graphs in the first column correspond to simulated data and those in the second column to experimental data. Values for Ψ and $\Delta\Psi$ parameters are $\Psi = 80°$, $\Delta\Psi = 10°$ for PI and $\Psi = 20°$, $\Delta\Psi = 10°$ for Hoechst.

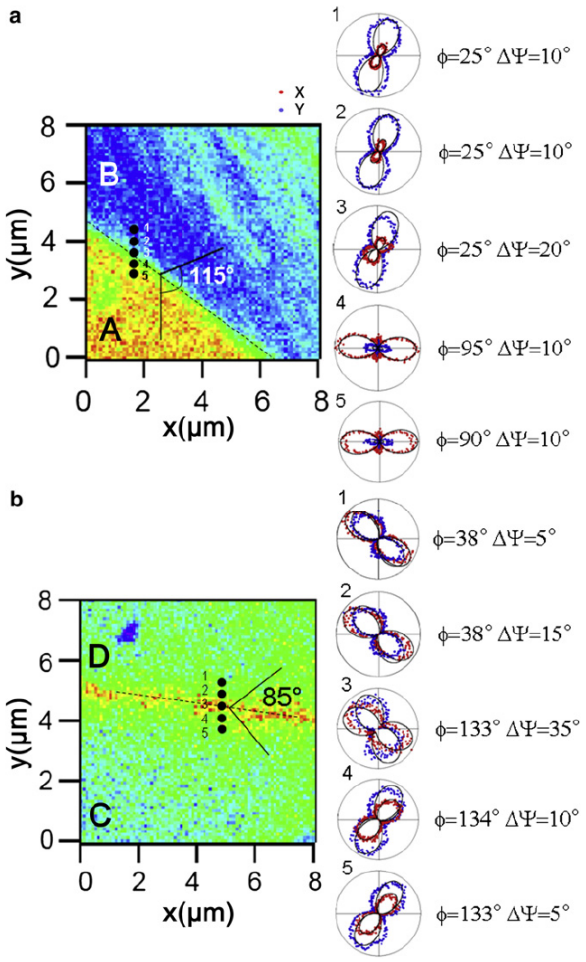

FIGURE 6 Two-photon fluorescence intensity raster scan of the border region between two LC domains of the characteristic zig-zag pattern at the perimeter of the dried DNA drop. The incident light is horizontally polarized. Polar graphs are measured in different points across the border line. (*a*) $\phi = 90°$ and $\phi = 25°$ for the lower (A) and upper (B) parts of the scan. (*b*) $\phi = 130°$ and $\phi = 38°$ for the lower (C) and upper (D) parts of the scan.

which means that the DNA strand orientation $-\phi$ should be symmetrical with respect to the border line. Two-photon polarimetric measurements were performed at different points across the contact line. The orientation of the DNA strands is almost constant within one domain but changes drastically after passing through the border line. A larger orientation distribution, $\Delta\Psi$, can be measured in the border region which means that the ordering is perturbed and entropy increases close to domain walls. The adjustment of the theoretical predictions to the experimental polar graphs revealed $\phi = 90°$ and $\phi = 25°$ for zones A and B, respectively, and $\phi = 133°$ and $\phi = 38°$ for zones C and D, respectively. Thus, the angle between the DNA strands in these domains is 115° in Fig. 6 *a* and 85° in Fig. 6 *b*. The relative orientations of the domains are symmetric with respect to the border line. In this way, by analyzing different points of the sample, it is possible to draw a DNA orientation map with lateral resolution currently down to 350 nm.

An important advantage of the nonlinear excitation is its intrinsic 3D sectioning capability, which enables analysis in all three dimensions. Fig. 7 shows two-photon fluorescence intensity raster scans and the associated polar graphs performed in different z layers of a PI-labeled DNA LC closed cell. As can clearly be seen in the scans, in the proximity of the bottom coverglass the alignment of DNA strands is significantly different from that in the volume of the sample. The scan at $z = 0.5$ μm does not show any well defined structures, whereas the scans at $z = 3.0$ μm and $z = 15$ μm present some degree of organization. The yz scan also shows a structured texture, even though its intensity decreases in the deeper regions because of the light scattering. The polar graphs were measured at different z-positions for the same x and y coordinates. The axial resolution of the microscope, as imposed by the diffraction limit is of the order of 0.8 μm. The polar graphs, measured by

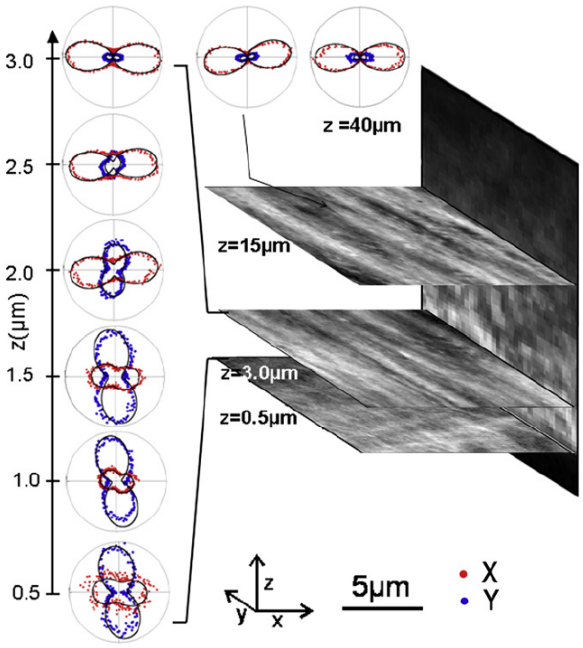

FIGURE 7 Two-photon fluorescence intensity raster scans in different depths of the DNA-LC closed cell along the z axis of the microscope. xy raster scans at different z positions (0.5, 3.0, and 15 μm). Polar plots measured with fixed x and y coordinated at different z positions were fitted with parameters as follows: $z = 0.5$ μm ($\phi = 165°$, $\Psi = 75°$, $\Delta\Psi = 15°$, 17% isotropic); $z = 1.0$ μm ($\phi = 165°$, $\Psi = 75°$, $\Delta\Psi = 15°$, 6% isotropic); $z = 1.5$ μm ($\phi = 165°$, $\Psi = 75°$, $\Delta\Psi = 15°$, 10% isotropic); $z = 2.0$ μm ($\phi = 80°$, $\Psi = 75°$, $\Delta\Psi = 15°$, 17% isotropic); $z = 2.5$ μm ($\phi = 85°$, $\Psi = 80°$, $\Delta\Psi = 15°$, +4% isotropic); $z = 3.0$ μm($\phi = 80°$, $\Psi = 80°$, $\Delta\Psi = 15°$); $z = 15$ μm ($\phi = 95°$, $\Psi = 80°$, $\Delta\Psi = 15°$); and $z = 40$ μm ($\phi = 90°$,$\Psi = 80°$, $\Delta\Psi = 15°$).

steps of 0.5 μm show important modifications, although the focal regions are superimposed. The orientation and shape of the lobes vary significantly over the first 3-μm-thick layers of the sample and then remain constant. This reorientation is probably due to interactions at the DNA/glass interface. The electrostatic interaction between the negatively charged DNA molecules and the glass surface might favor a different orientation from that imposed by the drying process, which becomes predominant further into the bulk of sample. These effects can be compared to anchoring effects, which are well documented but complex phenomena in liquid crystals (25). Similar effects were observed for DNA nematic dehydrated sheared films (26). However, in our case, the glass surface was not submitted to rubbing or related surface preprocessing that would have favored reorientation effects. Anchoring effects depend on factors such as the structure of the molecules, sample thickness, surface treatment, and interfacial properties (27,28). In our samples these effects also induce partial realignment and a subsequent loss of orientation of DNA molecules. To reach a better agreement with experimental data, an isotropic component of the DNA strand distribution has been introduced. Its relative proportion represents 17% at 0.5 μm from the glass surface and vanishes in the deeper regions.

It should be noted that polar graphs clearly point out the orientation of the dyes in deep regions of the samples (40 μm) also, even when the two-photon fluorescence intensity is low.

DISCUSSION AND CONCLUSIONS

In this work, we have presented a polarization sensitive nonlinear microscopy study of the orientation of DNA in organized liquid-crystalline domains. The polarimetric analysis of two-photon fluorescence emitted by DNA-bound dyes shows that this technique is suitable for analyzing the orientation of molecules that associate in a specific way with DNA. The satisfactory correlation of the experimental results with our theoretical modeling makes it possible to distinguish between different DNA binding modes (intercalators or groove binding molecules). Working with fluorophores with well-known binding modes, this technique can be applied to study specific molecular arrangements of other types of LC phases and to realize a polarimetric map of the sample with high lateral and axial resolution.

The experimental data fit well with theoretical predictions, but some discrepancies remain, calling for the adjustment of the relative maximum intensity of x and y polarization components of the emitted fluorescence. The theoretical model is based on the assumption that all dipoles follow the same conical distribution. However, some depolarizing effects responsible for increasing the isotropic fluorescence background may occur due to partial disorder related to the nature of the samples. First, DNA molecules are not perfectly straight. The persistence length of a DNA molecule is of the order of 50 nm, leading to, on average, seven persistence lengths within a 350-nm focal spot of the microscope. Consequently, the emission dipoles are not perfectly aligned in the focus and the emitted fluorescence is partially depolarized. Second, in our experimental conditions, isotropic or amorphous domains coexist with organized ones, leading to the introduction of an isotropic component.

It should be noted that working with light-sensitive dyes raises the issue of light-induced effects. Measurements performed at different sample orientation in the xy plane (ϕ) show that the orientation of the dye follows the rotation of the sample and, thus, that the binding of the dye to the DNA strand is not disturbed by eventual light-induced forces related to irradiation.

These results show that the nonlinear polarimetry technique can be interesting for studying structural phase transition processes or coexistence of isotropic and anisotropic domains. Obviously, various experimental techniques are used to visualize the structure of liquid-crystalline phases. Most of these techniques provide only 2D information and are invasive to the sample to access the axial dimension (8,10,22). Scanning microscopy techniques are the best compromise toward 3D resolution, as they preserve the integrity of the sample. Z-sectioning can be achieved by rejecting the light from the out-of-focus planes by adding a pinhole to the excitation and detection optical path (confocal setup). Fluorescence confocal polarizing microscopy (FCPM) was successfully applied to the study of liquid crystals (11,22). Using this technique, the orientation of the emitting dipoles is derived from the fluorescence intensity measurement at fixed analyzer and polarizer orientations. However, the intensity-orientation relationship is conditioned by the homogeneity of the dye and DNA concentration (11). To make the measurement independent of the eventual concentration gradient of the dye or DNA, in this work, the polarimetry measurements are achieved locally by rotating the incident polarization angle by 360° at a given position within the sample. Besides this possibility of analysis of heterogeneous samples, a polarization analysis makes possible the precise determination of Ψ, $\Delta\Psi$, and ϕ. Indeed, 3D sectioning is intrinsic to the excitation process, which requires a high concentration of incident photons and thus occurs exclusively at the focal spot. The advantage of nonlinear excitation is the significantly lower level of photobleaching of out-of-focus molecules and a deeper penetration of the excitation light into the sample. We note, therefore, that the nature of the information provided by FCPM and two-photon polarimetry is complementary. Assuming fixed and well determined dye binding to the host molecule, FCPM provides global information about the orientation of the director that is the average orientation of DNA chains. In contrast, two-photon polarimetry allows us to study locally and with high angular precision the position of the dye relative to the DNA strand and/or the orientation distribution of DNA molecules.

It should be mentioned, however, that DNA-dye interactions may influence the generation of liquid-crystalline phases compared to pure DNA (29). Indeed, intercalating dyes might significantly increase the length of DNA chains and the twist of the molecule, and thus perturb the organization of LC domains. Studies of doped DNA solutions reveal that the values of DNA concentration related to phase transition parameters are shifted, and that additional liquid-crystalline structures may also appear (21). Consequently the concentration of the dye should be kept at the lowest possible level compatible with the detection threshold to minimize the perturbation of the DNA structure.

Finally, the quality of the z-sectioning investigations depends on the conservation of the light beam features when traversing the sample. Scattering, defocusing effects, and modifications of the polarization of the incident light are minimal provided $(\Delta n^* z)/\lambda$ (where Δn is the birefringence of the sample) is less than unity. Two-photon excitation that uses the infrared light thus offers a considerable advantage compared to single-photon microscopy.

The spatial resolution limit of two-photon microscopy (~350 nm) is sufficient at the scale of DNA liquid-crystalline domains, which have a size of a few micrometers. Applications to the field of biology are also of interest, since it has been proposed that the process of self-organization driven by noncovalent binding plays an important role in ordering of DNA and chromatin structures. The ordered structure is the best compromise for packing a maximum DNA length into a minimum volume, and the liquid properties are essential for the flexibility and accessibility of the regulation and transcription enzymes. Hence, liquid crystals are a plausible hypothesis of the natural organization of DNA (2,7,30).

Atomic force microscopy measurements show that sperm DNA packaged by protamines adopts a toroidal structure containing up to 60 kbp of DNA (31). Electron micrographs and circular dichroism studies of dinoflagellate

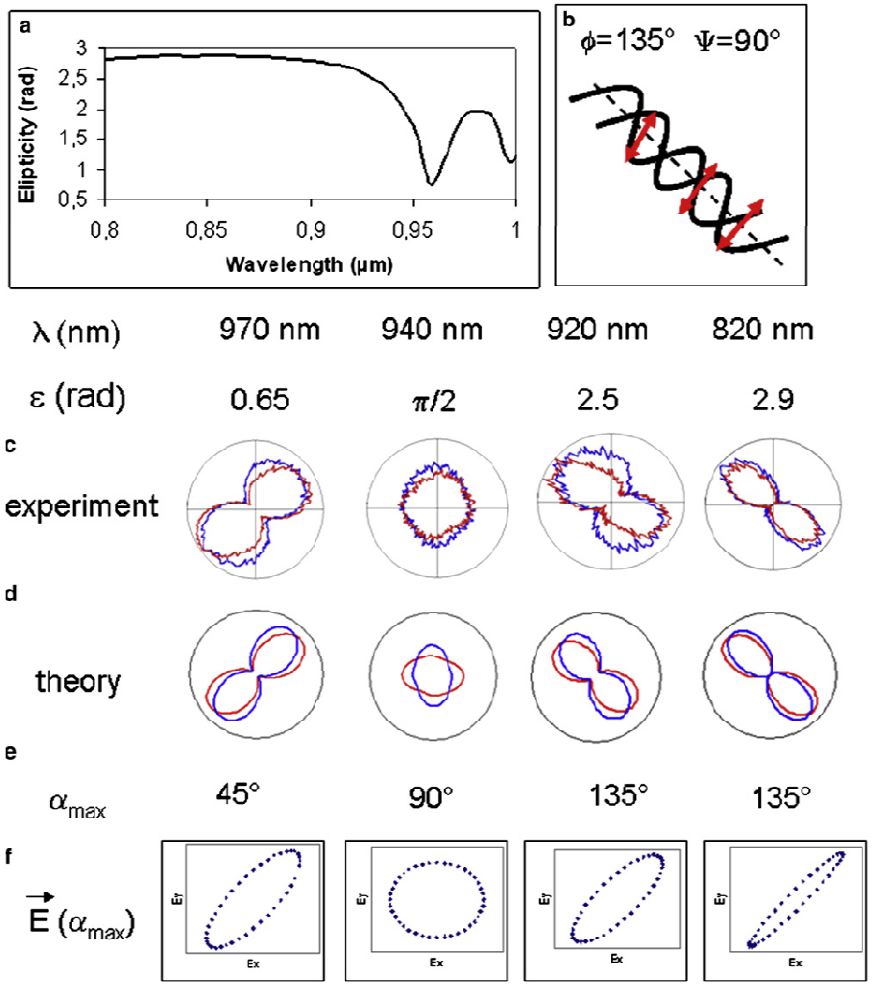

FIGURE 8 Ellipsometric measurements of the DM at the incident angle of 45° and its influence on fluorescence intensity. (*a*) Wavelength dependence of ellipticity $\varepsilon(\lambda)$. (*b*) Scheme of the DNA double-strand labeled by the PI (intercalator). (*c–f*) Polar graphs representing the intensities of the x and y polarization components of the two-photon fluorescence emitted. Experimental results (*c*) are measured with PI-labeled DNA, with the orientation of DNA domains at 135. The theoretical graphs (*d*) are calculated with $\Psi = 80°$, $\Delta\Psi = 10°$, and $\phi = 135°$ (see Fig. 1). The angle of maximum fluorescence intensity, α_{max} (*e*), changes with the excitation wavelength, but the direction of polarization of the electric field impinging on the sample at this angle, $\vec{E}(\alpha_{max})$ (*f*), remains the same, giving the polarization state.

chromosomes present a characteristic pattern for a cholesteric LC phase (32–34). X-ray scattering from bacteria with high-copy-number plasmids has also revealed the presence of cholesteric phases (30). These works suggest that DNA liquid-crystalline phases represent an efficient way of packaging high-copy-number plasmids (6). Moreover, it has been reported that due to specific geometric arrangements and secondary structures, DNA liquid crystals influence the regulation of intermolecular interactions of structures such as nucleosomes (2). The presence of liquid-crystalline domains has been described in nucleosome particle solutions (5,35), which indicates that they may play an important role in formation of nucleoprotein complexes. The work of Livolant et al. (20) has shown that because of the strong negative charge on the nucleosome surface due to the DNA molecule, the transitions between columnar isotropic, lamellocolumnar, and columnar hexagonal phases are driven by the ionic strength of the solution and the applied pressure. Even if the correspondence between these models and the real chromatin higher-order structures is not fully clarified, these works provide a library of possible structures for chromatin organization in vivo (2); for instance, it has been proposed that telomeric chromatin is organized in a columnar phase (36).

Finally, to allow a detailed examination of tiny structures such as 30-nm nucleosome fibers or the chromatin topology in the nucleus, resolution should be further increased by use of subdiffraction microscopy techniques. The increase of the resolution to nanoscopic scale (37) would promote nonlinear polarimetry as a relevant tool for inferring DNA organization in physiological structures.

APPENDIX A

To analyze the polar graphs, it should be noted that the variable angle α corresponds to the polarization angle of the incident light before the reflection by the DM, whereas the angle of maximum fluorescence intensity, α_{max}, depends on the orientation of the sample molecules and the polarization of the light impinging on the sample after the DM reflection. The depolarizing effects of the DM, such as the ellipticity, ε, and relative reflectivity, δ, for s and p polarization components should thus be taken into account (23). As measured by ellipsometry, the δ value is ~1.02 and can be considered constant throughout the wavelength range. On the contrary, the ellipticity, ε, shows important variations in the spectral region between 900 and 1000 nm (Fig. 8 *a*). The consequences of such modifications are illustrated by polar graphs corresponding to constant DNA orientation ($\phi = 135°$) (Fig. 8 *b*), but at different excitation wavelengths ($\lambda = 970$ nm, 940 nm, 920 nm, and 820 nm). The experimental data are measured with PI-labeled DNA that forms LC phases in a closed-cell environment. All experimental parameters are kept constant with the exception of the excitation wavelength. As shown in Fig. 8 *c*, the orientation and the form of the x and y intensity components vary in an important way. These experimental results are compared to simulated curves with the parameters $\Psi = 90°$, $\Delta\Psi = 5°$, $\phi = 135°$, and with different ε values equal 0.65, $\pi/2$, 2.5, and 2.9 rad, corresponding to the DM-induced ellipticity, ε, at the selected wavelengths (Fig. 8 *d*). The corresponding graphs are in good agreement with experiments. The angle of maximum emission in the polar graphs, α_{max} (Fig. 8 *e*), is dependent on the average orientation of the emission dipoles and on ε. Since we consider a sample with PI molecules oriented at ~45°, the polarization impinging on the sample at α_{max} is set at a fixed orientation (Fig. 8 *f*). The direction equals 45° in all graphs.

This example shows that considering both the orientation and the shape of the lobes, the analysis of polar patterns is strongly dependent on the ε value and thus on the choice of excitation wavelength. Overlooking the anisotropies of the DM can clearly lead to important errors in the interpretation of polarimetric data.

Taking into account the DM ellipticity, the excitation wavelengths used in the experiments for PI and Hoechst were 920 nm and 810 nm, with ellipticity values $\varepsilon = 2.5$ rad and $\varepsilon = 2.8$ rad, respectively.

We are grateful to Prof. J.-F. Mouscadet and Dr. S. Bury-Moné for their constructive comments concerning DNA structure and topology. We thank Dr. Thanh Nguyen for the ellipsometry measurements of the dichroic mirror, and Dr. Sophie Brasselet and Dr.Véronique Le Floc'h for previous works on the nonlinear microscope setup.

This work was supported by grants from the French National Resource Agency (ANR Imfovir PCV-2006) and from Région Ile-de-France, and by the European Commission through the Human Potential Programme (Marie-Curie RTN BIMORE, MRTN-CT-2006-035859 and N50713231/3302).

REFERENCES

1. Zakharova, S. S., W. Jesse, C. Backendorf, and J. R. van der Maarel. 2002. Liquid crystal formation in supercoiled DNA solutions. *Biophys. J.* 83:1119–1129.
2. Livolant, F., S. Mangenot, A. Leforestier, A. Berlin, M. Frutos, et al. 2006. Are liquid crystalline properties of nucleosomes involved in chromosome structure and dynamics? *Philos. Transact. A Math. Phys. Eng. Sci.* 2615–2633.
3. Fraden, S., and R. D. Kamien. 2000. Self-assembly in vivo. *Biophys. J.* 78:2189–2190.
4. Strzelecka, T. E., M. W. Davidson, and R. L. Rill. 1988. Multiple liquid crystal phases of DNA at high concentrations. *Nature.* 331: 457–460.
5. Leforestier, A., and F. Livolant. 1997. Liquid crystalline ordering of nucleosome core particles under macromolecular crowding conditions: evidence for a discotic columnar hexagonal phase. *Biophys. J.* 73:1771–1776.
6. Reich, Z., E. J. Wachtel, and A. Minsky. 1994. Liquid-crystalline mesophases of plasmid DNA in bacteria. *Science.* 264:1460–1463.
7. Bloomfield, V. A. 1996. DNA condensation. *Curr. Opin. Struct. Biol.* 6:334–341.
8. Merchant, K., and R. L. Rill. 1997. DNA length and concentration dependencies of anisotropic phase transitions of DNA solutions. *Biophys. J.* 73:3154–3163.
9. Kassapidou, K., W. Jesse, J. A. van Dijk, and J. R. van der Maarel. 1998. Liquid crystal formation in DNA fragment solutions. *Biopolymers.* 46:31–37.
10. Morii, N., G. Kido, H. Suzuki, and H. Morii. 2005. Annular self-assembly of DNA molecular chains occurring in natural dry process of diluted solutions. *Biopolymers.* 77:163–172.
11. Smalyukh, I., S. V. Shiyanovskii, and O. D. Lavrentovich. 2001. Three-dimensional imaging of orientational order by fluorescence confocal polarizing microscopy. *Chem. Phys. Lett.* 336:88–96.
12. Denk, W., J. H. Strickler, and W. W. Webb. 1990. Two-photon laser scanning fluorescence microscopy. *Science.* 248:73–76.
13. Le Floc'h, V., S. Brasselet, J. F. Roch, and J. Zyss. 2003. Monitoring of orientation in molecular ensembles by polarization sensitive nonlinear microscopy. *J. Phys. Chem. B.* 107:12403–12410.
14. Brasselet, S., V. LeFloc'h, F. Treussart, J. F. Roch, and J. Zyss. 2004. In situ diagnostics of the crystalline nature of single organic nanocrystals by nonlinear microscopy. *Phys. Rev. Lett.* 92:2074701.
15. Brasselet, S., and J. Zyss. 2007. Nonlinear polarimetry of molecular crystals down to the nanoscale. *C.R. Phys.* 8:165–179.

16. Le Xuan, L., Ch. Zhou, A. Slablab, D. Chauvat, C. Tard, et al. 2007. Photostable single KTiOPO4 nanocrystals for second-harmonic generation microscopy. *Proc. iEEE/LEOS Internatl. Conf. Opt. MEMS Nanophotonics*. 39–40.

17. Pjura, P. E., K. Grzeskowiak, and R. E. Dickerson. 1987. Binding of Hoechst-33258 to the minor groove of B-DNA. *J. Mol. Biol.* 197: 257–271.

18. Windsor, S. A., and M. H. Tinker. 1996. Binding of biologically important molecules to DNA, probed using electro-fluorescence polarization spectroscopy. *Biophys. Chem.* 58:141–150.

19. Le Floc'h, V., S. Brasselet, J. Zyss, B. R. Cho, S. H. Lee, et al. 2005. High efficiency and quadratic nonlinear optical properties of a fully optimized 2D octupolar crystal characterized by nonlinear microscopy. *Adv. Mater.* 17:196–200.

20. Livolant, F., and A. Leforestier. 1996. Condensed phases of DNA: structures and phase transitions. *Prog. Polym. Sci.* 21:1115–1164.

21. Olesiak, J., K. Matczyszyn, H. Mojzisova, M. Zielinski, D. Chauvat, et al. 2009. Liquid crystalline phases in DNA and DNA-doped soutions analysed by polarized linear and nonlinear microscopy and differential scanning calorimetry. *Mater. Sci. Poland*. In press.

22. Smalyukh, I. I., O. V. Zribi, J. C. Butler, O. D. Lavrentovich, and G. C. Wong. 2006. Structure and dynamics of liquid crystalline pattern formation in drying droplets of DNA. *Phys. Rev. Lett.* 96: 177–801.

23. Schon, P., F. Munhoz, A. Gasecka, S. Brustlein, and S. Brasselet. 2008. Polarization distortion effects in polarimetric two-photon microscopy. *Opt. Express*. 16:20891–20901.

24. Morii, N., G. Kido, T. Konakahara, H. Morii, et al. 2005. Orientation of dye molecules in DNA-based films with chain alignment and judgment of their DNA-binding modes. *J. Phys. Chem. B*. 109:15636–15644.

25. Jerome, B. 1991. Surface effects and anchoring in liquid crystals. *Rep. Prog. Phys.* 54:391–451.

26. Nakata, M., G. Zanchetta, M. Buscaglia, T. Bellini, N. A. Clark, et al. 2008. Liquid crystal alignment on a chiral surface: interfacial interaction with sheared DNA films. *Langmuir*. 24:10390–10394.

27. Bonvent, J. J., I. H. Becgtold, M. L. Vega, E. A. Oliveira, et al. 2000. Alignment and phase transition induced by surface action in lyotropic nematic liquid crystals. *Phys. Rev. E Stat. Phys. Plasmas Fluids Relat. Interdiscip. Topics*. 62:3775–3779.

28. Guyotsionnest, P., H. Hsiung, and Y. R. Shen. 1986. Surface polar ordering in a liquid crystal observed by optical second-harmonic generation. *Phys. Rev. Lett.* 57:2963–2966.

29. Lerman, L. S. 1961. Structural considerations in interaction of DNA and acridines. *J. Mol. Biol.* 3:18–30.

30. Reich, Z., S. Levin-Zaidman, S. B. Gutman, T. Arad, and A. Minsky. 1994. Supercoiling-regulated liquid-crystalline packaging of topologically-constrained, nucleosome-free DNA molecules. *Biochemistry*. 33:14177–14184.

31. Hud, N. V., M. J. Allen, K. H. Downing, J. Lee, and R. Balhorn. 1993. Identification of the elemental packing unit of DNA in mammalian sperm cells by atomic force microscopy. *Biochem. Biophys. Res. Commun.* 193:1347–1354.

32. Rill, R. L., F. Livolant, H. C. Aldrich, and M. W. Davidson. 1989. Electron microscopy of liquid crystalline DNA: direct evidence for cholesteric-like organization of DNA in dinoflagellate chromosomes. *Chromosoma*. 98:280–286.

33. Livolant, F., and Y. Bouligand. 1978. New observations on twisted arrangement of dinoflagellate chromosomes. *Chromosoma*. 68:21–44.

34. Bouligand, Y., and V. Norris. 2001. Chromosome separation and segregation in dinoflagellates and bacteria may depend on liquid crystalline states. *Biochimie*. 83:187–192.

35. Mangenot, S., A. Leforestier, D. Durand, and F. Livolant. 2003. Phase diagram of nucleosome core particles. *J. Mol. Biol.* 333:907–916.

36. Fajkus, J., and E. N. Trifonov. 2001. Columnar packing of telomeric nucleosomes. *Biochem. Biophys. Res. Commun.* 280:961–963.

37. Hell, S. W. 2003. Toward fluorescence nanoscopy. *Nat. Biotechnol.* 21:1347–1355.

Efficient second-harmonic generation from a single gold dimer

A. Slablab, L. Le Xuan, M. Zielinski, Y. de Wilde, V. Jacques, D. Chauvat, and J.-F. Roch
Laboratoire de Photonique Quantique et Moléculaire,
Ecole Normale Supérieure de Cachan, UMR CNRS 8537, Cachan, France and
Institut Langevin, ESPCI ParisTech, CNRS, Paris, France
(Dated: July 19, 2010)

We show that a dimer made of two gold nanospheres exhibits a remarkable efficiency for second-harmonic generation under femtosecond optical excitation. The nonlinear emission is obtained only when the two nanoparticles are as close as possible to contact, as in situ controlled and measured using the tip of an atomic force microscope. The excitation wavelength dependence of the second-harmonic signal supports a coupled plasmon resonance origin with radiation from the dimer gap. This nanometer-size coherent source can be used for high-resolution near-field optical microscopy.

PACS numbers:

During the last decade, nonlinear nanoparticles have been extensively studied as new light sources at the nanoscale. In particular nanoparticles made of non-centrosymmetric material exhibit second-harmonic generation (SHG)[1–7] which can be used for nonlinear optical microscopy [8]. In the case of noble metals, high electron polarisability could yield to much stronger nonlinear effects. However inversion symmetry of the metallic crystalline structure forbids bulk second-order electric dipole response. In the case of a metallic nanosphere, second-order polarization associated to induced surface dipole moments and volumic quadrupole moments lead to weak SHG signals [10–12], with a strong dependence to the nanoparticle shape and size as demonstrated at the ensemble level [13] and the single-particle one [14]. Plasmon resonance associated to metallic nanostructures with specific geometry can lead to an enhanced second-harmonic nonlinear response, as demonstrated by using a sharp near-field metal tip [15], and in engineered nanostructures such as cylindrical nanodot arrays [16], bowtie-shaped nano-antenna [17], and T-shaped gold nano-dimers [18]. For that purpose, a dimer structure consisting of two metallic nanospheres appears as a simple testbed for studying the plasmon coupling influence on the optical response. Indeed, the linear scattering of this composite nanostructure exhibits a wealth of specific properties depending on the geometrical parameters. The coupled plasmon modes have resonance frequencies which can be tuned over the whole visible spectrum by changing the dimer geometry [19–22]. Moreover, the electromagnetic field density is greatly enhanced at the dimer gap and enhanced four-wave mixing has been observed in metallic dimers [23, 24].

In this Letter, we explore the second-order nonlinear properties of the dimer model with controlable geometry, and show that such a single dimer consisting of gold nanospheres (GNs) leads to highly efficient second harmonic generation under femtosecond optical illumination in spite of the apparent centrosymmetry of the nanostructure. The relative position of the two GNs is adjusted with nanometer accuracy using the tip of an atomic force microscope (AFM). This control allows us to demonstrate that the strong SHG signal only appears when the GNs are very close to contact. The variation of the SHG intensity with the excitation wavelength supports the role of an infrared resonance resulting from the coupling of the plasmon oscillations in the two gold nanospheres. The nonlinear emission is highly dependent on the linear excitation polarization with maximum efficiency along the dimer axis.

The principle of the experiment is shown in Fig. 1(a). The nonlinear optical response of the coupled GNs is investigated using a nano-optomechanical setup consisting of the AFM on top of an inverted optical microscope. The sample is prepared by spin-coating a colloidal solution of $100-$ nm diameter GNs on a silanized glass coverslip, with a dispersion on the substrate such that well-isolated GNs are obtained. The AFM is used both to measure the surface topography of the sample and to perform mechanical manipulation of the GNs. The formation of a single gold dimer is gradually achieved by pushing a GN toward another with the AFM tip, thus controlling the interparticle distance from large separation to contact between the two spheres. A titanium-doped sapphire (Ti:Sa) laser emitting $100-$ fs pulses in the $800-1000\,$nm wavelength range at $80-$ MHz repetition rate is tightly focused onto the sample through a high numerical aperture microscope objective. The light emitted by the GNs is collected with the same objective, spectrally filtered from the remaining pump light using a dichroic beamsplitter, and finally directed either to a spectrograph or to a silicon avalanche photodiode (APD) working in the photon counting regime. The AFM tip and the excitation laser are carefully aligned on the same axis. Simultaneous record of the topography and optical response allows us to monitor the apparition of second-order nonlinear effects as the dimer is formed.

A typical realization of the experiment is depicted in Figs. 1(b) and (c). At the laser input power used in the experiment ($< 1\,$mW), the nonlinear optical re-

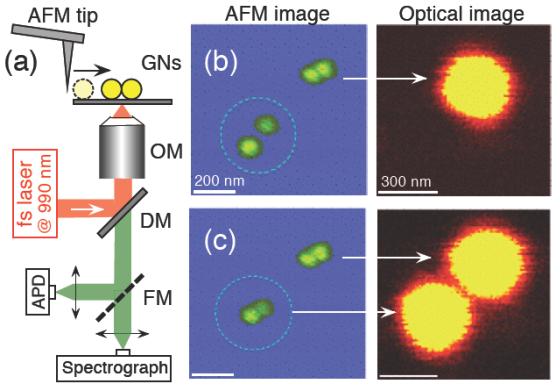

FIG. 1: (color online). Principle of the experiment. (a)-Sketch of setup allowing to monitor the nonlinear emission of gold nanosphere (GN) dimers while controlling the interparticle distance using an AFM tip. OM: oil immersion microscope objective (×100, NA = 1.4); DM: dichroic mirror; FM: flip mirror directing the collected light either to an imaging spectrograph equipped with a back-illuminated CCD matrix, or to a silicon avalanche photodiode (APD). (b)-When two GNs are forming a dimer (see topography image), a strong nonlinear emission is observed (see optical image), which fully vanishes for isolated single GNs. (c)-Using the AFM tip as a mechanical nanopositioner, two isolated GNs can be brought in contact, thus forming a dimer, and nonlinear-optical response is again detected.

sponse associated with isolated GNs is below our detection threshold (see Fig. 1(b)). We note that at much higher excitation power (10 mW??) a weak nonlinear second-order emission from single GNs can be detected, as expected [9,12] and recently observed [14]. Using the AFM-based nanopositioning technique, two isolated GNs are then brought to contact, leading to the observation of a strong signal (Fig. 1(c)).

Spectra recorded from this gold dimer emission while tuning the excitation laser wavelength from 850 nm to 1000 nm are shown in Fig. 2(a). For each excitation wavelength, a narrow emission line is observed at half the excitation wavelength and its intensity scales quadratically with the laser power. We then conclude that this emission originates from SHG. Furthermore the emission spectra clearly exhibit a maximum of SHG when the excitation laser wavelength is within the 950 to 1000 nm range, supporting the role of an infrared dimer coupled mode. We also observe the expected broad incoherent two-photon luminescence from the GNs, although at an intensity much weaker than the coherent SHG part.

This spectral behaviour of of the second-harmonic response is explained using the analysis of Ref. [21] which theoretically describes the linear optical response of a gold dimer in the nearly touching regime. When the two GNs are getting close to contact, plasmon resonances of the two single nanospheres are coupled, and one of the new dimer modes is rapidly shifted towards the infrared. We confirm this prediction with a finite difference time domain (FDTD) simulation of the linear optical properties of a gold dimer using our experimental conditions. For this simulation, we use the gold dielectric constants reported in [Jonhson and Christy] for a 500−1400 nm wavelength range. In agreement with Ref. [21], a resonant behaviour of the scattering cross-section is observed as well as a rapid shift of this resonance to the infra-red as the gap is reduced (not shown). Choosing a 0.08−nm gap distance, we obtain the linear scaterring cross-section of a gold dimer made of two 100−nm spheres displayed in the inset of Fig. 2(a). It exhibits a maximum at 990 nm which is very similar to the SHG excitation spectra. This gap value, almost corresponding to contact within an atomic layer, is in agreement with gap distances found experimentally as discussed below.

To further characterize the nature of this coupled mode, a polarization analysis is performed while exciting the dimer in resonance at $\lambda_{ex} = 990$ nm and rotating the linear excitation polarization using a half-wave plate. The polar diagrams measured for two different dimers are

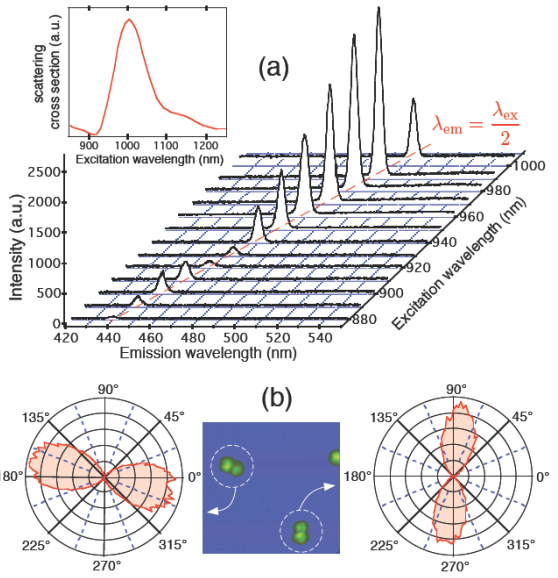

FIG. 2: (color online). Second-harmonic generation from a gold dimer. (a)-Emission spectra from a gold dimer recorded while tuning the excitation laser wavelength λ_{ex} from 850 nm to 1000 nm. The inset shows the FDTD simulation of the scattering cross-section of a gold dimer consisting of two 100−nm gold spheres at a 0.08−nm gap distance. (b)-Polar diagrams showing the SHG efficiency as a function of the angle of the linearly-polarized excitation laser for two different dimers (see topography image). Intense lobes along the dimer axis are observed, which is a signature of a dipole-like excitation mode associated to the coupled charge distributions in the two pheres at contact.

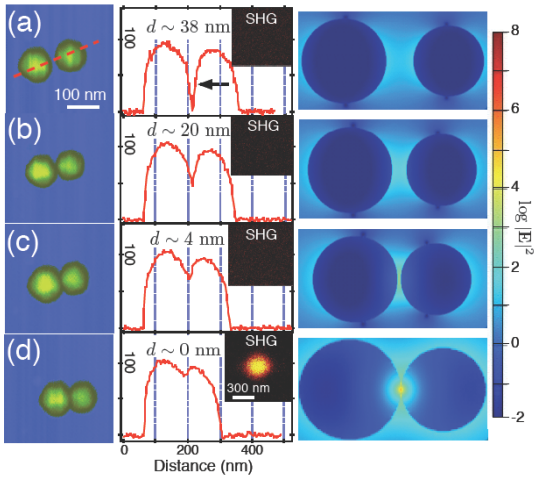

FIG. 3: (color online). From row (a) to (d), a gold dimer is gradualllly formed while approaching step by step one GN toward another with the AFM tip. In a row, (left) topography image of the GN, (middle) cross-section corresponding to the red dot line in the topography image, inset showing the SHG signal, and (right) FDTD simulation of the electromagnetic field intensity. Note the log scale showing a six order of magnitude increase of the field at the dimer gap, between the extreme values of the gap distance.

shown in Fig. 2(b). The SHG intensity is vanishing when the excitation polarization is perpendicular to the dimer axis, and increases to a maximum value when the polarization is set along the dimer axis, as revealed by the corresponding AFM topographic images. This dipolar-like response can be simply explained by the coupling between the plasmon oscillations in the two GNs. At the dimer gap, a strong accumulation of opposite charges close to each other is induced. Any charge oscillations driven by external light within the gap is accompanied by charge redistribution over each particle in order to maintain intraparticle charge neutrality. Such a charge redistribution finally leads to a large dipole strength of the gold dimer as a whole. While the interaction of light with charges is small for an exciting electric field perpendicular to the dimer axis, the plasmon mode coupling becomes efficient when the field is applied along this axis, as observed in the experiments (see Fig. 2(b)). With respect to existing theory of the coupling between nearly-touching GNs [21], it is relevant to study the onset of the nonlinear optical response while controlling the interparticle distance from large separation to contact. For that purpose, a gold dimer is gradually formed with nanometric step by pushing a GN toward another with the AFM tip. After each displacement, an AFM topography image as well as a raster scan SHG image are acquired. Four intermediate situations are shown in Fig. 3(a)-(d). Despite a relatively small AFM tip radius (~ 7 nm), a direct measurement of the gap distance d between the two nanoparticles is obviously not possible. However, this gap can be estimated accurately down to a few nanometers using a fit of the dip in a topographic cross section of the dimer (see red dashed line Fig. 3 (middle panel)), once the size of the GNs and the tip radius are known. In particular it is possible to determine whether the two GNs are close to contact.

As the GN is displaced with nanometric steps, one could expect a graduate appearance of the SHG signal. However, no SHG is detected until the two gold nanoparticles are very close to contact (see inset in Fig. 3 (middle panel)), in which case a large number of photons are emitted. Starting from this geometry corresponding to the onset of SHG, we then try to push further one GN towards the other with the AFM tip. Interestingly, the observed SHG signal remains unchanged. Such an observation appears to be reproducible and supports the fact that the SHG signal is emitted only when the two NPs are in contact or very close to contact.

This onset of a bright SHG emission only close to contact is associated to a sudden increase of the excitation field for very small gap distances. Indeed, at the dimer gap, the strong induced accumulation of opposite charges discussed above evidently leads to a greatly enhanced excitation electromagnetic field. As appears on the simulation in Fig. 3, from a gap distance of 4 nm to a 0.08 nm, the excitation field gains about 6 orders of magnitude. SHG finds its origin in this huge field which is confined in a nanometric volume at the dimer gap. This localized excitation is further confirmed by SHG raster-scan images

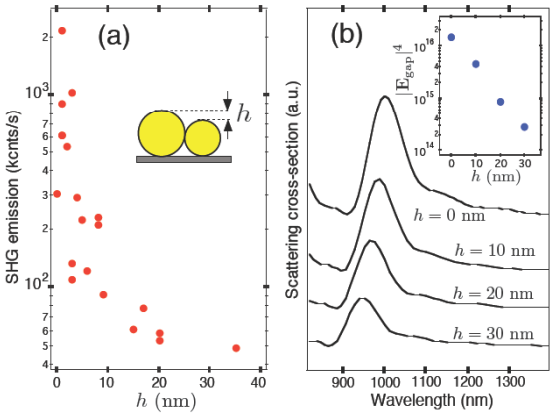

FIG. 4: (color online). (a) SHG efficiency on a log scale as a function of the size difference h between the two GNs. Inset: scheme of the two different nanospheres forming an asymmetric dimer. (b) Simulation of the scattering cross-section of an asymmetric dimer for different values of h. Inset: dependence of the electromagnetic intensity at the dimer gap at a fixed 990−nm excitation wavelength as a function of h on a log scale.

(see Fig.1(c)), showing bright spots with a diffraction-limited size (FWHM$\sim$ 320 nm), as expected for a quasi point-like emission.

Second-order nonlinear optical processes not only require strong local fields but also and primarily an overall noncentrosymmetry of the emitter. This required noncentrosymmetry might have distinct origins with different weigths. In particular, it could be simply ensured by considering a broken symmetry when the dimer is made of two particles with slightly different sizes as suggested in Ref. [23]. Using such an argument, the SHG efficiency should decrease with the size difference h of the GNs (see Fig. 4). Eventually a zero efficiency would be observed from two rigorously identical GNs ($h = 0$) in the absence of any other SHG process. In order to check this assumption, the SHG efficiency is measured as a function of h for an ensemble of 19 single dimers for an excitation wavelength fixed at the optimal 990−nm wavelength for the quasi-null gap. The results are shown in Fig. 4(a). Surprisingly, we observe a behavior opposite to the expected one. We obtain evidence that the SHG efficiency is increasing by more than one order of magnitude when h is decreasing from 35 nm to 0 nm. We can therefore conclude that the observed SHG can not be fully explained by a broken symmetry of a dimer made of two particles with different sizes.

FDTD simulation of the optical scattering of the dimer as function of h sheds light on this unexpected SHG variation (see Fig. 4)(b). As the asymmetry measured by h is increased, the resonance resulting from the coupling of plasmon modes in the two nanospheres is blue-shifted and its maximum decreases. Therefore, at the fixed 990−nm excitation wavelength, the electric field intensity in the gap decreases by almost one order of magnitude for h varying from 0 to 35 nm. Consequently, it appears that the dimer asymmetry has rather a negative effect on the electric field intensity at the gap, rather than a positive one through the obvious noncentrosymmetry of the nanostructure.

Most likely the SHG may then result from nonlocal electric-dipole surface-allowed SHG from the two portions of spherical surfaces facing each other and surrounding the gap, and local volumic quadrupolar coupling from the nearby metallic material, just as in the weak SHG emission from a single gold nanosphere [9, 13]. Besides the noncentrosymmetry may have other contributions due to the imperfect geometry at the gap, since GNs usually exhibit facets. Further work is required to analyze the role of such fine details at the gap.

In conclusion, we have experimentally demonstrated that a highly efficient SHG is obtained from two GNs when very close to geometrical contact. Spectral analysis of the SHG response and polarization analysis suggest a coupled plasmon resonance origin of the nonlinear emission. Since SHG is most likely emitted from a nanometric volume at the dimer gap, it could be used as a nanosource for the development of high-resolution near-field imaging. In addition, the reported SHG is coherent with the fundamental excitation field, and thus could be used in advanced nonlinear microscopy techniques [25]. Using the AFM-tip pushing technique, other nanostructures could be formed, such as a trimer nanoparticle that can lead to a tunable nano-half wave plate [26], or a succession of metallic beads with decreasing size which forms an efficient plasmonic nano-lens with high field concentration [27]. These complex structures would certainly show surprising nonlinear properties.

We thank S. Perruchas and T. Gacoin for providing GNs sample. We are also grateful to J.-J. Greffet and F. Marquier for fruitful discussions. This work is supported by C'Nano Île-de-France.

[1] J. C. Johnson *et al.*, Nano Lett. **2**, 279 (2002).
[2] A. B. Djurisić and Y. H. Leung, Small **2**, 944-961 (2006).
[3] L. Bonacina *et al.*, Applied Physics B **87**, 399 (2007).
[4] L. L. Xuan *et al.*, Small **4**, 1332 (2008).
[5] M. Zielinski, D. Oron, D. Chauvat, and J. Zyss, Small **5**, 2835 (2009).
[6] C.-L. Hsieh, R. Grange, Y. Pu, and D. Psaltis, Opt. Express **17**, 2880 (2009).
[7] A. V. Kachynski, A. N. Kuzmin, M. Nyk, I. Roy, and P. N. Prasad, J. Phys. Chem. C **112**, 10721 (2008).
[8] Y. Nakayama *et al.*, Nature **447**, 1098 (2007).
[9] J. Dadap, J. Shan, K. B. Eisenthal, and T. F. Heinz, Phys. Rev. Lett. **83**, 4045 (1999).
[10] V. L. Brudny, B. S. Mendoza, and W. L. Mochan, Phys. Rev. B **62**, 11152 (2000).
[11] J. Dadap, J. Shan, and T. F. Heinz, J. Opt. Soc. Am. B **21**, 1328 (2004).
[12] J. Shan, J. I. Dadap, I. Stiopkin, G. A. Reider, and T. F. Heinz, Phys. Rev. A **73**, 23819 (2006).
[13] J. Nappa *et al.*, Phys. Rev. B **71**, 165407 (2005).
[14] J. Butet *et al.*, Nano Lett, **xx**, xxx (2010).
[15] A. Bouhelier, M. R. Beversluis, A. Hartschuh, and L. Novotny, Phys. Rev. Lett. **90**, 013903 (2003).
[16] B. K. Canfield *et al.*, New J. Phys. **10**, 013001 (2008).
[17] T. Hanke *et al.*, Phys. Rev. Lett. **103**, 257404 (2009).
[18] B. K. Canfield *et al.*, Nano Lett. **5**, 1251 (2007).
[19] W. Rechberger, A. Hohenau, A. Leitner, J. R. Krenn, B. Lamprecht, and F. R. Aussenegg, Opt. Com. **220**, 137 (2003).
[20] T. Atay, J.-H. Song, and A. V. Nurmikko, Nano Lett. **4**, 1627 (2004).
[21] I. Romero, J. Aizpurua, G.W. Bryant, and F. D. García de Abajo, Opt. Express **14**, 9988 (2006).
[22] P. K. Kain and M. A. El-Sayed, Chem. Phys. Lett. **487**, 153 (2010).
[23] M. Danckwerts and L. Novotny, Phys. Rev. Lett. **98**, 026104 (2007).
[24] S. Palomba and L. Novotny, Nano Lett. **9**, 3801 (2009).
[25] L. L. Xuan *et al.*, Appl. Phys. Lett. **89**, 121118 (2008).
[26] Z. Li, T. Shegai, G. Haran, and H. Xu, ACS Nano **3**, 637 (2009).
[27] K. Li, M. I. Stockman, and D. J. Bergman, Phys. Rev. Lett. **91**, 227402 (2003).

Bibliography

1 Le Xuan, L. *et al.* Photostable Second-Harmonic Generation from a Single $KTiOPO_4$ Nanocrystals for Nonlinear Microscopy. *Small* **4**, 1332-1336 (2008).

2 Hsieh, C.-L., Grange, R., Pu, Y. & Psaltis, D. Three-dimensional harmonic holographic microcopy using nanoparticles as probes for cell imaging. *Optics Express* **17**, 2880-2891 (2009).

3 Jacobsohn, M. & Banin, U. Size Dependence of Second Harmonic Generation in CdSe Nanocrystal Quantum Dots. *The Journal of physical Chemistry B* **104**, 1-5 (2000).

4 Zielinski, M., Oron, D., Chauvat, D. & Zyss, J. Second-Harmonic Generation from a Single Core/Shell Quantum Dot. *Small* **5**, 2835-2840 (2009).

5 Winter, S., Zielinski, M., Chauvat, D., Zyss, J. & Oron, D. Characterization of the Second Order Nonlinear Susceptibility of Quantum Confined Semiconductors. *The Journal of Physical Chemistry C, accepted* (2011).

6 Pu, Y., Grange, R., Hsieh, C.-L. & Psaltis, D. Nonlinear Optical Properties of Core-Shell Nanocavities for Enhanced Second-Harmonic Generation. *Physical Review Letters* **104**, 207402-207406 (2010).

7 Shaviv, E. & Banin, U. Synergistic Effects on Second Harmonic Generation of Hybrid CdSe−Au Nanoparticles. *ACS Nano* **4**, 1529-1538 (2010).

8 Zielinski, M. *et al.* Nanoegineering the Second Order Susceptibility in Semiconductor Quantum Dot Heterostructures. *Optics Express, accepted* (2011).

9 Brus, L. Quantum crystallites and nonlinear optics. *Applied Physics A: Materials Science & Processing* **53**, 465-474 (1991).

10 Alivisatos, A. P. Semiconductor Clusters, Nanocrystals, and Quantum Dots. *Science* **271**, 933-937 (1996).

11 Brus, L. E. A simple model for the ionization potential, electron affinity, and aqueous redox potentials of small semiconductor crystallites. *Journal of Chemical Physics* **79**, 5566-5572 (1983).

12 Brus, L. Electronic wave functions in semiconductor clusters: experiment and theory. *The Journal of Physical Chemistry* **90**, 2555-2560 (1986).

13 Alivisatos, A. P., Harris, A. L., Levinos, N. J., Steigerwald, M. L. & Brus, L. E. Electronic states of semiconductor clusters: Homogeneous and inhomogeneous broadening of the optical spectrum. *The Journal of Chemical Physics* **89**, 454833-454844 (1988).

14 Kittel, C. *Introduction to Soild State Physics*. eighth edn, (John Wiley & Sons, Inc., 2005).

15 Wei, S.-H. & Zunger, A. Calculated natural band offsets of all II–VI and III–V semiconductors: Chemical trends and the role of cation d orbitals. *Applied Physics Letters* **72**, 2011-2013 (1998).

16 Efros, A., L, & Rosen, M. Quantum size level structure of narrow-gap semiconductor nanocrystals: Effect of band coupling. *Physical Review B* **58**, 7120-7135 (1998).
17 Norris, D. J., Sacra, A., Murray, C. B. & Bawendi, M. G. Measurements of the Size Dependent Hole Spectrum in CdSe Quantum Dots. *Physical Review Letters* **72**, 2612-2615 (1994).
18 Norris, D. J. & Bawendi, M. G. Measurement and assignment of the size-dependent optical spectrum in CdSe quantum dots. *Physical Review B* **53**, 16338-16346 (1996).
19 Norris, D. J., Efros, A., L,, Rosen, M. & Bawendi, M. G. Size dependence of exciton fine structure in CdSe quantum dots. *Physical Review B* **53**, 16347-16354 (1996).
20 Wuister, S. F., van Driel, F. & Meijerink, A. Luminescence of CdTe nanocrystals. *Journal of Luminescence* **102-103**, 327-332 (2003).
21 Maumoto, Y. & Sonobe, K. Size-dependent energy levels of CdTe quantum dots. *Physical Review B* **56**, 9734-9737 (1997).
22 Hines, M., A. & Scholes, G. D. Colloidal PbS Nanocrystals with Size-Tunable Near-Infrared Emission: Observation of Post-Synthesis Self-Narrowing of the Particle Size Distribution. *Advanced Materials* **15**, 1844–1849 (2003).
23 Hines, M., A. & Guyot-Sionnest, P. Bright UV-Blue Luminescent Colloidal ZnSe Nanocrystals. *The Journal of Physical Chemistry B* **102**, 3655–3657 (1998).
24 Klimov, V. I. *Semiconductor and Metal Nanocrystals: Synthesis and Electronic and Optical Properties*. (Marcel Dekker, Inc., 2004).
25 Bastard, G. *Wave mechanics applied to semiconductor heterostructures*. (John Wiley and Sons, Inc., 1990).
26 Scholes, G. D. Controlling the Optical Properties of Inorganic Nanoparticles. *Advanced Functional Materials* **18**, 1157-1172 (2008).
27 Sercel, P. C. & Vahala, K. J. Analytical formalism for determining quantum-wire and quantum-dot band structure in the multiband envelope-function approximation. *Physical Review B Condens Matter* **42**, 3690-3710 (1990).
28 Banin, U. *et al.* Size-dependent electronic level structure of InAs nanocrystal quantum dots: Test of multiband effective mass theory. *Journal of Chemical Physics* **109**, 2306-2309 (1998).
29 van Driel, A. F. *et al.* Frequency-Dependent Spontaneous Emission Rate from CdSe and CdTe Nanocrystals: Influence of Dark States. *Physical Review Letters* **95**, 2368041-2368041 (2005).
30 Efros, A., L, *et al.* Band-edge exciton in quantum dots of semiconductors with a degenerate valence band: Dark and bright exciton states. *Physical Review B* **54**, 4843–4856 (1996).
31 Brus, L. Electron–electron and electron-hole interactions in small semiconductor crystallites: The size dependence of the lowest excited electronic state. *Journal of Chemical Physics* **80**, 4403-4410 (1984).
32 Efros, A., L, & Rosen, M. The Electronic Structure of Semiconductor Nanocrystals. *Annual Review of Materials Science* **30**, 475-521 (2000).
33 Huang, M.-Z. & Ching, W.-Y. A minimal basis semi-ab initio approach to the band structures of semiconductors. *Journal of Physics and Chemistry of Solids* **46**, 977-995 (1985).
34 Yoffe, A. D. Low-dimensional systems: quantum size effects and electronic properties of semiconductor microcrystallites (zero-dimensional systems) and some quasi-two-dimensional systems *Advances in Physics* **42**, 173-262 (1993).
35 Richard, T., Lefebvre, P., Mathieu, H. & Allègre, J. Effects of finite spin-orbit splitting on optical properties of spherical semiconductor quantum dots. *Physical Review B* **53**, 7287–7298 (1996).

36 Masumoto, Y. & Sonobe, K. Size-dependent energy levels of CdTe quantum dots. *Physical Review B* **56**, 9734-9737 (1997).

37 Moret, N. *Exciton Localization and Diffusion in Low-Dimensional Nanostructures Formed on Non-Planar Substrates* Ph.D. thesis, EPFL, (2008).

38 Stroscio, M., A. & Dutta, M. *Phonons in Nanostructures*. (Cambridge University Press, 2004).

39 Hlídek, P., Bok, J., Franc, J. & Grill, R. Refractive index of CdTe: Spectral and temperature dependence. *Journal of Applied Physics* **90**, 1672 (2001).

40 Dabbousi, B. O. *et al.* (CdSe)ZnS Core−Shell Quantum Dots: Synthesis and Characterization of a Size Series of Highly Luminescent Nanocrystallites. *The Journal of Physical Chemistry B* **101**, 9463–9475 (1997).

41 Lauhon, L. J., Gudiksen, M. S., Wang, D. & Lieber, C. M. Epitaxial core–shell and core–multishell nanowire heterostructures. *Nature* **420**, 57-61 (2002).

42 Kim, S., Fisher, B., Eisler, H.-J. & Bawendi, M. Type-II Quantum Dots: CdTe/CdSe(Core/Shell) and CdSe/ZnTe(Core/Shell) Heterostructures. *Journal of The American Chemical Society* **125**, 11466–11467 (2003).

43 Villars, P. & Calvert, L. D. *Pearson's Handbook of Crystallographic Data for Intermetallic Phases*. (ASM International, 1991).

44 Masui, H., Cruz, S. C., Nakamura, S. & DenBaars, S. P. Geometrical Characteristics and Surface Polarity of Inclined Crystallographic Planes of the Wurtzite and Zincblende Structures. *Journal of Electronic Materials* **38**, 756-760 (2009).

45 Yu, W. W., Qu, L., Guo, W. & Peng, X. Experimental Determination of the Extinction Coefficient of CdTe, CdSe, and CdS Nanocrystals. *Chemistry of Materials* **15**, 2854–2860 (2003).

46 Smith, A. M. & Nie, S. Semiconductor Nanocrystals: Structure, Properties, and Band Gap engineering. *Accounts of Chemical Research* **43**, 190-200 (2010).

47 Boieriu, P., Sporken, R., Xin, Y., Browning, N. D. & Sivananthan, S. Wurtzite CdS on CdTe grown by molecular beam epitaxy. *Journal of Electronic Materials* **29**, 718-722 (2000).

48 Manna, L., Millirion, D. J., Meisel, A., Scher, E. C. & Alivisatos, A. P. Controlled growth of tetrapod-branched inorganic nanocrystals. *Nature Materials* **2**, 382 - 385 (2003).

49 Milliron, D. J. *et al.* Colloidal nanocrystal heterostructures with linear and branched topology. *Nature* **430**, 190-195 (2004).

50 Toyama, T., Matsune, K., Oda, H., Ohta, M. & Okamoto, H. X-ray diffraction study of CdS/CdTe heterostructure for thin-film solar cell: influence of CdS grain size on subsequent growth of (111)-oriented CdTe film. *Journal of Physics D: Applied Physics* **39**, 1537-1542 (2006).

51 Fiore, A. *et al.* Tetrapod-Shaped Colloidal Nanocrystals of II-VI Semiconductors Prepared by Seeded Growth. *Journal of the American Chemical Society* **191**, 2274–2282 (2009).

52 McDaniel, H. & Shim, M. Size and Growth Rate Dependent Structural Diversification of Fe_3O_4/CdS Anisotropic Nanocrystal Heterostructures. *ACS Nano* **3**, 434-440 (2009).

53 van Embden, J., Jasieniak, J. & Mulvaney, P. Mapping the Optical Properties of CdSe/CdS Heterostructure Nanocrystals: The Effects of Core Size and Shell Thickness. *Journal of the American Chemical Society* **131**, 14299–14309 (2009).

54 McBride, J., Treadway, J., Feldman, L. C., Pennycook, S. J. & Rosenthal, S. J. Structural Basis for Near Unity Quantum Yield Core/Shell Nanostructures. *Nano Letters* **6**, 1496–1501 (2006).

55 Hines, M. A. & Guyot-Sionnest, P. Synthesis and Characterization of Strongly Luminescing ZnS-Capped CdSe Nanocrystals. *The Journal of Physical Chemistry* **100**, 468–471 (1996).
56 Gannaway, J. N. & Sheppard, C. J. R. Second-harmonic imaging in the scanning optical microscope. *Optical and Quantum Electronics* **10**, 435-439 (1978).
57 Freund, I. & Deutsch, M. Second-harmonic microscopy of biological tissue. *Optics Letters* **11**, 94-96 (1986).
58 Boyd, R. W. *Nonlinear Optics*. 3 edn, (Academic Press, 2008).
59 Le Xuan, L. *et al.* Balanced homodyne detection of second-harmonic generation from isolated subwavelength emitters. *Applied Physics Letters* **89**, 121118-121121 (2006).
60 Yazdanfar, S., Laiho, L. H. & So, P. T. C. Interferometric second harmonic generation microscopy. *Optics Express* **12**, 2739-2745 (2004).
61 Anceau, C., Brasselet, S. & Zyss, J. Local orientational distribution of molecular monolayers probed by nonlinear microscopy. *Chemical Physics Letters* **411**, 98-102 (2005).
62 Slablab, A. *et al.* Efficient second-harmonic generation from a single gold dimer. *Physical Review Letters, in submission* (2010).
63 Anceau, C., Brasselet, S., Zyss, J. & Gadenne, P. Local second-harmonic generation enhancement on gold nanostructures probed by two-photon microscopy. *Optics Letters* **28**, 713-715 (2003).
64 Denk, W., Strickler, J. H. & Webb, W. W. Two-photon laser scanning fluorescence microscopy. *Science* **248**, 73-76 (1990).
65 Zipfel, W. R. *et al.* Live tissue intrinsic emission microscopy using multiphoton-excited native fluorescence and second harmonic generation. *PNAS* **100**, 7075-7080 (2003).
66 Campagnola, P. J., de Wei, M., Lewis, A. & Loew, L. M. High-Resolution Nonlinear Optical Imaging of Live Cells by Second Harmonic Generation. *Biophysical Journal* **77**, 3341–3349 (1999).
67 Campagnola, P. J. *et al.* Three-dimensional high-resolution second-harmonic generation imaging of endogenous structural proteins in biological tissues. *Biophysical Journal* **82**, 493-508 (2002).
68 Göppert, M. Über die Wahrscheinlichkeit des Zusamenwirkens Zweier Lichtquanten in einem Elementarakt. *Die Naturwissenschaften*, **17**, 932 (1929).
69 Göppert-Mayer, M. Über Elementarakte mit zwei Quantensprüngen. *Ann. Phys.* **9**, 273-294 (1931).
70 Xu, C. & Webb, W. W. Measurements of two-photon excitation cross-sections of molecular fluorophores with data from 690 nm to 1050 nm. *Journal of Optical Society of America B* **13**, 481-491 (1996).
71 Xu, C., Zipfel, W., Shear, J. B., Williams, R. M. & Webb, W. W. Multiphoton fluorescence excitation: new spectral windows for biological nonlinear microscopy. *PNAS* **93**, 10763-10768 (1996).
72 Zipfel, W. R., Williams, R. M. & Webb, W. W. Nonlinear magic: multiphoton microscopy in the biosciences. *Nature Biotechnology* **21**, 1369-1377 (2003).
73 Masters, B. R. & So, P. T. C. *Handbook of Biomedical Nonlinear Optical Microscopy*. (Oxford University Press, Inc., New York, 2008).
74 Larson, D. R. *et al.* Water-Soluble Quantum Dots for Multiphoton Fluorescence Imaging in Vivo. *Science* **300**, 1434 - 1436 (2003).
75 Floc'h, V. L. *Caractérisation de l'organisation moléculaire par microscopie non-linéaire cohérente et incohérente* Ph.D. thesis, ENS Cachan, (2004).

76 Franken, P. A., Hill, A. E., Peters, C. W. & G., W. Generation of Optical Harmonics. *Physical Review Letters* **7**, 118-119 (1961).

77 Sutherland, R. L. *Handbook of Nonlinear Optics*. (Marcel Dekker, Inc., 2003).

78 Zyss, J. & Oudar, J. L. Relations between microscopic and macroscopic lowest-order optical nonlinearities of molecular crystals with one- or two-dimensional units. *Physical Review A* **26**, 2028-2048 (1982).

79 Moreaux, L., Sandre, O., Charpak, S., Blanchard-Desce, M. & Mertz, J. Coherent Scattering in Multi-Harmonic Light Microscopy. *Biophysical Journal* **80**, 1568-1574 (2001).

80 Kielich, S. *Molekularna Optyka Nieliniowa*. (PWN, 1977).

81 Malmqvist, L. & Hertz, H. M. Second-harmonic generation in optically trapped nonlinear particles with pulsed lasers. *Applied Optics* **34**, 3392-3397 (1995).

82 Bohren, C. F. & Huffman, D. R. *Absorption and Scattering of Light by Small Particles*. (Wiley-VCH, 2004).

83 Gauderon, R., Lukins, P. B. & Sheppard, C. J. R. Optimization of second-harmonic generation microscopy. *Micron* **32**, 691-700 (2001).

84 Johnson, J. C. *et al.* Near-Field Imaging of Nonlinear Optical Mixing in Single Zinc Oxide Nanowires. *Nano Letters* **2**, 279–283 (2002).

85 Johnson, J. C. *et al.* Ultrafast Carrier Dynamics in Single ZnO Nanowire and Nanoribbon Lasers. *Nano Letters* **4**, 197–204 (2004).

86 Nakayama, Y. *et al.* Tunable nanowire nonlinear optical probe. *Nature* **447**, 1098-1101 (2007).

87 Magrez, A. *et al.* Growth of Single-Crystalline $KNbO_3$ Nanostructures. *The Journal of Physical Chemistry B* **110**, 58–61 (2006).

88 Bonacina, L. *et al.* Polar $Fe(IO_3)_3$ nanocrystals as local probes for nonlinear microscopy. *Applied Physics B - Lasers nad Optics* **87**, 399-403 (2007).

89 Hsieh, C.-L., Pu, Y., Grange, R. & Psaltis, D. Second harmonic generation from nanocrystals under linearly and circularly polarized excitations. *Optics Express* **18**, 11917-11932 (2010).

90 Le Xuan, L. *Génération de seconde-harmonique des nanoparticules* Ph.D. thesis, ENS Cachan, (2009).

91 Bihari, B., Kumar, J., Stauf, G. T., Buskirk, P. C. V. & Hwang, C. S. Investigation of barium titanate thin films on MgO substrates by second-harmonic generation. *Journal of Applied Physics* **76**, 1169-1175 (1994).

92 Adachi, S. *Properties of Group-IV, III-V and II-VI Semiconductors*. (John Wiley & Sons, Ltd., 2006).

93 Bieniewski, T., M. & Czyzak, S., J. Refractive indexes of single hexagonal ZnS and CdS crystals. *Journal of Optical Society of America* **53**, 496-497 (1963).

94 Shoji, I., Kondo, T., Kitamoto, A., Shirane, M. & Ito, R. Absolute scale of second-order nonlinear-optical coefficients. *Journal of Optical Society of America B* **14**, 2268-2294 (1997).

95 Zappettini, A., Pietralunga, S. M., Milani, A., Martinelli, M. & Mycielski, A. Measurements of second-order susceptibility at λ=1.5 μm in CdTe-based ternary alloys for efficient wavelength conversion. *Journal of Applied Physics* **88**, 4913-4915 (2000).

96 Michalet, X. *et al.* Quantum Dots for Live Cells, in Vivo Imaging, and Diagnostics. *Science* **307**, 538-544 (2005).

97 Pinaud, F. *et al.* Advances in fluorescence imaging with quantum dot bio-probes. *Biomaterials* **27**, 1679-1687 (2006).

98 Medintz, I. L., Mattoussi, H. & Clapp, A. R. Potential clinical applications of quantum dots *International Journal of Nanomedicine* **3**, 151-167 (2008).
99 Born, M. & Wolf, E. *Principles of Optics*. seventh edn, (Cambridge University Press, 1999).
100 Mertz, J. & Moreaux, L. Second-harmonic generation by focused excitation of inhomogeneously distributed scatterers. *Optics Communications* **196**, 325-330 (2001).
101 Rayleigh, L. Investigations in optics with special reference to the spectroscope. *Philosophical Magazine* **8**, 261-274 (1879).
102 Goodman, J. W. *Introduction to Fourier Optics*. second edn, (The McGraw-Hill Companies, Inc., 1996).
103 Abbe, E. Beiträge zur Theorie des Mikroskops und der mikroskopischen Wahrnehmung. *Archiv für Mikroskopische Anatomie* **9**, 413-468 (1873).
104 Michalet, X. & Weiss, S. Using photon statistics to boost microscopy resolution. *PNAS* **103**, 4797-4798 (2006).
105 Becker, W. *Advanced Time-Correlated Single Photon Counting Techniques*. (Springer-Verlag, 2005).
106 Becker, W. *et al.* Time-resolved detection and identification of single analyte molecules in microcapillaries by time-correlated single-photon counting (TCSPC). *Review of Scientific Instruments* **70**, 11149677-11149684 (1999).
107 Patterson, G. H. & Piston, D. W. Photobleaching in Two-Photon Excitation Microscopy. *Biophysical Journal* **78**, 2159-2162 (2000).
108 Nirmal, M. *et al.* Fluorescence intermittency in single cadmium selenide nanocrystals. *Nature* **383**, 802-804 (1996).
109 Frantsuzov, P., Kuno, M., Jankó, B. & Marcus, R. A. Universal emission intermittency in quantum dots, nanorods and nanowires. *Nature Physics* **4**, 519-522 (2008).
110 Stefani, F. D., Hoogenboom, J. P. & Barkai, E. Beyond quantum jumps: Blinking nanoscale light emitters. *Physics Today* **62**, 34-39 (2009).
111 Rosen, S., Schwartz, O. & Oron, D. Transient Fluorescence of the Off State in Blinking CdSe/CdS/ZnS Semiconductor Nanocrystals Is Not Governed by Auger Recombination. *Physical Review Letters* **104**, 1574041-1574044 (2010).
112 Son, D. H., Wittenberg, J. S., Banin, U. & Alivisatos, A. P. Second Harmonic Generation and Confined Acoustic Phonons in Highly Excited Semiconductor Nanocrystals. *The Journal of Physical Chemistry B* **110**, 19884–19890 (2006).
113 Cao, Y. C. & Wang, J. One-Pot Synthesis of High-Quality Zinc-Blende CdS Nanocrystals. *Journal of American Chemical Society* **126**, 14336–14337 (2004).
114 Cao, H., Wang, G., Zhang, S., Zhang, X. & Rabinovich, D. Growth and Optical Properties of Wurtzite-Type CdS Nanocrystals. *Inorganic Chemistry* **45**, 5103–5108 (2006).
115 Extermann, J. *et al.* Nano-FROG: Frequency resolved optical gating by a nanometric object. *Optics Express* **16**, 10405-10411 (2008).
116 Brasselet, S. *et al. In Situ* Diagnostics of the Crystalline Nature of Single Organic Nanocrystals by Nonlinear Microscopy. *Physical Review Letters* **92**, 2074011-2074014 (2004).
117 Le Floc'h, V., Brasselet, S., Roch, J.-F. & Zyss, J. Monitoring of Orientation in Molecular Ensembles by Polarization Sensitive Nonlinear Microscopy. *The Journal of Physical Chemistry B* **107**, 12403–12410 (2003).
118 Brasselet, S. & Zyss, J. Nonlinear polarimetry of molecular crystals down to the nanoscale. *Comptes Rendus Physique* **8**, 165-179 (2007).

119 Sandeau, N. *et al.* Defocused imaging of second harmonic generation from a single nanocrystal. *Optics Express* **15**, 16051-16060 (2007).

120 Peng, X. *et al.* Shape control of CdSe nanocrystals. *Nature* **404**, 59-61 (2000).

121 Scher, E. C., Manna, L. & Alivisatos, A. P. Shape control and applications of nanocrystals. *Philosophical Transactions of The Royal Society A* **361**, 241-257 (2003).

122 Jun, Y.-w., Choi, J.-s. & Cheon, J. Shape Control of Semiconductor and Metal Oxide Nanocrystals through Nonhydrolytic Colloidal Routes. *Angewandte Chemie International Edition* **45**, 3414-3439 (2006).

123 Kudera, S. *et al.* Synthesis routes for the growth of complex nanostructure. *Physica E: Low-dimensional Systems and Nanostructures* **37**, 128-133 (2007).

124 Figuerola, A. *et al.* Epitaxial CdSe-Au Nanocrystal Heterostructures by Thermal Annealing. *Nano Letters* **10**, 3028–3036 (2010).

125 He, J., Lo, S. S., Kim, J. & Scholes, G. D. Control of Exciton Spin Relaxation by Electron−Hole Decoupling in Type-II Nanocrystal Heterostructures. *Nano Letters* **8**, 4007-4013 (2008).

126 Brasselet, S. & Zyss, J. Multipolar molecules and multipolar fields: probing and controlling the tensorial nature of nonlinear molecular media. *Journal of Optical Society of America B* **15**, 257-288 (1998).

127 Le Floc'h, V. *et al.* High efficiency and quadratic optical properties of a fully optimized 2D octupolar crystal by nonlinear microscopy. *Advanced Materials* **17**, 196-200 (2005).

128 Zyss, J. Molecular engineering implications of rotational invariance in quadratic nonlinear optics: From dipolar to octupolar molecules and materials. *Journal of Chemical Physics* **98**, 6583 (1993).

129 Alouani, M., Brey, L. & Christensen, N. E. Calculated optical properties of semiconductors. *Physical Review B* **37**, 1167-1179 (1988).

130 Baker, A. K. & Dyer, P. E. Refractive-index modification of polymethylmethacrylate (PMMA) thin films by KrF-laser irradiation. *Applied Physics A: Materials Science & Processing* **57**, 543-544 (1993).

131 Petrov, D. V., Santos, B. S., Pereira, G. A. L. & de Mello Donegá, C. Size and Band-Gap Dependences of the First Hyperpolarizability of CdxZn1-xS Nanocrystals. *The Journal of Physical Chemistry B* **106**, 5325–5334 (2002).

132 Santos, B. S., Pereira, G. A. L., Petrov, D. V. & de Mello Donegá, C. First hyperpolarizability of CdS nanoparticles studied by hyper-Rayleigh scattering. *Optics Communications* **178**, 187-192 (2000).

133 Prasad, P. N. & Williams, D. J. *Introduction to Nonlinear Optical Effects in Molecules and Polymers*. (John Wiley & Sons Inc., 1991).

134 Campo, J., Desmet, F., Wenseleers, W. & Goovaerts, E. Highly sensitive setup for tunable wavelength hyper-Rayleigh scattering with parallel detection and calibration data for various solvents. *Optics Express* **17**, 4587-4604 (2009).

135 Kanis, D. R., Ratner, M. A. & Marks, T. J. Design and construction of molecular assemblies with large second-order optical nonlinearities. Quantum chemical aspects. *Chemical Reviews* **94**, 195-242 (1994).

136 Wang, L.-W. & Zunger, A. Pseudopotential calculations of nanoscale CdSe quantum dots. *Physical Review B* **53**, 9579-9582 (1996).

137 Woodford, J. N., Pauley, M. A. & Wang, C. H. Solvent Dependence of the First Molecular Hyperpolarizability of p-Nitroaniline Revisited. *The Journal of Physical Chemistry A* **101**, 1989–1992 (1997).

138 Pantazis, P., Maloney, J., Wu, D. & Fraser, S. E. Second harmonic generating (SHG) nanoprobes for in vivo imaging. *PNAS* **107**, 14535-14540 (2010).

139 Yao, J., Larson, D. R., Vishwasrao, H. D., Zipfel, W. R. & Webb, W. W. Blinking and nonradiant dark fraction of water-soluble quantum dots in aqueous solution. *PNAS* **102**, 14284-14289 (2005).